

Base Catalysed Hydrothermal Reform- mation of Kraft Lignin

zur Erlangung des akademischen Grades eines

Doktors der Ingenieurwissenschaften

von der Fakultät für Chemieingenieurwesen und Verfahrenstechnik
des Karlsruher Instituts für Technologie (KIT) genehmigte

Dissertation

von

Malte Otromke

aus Lüneburg

Tag der mündlichen Prüfung: 17.05.2018

Erster Gutachter: Prof. Dr. Jörg Sauer

Zweite Gutachterin: Prof. PhD Marie-Pierre Laborie

Danksagung

Auch diese Dissertation ist unterfüttert mit den hilfreichen Ideen und Taten Dritter. An erster Stelle steht hier natürlich meine Frau Marina, die mir immer wieder vor Augen führte, dass jede Durststrecke überwunden werden kann. Außerdem meine kleine Tochter Lyra, die mir die wichtigen Dinge des Lebens wieder näherbrachte. Meistens so gegen drei Uhr nachts.

Danken möchte ich auch an dieser Stelle meinem Betreuer vom KIT, Herrn Professor Sauer. Diverse Diskussionen und seine Herangehensweise ließen mich einige Hürden, gerade in der Reaktorkonstruktion, leichter meistern. Auch meine drei Betreuer vom Fraunhofer ISE, Thomas Aicher, Achim Schaadt und Robin White gaben mir die Freiräume und Unterstützung, die notwendig waren.

Ganz besonderer Dank gebührt dem Team-Dendro am ISE. In order of appearance: Lara Theiss, Mrs. Guajakol. Viele interessante Diskussionen und ihre pragmatische Art waren gerade zu Beginn sehr hilfreich. Dies führte auch zu einem zweiten späteren Gastauftritt im Reaktorbau und diversen: „Wir haben wieder eine Spritze am GC verloren.“. Anna Wunsch, mit niedermolekularen organischen Säuren bis einschließlich Buttersäure am großen Reaktor bei 40 bar: „Ich glaube da ist was undicht...“ Benedikt Will mit unserem ersten kontinuierlichen selbstgebauten Testreaktor: „Kleiner, aber weniger undicht.“ Monika Bosilj mit Weizenstroh + Ba(OH)₂ -> Milchsäure: „The smell of the stuff has some nuances of weird and a lot nuances of disgusting.“ Sandy Lama mit den ersten Versuchen des Ni-Kats vom MPI in Golm: „We can use Raman, it will give us the same ambiguous results.“ Ahmed Ayad, der mir beim Umbau des Reaktors und dessen Wiederinbetriebnahme zur Seite stand. Diskussionen hinsichtlich H₂ inklusive: „Hydrogen? We use hydrogen!?!“ Alex Impola, der im Labor die meisten kontinuierlichen Versuche betreute und zum Glück keine Acro-Yoga session im Abzug anbot. Und natürlich Heather Buckley, die wesentlich mit ihrer Erfahrung im Labor und ihren Kenntnissen im Bereich der Chemie und Giraffen zum Erfolg dieser Arbeit beitrug: „How do we improve our analytics? – Well, we could yell at it.“ Nicht Team-Dendro aber genauso wichtig: Katharina „Kadda“ Pautsch meine Bürokollegin ohne die ich sinnlose Selbstgespräche hätte führen müssen. Denn: Sinnlose Gespräche führt man am besten zu zweit. Und Alexander Susdorf, den Meister des GC.

Weiterhin geht ein großes Dankeschön an Harald Scherer von der Uni Freiburg für diverse 2D HSQC Messungen, sowie an Zeyneb Ygit vom IKFT am KIT für die Messungen am ¹³C CP MAS solid state NMR.

Zusammenfassung

Das in der Papierindustrie verarbeitete Holz besteht zu etwa 20 – 30 wt.% aus Lignin, welches potentiell als nachwachsender Rohstoff für aromatische Grundchemikalien dienen kann. Zurzeit wird dieses Lignin energetisch verwertet und stellt die Versorgung der Papiermühle Wärme und Elektrizität sicher. Mit dem Aufkommen neuer Technologien zum Ausfällen des Lignins aus den Prozessströmen der Papiermühlen (vgl. LignoBoost® und LignoForce™), wird die Verfügbarkeit von Lignin im Allgemeinen und Kraft Lignin (KL) im Besonderen in Zukunft zunehmen. Dieses Lignin als Grundlage für diverse Chemikalien und Materialien verwendet werden, was aus ökonomischer und ökologischer Perspektive vielversprechender ist. In diesem Rahmen ist insbesondere die Möglichkeit als Karbonfaserprekursor zu nennen, welche in der aktuellen Forschung großes Interesse genießt. Einerseits macht der hohe Kohlenstoffanteil von ca. 60 wt.% macht KL zu einem vielversprechenden Kandidaten für Karbonfasern, andererseits führt die chemische Struktur und Heterogenität zu Herausforderungen hinsichtlich des Spinnens, Stabilisierens und Karbonisierens. Dies macht eine Vorbehandlung notwendig, welche einfach und kostengünstig ist. Der Fokus dieser Arbeit liegt auf der Entwicklung eines Prozesses basierend auf einer Fest-Flüssig-Extraktion und einer anschließenden basisch katalysierten Reformierung von technischen Weichholz-KL mit dem Ziel die thermische Stabilität und Kohlenstoffanteil zu erhöhen und gleichzeitig die Polydispersität (PDI) zu erniedrigen.

In einem ersten Schritt wurde das KL getrocknet und mittels CH₃OH-(MeOH)-Extraktion in zwei Fraktionen geteilt. Dies erzeugte eine lösliche niedermolekulare Fraktion (LMW, ca. 20 wt.%) und eine unlösliche hochmolekulare Fraktion (HMW, ca. 80 wt.%). Der darauffolgende Prozess für HMW-Fraktion wurde unter der Prämisse ausgewählt, dass er einfach in eine Kraftmühle zu integrieren sei. Die Fraktion wurde in 1 M NaOH (aq) gelöst und in einem kontinuierlichen Strömungsrohr bei 300 °C für 8 bis 24 min gekocht. Das Produkt wurde durch schrittweiser Fällung mittels HCl (aq) aus der Reaktionslösung gewonnen. Hierbei entstanden drei Fraktionen: pH 10 Feststoff, pH 2 Feststoff und pH 2 wässrige Phase. Die Feststofffraktionen zeigten einen klaren Anstieg in thermischer Stabilität, eine um den Faktor Drei erhöhte Löslichkeit in MeOH und eine Erhöhung des Kohlenstoffanteils auf etwa 70 wt.%. Die mittlere Molmasse (M_w) wurde um ca. 66% reduziert was mit einer Verringerung der PDI auf 35% des Ursprungwertes einherging. Die Analyse mittels ¹³C magic angle spinning nuclear magnetic resonance (CP MAS NMR) zeigte eine signifikante Verringerung aller Signale, was auf eine Reduzierung an Heterogenität und ein Verschmelzen von aromatischen Ringen hinweist. Mit Hilfe von 2D heteronuclear single quantum correlation (HSQC) NMR Spektroskopie konnte eine starke Zunahme an äußeren Methyl- und Ethylgruppen nach relativ kurzer Verweilzeit ($t_{\text{retention}}$) nachgewiesen werden. Der Grad an Demethoxylierung und das Spalten von Ethergruppen konnte mittels dieser Methode auch quantitativ beschrieben werden. Attenuated total reflection fourier transformed infrared (ATR FT-IR) Spektroskopie bestätigte diese Ergebnisse und bietet somit eine

schnelle und einfache Möglichkeit die Produkte diesbezüglich zu bewerten. Thermogravimetrische Analysen zeigten eine stark erhöhte thermische Stabilität, während differential scanning calorimetry (DSC) in den Produkten keine klare Glassübergangstemperatur nachweisen konnte.

Eine ökonomische Bewertung des entwickelten Prozesses ergab, dass mit einer Investition von 18.54 M€ über zwei Jahre eine Anlage für die Verarbeitung von 75 t/d in eine Kraftmühle implementiert werden kann. Mit einem Preis von 1.600 €/t und einem angenommenen ROI von 15% sind die Hauptkostenfaktoren das Lignin (62,3%), Abschreibungen (11,6%) und Energie (10,5%).

Eine weitere Möglichkeit zur Verwertung von Lignin und Ligninderivaten ist die Umwandlung in Plattformchemikalien. In diesem Zusammenhang wird im letzten Kapitel dieser Arbeit die hydrothermale Reformierung der Ligninmodellsubstanzen Guajakol und Syringol über geträgerte Pt-Katalysatoren untersucht. Ein abgeleitetes Reaktionsnetzwerk und dessen kinetische Parameter werden unter Zuhilfenahme eines Minimalwertproblems bestimmt. Die Reaktionen wurden mit und ohne Zugabe von stöchiometrischen Mengen von MeOH durchgeführt. Letzteres dient als *in-situ* Wasserstoffdonor und gibt eine Möglichkeit die Reaktionen innerhalb des Netzwerkes in Richtung der gewünschten Produkte zu beeinflussen.

Abstract

Lignin comprises *ca.* 20 - 30 wt.% of the wood that is used in the pulp & paper industry and is a potentially viable renewable source of aromatic chemicals. Conventionally, lignin product streams from pulping are used as an energy source. With the introduction of new technologies at pulp mills (e.g. LignoBoost® or LignoForce™), it is expected that the availability of lignin and particularly Kraft Lignin (KL) will increase in the future. Instead of using this bio-resource as energy carrier for fuelling the mills' processes, the lignin streams could be used as a platform from which to produce a number of chemicals and materials. In this context, a recently considered possibility is the usage of KL as a precursor for the production of carbon fibres. The high carbon content of KL (*ca.* 60%) makes it a promising candidate for this application, although its chemical structure / heterogeneity still implies a number of challenges regarding successful spinning, stabilisation, and carbonisation. Therefore, it is necessary to improve the properties of lignin (e.g. KL) for improved usage in the three aforementioned methods, ideally performed in an as easy to apply pre-process as possible. In this context, the focus of this thesis is upon the development of a process based on solvent extraction and a subsequent base catalysed reformation of technical softwood KL with the aim of increasing product thermal stability and carbon content whilst reducing the polydispersity (PDI).

In a first step, the lignin was dried and divided into two fractions *via* CH₃OH (denoted hereon as MeOH) extraction, to produce a MeOH soluble low molecular weight fraction (LMW, *ca.* 20 wt.%) and an insoluble high molecular weight fraction (HMW, *ca.* 80 wt.%). The subsequent process for the HMW fraction was chosen, so that it can easily be integrated into a pulp mill. The fraction was dissolved at 10 wt.% in 1 M NaOH (aq) and treated in a continuous reactor at 300 °C for 8 to 24 min. The product was precipitated by step-wise acidification with HCl (aq) and three fractions were obtained: pH 10 solids, pH 2 solids and a pH 2 aqueous phase. It was found that the precipitated solids experienced a dramatic increase in thermal stability, their solubility in MeOH increased up to three-fold, and the carbon content increased to 70%. The average molecular weight (*M_w*) decreased by *ca.* 66%, whilst PDI was reduced by 35%. Analysis by ¹³C cross polarisation magic angle spinning nuclear magnetic resonance (CP MAS NMR) showed a significant decrease in the diversity of carbon environments and increased material condensation. 2D heteronuclear single quantum correlation (HSQC) NMR spectroscopy analysis indicated a strong increase in resonances associated with aliphatic side chains after short retention time (*t_{retention}*), with the degree of demethoxylation and cleavage of ether groups quantitatively assessed. Attenuated total reflection fourier transformed infrared (ATR FT-IR) spectroscopy confirmed these findings and can be used as a fast and convenient possibility of product evaluation. Thermogravimetric analysis showed a strong increase in thermal stability, while differential scanning calorimetry (DSC) indicated a lack of a clear glass transition temperature.

An economical evaluation of the developed process showed that with an investment of 18.54 M€ and a construction time of two years, a plant for 75 t/d could be implemented at a pulp mill. With a price of 1,600 €/t and an assumed ROI of 15%, the main cost drivers were found to be the lignin (62.3%), depreciation (11.6%), and energy (10.5%).

Another possibility regarding the valorisation of lignin and lignin-derived products is the production of platform chemicals. In this regard, the last chapter of this thesis introduces and discusses the hydrothermal reformation of lignin-related model compounds, namely guaiacol and syringol, employing supported Pt catalysis. A reaction network is proposed and associated kinetic parameters were determined *via* solving of a minimum value problem. Reactions were performed with and without the addition of stoichiometric amounts of MeOH, which served as an *in-situ* hydrogen donor and was used as a handle to direct the reaction pathways towards desired products.

Table of contents

Zusammenfassung.....	iii
Abstract.....	v
Table of contents.....	vii
List of figures.....	ix
List of tables.....	xiii
List of abbreviations.....	xvi
1 Introduction.....	17
1.1 Motivation and Objectives.....	18
1.2 Technical Lignin: Availability, Structure, and Potential Products.....	19
1.2.1 Paper Mills and Lignin Production Processes.....	19
1.2.2 The Chemical Structure of Lignin.....	22
1.2.3 Technical Lignin.....	25
1.3 Kraft Lignin as a Precursor in Materials Synthesis.....	31
1.3.1 Carbon Fibres.....	31
2 Materials and Methods.....	35
2.1 Chemicals.....	35
2.1.1 Reagents.....	35
2.1.2 Solvents.....	35
2.1.3 Gases.....	35
2.2 Methanol Extraction from Kraft Lignin.....	35
2.3 Continuous Hydrothermal Reactions.....	36
2.3.1 Reactor Set-Up and Reaction Runs.....	36
2.3.2 Feed Preparation and Product Treatment.....	38
2.4 Analytical Techniques.....	41
2.4.1 Gel Permeation Chromatography (GPC).....	41
2.4.2 Elemental Analysis (EA).....	42
2.4.3 Thermogravimetric Analysis (TGA/DTG).....	42
2.4.4 Differential Scanning Calorimetry (DSC).....	42
2.4.5 Gas Chromatography (GC).....	42
2.4.6 Fourier Transformed Infrared Spectroscopy (FT-IR).....	43
2.4.7 Solid State ¹³ C Cross Polarisation Magic Angle Spinning (CP MAS) NMR.....	43
2.4.8 Liquid Phase 2D Heteronuclear Single Quantum Correlation (HSQC) NMR.....	43
2.4.9 Liquid Phase ¹ H and ¹³ C NMR.....	44
2.4.10 Gas Sorption (BET).....	45
3 Solvent Extraction from Lignin.....	46
3.1 Theory and Prior Art.....	46
3.2 Results & Discussion.....	51
3.2.1 Gel Permeation Chromatography (GPC).....	52
3.2.2 Elemental Analysis (EA).....	55
3.2.3 Thermogravimetric Analysis (TGA/DTG/DSC).....	55

3.2.4	Gas Chromatography (GC)	58
3.2.5	¹³ C Cross Polarisation Magic Angle Spinning (CP MAS) NMR	60
3.2.6	¹ H and 2D Heteronuclear Single Quantum Correlation (HSQC) NMR	62
3.2.7	Attenuated Total Reflection Fourier Transform Infrared (ATR FT-IR)	68
3.2.8	Summary & Conclusions	69
4	Base Catalysed, Hydrothermal Treatment of Lignin	71
4.1	Theory and Prior Art	71
4.1.1	A General Mechanistic Description of BCD	72
4.1.2	Reactions of Lignin under Basic, Hydrothermal Conditions	72
4.2	Results & Discussion	76
4.2.1	Runs #B1-5	76
4.2.2	Runs #K1-5	89
4.3	Techno-Economic Evaluation of a Continuous Base Catalysed Depolymerisation of Lignin in a Kraft Mill	122
5	Hydrodeoxygenation of Lignin Model Compounds	131
5.1	Theory and Prior Art	131
5.2	Analytics and Methods	132
5.2.1	Batch Reactions	132
5.2.2	Continuous Reactions	137
5.3	Results & Discussion	138
5.3.1	Pt/ZrO ₂	141
5.3.2	Pt/γ-Al ₂ O ₃	150
5.3.3	Pt/TiO ₂	152
5.3.4	Pt/C	152
5.3.5	Ni/C	152
6	Summary & Outlook	153
	References	156
	Appendix	163

List of figures

Figure 1:	Process scheme for the production of a carbon fibre precursor out of KL.	19
Figure 2:	Flow of chemicals in the Liquor and Lime cycles of a Kraft mill with added LignoBoost® and base catalyzed depolymerization (BCD) technology described in this work.	21
Figure 3:	Structure of native lignin with most occurring bonds described. The three phenylpropanoid monomers constituting the lignin macro molecule are shown on the right. These are comprised of the three base types: (H) p-hydroxy-phenyl, (G) p-guaiacyl, (S) p-syringyl	24
Figure 4:	Lignin cleavage under Kraft process conditions. The formation of the quinone methide intermediate (upper right) leads to a dead end under alkaline pulping conditions. The usage of Na ₂ S enables further cleavage of the intermediate. Scheme adopted and adjusted from Ref. ⁵⁹	27
Figure 5:	Proposed structure of KL. Condensation reactions lead to many ortho-positions being occupied. Sulphur moieties are not included in this structure.....	28
Figure 6:	Mechanism of sulphite pulping under acidic conditions. The R at the α-position is either a proton or a polysaccharide and is replaced by an SO ₃ – group. ¹²	29
Figure 7:	Organosolv process with CH ₃ CH ₂ OH:H ₂ O as solvent. Typical process conditions for the digester are: CH ₃ CH ₂ OH:H ₂ O 6:4, $\vartheta = 180 - 200$ °C and $\tau = 2 - 4$ h. Addition of ca. 1 wt.% H ₂ SO ₄ gives increased delignification and enables a 30 °C lower temperature.	30
Figure 8:	Cost breakd down for the production of carbon fibres from PAN.	31
Figure 9:	Carbon fibre processing steps using a PAN precursor.	32
Figure 10:	Possible structure of mesophase pitch. Structure drawn after information from Newman ⁹³ and Singer ⁹⁴	33
Figure 11:	Sequential dissolution of KL in MeOH. The solution of lignin in MeOH was used as new solvent for each subsequent step.....	36
Figure 12:	Flow diagram of the continuous flow test rig.	37
Figure 13:	Process and analytics overview of the continuous reactions of lignin compounds in 1 M NaOH (aq).	40
Figure 14:	Structural formula of stilbenes (a) and benzodioxocin (b).	51
Figure 15:	Molecular weight distribution of original KL and the MeOH soluble and insoluble fraction after extraction at 250 mg/mL measured via GPC.	53
Figure 16:	(a) m_i/m and (b) n_i/n for specific chain length of KL, HMW, and LMW. The values are generated from the GPC data and the value used in the calculation of n_i is taken as mean value from the ranges (e.g. 15 for 15-20).	54
Figure 17:	DSC traces of the fractions KL, HMW, LMW. Glass transition temperatures were determined via the TA Universal software within the indicated limits.	56
Figure 18:	Thermogravimetric analysis plots of KL and the MeOH insoluble (HMW) and soluble (LMW) fractions (a) and their respective derivatives (b).	57
Figure 19:	¹³ C CP MAS NMR spectra of KL, MeOH soluble fraction (LMW) and MeOH insoluble fraction (HMW).	60
Figure 20:	Chemical structure of TMS ⁺ P. Internal standard used at ¹³ C CP MAS NMR.	62

Figure 21:	Liquid ¹ H NMR spectra of KL, MeOH soluble and MeOH insoluble fraction in DMSO-d ₆63
Figure 22:	Integrated ¹ H NMR spectra of KL, MeOH soluble and MeOH insoluble fraction in DMSO-d ₆ (as normalised to the standard).....63
Figure 23:	2D HSQC NMR spectra of the aromatics region of KL. The areas of G2, G5, and G6 are colour-coded and given as relative areas to the DMSO-d ₆ solvent.66
Figure 24:	Fingerprint region of the ATR FT-IR spectra of KL, MeOH insoluble fraction (HMW), and MeOH soluble fraction (LMW).....69
Figure 25:	Condensation reaction mechanism of guaiacylic lignin units with formaldehyde (FA) as proposed by Chakar and Ragauskas. ¹²⁹72
Figure 26:	Reaction of anisole under hydrothermal basic conditions into phenol and MeOH73
Figure 27:	Yields of the different fractions of the reactions #B.77
Figure 28:	GPC analysis of precipitated solids after reaction at T = 300 °C / tretention = 16 min. (a) the three reactions with HMW as feed compared to HMW and (b) comparison between the precipitates resulting from the three feed types HMW, LMW, and KL.....79
Figure 29:	GPC analysis of precipitated solids after reaction at T = 300 °C / tretention = 16 min in direct comparison to the feed. (a) KL as feed, (b) LMW as feed.80
Figure 30:	(a) mi/m and (b) ni/n for specific chain length of runs #B2, #B4, and #B5 with HMW, LMW, and KL as feed, respectively. The values are generated from GPC data and chain length for Mi calculation is the mean value of the respective number range.....81
Figure 31:	TGA and DTG plots of the pH 10 and pH 2 solids of reactions #B3 (HMW), #B4 (LMW), and #B5 (KL)84
Figure 32:	GC-FID chromatogram of the oil phase of #B3 (154 mg) dissolved in 10 mL acetone. .85
Figure 33:	¹³ C CP MAS NMR spectra of the pH 10 solids of reaction #B1 compared to the HMW fraction.87
Figure 34:	ATR FT-IR spectra of the HMW fraction and the pH 10 and pH 10 solids of reaction #B3.88
Figure 35:	Yields of solids, oil, and undetermined compounds of the kinetic runs #K1-5.....90
Figure 36:	Titration curves of the kinetic runs #K1-5 and the HMW fraction.92
Figure 37:	GPC analysis of the pH 10, pH 2, and oil fractions of the runs at tretention = 8, 16, and 24 min.93
Figure 38:	(a) mi/m and (b) ni/n for specific chain length of the solid fractions runs #K1, #K2, and #K3 at tretention = 8, 16, 24 min, respectively. The values are generated from the GPC data and chain length for Mi calculation is the mean value of the respective number range95
Figure 39:	(a) mi/m and (b) ni/n for specific chain length of the oil fractions of runs #K1, #K2, and #K3 at tretention = 8, 16, 24 min, respectively. The values are generated from the GPC data and chain length for Mi calculation is the mean value of the respective number range.....96
Figure 40:	Elemental composition as a function of tretention for pH 10 and pH 2 solids of the #K runs.....98

Figure 41:	Solid residue of the pH 10 and pH 2 solids from reactions #K as a function of t _{retention}	99
Figure 42:	TG (mass loss as a function of increasing T) analysis of the pH 10 solids (a) and pH 2 solids (b) compared to the HMW fraction, relating to increasing t _{retention}	100
Figure 43:	DTG (mass loss as a function of increasing T) analysis of the pH 10 solids (a) and pH 2 solids (b) compared to the HMW fraction, relating to increasing t _{retention}	101
Figure 44:	DSC traces of the #K runs t _{retention} = 8, 16, and 24 min compared to the KL, HMW (feed); and LMW fractions.	102
Figure 45:	Main GC detectable compounds in the oil fractions of the #K runs as a function of t _{retention}	103
Figure 46:	Solid state ¹³ C CP MAS NMR spectra of the #K1 pH 10 and pH 2 solids (8 min) and #B1 pH 10 solids (16 min).	105
Figure 47:	Liquid phase ¹ H NMR spectra of the HMW fraction and the solids precipitated at t _{retention} = 8, 16, and 24 min. (a) pH 10 solids and (b) pH 2 solids in DMSO-d ₆	106
Figure 48:	Liquid phase ¹ H NMR spectra of the oil fractions recovered at t _{retention} = 8, 16, and 24 min.	107
Figure 49:	DMSO-normalised area integration of the ¹ H NMR spectra for (a) pH 10 solids, (b) pH 2 solids, and (c) the oil fractions.	108
Figure 50:	2D HSQC NMR spectra overview: (a) HMW fraction; pH 10 solids at t _{retention} = (b) 8 min; (c) 16 min; (d) 24 min.	109
Figure 51:	2D HSQC NMR spectra overview: (a) HMW fraction; pH 2 solids at t _{retention} = (b) 8 min; (c) 16 min; (d) 24 min.	110
Figure 52:	(a) 2D HSQC NMR spectrum of the oil fraction at t _{retention} = 16 min. Zoomed on the area for the benzaldehyde groups. (b) Relative area of the two peaks compared to the DMSO-d ₆ peak as a function of t _{retention}	111
Figure 53:	Trends of the G2, G5, and G6 C-H correlations as measured by 2D HSQC of the pH 10 solids (a) and pH 2 solids (b). (c), (d), and (e) show the yields of catechol, vanillin, and acetovanillone calculated via the 2D HSQC data compared to the values determined by GC FID.	113
Figure 54:	Relative areas of the 2D HSQC NMR spectroscopy analysis of the methoxy groups (-OCH ₃) and the area assigned to the β-O-4 linkages. (a) pH 10 solids, (b) pH 2 solids. The values of the 8 min samples for the pH 2 solids are, as discussed in the text, unusually high.	116
Figure 55:	ln(c _i (t)/c ₀) over t _{retention} of the concentrations of the side chain groups of the pH 10 solids determined by 2D HSQC. The values for k are given in the figure along with the R ² of the linear fit.	117
Figure 56:	Evolution of the aliphatics region of the 2D HSQC NMR spectroscopy analysis of (a) pH 10 solids, (b) pH 2 solids.	118
Figure 57:	ATR FT-IR spectra of the #K reactions. (a) pH 10 solids; (b) pH 2 solids; (c) oil; (d) pH 10 solids, pH 2 solids, and oil of run #K3 at t _{retention} = 16 min.	120
Figure 58:	Process flow sheet with mass and energy flows.	124
Figure 59:	NPV for scenario 1 (by-product sold for 400 €/t) as function of plant utilisation.	130

Figure 60:	250 mL batch reactor set-up. Sampling tube volume = 5 mL. The tube was purged after each sample extraction with N ₂	133
Figure 61:	Reaction network for the hydrothermal decomposition of syringol and guaiacol with Pt/metal catalyst including the decomposition of MeOH.	140
Figure 62:	Progression of the reaction of guaiacol in water at T = 245 °C over Pt/ZrO ₂ ; (a) without addition and MeOH, (b) with addition of MeOH.	143
Figure 63:	Comparison between measured values and simulation results for the reaction of guaiacol with Pt/ZrO ₂	144
Figure 64:	Comparison between measured values and simulation results for the reaction of guaiacol with Pt/ZrO ₂ , and addition of MeOH.	145
Figure 65:	Continuous runs with guaiacol in water over Pt/ZrO ₂ catalyst for determination of deactivation. (a) Conversion over loading of the fresh and reactivated catalyst and (b) yield of the main components catechol, phenol, and coke & poly for the runs with the fresh catalyst. At a loading value of 3.5 the run was interrupted for 1 week.	147
Figure 66:	Progression of the reaction of syringol in H ₂ O at 245 °C with Pt/ZrO ₂ catalyst. (a) without addition and MeOH, (b) with addition of MeOH.	149
Figure 67:	$\ln(n(G,S)(t)/n(G,S),0)$ vs. $t_{\text{retention}}$ of the amount of guaiacol or syringol for the reaction over Pt/ZrO ₂ at 245 °C in H ₂ O. For the linear regression of syringol, the first step is omitted, since it probably includes adsorption.	150
Figure 68:	Progression of the reaction of guaiacol in water at 245 °C with Pt/ γ -Al ₂ O ₃ catalyst.	151
Figure 69:	Progression of the reaction of guaiacol in water at 245 °C with Pt/ γ -Al ₂ O ₃ catalyst.	152

List of tables

Table 1:	Reserves over Production (R/P) ratio of the three main fossil fuels	17
Table 2:	Chemical composition of wood species commonly used in pulping processes. ¹⁴	20
Table 3:	Global capacities for pulp production as indicated by the Food and Agricultural Organization (FAO) of the United Nations.....	22
Table 4:	Bond dissociation energies (BDE) of the linkages shown in Figure 3. ¹⁵	24
Table 5:	Abundance of different linkages in woods and grasses in percentage. Values taken from Rinaldi et al., for a detailed description of the linkages the reader is referred to the original source. ¹⁵	25
Table 6:	Feed types and flow rates of the continuous reactions.	38
Table 7:	Yields, elemental composition, methoxyl content and thermal properties of the sequential solvent extraction performed by Mörck et al. ⁶⁹ For thermal properties see Yoshida et al. ¹¹³	48
Table 8:	Molecular weight distribution and thermal properties of the MeOH fractionated softwood KL as reported by Saito et al. ¹⁰⁸	49
Table 9:	Resonance assignment of ¹³ C NMR in DMSO-d ₆ (performed by Saito et al. ¹¹⁴).	49
Table 10:	Molecular weight distribution, elemental analysis, methoxyl content, and thermal properties of the fractionated softwood KL from the Domtar pulp mill as reported by Jiang et al. ¹⁰⁵	50
Table 11:	Elemental analysis and substructures of Domtar KL ¹¹⁵ , Indulin AT, and pine milled wood lignin (MWL)	50
Table 12:	Dissolution of KL in MeOH and MeOH:H ₂ O under ambient conditions at different concentrations ($\rho_{\text{MeOH}} = 0.791 \text{ g/mL}$).....	51
Table 13:	Average molecular weights and polydispersity of the KL after MeOH extraction as determined via GPC.	53
Table 14:	Elemental analysis of KL, LMW, and HMW.....	55
Table 15:	Decomposition temperature (T_d), maximum in DTG, and residual mass at 600 °C of the Domtar KL and the MeOH extracted fractions.	55
Table 16:	Glass transition of the KL, HMW, and LMW fractions determined via DSC.....	56
Table 17:	Hansen solubility parameters of different compounds. ¹⁰²	58
Table 18:	Major monomeric and dimeric compounds in the untreated KL.	59
Table 19:	Chemical shift assignments for the ¹³ C CP MAS NMR spectra of KL, MeOH soluble fraction (LMW) and MeOH insoluble fraction (HMW).	60
Table 20:	Chemical shift assignments for the ¹³ C NMR analysis of lignin.	61
Table 21:	Chemical shift assignments for the ¹ H NMR spectroscopic analysis of lignin.	64
Table 22:	Free G2, G5, and G6 positions per aromatic ring in KL, HMW, and LMW fractions.	66
Table 23:	C9-formula and β -O-4 content of the MeOH extracted lignin.....	67
Table 24:	Aliphatic side chains per 100 C9 units of the original KL and the MeOH insoluble (HMW) and soluble (LMW) fraction	68
Table 25:	Overview of reactions performed with lignin in NaOH (aq).	74

Table 26:	Molecular weight distribution data for #B reactions. Comparison between feed types and solids precipitated at different pHs.	78
Table 27:	Elemental analysis of the #B reactions. Comparison between feed types and solids precipitated at different pHs. The elemental composition of the feed types is added for easier comparison.	82
Table 28:	C ₉ -Formulae of the #B runs and the three fractions from MeOH extraction (The latter are presented without the methoxy groups for better comparison to the #B runs / Values are derived from the elemental analysis).	83
Table 29:	Elemental analysis data regarding the composition and molecular formula of the lost mass for reactions #B.	83
Table 30:	TGA results for the reaction runs #B.	85
Table 31:	Monomer yields of the #B runs determined via GC-FID.	86
Table 32:	Compounds detected via GC-FID analysis of the pH 2 (aq) solution (after being extracted with ethyl acetate).	91
Table 33:	Molecular weight distribution data for the #K1-3 reactions.	93
Table 34:	Elemental Analysis of the #K reactions. Comparison between feed types and solids precipitated at different pHs. The elemental composition of the feed types is added for easier comparison.	97
Table 35:	Elemental analysis and proposed molecular formula of the lost mass for the reactions #K.	97
Table 36:	TG residue data and corresponding DTG peak positions for the pH 10 and pH 2 solids fractions of the #K runs.	99
Table 37:	Change in isobaric specific heat (cp) over temperature for the solids of reactions #K.	103
Table 38:	Oil yield, GC detectables, and monomeric compounds yield of the retention dependent runs #K.	104
Table 39:	C ₉ -formula and β-O-4 content of the #K reactions after 8, 16, and 24 min.	115
Table 40:	General data for the simulation of the process.	122
Table 41:	Net chemicals usage in the base catalysed process implemented into a Kraft mill.	125
Table 42:	Prices for the main components of the different unit operations described in the flow sheet in Figure 58.	126
Table 43:	Yearly absolute and relative variable and fix costs per tonne of product without by-product credits at an average utilisation of 8,000 h/a.	127
Table 44:	Product value and cost overview in correlation with by-product value (see scenarios 1 to 4).	128
Table 45:	Product value and cost overview for a by-product value of 400 €/t in correlation with plant utilisation.	129
Table 46:	Reactions and reactions' rates of the model compounds' reactions starting with Syringol and Guaiacol under hydrothermal conditions.	135
Table 47:	Conversion and yield of the liquid products of the reactions with Guaiacol (G) and Syringol (S) under hydrothermal conditions with different catalysts. Starting concentration 0.024 mol guaiacol in 200 mL H ₂ O, t _{retention} = 10 h / T = 245 °C.	138

Table 48:	Conversion and yield of the gaseous products of the reactions with Guaiacol (G) and Syringol (S) under hydrothermal conditions with different catalysts. Starting concentration 0.024 mol guaiacol in 200 mL H ₂ O, $t_{\text{retention}} = 10 \text{ h}$ / $T = 245 \text{ }^\circ\text{C}$139
Table 49:	Reaction rate starting and final parameters of minimum value problem for the reactions of guaiacol on Pt/ZrO ₂ with and without MeOH addition.142

List of abbreviations

Acronym	Unit	Description
ad(m)t	[t]	air dried (metric) tonnes
ATR		Attenuated total reflection
c_p	[J mol ⁻¹ K ⁻¹]	Isobaric heat capacity
CP MAS		Cross polarisation magic angle spinning
DSC		Differential scanning calorimetry
EA		Elemental analysis
FAO		Food and Agricultural Organization of the United Nations
FID		Flame ionisation detector
FT-IR		Fourier transform infrared
GC		Gas chromatography
GPC		Gel permeation chromatography
HMW		High molecular weight fraction (after MeOH extraction)
HSQC		Heteronuclear single quantum coherence
HTSEC		High temperature size exclusion chromatography
KL		Kraft Lignin
LMW		Low molecular weight fraction (after MeOH extraction)
MS		Mass spectroscopy
NMR		Nuclear magnetic resonance
NPV	[€]	Net present value
OL		Organosolv lignin
TGA		Thermogravimetric analysis
THF		Tetrahydrofuran
$t_{\text{retention}}$	[min]	Retention time
XPS		X-Ray photon scattering

1 Introduction

The usage of fossil reserves (i.e. oil, coal, and gas) and establishment of associated industries to provide not only energy for society but also the production of industrial chemicals and in turn a variety of consumer products (e.g. plastics) has led to a strong dependency on these feedstocks. These fossil reserves, as a consequence of their precursors and the geochemical processes that formed them, are highly condensed carbon-based materials. Therefore, their use, as a consequence of the significant quantity of “bound” carbon, results typically in the emission of CO₂ (and equivalents). In the context of CO₂ emissions, the EU has decided to cut primary energy consumption in 2020 by 20% (relative to 1990), whilst the US Department of Energy (DOE) has a performance goal for new fossil power plants having 60% efficiency (coal higher heating value (HHV)) with > 90% CO₂ capture.^{1,2} These positions have been further strengthened by the recent ratification by a number of countries of the COP21 agreement.³ As a consequence of these agreements and frameworks there is an ever increasing awareness of global climate change and its consequences. To reach these targets and ultimately to establish a sustainable chemical/energy economy, the use of renewable resources is increasingly more important (e.g. for the production of energy carriers and chemicals).

The amount of CO₂ in the atmosphere increased from 280 ppm (pre-industrial level) to ca. 400 ppm at the time of writing and strongly correlates with an observed increase in global temperature and associated climate change.⁴ Furthermore, the supply of fossil fuels is limited. The BP 2016 Statistical Review of World Energy gives Reserves/Production (R/P) ratios for oil and gas of ca. 50 years and for coal of 100 years (Table 1).⁵ While these ratios are adjusted every year and “peak oil” has been forecast for the next five years to come in the last sixty years, eventually these sources will become economically unviable. Olah *et al.* give ranges of up to 100 years for oil and gas and 300 years for coal when more sophisticated sources are tapped.⁶

Table 1: Reserves over Production (R/P) ratio of the three main fossil fuels

Resource	Total Proved Reserves	Yearly Production	R/P ratio
Oil	239.4 Gt	4.36 Gt	50.7
Coal	891.5 Gt	3.83 Gt (of oil equivalent)	114
Gas	186.9 x 10 ¹² m ³	3.5 x 10 ¹² m ³	52.8

Therefore, in the long run, society must reduce its dependence on the energy stored in fossil resources and switch to the use of renewables (e.g. solar, wind, biomass, *etc.*). This can in large be performed *via* the elaboration and establishment of circular, integrated chemical/energy economies (e.g. H₂-, CH₃OH-based economies supported by biorefinery concepts).⁶⁻⁸ In this context, the provision of chemical building blocks from biomass, which otherwise would have been supplied *via* fossil resources, is foreseen as a key component in achieving this aim. Schmieid *et al.* have shown that using 1st generation energy crops could potentially supply up to 100 EJ per annum in 2050, which would cover ca. 70% of the estimated global energy demand per year, but also hint at the

problematic situation with competition of the land usage to food crops and monocropping.⁹ Using biomass as a long-lasting construction material is also a possibility with regard to reducing atmospheric CO₂ concentration, provided of course that this biomass (or “carbon sink”) can be replenished in an appropriate and time scale relevant manner.

The use of biomass in industry is well known and in fact one of the first production methods of CH₃OH was based on the conversion of lignocellulose, leading to the original naming of the alcohol as “wood alcohol”. Currently, one of the main industries involved in biomass conversion is the pulp and paper industry. The *Food and Agricultural Organization of the United Nations* (FAO) estimates a total capacity of ca. 160 Mt/a (2016) of dried wood pulp which is used in the production of paper and paperboard.¹⁰ In this context, the main process for producing pulp is the “Kraft Process”, accounting for 90% of total virgin pulp produced.¹¹ This process is designed and optimised for the production of cellulose and does this with a yield of ca. 45%.¹² This means that ca. 50% of the wood fed to the process is considered waste and is viewed primarily as an energy carrier. Not only from an environmental point of view, but also from an economic perspective, it is essential to establish processes where a holistic valorisation of the biomass is considered, whereby the usage as an energy carrier is only considered as a last resort. The economic perspective can be addressed by developing new markets for existing products including cellulose nanofibres but also by generating valorisation opportunities and in turn markets for the waste streams from these pulp mills (e.g. lignin).

1.1 Motivation and Objectives

The author anticipates an increased availability of lignin and in particular Kraft lignin (KL). The continued introduction of CO₂-based precipitation processes such as LignoBoost®, LignoForce™, and Sequential Liquid-Lignin Recovery and Purification (SLRP) will generate a market for relatively inexpensive and readily available KL. In this context, the aim of this thesis is to evaluate the suitability of a solvent extraction in combination with a base catalysed hydrothermal process to adjust the physicochemical properties of technical KL for rendering it more suitable as a precursor for carbon fibres (Figure 1). The literature on the production of carbon fibres based on lignin and also the base catalysed hydrothermal processes is thoroughly analysed and criteria for a suitable carbon fibre precursor are described. Reactions performed at varying retention times ($t_{\text{retention}}$) give the possibility to derive a time dependent product evolution. The treated KL and its components are characterised *via* nuclear magnetic resonance (NMR) (¹H and 2D heteronuclear single quantum coherence (HSQC)), gas chromatography (GC) attenuated total reflection fourier-transform infrared (ATR FT-IR), and thermogravimetric analysis in order to evaluate the changes. A base catalysed hydrothermal process is of particular interest as it could be in principle easily implemented at a Kraft mill, since the required chemicals and infrastructure are typically available. Complementarily, a techno-economical evaluation of the developed process is also performed with a focus on its installation at a Kraft mill, with a hypothetical product price for a defined net present value (NPV) calculated.

Regarding the production of chemicals of interest to the chemical industry and offering a further mechanism for lignin valorisation, a possible downstream process is also introduced and discussed regarding the mono- and

dimeric fraction (i.e. pH 2 aqueous phase). In this regard, a heterogeneous catalysed hydrothermal reaction employing a Pt-based catalyst is introduced. Reactions with model compounds were performed with the main objective to establish a reaction network and associated kinetics. Furthermore, catalyst deactivation is described as applied in a continuous process. The controlled addition of MeOH as a hydrogen donor is evaluated and its impact onto the reaction network described.

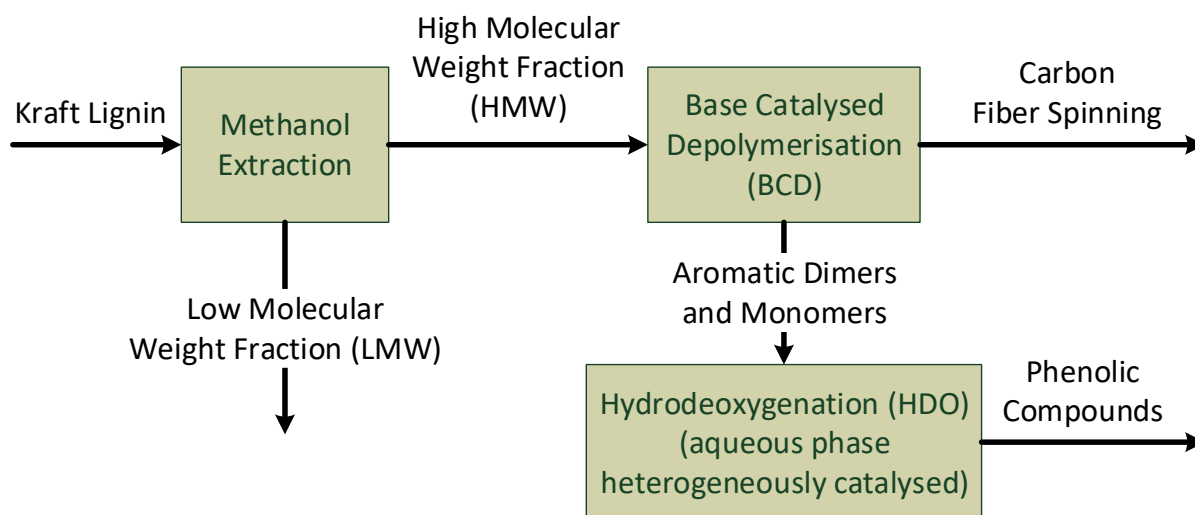


Figure 1: Process scheme for the production of a carbon fibre precursor out of KL.

1.2 Technical Lignin: Availability, Structure, and Potential Products

1.2.1 Paper Mills and Lignin Production Processes

Biomass is a complex mixture of mainly cellulose, hemicellulose, lignin, and a small amount of other extractives (Table 2), therefore, a separation process must stand in the beginning.¹² The usage of lignocellulosic biomass in altered and unaltered form has been performed for thousands of years. It was not until the 19th century that several processes were developed and applied at an industrial scale with the goal of producing pulp and eventually paper.¹² Several different processes emerged, with the so-called “Kraft” process becoming the dominating technology due to its applicability to either hard or softwood, its production of the strongest fibres, and an incorporated regeneration cycle for the chemicals used.^{12,13} Nowadays, the magnesium bisulphite process has an even easier recovery process but the fibre from the Kraft process is still the strongest, so this technique prevails.¹² The lignin produced during the “cook” of the Kraft process is in most cases not separated, remaining in the black liquor with parts of the hemicellulose and also some peeled-off cellulose, and is burnt for producing steam as well as to recover most of the chemicals used.^{11,12} Since the combustion of the organic content in the black liquor produces more heat than is necessary for the mill, additional electricity can be generated *via* the high-pressure steam. For example, the Mercer pulp mill in Stendal, Germany has a capacity of 660 kt_{pulp}/a and produces

135 MW of electricity. As a consequence this mill is the largest supplier of renewable bio-fuel electricity in Germany.^a As a consequence of the large scale of pulp making in general, black liquor is the most important renewable bio-fuel worldwide.¹¹

Table 2: Chemical composition of wood species commonly used in pulping processes.¹⁴

Wood component		wt.% in wood				
		Pine	Spruce	Birch	Eucalyptus	
					E. globulus	E. urograndis
Lignin	Klason	28.2	27.2	19.1	17.9	26.8
	Acid soluble	0.3	0.2	4.0	6.0	3.6
Hemicellulose	Xylan	7.8	8.7	25.6	20.8	15.6
	Glucomannan	18.2	19.2	3.7	4.2	3.0
Cellulose		44.2	44.4	44.8	51.0	50.6
Extractives		1.3	0.2	2.8	0.2	0.4

Lignin is the only renewable resource providing aromatic compounds in significant amounts and the usage of lignin as a source for these compounds to supply the chemical industry has been pursued for > 50 years. Until now, no process has emerged that is used on an industrial scale valorising lignin for the specific production of chemicals. On the one hand this is due to the highly condensed and diverse structure of current technical lignin and, on the other hand, as a consequence of the low technological readiness level of alternative biomass separation processes that are capable of separating lignin from the original biomass and release monomers *in situ*.¹⁵ The FAO estimates a capacity of 118 Mt/a of chemical pulp for the year 2016 (Table 3).¹⁰ The amount of bleached sulphate + soda pulp for 2016 is *ca.* 65.1 Mt of which 44.5 Mt and 22.7 Mt was generated from coniferous softwood and non-coniferous hardwood respectively. The availability of unbleached pulp is predicted to be at 33.2 Mt/a with its production predominantly based on softwood (80%). This means a total of 50.3 Mt/a and 48.0 Mt/a hardwood and softwood, respectively. Softwood leads to an amount of *ca.* 490 kg_{lignin}/t_{pulp} compared to a value of 330 kg_{lignin}/t_{pulp} for hardwood, which results in a total amount of KL of 40.1 Mt/a. It is assumed that at a maximum of 75% are extractable *via* CO₂ precipitation for keeping an undisturbed operation of the recovery boiler leading to an available amount of approximately 30 Mt/a.^{14,16} The sheer amount of this resource, which is typically burnt to produce energy, implies the development of new processes. Simultaneously a cost effective and sustainable way to substitute the lignin as a fuel to provide for the energy needs of the Kraft mills has to be concurrently explored.

The actual market for lignin is estimated to be between 0.8 - 1.0 Mt/a, from which 90% are lignosulfonates produced *via* the magnesium bisulphite process; the remaining 10% is KL.¹⁷ The lignosulfonate market size was valued at 700 M US\$ in 2015, with animal feed binder and concrete admixtures representing the major products (*ca.* 30% each), followed by dust control (15%), oil-well additives (10%) and other uses (15%). Lignosulfonates in

^a <http://www.zellstoff-stendal.de/>

and subsequently used as fuel for a gas turbine.^{31–35} This also facilitates CO₂ removal when the CO is shifted towards CO₂ *via* the reaction with H₂O (i.e. water-gas shift reaction). Using the co-generated H₂ in a fuel cell (IGFC) can lead to further improvements in efficiency.³² The CO₂ can then be used in the lignin separation process. These two possibilities alone are supposed to recapitalise the installation of a LignoBoost® plant, so, if true, the availability of KL should increase in the future.^{28,30} The LignoBoost® process is not the only process for precipitating lignin out of the black liquor. The LignoForce™ process, as developed by FPIInnovations in Canada, adds a preliminary oxidation step which is reported to lead to improved filterability.^{36,37} This process was installed in the Hinton pulp mill of West Fraser Mills Ltd. with a capacity of 30 t/d. The investment accumulated to 30 M CAN\$ and the plant went online in 2016.³⁸ As a third lignin precipitation process, the SLRP process adds CO₂ to the black liquor under pressure (up to 4 bar) thereby keeping it in a liquid state, enabling the use of a decanter centrifuge for phase separation, bypassing the use of a filter press in the first step.^{39,40} The SLRP process is less mature than LignoBoost® or LignoForce™, but a pilot plant was constructed at Clemson University (South Carolina, USA).⁴⁰

Table 3: Global capacities for pulp production as indicated by the Food and Agricultural Organization (FAO) of the United Nations

				Amount [Mt/a]	
Wood pulp for paper + paper-board	Mechanical pulp			13.16	
	Thermo-mechanical pulp			7.85	
	Semi-mechanical pulp			5.07	
	Chemical pulp	Kraft	Bleached	65.05	118.07
			Unbleached	33.23	
		Sulphite		1.3	
	Others	Straw		0.03	0.72
		Bagasse		0.55	
Bamboo		0.05			
Dissolving pulp				3.18	
Total				148.05	

1.2.2 The Chemical Structure of Lignin

Native Lignin

The structure of lignin was described analytically in the 1930s to 1950s by Hibbert *et al.*^{41–50} This research included the description of a vanillin producing reaction with NaOH, based on the conversion of spent sulphite liquor and first propositions regarding the structure of lignin based on organic solvents extraction.^{47–50} They found that extracted lignin consisted of α -O-4 and β -5 connected phenyl propanoid subunits and also found in softwood only guaiacyl units while hardwood consisted of both, guaiacyl and syringyl units (Figure 3).⁴⁷ In the 1970s Pepper and Lee analysed lignin *via* the hydrogenolysis of spruce wood with heterogeneous catalysts such as 5% Rh/C, Rh/Al₂O₃, Ru/C, Ru/Al₂O₃, and Raney nickel.^{51–57} Reactions were performed in dioxane:H₂O (1:1 v:v) for 5 h at 195 °C with an H₂ pressure of 500 psi (3.45 MPa). The goal was to determine the structure of lignin *via* its hydrogenolysis products. The spruce wood was pre-extracted with an CH₃CH₂OH:benzene (1:1) mixture and then treated under the stated conditions. The reaction products were filtered and the filtrate extracted with chloroform and diethyl ether. The extract was analysed *via* gas-liquid-chromatography and in the late 1970s also

via NMR spectroscopy.^{55–57} The reported structure was comparable to that reported by the Hibbert group, providing an additional insight into the different components which make up the structure of lignin. Since solely spruce wood was investigated, a comparison of soft- and hardwood could not be given.

All these analytical approaches lead to a rather generalised structure for native lignin from both softwood and hardwood. With the refinement and improvement in analytical methods and the combination of the results from different sources, it has since become clear that the chemical structure of lignin is incredibly complex and variable, and strongly depends on firstly the plant species under investigation and indeed the separation process applied, and furthermore the geo-location and climate in which the tree/plant was grown. Rinaldi *et al.* have provided a good description of these effects in a recent review.¹⁵ Complimentarily, in 2015 Lupoi *et al.* summarised and evaluated the analytical technique applied thus far in the characterisation of different lignin.⁵⁸ In this report, the authors suggested that the ratio of the three phenyl propanoid structures (S/G/H) could be used as plant type / chemical identifier, with the total native lignin structure referred to as “*a randomly radical induced polymerized phenylpropanoid polymer*”.⁵⁸

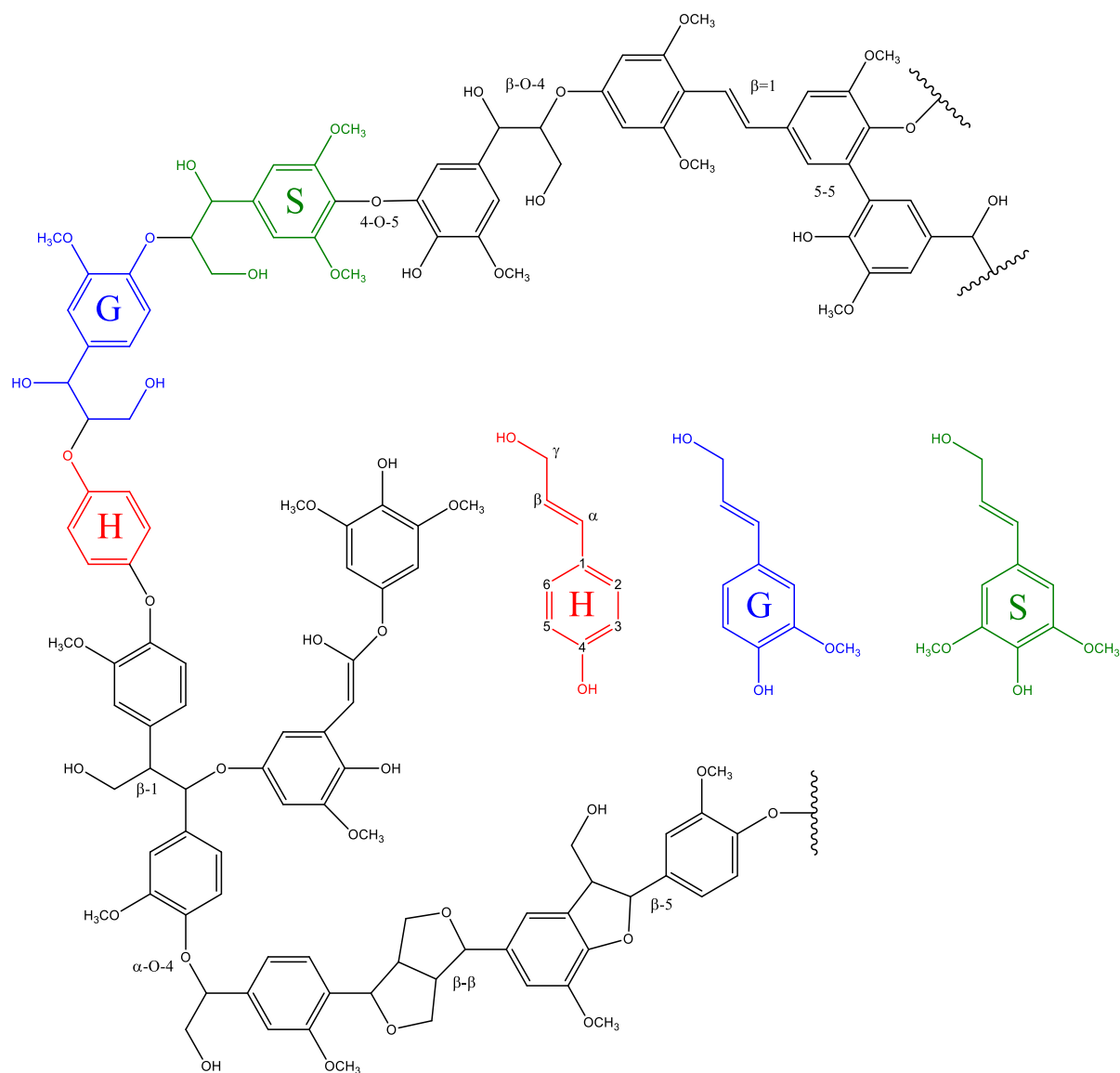


Figure 3: Structure of native lignin with most occurring bonds described. The three phenylpropanoid monomers constituting the lignin macro molecule are shown on the right. These are comprised of the three base types: (H) p-hydroxy-phenyl, (G) p-guaiacyl, (S) p-syringyl

The main linkages in native lignin are ether linkages and mainly β -O-4 and α -O-4 connections (Figure 3). These linkages have a bond dissociation energy (BDE) of 200 to 300 kJ/mol and are easily cleaved under alkaline (Kraft) pulping conditions.⁵⁹⁻⁶⁴ During the pulping, lignin fragments are freed from the main fibre and consequently undergo (re)-polymerisation and condensation reactions to form C-C and Ph-O-Ph linkages, referred to as 5-5 and 4-O-5 bonds. These are practically non-existent in native lignin (< 5% in total) and have BDEs of 325 to 500 kJ/mol.¹⁵ An overview of the bond dissociation energies is given in Table 4.

Table 4: Bond dissociation energies (BDE) of the linkages shown in Figure 3.¹⁵

Type	5-5	β -O-4	4-O-5	β -1	α -O-4	β - β
BDE [kJ/mol]	481-493	226 - 301	326 - 347	272 - 288	209 - 234	339

Table 5: Abundance of different linkages in woods and grasses in percentage. Values taken from Rinaldi *et al.*, for a detailed description of the linkages the reader is referred to the original source.¹⁵

	β -O-4 β -aryl-ether	α -O-4 Phenyl-coumaran	5-5 Biphenyl	4-O-5 Diaryl-ether
Softwood	45-50	9-12	5-7	2
Hardwood	60-62	3-11	<1	2
Grasses	74-84	5-11	--	--

1.2.3 Technical Lignin

Technical lignin is lignin that has been separated from the bulk biomass in an industrial process. The main process applied is the Kraft process for the production of pulp, which can be used for paper and hygienic products. These processes alter the structure of the lignin, thus technical lignin generated from contemporary processes differ significantly from their native form.

Kraft Lignin (Sulphate Lignin)

The Kraft process is the major industrial process for generating pulp with 95% of chemical pulp production originating from this process. It uses a mixture of NaOH and Na₂S in H₂O as solvent. This mixture is called “white liquor” and has a NaOH/Na₂S molar ratio of 5 - 7 while the NaOH concentration is 0.875 M (aq). These conditions are varied and optimised for a particular wood type, with softwood generally requiring a higher concentration of chemicals and a 10 °C higher temperature (i.e. at 140 - 170 °C for 3 - 4 h).¹²



The treatment of the wood often referred to as the “cook” is divided into three stages, namely the initial, bulk, and residual phase. Delignification of the wood proceeds fastest in the bulk phase and is a first order reaction with regard to lignin as long as [HO]⁻ and [HS]⁻ are considered constant.¹³ The residual phase starts when only some 2 - 3% of the lignin is left and the rate of delignification decreases at that point leading to longer cooking times. This not only decreases the yield of cellulose through so called peeling reactions but also leads to an increase in the level of condensation and the amount of phenolic-OH groups within the KL.^{13,65,66} After cooking the biomass, the cellulose is separated and the chemicals, lignin, and parts of the hemicellulose and some cellulose remain in the black liquor. This is subsequently concentrated to 60 - 80% dry solids (ds) in the evaporator train and burnt in the recovery boiler.¹² The lower part of the boiler, where the liquor is injected, runs under reducing conditions, so that the chemicals leave the boiler as a liquid (green liquor) consisting mostly of Na₂S and NaCO₃. The Na₂CO₃ is treated with caustic lime (CaO) in the aqueous phase. The thus formed CaCO₃ precipitates as solid

and is regenerated *via* calcination in the lime kiln by removal of CO₂. Modern pulp mills can regenerate $\geq 90\%$ of their chemicals in the recovery process.^{11,12}

Most pulp mills produce more energy in their recovery boiler than is needed for the process. High pressure (6 MPa, 400 °C) and medium pressure (1 MPa, 200 °C) steam cycles are used for turbines to co-generate electricity, whereas the low-pressure cycle (0.4 MPa, 165 °C) is designed to provide the heat needed for the evaporator train and the remaining unit operations. Taking lignin out of the black liquor leads to less steam being generated and more steam being needed, since the separation process adds H₂O to the system. Kannangara *et al.* analysed the impact on these values by assuming a precipitation of 15% of the total lignin (*ca.* 65 adt/d) for a 750 adt/d Kraft pulp mill.⁶⁷ Their findings imply that with this amount of lignin, the steam production was decreased by 13.5% while its usage was increased by 2.4 to 14.6%. The wide range of the data is caused by inserting the washing solution after precipitation either at the beginning or in the middle of the evaporator train. Furthermore, also the amount of recycled filtrate is varied from 0 to 6 t/t_{lignin}.⁶⁷

When lignin originating from this process is precipitated out of the black liquor, its structure is relatively condensed. The main reactions taking place during Kraft pulping were described by Gierer in 1980.⁵⁹ Nucleophilic attacks of HS⁻ and HO⁻ leads to a deprotonation of phenolic-OH groups, thereby destabilising the aromatic system in turn leading to ether bond cleavage at the α -position (Figure 4).

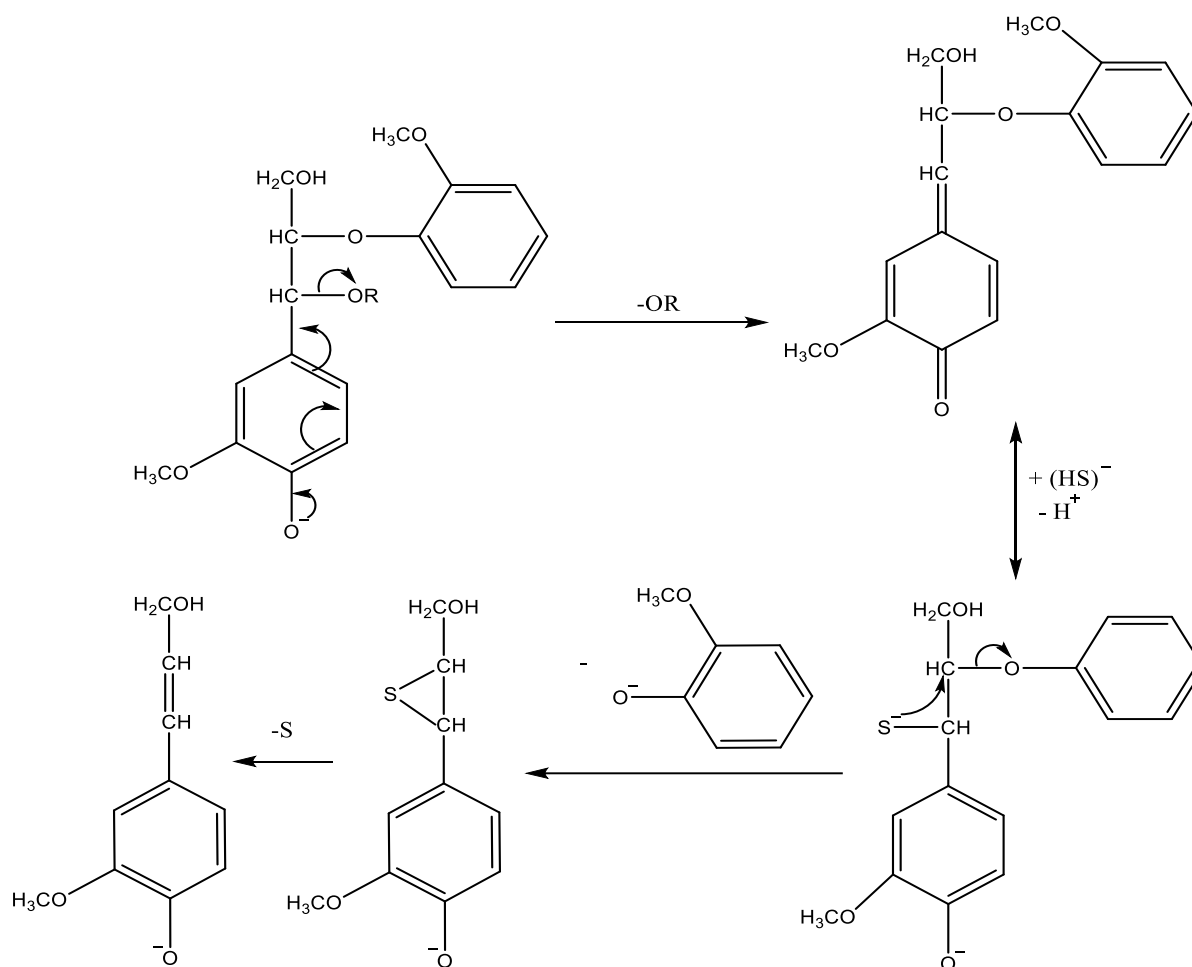


Figure 4: Lignin cleavage under Kraft process conditions. The formation of the quinone methide intermediate (upper right) leads to a dead end under alkaline pulping conditions. The usage of Na_2S enables further cleavage of the intermediate. Scheme adopted and adjusted from Ref.⁵⁹

Non-phenolic groups, which are the majority in native lignin, can undergo nucleophilic attack at the α -position, if an $-\text{OR}$ group is present. The cleavage of α -aryl-ethers and β -aryl-ethers forms quinone methide intermediates. These are cleaved *via* the sulphidolytic pathway, i.e. they are stable under pure alkaline pulping conditions.⁵⁹ The cleavage of lignin ether bonds leads to a strong increase in phenol-type groups. Alekhina *et al.* showed that softwood lignin precipitated from black liquor of the residual stage cook of a Kraft mill contains three times as much phenolic-OH groups compared to dissolved wood lignin (DWL).⁶⁵ The DWL was extracted as described in the method by Fasching *et al.* and is very similar to ball milled wood lignin, i.e. native lignin.⁶⁸ Compared to this DWL, the number of primary and secondary aliphatic hydroxyls in KL was reduced by 50%, whilst aromatic methoxy groups decreased by 20%. The amount of cross-linked aromatics increased *via* condensation reactions, while oxygenated and protonated aromatics were both decreased.⁶⁵ Mörck *et al.* state that during the Kraft cook saturated hydrocarbons are inserted into the sidechains of the lignin.⁶⁹ In summary, KL is more condensed compared to native lignin, i.e. it has more C-C bonds while fewer aromatic C-H and C-O are present. Often cross-linking takes place at the free *ortho*-position of the guaiacyl rings (Figure 5). In total the oxygenated aromatics are decreased by *ca.* 10%. The transformation of a β -O-4 linkage into a phenolic-OH does not change this number, so

this should result mainly from demethoxylation of guaiacylic units (softwood was used for the study, so no syringyl units are present).⁶⁵

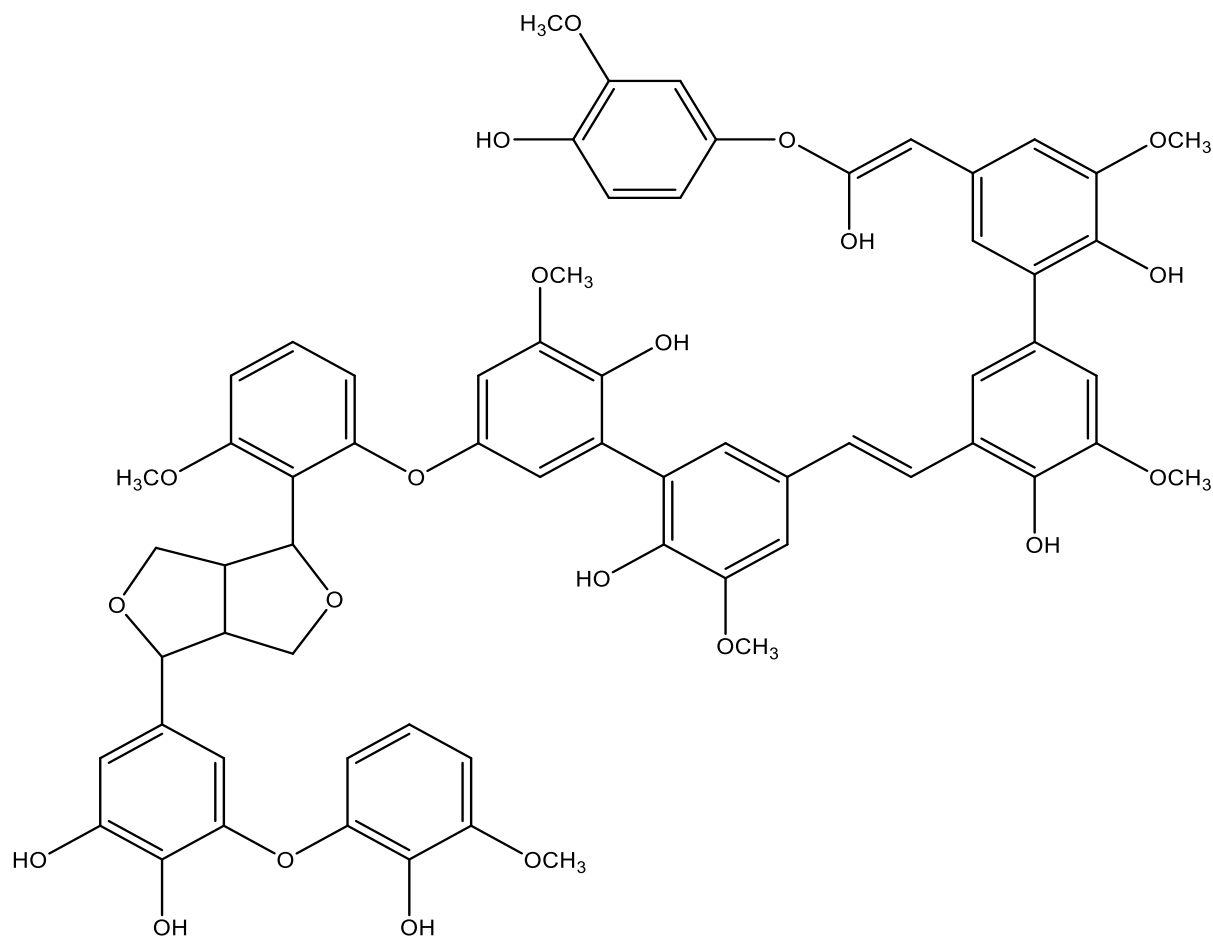


Figure 5: Proposed structure of KL. Condensation reactions lead to many ortho-positions being occupied. Sulphur moieties are not included in this structure.

Lignosulfonates

Lignosulfonates are generated by the bisulphite process which uses HSO_3^- and Ca^{2+} , Mg^{2+} , Na^+ , or NH_4^+ as counterion. The two most used processes are magnesium bisulphite processes either in pH 1.5 (acid bisulphite) or pH 4 (magnefite).¹² During the process ether bonds at the α -position connecting with polysaccharides of the lignin carbohydrate complex are protonated leading to bond scission and introduction of SO_3^- groups (Figure 6).

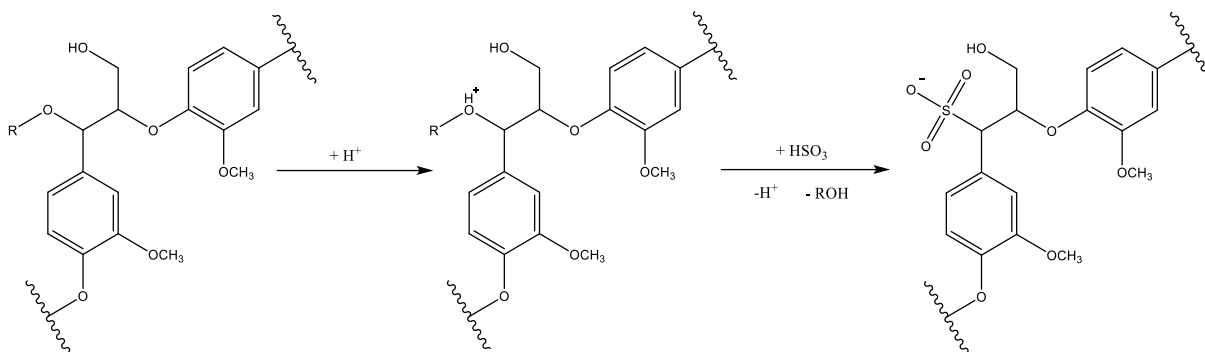


Figure 6: Mechanism of sulphite pulping under acidic conditions. The R at the α -position is either a proton or a polysaccharide and is replaced by an SO_3^- group.¹²

This strongly increases the polarity making lignosulfonates H_2O soluble and organics insoluble. Lignosulfonates have also a much higher average molar mass (M_w) and an average sulphur content of 8 wt.%. During the recovery process, the black liquor of the bisulphite process is concentrated in an evaporator train similar to the Kraft process and burnt in a combustion furnace. The chemicals are removed *via* the flue gas, with the gas stream cleaned by scrubbing and recycled for the process. The spent sulphite liquor contains considerable amounts of furfural, acetic acid, and MeOH which are either transformed into salts by neutralisation or washed out of the flue gas. 80 - 90% of the chemicals can be recovered such that 10 – 15 kg of MgO and SO_2 are needed as make up per t_{pulp} .¹² Lignosulfonates are sold at *ca.* 1 Mt/a, either in solution or spray dried as salts. This generates additional revenue but also removes chemicals and fuel from the process.

Organosolv Lignin

The term “*Organosolv Lignin*” (OL) is imprecise, since it does neither limit the organic solvent nor gives limits to the process conditions. McDonogh and Joseph have provided overview on the mechanism of organosolv delignification, with Rinaldi previously highlighting the importance of solvent properties.^{70,71} OLs were intensively analysed and often self-prepared ones were used.^{72–81} While, as in the ALCELL® process, most groups applied a $\text{CH}_3\text{CH}_2\text{OH}:\text{H}_2\text{O}$ extraction procedure at elevated temperatures, Barta *et al.* employed a MeOH-based extraction process (with addition of 1 wt.% HCl (aq)) from aspen wood sawdust as in Harris *et al.*^{74,82} This extraction process was also applied to candlenut shells and since only the MeOH soluble lignin at room temperature is used, it results in a lignin that is already of very low molecular weight.^{78,82} Klamrassamee *et al.* used a mixture of methyl isobutyl ketone:MeOH: H_2O (25:42:33) with the addition of H_2SO_4 to extract lignin from biomass.⁷⁹ All these procedures have in common the aim to employ a downstream process, for example a heterogeneous catalyst or supercritical solvent treatment, for the production of mono aromatics. However, these approaches thus far remain at the laboratory scale.

Regarding more mature technologies, the ALCELL® process developed by Repap Enterprises is probably the best known organosolv process and uses an $\text{CH}_3\text{CH}_2\text{OH}:\text{H}_2\text{O}$ mixture (6:4 v:v) with H_2SO_4 as catalyst at 150 – 200 °C for 2 – 4 h to separate the biomass constituents (Figure 7).⁸³ A demonstration plant was established in 1989 (at Miramichi, New Brunswick, Canada), operating at a capacity of 30 t/d. It was purchased by UPM in 2000 and

eventually closed due to economic pressure in 2006. A commercial scale plant was planned with a capacity of ca. 140,000 t_{pulp}/a , 55,000 t_{lignin}/a , and 15,000 t/a furfural and acetic acid but was never constructed.

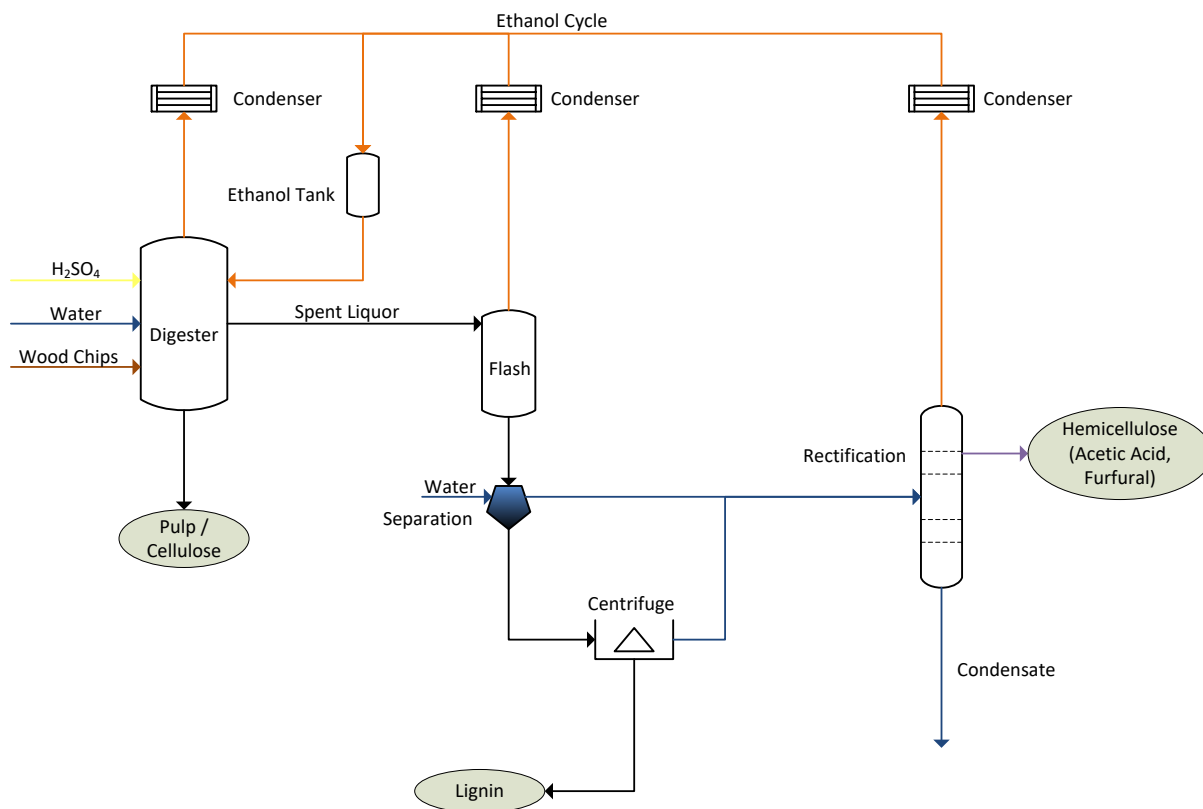


Figure 7: Organosolv process with $\text{CH}_3\text{CH}_2\text{OH}:\text{H}_2\text{O}$ as solvent. Typical process conditions for the digester are: $\text{CH}_3\text{CH}_2\text{OH}:\text{H}_2\text{O}$ 6:4, $\vartheta = 180 - 200$ °C and $\tau = 2 - 4$ h. Addition of ca. 1 wt.% H_2SO_4 gives increased delignification and enables a 30 °C lower temperature.

The $\text{CH}_3\text{CH}_2\text{OH}:\text{H}_2\text{O}$ -based organosolv process has since been further developed at the Fraunhofer Center for Chemical-Biotechnological Processes CBP (Leuna, Germany), with 400 L batch digester installed, serving as a basis for a virtual scale-up to a 280,000 admt/a plant in cooperation with Linde.⁸⁴

The organocell process uses MeOH or $\text{CH}_3\text{CH}_2\text{OH}$ at elevated temperatures to extract the wood (1:1 alcohol:wood) and then cooks the wood in aqueous alkali with anthraquinone including residual alcohol.⁸⁵ The first step allows deacetylation and cleavage of α -aryl ether linkages while avoiding secondary condensation reactions. The second step removes lignin from spruce wood to a kappa number of 20 - 30 which is in the range for bleachable pulps. The kappa number is a measure for the lignin content and is defined by the ISO 302:2015.⁸⁶ Its value is $\kappa \approx 6.57 \times [\text{lignin content in percent}]$.

The CIMV organosolv process uses acetic acid:formic acid: H_2O (55/30/15) at 105 °C for 3 h in a 1:10 biomass:solvent ratio to produce pulp, C₅-sugars and lignin.⁸⁷ A patent has been filed regarding the use of the lignin produced in this process as a substitute in a phenylfomaldehyde resin preparation.⁸⁸

1.3 Kraft Lignin as a Precursor in Materials Synthesis

1.3.1 Carbon Fibres

Carbon fibres (CF) contain at least 90% carbon by weight and any polymeric material that leaves a carbon residue and does not melt upon pyrolysis can serve as precursor.⁸⁹ Although, in the beginning cellulose was used as precursor, today polyacrylonitrile (PAN) and petroleum pitch are used, while > 95% are PAN based fibres.⁹⁰ Global demand for CFs in 2012 was *ca.* 50,000 t, with demand mainly limited to the high price of the fibre, i.e. the precursor (Figure 8). CFs are mainly used in industrial applications (e.g. in blades for wind turbines) but also as nonwovens with high thermal and chemical stability. CFs are a light weight, high tensile strength and modulus construction component and are manufactured based on a thermal decomposition of the selected precursor, after fibre spinning and stabilisation (Figure 9).⁹¹ A very good overview on CFs and their precursors has been published by Buchmeiser *et al.*, including discussion regarding alternative precursors as lignin and cellulose.⁹²

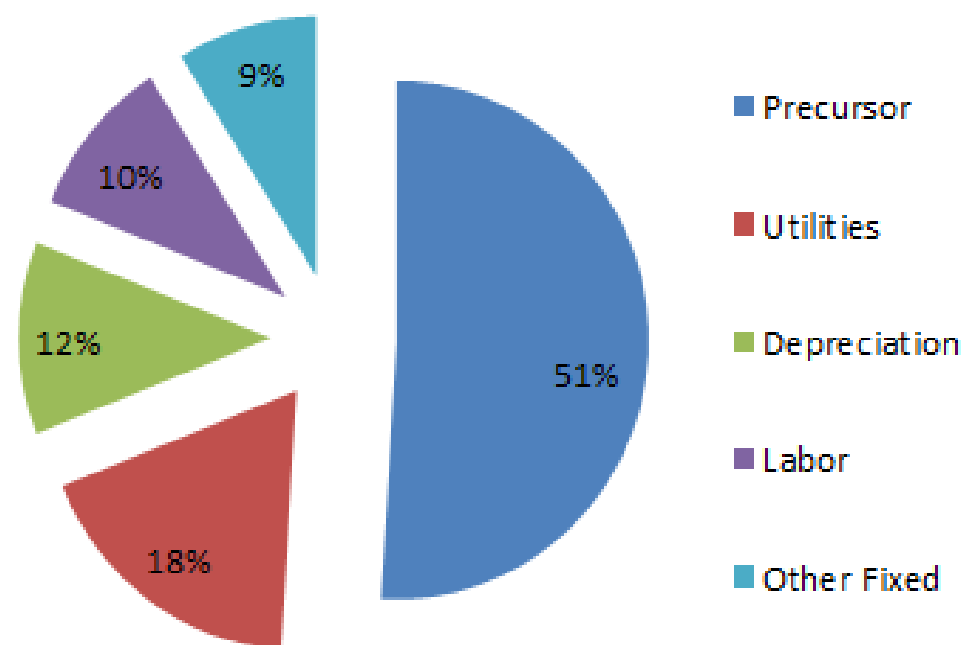


Figure 8: Cost break down for the production of carbon fibres from PAN.

In industrial processes pure PAN is not used single component, but rather as a blend with 2 - 15% acrylic acid, methacrylic acid, methacrylate, and/or itaconic acid, which affects the molecular alignment and the stabilisation conditions.⁸⁹ The stabilisation and carbonisation steps are performed under stress, i.e. the fibres are held under tension, leading to a higher, final tensile strength. The latter is a more or less linear function of the carbonisation temperature up to 1000 °C, where it reaches a plateau and then decreases again slowly. The Young's modulus (E) as well as thermal and electrical conductivities are proportional functions of T up to 3000 °C and if a fibre with a higher stiffness ($E > 300$ GPa) is needed, the trade-off will be a lower tensile strength.⁸⁹ During the production process of the PAN-based fibre and its heating to 1000 °C, *ca.* 30% of the released decomposition gas is HCN.⁸⁹ This release of HCN during carbonisation requires significant safety consideration.⁹⁰ After carbonisation the fibres

are treated to introduce specific polar chemical groups, which then can interact with the matrix. Since CFs are thermally stable up to 2000 °C but degrade under oxidative conditions (at $T = ca. 400$ °C), coatings with SiC, Si₃N₄, BN, and Al₂O₃ are often used to prevent oxidation reactions.⁸⁹

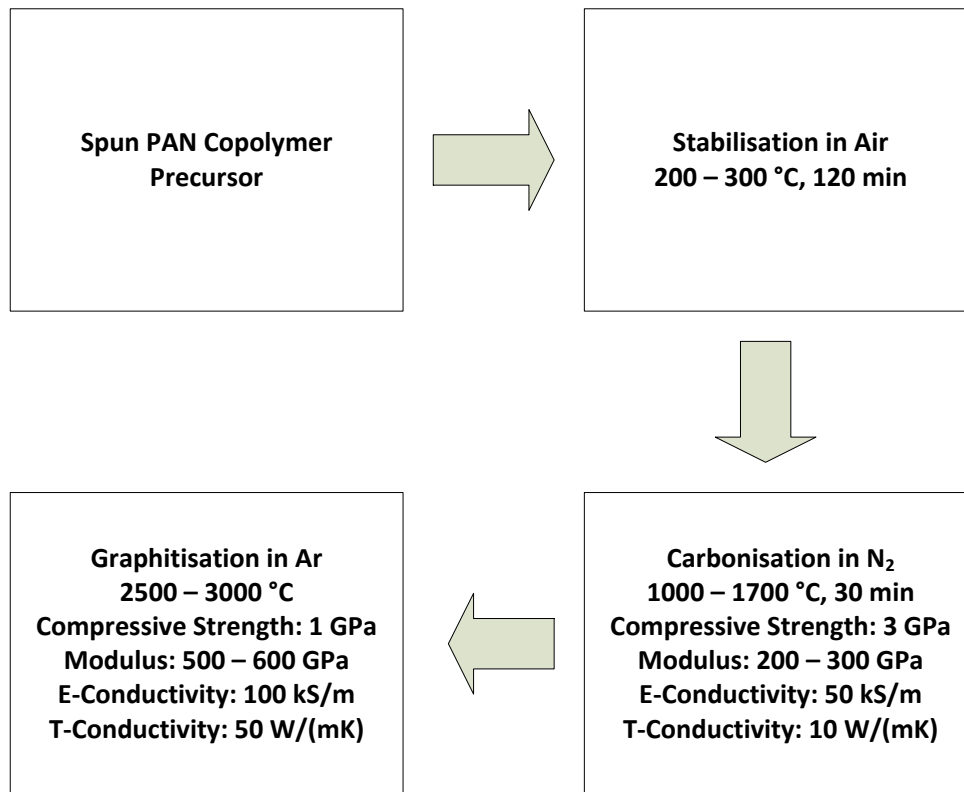


Figure 9: Carbon fibre processing steps using a PAN precursor.

Since KL resembles more a “pitch” in terms of materials precursor compared to PAN, it is important to consider the processing steps required to produce CFs based on pitches. When using pitch as a precursor different pre-processes have to be applied in order to achieve either anisotropic pitch or mesophase pitch.⁹² Pitch itself is a tar-related substance with a high viscosity or even solid at RT. It is inhomogeneous and has molecular weights of *ca.* 1000 g/mol (Figure 10). The pitch is treated in order to achieve higher molecular weight phases and to reduce the ash content to < 1000 ppm before it is melt spun. The melt spinning itself is a difficult procedure during which the nozzle temperature has to be kept within a narrow set of parameters, since viscosity and mesophase texture are vary with T. A turbulent flow must be ensured at the spinneret to avoid a cracked radial structure which can induce cracks during carbonisation.⁹² While having turbulence is a function of the viscosity, this is, again, also a function of the spinning temperature.

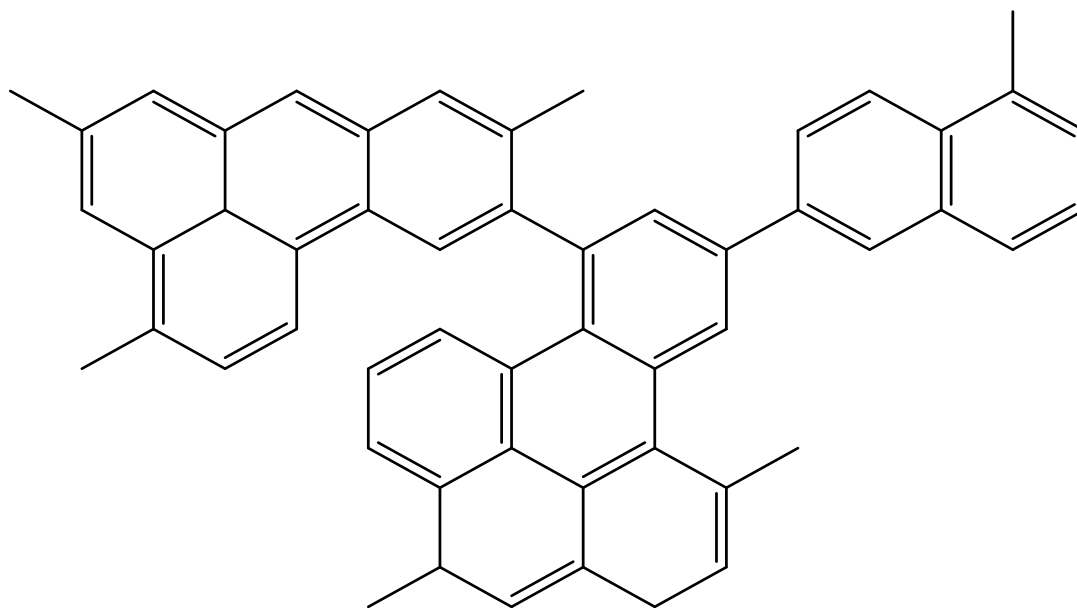


Figure 10: Possible structure of mesophase pitch. Structure drawn after information from Newman⁹³ and Singer⁹⁴.

As already stated, the high price of the PAN based precursor limits the applicability of CFs. Prices range from 22 \$/kg for intermediate-modulus CFs up to 3,300 \$/kg for high-end CFs. As a magical limit, a price of 5 \$/lb for a fibre was set by the automotive industry if it were to receive interest and application in the mass production of cars. Baker and Rials state in their 2013 review paper, that the automotive industry requires a price between 11 - 15.4 \$/kg and the fibre should have a tensile strength > 1.72 GPa and a modulus > 172 GPa.⁹⁵ The price of corresponding fibres was at 30 \$/kg in 2010. *Ca.* 50% of the costs for a PAN based fibre stems from the precursor alone (Figure 8). This also means that the processing costs are 15 \$/kg, so that even if the precursor was available at zero cost, the automotive industry would consider the product as too expensive.

As an alternative, potentially inexpensive precursor for CFs production could be lignin waste from Kraft mills. Lignin is a poly-aromatic with a high carbon content of *ca.* 60 wt.%. The first patent application for producing a carbonised lignin-based CF was issued by Nippon Kayaku in 1969.⁹⁶ Softwood and hardwood KLs were melt and dry spun, stabilised in air and then carbonised under a N₂ atmosphere. Tensile strengths of 0.3 to 0.8 GPa were reported. Furthermore, the addition of sulphur and usage of lignosulfonates were also investigated. This CF was briefly available as Kayacarbon brand as a fibre prepared from dry spinning with poly-(vinyl alcohol) as copolymer until 1973. The main motivation for producing CFs from lignin was and is to minimise costs. In this context, it is also important to consider that KL is not a homogeneous precursor. It differs greatly if hard- or softwood is used and the pulping conditions in turn also have an influence. Softwood lignin can be easily stabilised while its spinnability is problematic. This is caused by its guaiacyl structure which leads to a high state of cross linked *ortho*-positions during pulping leading to a bulky structure. The spinnability is hampered by a glass transition temperature (T_g) which changes during melting as cross-linking reactions can occur, with the material even reaching the state of a thermoset before spinning is finished. Hardwood lignin has fewer free *ortho*-positions as it is composed of *ca.* 50% syringyl units. This leads to a more linear structure and lesser change of this structure during melt spinning. The subsequent stabilisation is problematic, since further cross linking is hindered by this lack of free

ortho-positions. The aforementioned characteristics of different lignin lead to the idea of using softwood lignin with additions of hardwood lignin as plasticiser.⁹⁷ Also other polymers have been tried in combination with adjustments in the process, i.e. stabilisation, carbonisation, and graphitisation. Innventia AB in Sweden and the Oak Ridge National Laboratories (ORNL), USA are pursuing the development of CFs based on lignin and are considering upscaling production.^{98,99} As a first market for lignin CF, the production of nonwovens for heat retardants and insulations has been proposed.¹⁰⁰

In summary, the criteria for a good precursor for CF are as follows:

1. Having a T_g well below the decomposition temperature and does not undergo polymerisation 30 K above the T_g .
2. The fibres do not fuse during carbonisation or they can be stabilised after having been spun, i.e. they are transformable into a thermoset.
3. The polymers in the precursor should have the same orientation to increase resulting tensile strength and modulus. For high modulus fibres at least 70% of the polymers must have the same orientation.⁹² An aromatic structure and preferred orientation must be present in the precursor; the carbonisation cannot create this.
4. A high yield is achieved through:
 - a. A high carbon content in the precursor.
 - b. Few Linear or branched alkyl chains. These are not stable during carbonisation.
 - c. A high content of double bonds or aromatics.
 - d. Connection of the aromatic rings by not more than one carbon atom (i.e. -Ar-CH₂-Ar-).
 - e. Heteroatoms in side groups or aromatic rings stabilise and increase yield (e.g. OH groups in phenol).

KL already fulfils some of these criteria, as a high carbon content and aromaticity combined with a high number of phenolic OH groups. On the other hand, due to a lack in thermal stability, KL tends to fuse during stabilisation/carbonisation. Furthermore, it does possess branched alkyl chains with more than one carbon atom as linkages between the aromatic rings. These parameters are supposed to be pushed into a more favourable direction *via* the processes employed. Additionally, a more homogeneous orientation of the precursor would be favourable. While achieving the latter *via* the methods employed is questionable.

2 Materials and Methods

2.1 Chemicals

2.1.1 Reagents

Lignin was supplied by UPM as originating from the Domtar pulp mill in Plymouth, NC, USA. It was precipitated *via* the LignoBoost® technology and contains *ca.* 35 wt.% H₂O. Before usage, it was dried at 80 °C under reduced pressure for 24 h. The trees used for the cooks at the pulp mill were northern pine, i.e. softwood.

Guaiacol (Acros, +99%), catechol (Alfa Aesar, 99%), phenol (Alfa Aesar, 99%), syringol (Sigma-Aldrich, 99%), 3-methoxyxatechol (Sigma-Aldrich, 99%), 4-methylcatechol (Alfa Aesar, 96%), 3-methylcatechol (Sigma Aldrich, 99%), 4-ethylcatechol (Sigma-Aldrich, 99%), 4-ethylguaiacol (Sigma-Aldrich, 99%), vanillin (Sigma-Aldrich, 99%), acetovanillone (Sigma-Aldrich, 98%), homovanillic acid (Sigma-Aldrich, 99%), NaOH (Carl Roth, 99%), Na₂SO₄ (Carl Roth, 99%), and HCl (Carl Roth, 32%) were used as procured.

2.1.2 Solvents

MeOH (Emsure, +99.9%), acetone (Technic France, 99%), ethyl acetate (Carl Roth, 99.9%), and DMSO-*d*₆ (Carl Roth, 99.8 atom%D) were used as procured. Deionised (DI) H₂O was supplied inhouse at Fraunhofer ISE having a specific resistance of 18 MΩ cm⁻¹.

2.1.3 Gases

He 4.5, N₂ 5.0, CO₂ 4.5, and H₂ 5.0 were supplied by Linde.

2.2 Methanol Extraction from Kraft Lignin

Extraction was performed using a 45 mL centrifuge vial at STP under vigorous shaking. After shaking, the mixture was let to mature for an additional 2 h and then was centrifuged at 9000 rpm (RCF = 7510) for 5 min. The resulting solution was separated by decantation. The procedure was conducted just once, i.e. no subsequent extractions from the undissolved solids were performed. The extractions were performed with different lignin concentrations (10 wt.%, 20 wt.%, 30 wt.%) to examine if concentration increased linearly. Additionally, a sequential dissolution of the KL in MeOH was performed (Figure 11) to estimate the maximum number of aromatic compounds dissolvable in MeOH. The feed solution for the base catalysed process was prepared at a concentration of 250 mg/mL. The two fractions obtained from each separation step were dried under reduced pressure at 60 °C for 24 h and analysed *via* GPC, EA, TGA, GC-MS-FID, 2D HSQC NMR, ¹³C CP MAS NMR, and ATR FT-IR.

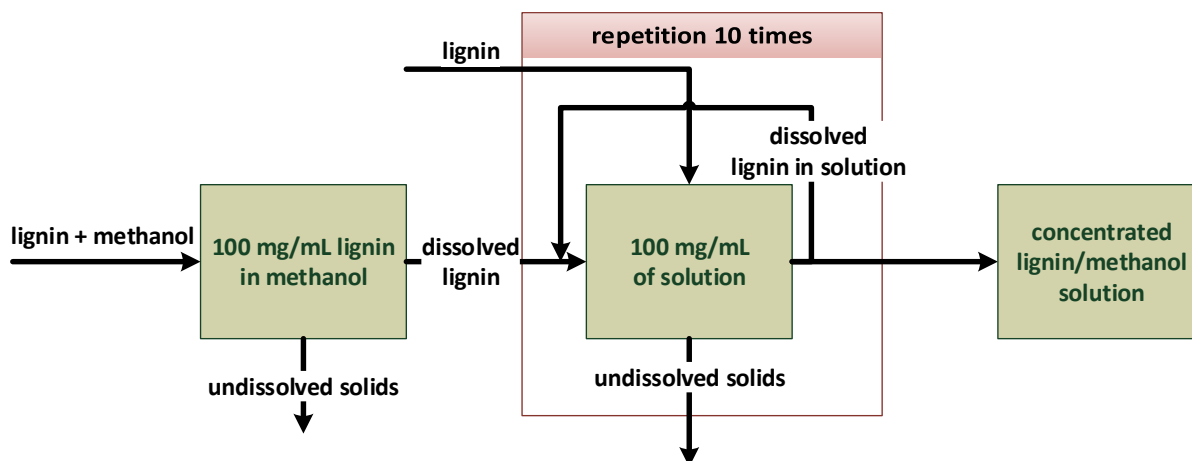


Figure 11: Sequential dissolution of KL in MeOH. The solution of lignin in MeOH was used as new solvent for each subsequent step.

2.3 Continuous Hydrothermal Reactions

2.3.1 Reactor Set-Up and Reaction Runs

The continuous reaction rig was set-up as indicated in Figure 12. As feed containers, 1 L HPLC bottles were used pressurised with N_2 to 0.1 bar to prevent the pump from running on gas and a 10 μm stainless steel filter was installed to prevent particles from clogging the pump. The HPLC pump is a Knauer Smartline 1000 with piston heads for a max flow rate of 10 mL/min. A possibility of adding gaseous hydrogen *via* a mass-flow controller was installed but not used for the reaction runs in this thesis. A tube-in-tube heat exchanger is installed before the feed enters the reactor. For improving the heating rate, the last 25 cm of the heat exchanger was heated with an electrical heating chord set at 50 K below T_{reaction} . The reactor is U-shaped for maximising reaction volume in the limited space of the GC oven. Figure A 1(a) shows a temperature profile as a function of volume. The first and the last point of the analytic measurement are outside the reactor giving the temperature at the end of the pre-heating track and the entrance of the cooling-track, respectively. The temperature of the oven was adjusted to read 300 °C (at thermocouple 4). With increasing flow rates, this lead to a flattened shape of the curve. This is explained by the laminar flow inside the tubes and the resulting non-optimal heat transfer. Even if the low viscosity of pure H_2O ($\nu = 1 \text{ mm}^2/\text{s}$) is assumed, the Reynolds (Re) number, given by $Re = \frac{v \cdot d}{\nu}$, is 723 at maximum, where the regime of turbular flows is reached at *ca.* 2,300 inside of tubes. The volume of the reactor is 50 mL and $t_{\text{retention}}$ for the kinetic runs were based on this volume. Corresponding flow rates are provided (Table 6), and since access to some of the analytical tools were limited (2D HSQC, GPC) a complete analysis could only be performed for runs #K1, #K2, and #K3. Runs #K4 and #K5 were added later in order to improve the resolution.

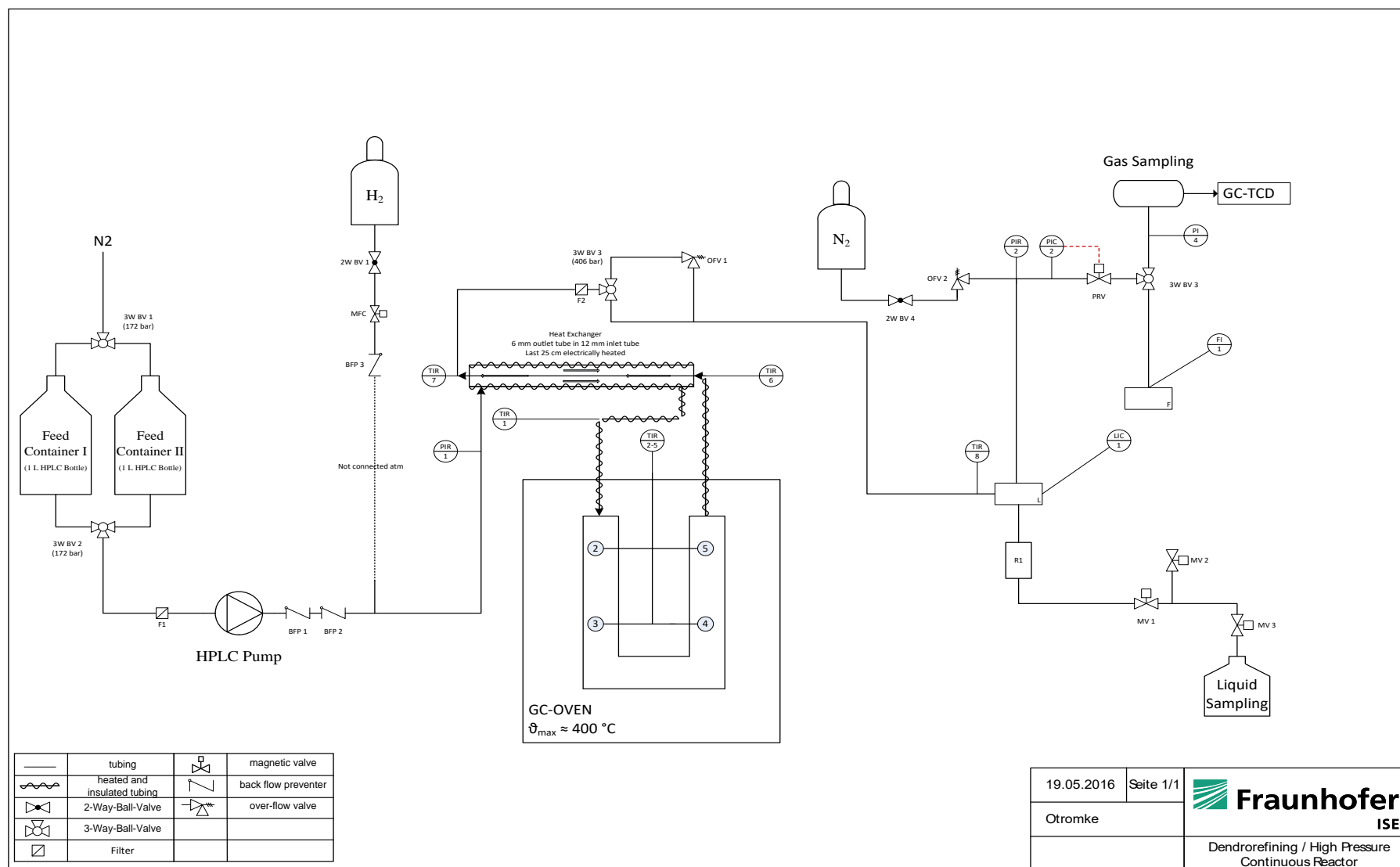


Figure 12: Flow diagram of the continuous flow test rig.

Table 6: Feed types and flow rates of the continuous reactions.

Run	Feed	Flow Rate [mL/min]	$t_{\text{retention}}$ [min]
#B1	HMW	3.125	16
#B2	HMW	3.125	16
#B3	HMW	3.125	16
#B4	LMW	3.125	16
#B5	KL	3.125	16
#K1	HMW	2.083	8
#K2	HMW	6.250	24
#K3	HMW	3.125	16
#K4	HMW	2.500	12
#K5	HMW	4.167	20

The pressure in the reactor is controlled *via* an overflow valve (OFV 1) set at 180 bar. The Gas and liquid phases were separated on the low-pressure side (1-2 bar) and both phases sampled. An optical sensor (LIC 1) controlled the liquid level in the phase separator and withdrew liquid *via* magnetic valves (MV 1-3). Over-pressure at the low-pressure side was controlled with a pressure regulation valve (PRV) and loss of pressure was compensated by a differential pressure valve (OFV 2) adding N₂ if needed. Reactor and periphery were constructed from X6CrNiMoTi17-12-2 steel (AISI 316Ti or DIN 1.4571).

The test-rig was filled with 1 M NaOH (aq) prior to each reaction run which is displaced by the feed solution. Since the reactor is not an ideal plug flow reactor a retention time characterisation was established to determine the time after which the first sample can be taken. Therefore a 1 wt.% guaiacol solution in H₂O was used to generate a Heaviside step response. The concentration at the outlet was measured *via* GC-FID as a function of $t_{\text{retention}}$ and compared to the signal of the feed solution. Figure A 1(b) shows the value of $c(t)/c_0$ versus Θ , where $c(t)$ is the concentration of guaiacol at the outlet at time t and c_0 is the concentration of the feed solution. Θ is the dimensionless $t_{\text{retention}}$ and given by $\Theta = \frac{\dot{V} \Delta t}{V}$. V is the volume of the total test rig including reactor and periphery and was measured to be 190 mL. Due to technical reasons the runs for 3.125 and 2.083 mL/min were aborted early. The value for Θ is set to 1.50, i.e. sampling for runs with $\dot{V} = 3.125$ mL/min started after 91.2 min.

All reactions were performed at $T = 300$ °C and $p = 180$ bar. The first set of five reactions #B1-5 was performed with the purpose of estimating reproducibility and analytical precision of the complete procedure and to evaluate the differences between using KL, HMW, and LMW fraction as feed. The second set, #K1-5, provided a time dependant resolution (Table 6).

2.3.2 Feed Preparation and Product Treatment

A coarse overview of the process and its analytics is provided in Figure 13. The feed solution is prepared by using 1 M NaOH (aq) and dissolution of the lignin derived solids at a ratio of $m_{\text{lignin}}:m_{\text{NaOH}} = 3:1$. Density and pH of the feed were recorded. For product analysis 200 mL was taken from each run and density and pH measured. The pH was lowered to 10 by adding 5 M HCl in portions of 0.5 to 1.0 mL and measuring the pH with a probe (HI991001, Hanna Instruments Inc. Woonsocket USA) The sample was stirred during the procedure and, after

reaching the desired pH, filtered under vacuum filtration through a Büchner funnel. The solid residue is thoroughly washed with H₂O and dried. The pH of the filtrate was then further lowered to pH 7 and pH 2, respectively. The pH 7 step was dropped for the five #K runs with different $t_{\text{retention}}$, since the solids precipitated between pH 10 and pH 7 were of minimal amount. For all samples from the #K runs a titration curve was recorded as a function of H₃O⁺-Ions per unit volume added to the solution. It has to be noted that the filterability of the pH 10 dispersion was very bad. The sample had to be centrifuged and decanted. The solid remains were then redispersed in H₂O and the pH lowered to 2 with 5 M HCl. The solid samples were dried after washing under reduced pressure at 80 °C over 24 h. Their masses were recorded and analysed *via* GPC, EA, TGA/DSC, ¹³C, ¹H, and 2D HSQC NMR, and ATR FT-IR. The pH 2 aqueous phase is extracted with ethyl acetate (EtOAc, 1:1, v:v) and the EtOAc phase is dried with Na₂SO₄. The EtOAc was then evaporated under reduced pressure at 40 °C and the mass of the resulting oil recorded. This oil was dissolved in 10 mL of acetone and an aliquot of 1.5 mL analysed *via* GC-MS-FID. From the remaining solution, the acetone was again evaporated and the oil further analysed by GPC, NMR, and ATR FT-IR. The aqueous phase after extraction was dried under ambient conditions and acetone was used to extract the organic compounds from the NaCl precipitate. Acetone was used since NaCl is sparingly soluble in this solvent and remained as a solid residue after removal of the H₂O.

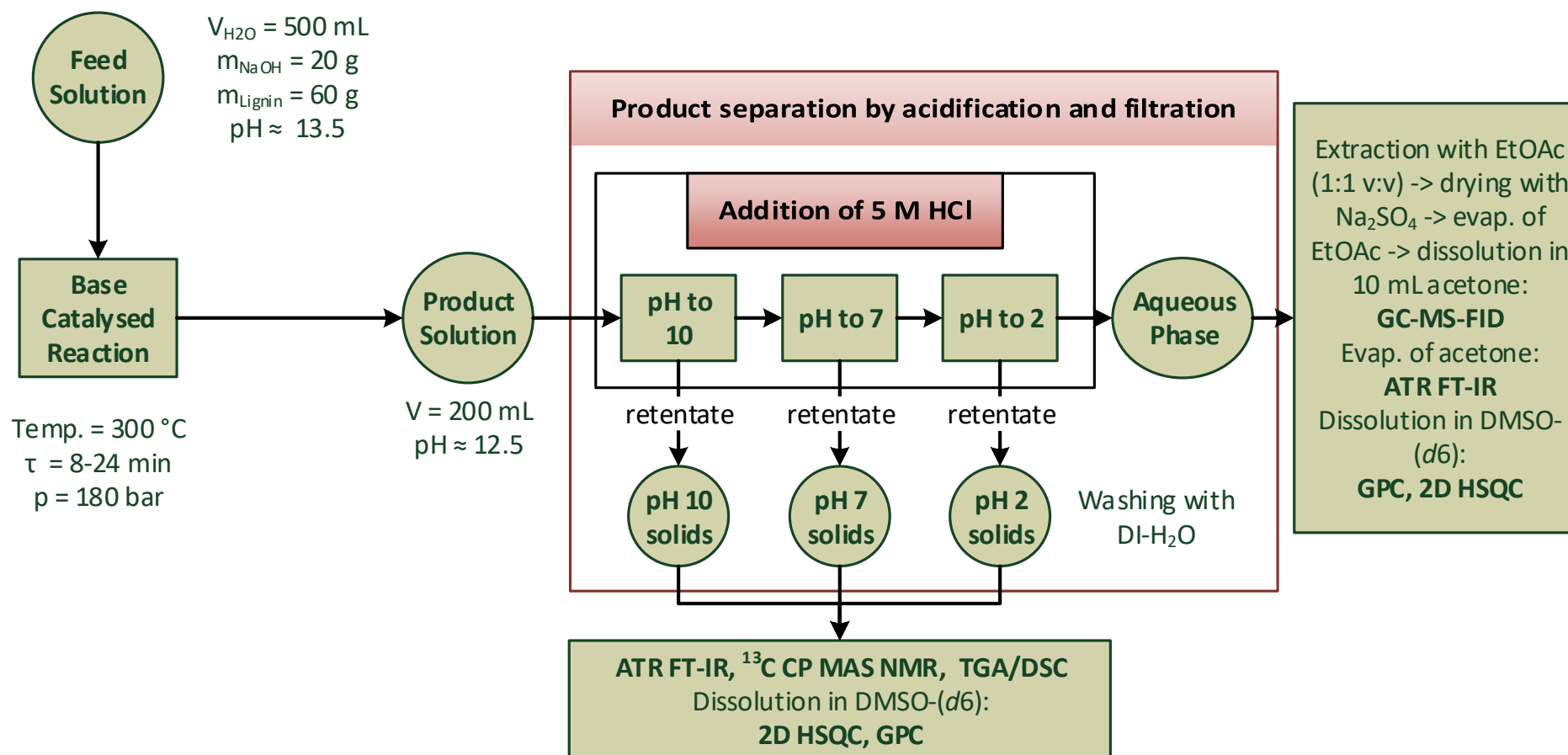


Figure 13: Process and analytics overview of the continuous reactions of lignin compounds in 1 M NaOH (aq).

2.4 Analytical Techniques

2.4.1 Gel Permeation Chromatography (GPC)

The analysis was performed by the Fraunhofer IAP in Golm, Potsdam, Germany. The pump (515), auto sampler (717 plus), column oven, refractive index (RI) detector (2414), and dual λ absorbance detector (2487) were all manufactured by Waters, Milford, MA, USA. GPC columns were polyhydroxy methacrylate (PHMA) copolymer-based as supplied by Polymer Standards Services GmbH, Mainz, Germany.

The PHMA Columns used were:

- Suprema 20 μm pre-column
- Suprema 1000 20 μm , 8 mm I.D. x 300 mm, 100 – 1,000,000
- Suprema 100 20 μm , 8 mm I.D. x 300 mm, 100 – 100.000

Samples were dissolved at a concentration of 2 mg/mL in DMSO with 0.1 M LiBr. The solutions were held at 80 °C for 60 min and then matured for another 24 h under continuous shaking at RT. Detection was performed using a UV detector ($\lambda = 280 \text{ nm}$) and a RI detector. Calibration was performed based on pullulan standards (180 – 1,540,000 g/mol).

Calculation of M_N and M_W was performed according to the OECD guideline for testing chemicals N° 118.¹⁰¹ The corresponding equations are given in equation (2-1) and (2-2), respectively.

$$M_N = \frac{\sum_i H_i}{\sum_i \frac{H_i}{M_i}} \quad (2-1)$$

$$M_W = \frac{\sum_i H_i M_i}{\sum_i H_i} \quad (2-2)$$

Where H_i is the detector signal at time i and M_i the corresponding molecular weight from the calibration curve. The summation was performed from a time smaller than the first elution signal until a $t_{\text{retention}} = 21 \text{ min}$, since this is the last calibration point. Figure A 2 shows the cut-off of the tail of the elution chromatogram at 21 min for the analysis of the three fractions after MeOH extraction.

The GPC chromatogram shows the differential weight fraction over $\log M$. When integrating over $\log M$ the summation curve of equation (2-3) is received, from which the percentiles of the weight fraction can be derived (i.e. the amount of wt.% that is larger than a specific value of M). For attaining the n_i/n values, equations (2-3) to (2-7) are used. The value of M_i is taken as a multitude of the C_9 -unit of the considered interval (equation (2-8)), e.g. 15 for (10,20]. For the low molecular weight part of the GPC chromatogram the upper boundary is taken as a multitude of the C_9 -unit (i.e. the interval (0,1] has $c = 1$ as factor). This leads to smaller values of n_i/n for the low chain length fractions compared to the continuous value, since the summed weight is divided by a larger number. These values seem more realistic, as the calibration of the GPC systematically overestimates the weight fraction of the monomers and dimers.

$$\omega_i = \frac{m_i}{m} \quad (2-3)$$

$$n_i = \frac{m_i}{M_i} \quad (2-4)$$

$$n_i = \frac{\omega_i m}{M_i} \quad (2-5)$$

$$n = \sum_i n_i \quad (2-6)$$

$$\frac{n_i}{n} = \frac{\frac{\omega_i}{M_i}}{\sum_i \frac{\omega_i}{M_i}} \quad (2-7)$$

$$M_i = c M_{C9} \quad \{c \in \mathbb{N}\} \quad (2-8)$$

2.4.2 Elemental Analysis (EA)

EA was performed by the chemical laboratory of the University of Freiburg on a vario EL Element Analyzer. 1.5 mg of sample were analysed in CHNS mode.

2.4.3 Thermogravimetric Analysis (TGA/DTG)

TGA was performed at the University of Freiburg using a Pyris 1 TGA from Perkin Elmer equipped with a standard furnace. For the inert atmosphere, N₂ was employed (purity 5.0) at a flow rate of 20 mL/min. Samples were analysed at a heating rate of 10 K/min. Additionally, TGA was also performed by Dr. Peter S. Shuttleworth (Institute of Polymer Science and Technology, Spanish National Research Council, Madrid, Spain (ICTP-CSIC) using a TA Instruments Q50 with 60 mL/min N₂. Samples were equilibrated at 50 °C and ramped to 800 °C at 10 K/min.

2.4.4 Differential Scanning Calorimetry (DSC)

DSC was performed by Dr. Peter S. Shuttleworth (ICTP-CSIC). Samples were analysed using a Perkin Elmer DSC 7 device. Samples were heated to 100 °C and then heated to the specified temperature, cooled, and the second heating was recorded. Ramping was performed at 5 °C/min. Samples were added to the analysis pan made from aluminium, the lid sealed and a pin hole inserted in the top of the pan. Pans were reweighed after testing and mass values modified accordingly. For determining the glass transition temperature, the TA Universal Analysis software was used.

2.4.5 Gas Chromatography (GC)

Lignin in Methanol and Acetone

GC was qualitatively performed on a GC-MS (Agilent Technologies 5975C, one column: HP-5ms: 30 m x 250 μm x 0.25 μm) and quantitatively *via* a GC-FID (Agilent Technologies 7890A, one column: DB-5ms: 30 m x 250 μm x 0.5 μm). For both analyses, He was employed as carrier gas (total flow rate = 27.634 mL/min). The temperature ramping program of the GCs started with a holding time of 6 min at 35 °C followed by an increase to 270 °C at 5 K/min and a final isothermal period of 5 min. For a first qualification, the NIST database (v2.0f, 2009) was used; the results were then verified *via* standard chromatograms of model compounds. Quantification was performed with 1 mg/mL syringol in acetone in sandwich injection mode. The temperature of the front inlet was set at 280 °C and a splitting ratio of 5:1 was used. The injection volume was 1 μL for both, the samples and the standard.

Model Compounds in Aqueous Phase

The liquid phase was qualitatively determined by a GC-MS (Agilent Technologies 5975C, one column: HP-5ms: 30 m x 250 μm x 0.25 μm) and quantified via a GC-FID (Agilent Technologies 7890A, one column: DB-5ms: 30 m x 250 μm x 0.5 μm). For both analyses, He was employed as carrier gas (total flow rate = 27.634 mL/min). The temperature ramping program of the GC-MS started with a holding time of 6 min at 35 °C followed by a temperature increase to 280 °C at 5 K/min, followed by an isothermal period of 15 min. The total run time for the GC-FID was 5 min. Initially the column started at 100 °C and maintained 0.5 min before being heated up to 190 °C at 20 K/min. For qualification, the NIST database (v2.0f, 2009) was used, quantification was performed *via* calibration curves based on external standards.

Gas Phase

Gas phase analysis of model compound reactions was performed using a GC-TCD (Agilent Technologies 7890A). Two different carrier gases were used: N₂ for H₂ detection (one column: mole-sieve: 25m x 320 μm x 7 μm) and He for the detection of hydrocarbons, N₂ and O₂ (1st column: DB-1: 35 m x 530 μm x 2.65 μm , 2nd column: poraplot q: 30 m x 530 μm x 2.65 μm , 3rd column: mole-sieve: 30 m x 530 μm x 2.65 μm). Regarding the temperature programme employed, an initial isothermal period of 5.4 min at 60 °C was employed, followed by an increased of 60 °C to 150 °C (dT/dt = 110 K/min). A short isothermal period of 0.2 min at this temperature was followed by a further increase to 180 °C (dT/dt = 110 K/min) and isothermal period of 1.3 min. The gas phase was either directly flushed from the autoclave into the GC-TCD or taken by a gas sampling bag.

2.4.6 Fourier Transformed Infrared Spectroscopy (FT-IR)

Samples were analysed using a Bruker Vertex70 IR device equipped with attenuated total reflectance (ATR) module with a germanium crystal. Scans were performed in the range of 4000 to 650 cm^{-1} , a resolution of 4 cm^{-1} , and 128 scans were performed per sample.

2.4.7 Solid State ¹³C Cross Polarisation Magic Angle Spinning (CP MAS) NMR

Solid state ¹³C CP-MAS NMR spectra were obtained using a Bruker AV 400 WB device located at the Department of Mechanical Process Engineering and Mechanics, Karlsruhe Institute of Technology (KIT). Analyses were performed by Ms. Zeyneb Ygit of the Institute for Catalysis Research and Technology of the KIT. Prior to analysis, samples were freeze dried. 120 mg of sample were weighed and 12 mg of sodium trimethylsilyl propionate (denoted hereon as TMSP) were added as internal standard. The spectra were recorded at 100 MHz with an acquisition time of 40.6 ms and 3600 scans were recorded.

2.4.8 Liquid Phase 2D Heteronuclear Single Quantum Correlation (HSQC) NMR

2D HSQC NMR spectra were acquired using a Bruker Avance III 400 located at the Department of Molecular and Coordination Chemistry, University of Freiburg. Analyses were performed by Dr. Harald Scherer. Samples (150 mg/mL) were made ready for analysis by dissolution in DMSO-*d*₆. The spectra were recorded at 400 MHz with an acquisition time of 183.0 ms and 100 MHz and 15.9 ms for ¹H and ¹³C respectively. Total number of scans was 32. The samples were dissolved over 24 h at a concentration of 150 mg/mL. No visible solid residue could be

detected. The oil phase concentration was only 50 mg/mL, since the amount of sample did not allow for a higher concentration.

DMSO-*d*6 was also used as an internal standard (resonance at $\delta_{13C} = 40.2$ ppm / $\delta_{1H} = 2.51$ ppm). The amount of deuteration was at > 99.8%, i.e. assuming that 0.2% 1H is present, the chance of one C-H correlation (for a given probability of a ^{13}C being present) is 1.2%, since DMSO comprises of six isotopes. The amount of lignin per volume of DMSO-*d*6 is known, i.e. the total number of C-H correlations for the distinct groups can be estimated.

$$n_{\text{signals}} = 2 (3 p_{H1} p_{13C}) n_{\text{DMSO-d6}} = 6 p_{1H} p_{13C} \frac{V_{\text{DMSO-d6}} \rho_{\text{DMSO-d6}}}{M_{\text{DMSO-d6}}} \quad (2-9)$$

$$\frac{n_{\text{C-H of area i}}}{m_{\text{lignin}}} = 0.012 \frac{\rho_{\text{DMSO-d6}}}{M_{\text{DMSO-d6}} c_{\text{lignin in DMSO-d6}}} \frac{\text{area}_i}{\text{area}_{\text{DMSO-d6}}} \quad (2-10)$$

Equations (2-9) and (2-10) give the relation for estimating the number of C-H correlations of a specific bond per mass of lignin. p_{1H} and p_{13C} are probabilities for the occurrence of a proton and ^{13}C atom respectively, V , ρ (1.19 g/mL), and M (84.17 g/mol) are volume, density, and molar mass of DMSO-*d*6. c_{lignin} is the concentration of lignin dissolved in DMSO-*d*6. area_i and $\text{area}_{\text{DMSO-d6}}$ are the integrated areas in the HSQC spectra. This is a very rough assumption and based on the level of deuteration in the DMSO-*d*6. Small deviations can give large errors, therefore data acquisition and handling were conducted in as precise a manner as possible and calculated *via* this method. Since errors are systematical (i.e. for all samples and compounds), at least a relative quantification is possible. The results of section 4.2.2, where the amount of single compounds of the oil fraction between GC-FID and 2D HSQC is compared (Figure 53(c)+(d)+(e)), indicate, that the amount of C-H correlations in the DMSO-*d*6 is *ca.* 1/3 of 0.2%. Therefore, adjustments in the respective calculations were performed, meaning that equation (2-10) is additionally divided by three.

The collected data was Fourier transformed with the software ACD/NMR and the resulting matrix exported to an ASCII file. This is then transferred into MatLab®, where normalisation and integrations were performed. The size of the matrix (defined by the resolution of the 2D NMR) was set at 1024 x 1024 and the scanned area ranged from $\delta_{13C} = 0.2$ to 159.81 ppm and is for most δ_{1H} from -2 to 10 ppm. This results in a resolution of $\Delta\delta_{13C} = 0.156$ ppm and $\Delta\delta_{1H} = 0.012$ ppm. Normalisation is performed by searching the defined DMSO-area (Table A 14) for its highest value and then dividing the whole matrix by this number. For integration, the noise of the results' matrices is removed by setting all values below the defined noise level to 0, i.e. only values above a certain value are considered for integration. The level is given in the respective 2D HSQC heat map legends (e.g. 0.02 for the maps in Figure 50).

2.4.9 Liquid Phase 1H and ^{13}C NMR

Liquid phase 1H and ^{13}C NMR spectra were acquired using a Bruker Avance III 400 located at the Department of Molecular and Coordination Chemistry, University of Freiburg. Analyses were performed by Dr. Harald Scherer. Samples (150 mg/mL) were made ready for analysis by dissolution in DMSO-*d*6. 1H NMR spectra were acquired at 400 MHz, 32 transients, and an acquisition time of 4.09 s.

2.4.10 Gas Sorption (BET)

N₂ adsorption was performed at the Fraunhofer ISE in the division Heating and Cooling Technologies in the group Sorption Materials by Philipp Hügenell. Isotherms were obtained on a Quantachrome® Nova at 77 K, after degassing under vacuum at 120 °C for 24 h. The surface area was determined using the Brunauer–Emmett–Teller (BET) theory.

3 Solvent Extraction from Lignin

As a first step in the process a solvent extraction is supposed to separate the lignin into two fractions. The aim is to generate a more homogeneous fraction devoid of low molecular weight compounds (Figure 1). The latter are viewed as problematic during preparation of CF (e.g. during carbonisation), since they can produce holes (during volatilisation) in the forming fibre matrix if they do not polymerise during stabilisation or carbonisation. This chapter will give a brief overview on solubilisation of polymers and the underlying theory. The process and the parameters will be described and the results will be discussed. The original lignin (i.e. dried softwood KL from the LignoBoost® process) will be set in relation to the extracted fractions. Furthermore, the literature on lignin extraction *via* organic solvents is reviewed with a focus on KL. Since the fractions are set in relation, a description of the original lignin will be performed.

3.1 Theory and Prior Art

Dissolution of one phase in another is described as the process of going from a highly ordered solid state into infinite separation (i.e. an ideal gas).¹⁰² Thermodynamically, the heat of evaporation has to be overcome in order to go from a homogeneous liquid phase into a mixed two-phase system. If this is performed with, e.g., two different liquids, it translates into a molecule of liquid *A* being evaporated out of the bulk of liquid *A* and subsequently condensed in the bulk of liquid *B* and vice versa. This process only happens spontaneously if the heat of vaporisation of the two molecules is not too different. More generally speaking, a spontaneous process only takes place when $\Delta G = \Delta H - T\Delta S < 0$. The value of ΔS will be positive for mixing two phases, so $T\Delta S > \Delta H$ applies. When mixing two pure liquids, ΔS is the main driving force behind the spontaneous process, since the increase in entropy is significant. When trying to dissolve a solid in a liquid or even mixing two polymers, the process is more enthalpy driven.¹⁰²

The energy necessary for removing a molecule out of its bulk phase is more precisely called cohesive energy (*E*) and is given by $E = \Delta H_{\text{vap}} - RT$, where ΔH_{vap} is the heat of vaporisation, *R* the gas constant, and *T* the absolute temperature.¹⁰² Since the cohesive energy itself is dependent on the size of the molecule it is set in relation to the molar volume *v*. This leads to the Hildebrand solubility parameter as calculated in equation (3-1). As a rule of thumb, a polymer is soluble in a solvent when the difference in the solubility parameters fulfil the conditions given in equation (3-2).¹⁰²

$$\delta = \sqrt{\frac{\Delta H_{\text{vap}} - RT}{v}} \quad (3-1)$$

$$|\delta_1 - \delta_2| \leq 1.8 \left(\frac{\text{cal}}{\text{cm}^3} \right)^{\frac{1}{2}} = 3.7 \text{ MPa}^{\frac{1}{2}} \quad (3-2)$$

This prediction only holds true as long as polymer and solvent have comparable polar and hydrogen bonding degrees. To overcome this limitation, Hansen developed a model comprising out of three distinct energies.¹⁰²

These energies are dispersion (E_d), polar (E_p), and hydrogen-bonding (E_h) and they add to the cohesive energy: $E = E_d + E_p + E_h$. In accordance with the Hildebrand model this translates to $\delta^2 = \delta_d^2 + \delta_p^2 + \delta_h^2$. These three parameters span a three-dimensional room, where each solvent, polymer, etc. is situated in. Solubility can be measured by distances between those points. Equation (3-3) gives a relation between the Hansen solubility parameters and solubility sphere radius.¹⁰² The radius R can be measured using “good” and “bad” solvents for a specific polymer. The good solvents define the radius and other solvents within this radius will as well be good solvents for the specific polymer.¹⁰²

$$\sqrt{4(\delta_{d1} - \delta_{d2})^2 + (\delta_{p1} - \delta_{p2})^2 + (\delta_{h1} - \delta_{h2})^2} \leq R \quad (3-3)$$

Lignin, in this case KL, is a heterogeneous, covalently bonded, mixture of aromatic compounds. The average molecular weight is in the range of 5,000 g/mol with a poly-dispersity of *ca.* 5, so the number average is 1,000 g/mol. While the majority are oligomers, the lignin contains also some monomers, dimers, and other smaller molecules. This diversity in the compounds is a major hindrance in further processing the lignin, since no matter what process is employed; it will be unsuitable for at least some of the constituents. Extracting from the lignin *via* the use of organic solvents to achieve fractions with a higher purity is a common technique and in 1952 Schuerch provided an overview on the solubility of different kinds of lignin in different solvents.¹⁰³ Beside other lignin, Indulin Kraft pine is in the list, and it was found that it is partially soluble in e.g. MeOH, CH₃CH₂OH, acetone, and chloroform while being completely soluble in diethylene glycol, pyridine, and dioxane.¹⁰³ Polar solvents (H₂O, glycerol) as well as traditional organic solvents (hexane, xylene) proved to be unsuitable for dissolving the lignin. Solubility of lignin increases as hydrogen-bonding power increases and the Hildebrand parameter approaches 22 MPa^{1/2}. The H-bonding capabilities of a solvent were described by the amount of shift of the oxygen deuterium band of deuterated MeOH (CH₃OD) at infrared.¹⁰³ Compounds with the same solubility parameter dissolved specific lignin in a very different amount and their ability for dissolving lignin was a function of their H-bonding capacity (i.e. the shift of the aforementioned band).¹⁰³ Schuerch stated that compounds with a Hildebrand parameter of 22 MPa^{1/2} and having a shift of > 0.14 μm are good lignin solvents.¹⁰³ This shift is a summary of the two non-atomic parameters of Hansen, the dipole-dipole energy and the hydrogen bonding energies. From Equation (3-3) it can be seen that these two parameters should be equal between solvent and polymer and not just larger than a certain value. Since all varieties of lignin are heterogeneous mixtures, each compound in this mixture has its own set of parameters, making it difficult to dissolve the complete lignin in one solvent but simultaneously giving the possibility to dissolve only specific compounds, thereby giving a means of separation.

Schuerch gives a δ value for MeOH of 28.6 MPa^{1/2}, which is a value higher than the suggested 22 MPa^{1/2} for lignin.¹⁰³ The shift for the O-D bond of deuterated MeOH in solution with normal MeOH is relatively high with $\Delta\mu = 0.28 \mu\text{m}$, which gives the MeOH an acceptable solvent capability.¹⁰³ These characteristics give the MeOH the capability of dissolving all of the low molecular weight compounds in the lignin, while not being able to dissolve the larger ones.¹⁰³ The goal is to remove H₂O insoluble monomers, dimers, and trimers (and some larger compounds) *via* the MeOH and thus creating a more homogeneous mixture of oligomers giving an increased stability during carbonisation. Since during the process a certain loss of solvent is to be expected, a cheap and

readily available solvent should be chosen. MeOH fulfils these criteria with a world market price of 250 – 350 US\$/t and world-wide demand of 70 Mt/a in 2015.¹⁰⁴

Solvent extraction from lignin with the aim of purification has been performed by several groups with different solvents.^{69,71,103,105–113} The usage of organic solvents in sequential procedure with the aim of structural investigation was described in detail by Mörck, Yoshida *et al.*^{69,112,113} They used mainly softwood derived KL from black liquor that was precipitated *via* sulphuric acid down to a pH of 9.5. The resulting precipitate was washed, dried, and sequentially extracted with CH₂Cl₂, CH₃CH₂CH₂OH, CH₃OH, CH₃OH/CH₂Cl₂ (7:3). Yields, elemental composition, methoxy content, and thermal properties are described in Table 7.

Table 7: Yields, elemental composition, methoxyl content and thermal properties of the sequential solvent extraction performed by Mörck *et al.*⁶⁹ For thermal properties see Yoshida *et al.*¹¹³

Fraction	Solvent	Yield of starting mat. [%]	Acetylated Mw [g/mol]	Elemental Analysis				Methoxy content [%]	10% weight loss [°C]
				C [%]	H [%]	O [%]	S [%]		
1	CH ₂ Cl ₂	9	620	67.8	6.43	23.0	2.7	15.4	256
2	CH ₃ CH ₂ CH ₂ OH	22	1290	65.3	6.48	26.8	1.4	16.0	294
3	CH ₃ OH	26	2890	64.7	5.96	27.7	1.5	14.9	317
4	CH ₃ OH/CH ₂ Cl ₂ (7:3)	28	82000	64.5	5.73	28.2	1.3	13.9	329
5	solid residue	14	180000	59.0	5.54	32.8	1.2	11.3	303
starting material	n.a.	100	39000	n.a.					306

In the extraction process it was started with a concentration of 200 mg/mL and CH₂Cl₂. This was constantly reduced since a comparable amount of solvent was used for each step with less amount of lignin residue. Molecular weight constantly increased with the fractions, as was expected. The carbon content was highest in the low molecular weight fraction 1 and decreases along the line, which is also true for hydrogen. Fraction 5 contained 8.7 wt.% carbohydrates which would explain the low methoxyl and high oxygen content. It is interesting that fraction 1 has relatively high sulphur content, meaning that the sulphur containing compounds are rather small and have a high affinity for CH₂Cl₂. Mörck *et al.* did also ¹³C NMR analyses in CDCl₃ and gave the amount of phenolic-OH, total-OH, and acidic groups. Phenolic-OH and acidic groups decrease from fraction 1 to 5, while total-OH is rather constant, with a resonance in fraction 2 and a low in fraction 5.⁶⁹ In a second study Yoshida *et al.* analysed the five fractions thermogravimetrically.¹¹³ The TGA up to 500 °C showed that the decomposition temperature increased with molecular weight from fraction 1 to 4. The decrease for 10% weight loss for fraction 5 can be attributed to the increased hydrocarbon content from remaining hemicellulose, this decomposes much faster between 200 and 300 °C compared to lignin.¹¹³

Wang *et al.* analysed *eucalyptus pellita* hardwood from a Kraft process with 0.1% anthraquinone addition.¹⁰⁹ The lignin was obtained from the black liquor by acidification to pH 2 with HCl (aq), washed and dried. The subsequent sequential extraction was performed with hexane, diethyl ether, CH₂Cl₂, MeOH, and dioxane and yielded 0.2,

1.6, 33.4, 59.1 and 4.4 wt.% respectively. Only trace amounts of solid residue could be found. The extraction was performed in a Soxhlet extractor and performed until the supernatant was light in colour.¹⁰⁹

Saito *et al.* used MeOH to extract from softwood KL at a concentration of *ca.* 140 mg/mL and repeated this washing three times.¹⁰⁸ The resulting fractions were dried and analysed by high temperature size exclusion chromatography (HTSEC), TGA/DSC, XPS, ³¹P and ¹³C NMR. As determined per HTSEC the MeOH washings removed subsequently the low molecular weight fraction from the lignin with a total yield of 50%.¹⁰⁸ The molecular weight distribution and thermal properties of the different fractions are shown in Table 8.

Table 8: Molecular weight distribution and thermal properties of the MeOH fractionated softwood KL as reported by Saito *et al.*¹⁰⁸

Fraction	M _w [g/mol]	M _n [g/mol]	T _g [°C]	10% weight loss [°C]	Residual char at 1000 °C [%]
As-received	7,190	2,360	153	301	41
MeOH soluble	3,000	1,590	117	260	32
MeOH insoluble	14,900	6,520	211	293	47

Thermal stability increases with molecular weight as does the value for the T_g. This is in agreement with the findings of Mörck and Yoshida *et al.*^{69,113} The chemical composition analysed by ¹³C NMR in DMSO-*d*₆ does not show significant differences. The interpretation of the results was performed by area integration of the spectra as shown in Table 9. Only the area for the aliphatic C-C bonds is significantly larger for the MeOH soluble fraction compared to the insoluble fraction (0.4 to 0.1).¹⁰⁸ This can be due to an increased number of saturated sidechains and/or linear aliphatic compounds.

Table 9: Resonance assignment of ¹³C NMR in DMSO-*d*₆ (performed by Saito *et al.*¹¹⁴).

δ ¹³ C [ppm]	Assignment
175-168	Aliphatic COOR
162-140	C _{Ar} -O
140-123	C _{Ar} -C
123-102	C _{Ar} -H
98-58	Aliphatic C-O
58-54	Methoxy OCH ₃
49-0	Aliphatic C-C

Jiang *et al.* used softwood KL from the Domtar Plymouth pulp mill, which is the same lignin this thesis is based upon.¹⁰⁵ Extraction was conducted by dissolving 5 g of lignin in 10 mL of a 7:3 v:v MeOH:acetone solution. This was then subsequently precipitated by the usage of organic solvents (100 mL ethyl acetate, 50 mL ethyl acetate/petroleum ether (1:1, v:v), 25 mL petroleum ether). A detailed description of the procedure is given in the paper.¹⁰⁵ Taking this information, the first solvent consisted out of 7 mL MeOH, 3 mL acetone, and 100 mL ethyl acetate dissolving 52% of the lignin. The remaining 48% were the high molecular weight fraction (F1) with a M_w of 10,000 g/mol and a polydispersity (PDI = M_w/M_n) of 3 (Table 10). The original lignin was measured to have a

M_w of 5,200 g/mol and a PDI of 3.3. The second fraction consisted of 39% of the original lignin and was precipitated out of 30 mL ethyl acetate by adding 25 mL of petroleum ether. This fraction had a M_w of 2,500 g/mol and a PDI of 1.5. The remaining two fractions were roughly 13% with a M_w of 750 and a PDI of 1.2.

Table 10: Molecular weight distribution, elemental analysis, methoxyl content, and thermal properties of the fractionated softwood KL from the Domtar pulp mill as reported by Jiang *et al.*¹⁰⁵

Fraction	Yield [%]	M_w / PDI [g/mol]	Elemental Analysis				Methoxyl content [%]	10% weight loss (Td) [°C]	Residual char at 600 °C [%]
			C [%]	H [%]	O [%]	S [%]			
KL	100	5202 / 3.33	65.0	6.0	27.5	1.4	12.9	277	45.2
F1	48	10244 / 3.02	64.2	5.9	28.5	1.3	12.1	251	46.6
F2	39	2468 / 1.50	65.9	5.9	26.7	1.4	12.3	231	37.5
F3	10	770 / 1.23	66.9	6.2	25.4	1.5	13.5	209	23.3
F4	3	407 / 1.12	n.d. (too little sample)						

The fractions were further analysed by EA showing again a decrease in carbon content with increasing M_w . Sulphur and hydrogen content were found to be rather constant. Jiang *et al.* also determined the relative amount of lignin substructures per 100 aromatic rings. This was achieved by a combination of the information from the ¹³C and 2D HSQC spectra according to Hu *et al.*¹¹⁵ Hu *et al.* did a complete analysis of the Domtar BioChoice™ KL and compared its structural features with the commercial Indulin AT KL and pine milled wood lignin (MWL) finding that the structural features of the Domtar lignin and the Indulin AT are very different from the MWL while being similar towards each other.¹¹⁵ Hu *et al.*¹¹⁵ did also a comparison of the Domtar KL with Indulin AT and pine milled wood lignin (MWL) from studies of Hu *et al.*¹¹⁶ and Holtman *et al.*¹¹⁷ (Table 11). Indulin AT is KL from liner grade pulp and is thus produced under less harsh pulping conditions than the Domtar KL since a higher amount of residual lignin in the cellulose fibres can be accepted.

Table 11: Elemental analysis and substructures of Domtar KL¹¹⁵, Indulin AT, and pine milled wood lignin (MWL)

Lignin	Elemental analysis [%]				Functional groups and side chains per 100 aromatic rings					
	C	H	O	S	Methoxyl content ^I	Free OH ^{II}		Stilbenes ^{III}	α -carbonyl ^{IV}	
						Phenolic	Aliphatic			
KL	65.0	6.7	26.5	1.6	12.8	74	35	6.2	8	
Indulin AT ^V	65.9	5.9	27.1	1.1	14.0	61	39	5.6	9	
MWL ¹¹⁶	65.0	5.8	29.2	—	16.0	28	114	n.d.		
Substructures per 100 aromatic rings ⁴										
	C ₉ -formula				β -O-4	β -5	dibenzo-dioxocin	enol ether	stilbenes	
KL	C ₉ H _{9.8} O _{2.0} (OCH ₃) _{0.74} S _{0.09}				2.2	1.1	0.8	2.2	7.3	
Indulin AT	C ₉ H _{8.1} O _{2.2} (OCH ₃) _{0.83} S _{0.06}				8.2	1.1	0.6	1.5	6.7	
MWL ¹¹⁷	C ₉ H _{7.8} O _{2.4} (OCH ₃) _{0.95}				41	9	8	—	—	

^I via GC; ^{II} via ³¹P NMR; ^{III} via UV-Vis; ^{IV} estimated by 2D HSQC and ¹³C NMR; ^V as-received and well-washed Indulin AT was used, these are the values for well-washed

During the Kraft cook a reduction of the methoxyl groups by *ca.* 20% takes place, most probably by demethylation *via* the reduced sulphur compounds (S^{2-} , HS^- , CH_3S^-).¹¹⁵ The amount of β -O-4 linkages is reduced by 95%, where these form new free phenolic-OH groups. Dibenzodioxocin structures are reduced by 90%, while alkaline stable stilbenes are produced in a significant amount (Figure 14).¹¹⁵

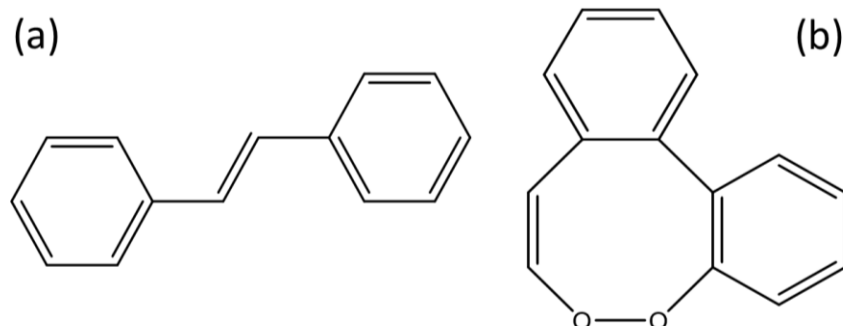


Figure 14: Structural formula of stilbenes (a) and dibenzodioxocin (b).

3.2 Results & Discussion

The aim of the solvent extraction is to remove the lower molecular weight compounds from the lignin, while retaining as much of the high molecular weight compounds as possible. In the beginning, it was assumed, that increasing the lignin concentration would lead to saturation and subsequent less amounts of lignin being dissolved with adding more lignin to the MeOH. Tests showed that this was not the case and the solubility was even increased at higher concentrations (Table 12).

Table 12: Dissolution of KL in MeOH and MeOH:H₂O under ambient conditions at different concentrations ($\rho_{\text{MeOH}} = 0.791 \text{ g/mL}$).

$\omega = \frac{m_{\text{lignin}}}{m_{\text{methanol}} + m_{\text{lignin}}}$ [-]	$\frac{m_{\text{lignin}}}{V_{\text{methanol}}} = \frac{\omega \rho_{\text{methanol}}}{1 - \omega}$ [mg/mL]	Dissolved lignin [wt.%]
0.1	87.9	40.3
0.2	197.8	22.6
0.3	339.0	34.4
MeOH:H ₂ O (v:v) [-]	Density [g/mL]	Dissolved lignin ($\omega = 0.1$) [wt.%]
1:3	0.942	8.3
1:1	0.916	14.1
3:1	0.850	31.3

Adding large amounts of lignin to the solvent (30 wt.% means $m_{\text{lignin}}/m_{\text{MeOH}} = 0.43$) will probably change the nature of the solvent itself and its Hansen parameters towards that of the lignin, i.e. a mixture of aromatics. This was tried to measure *via* a sequential dissolution (Figure 11). A 100 mg/mL lignin:MeOH solution was prepared and after removal of the non-dissolvable fraction, this solution was used as solvent with the same concentration. A sequential approach was chosen, since it was not possible adding more than 30 wt.% (*ca.* 340 mg/mL) in one step as the lignin soaked up the MeOH. After nine repetitions, a highly viscous oil was produced with a density

of 0.95 g/mL that contained in total 40 wt.% solids after drying at ambient conditions for five days. A minimum for dissolved lignin could be seen at *ca.* 200 - 250 mg/mL with 20 – 25% of the lignin dissolved. Since the lignin from the Domtar mill leaves the LignoBoost® plant undried with a H₂O content of *ca.* 35 wt.%, the solubility of the lignin in MeOH:H₂O mixtures at different concentrations was analysed (Table 12) and found that H₂O decreases the solvent capabilities of MeOH. Schuerch¹⁰³ and Hansen¹⁰² state, that the usage of a co-solvent can shift the solubility capabilities of a bad solvent towards a good solvent. Especially H₂O:CH₃CH₂OH mixtures use this effect for efficiently dissolving lignin, e.g. in the ALCELL® process.¹¹⁸ The used KL seems not to benefit from these properties, at least not at room temperature and the solvent power is lower at any mixtures of MeOH:H₂O compared to pure MeOH. As a result, a concentration of 250 mg/mL for the extraction process was chosen on the basis that at this concentration the amount of extracted lignin is lowest, while still providing low viscosity resulting in good pumpability of the liquid.

3.2.1 Gel Permeation Chromatography (GPC)

GPC analysis indicates that a fractionation into a high molecular weight fraction (HMW) and a low molecular weight fraction (LMW) is achieved after MeOH extraction (Figure 15, Table 13). Starting point for the summation in the elution diagram is 10 min. The GPC was performed after extraction at a concentration of 250 mg/mL (lignin/MeOH), while at this concentration *ca.* 20% of the lignin is dissolvable. The calibration gives a M_w for the KL of 5,300 g/mol, which is in the same range as the 6,700 g/mol reported by Hu *et al.*¹¹⁵ and 5,200 for Jiang *et al.*¹⁰⁵ When comparing the direct elution chromatograms (Figure A 2), a broad peak for very large compounds and a distinct peak for large compounds can be seen for Hu *et al.* The GPC analyses for the lignin in this work gave a purely monomodal distribution. All GPC chromatograms indicate signals for compounds with $t_{\text{retention}} = 21$ min. These would correspond to molecules smaller than 50 g/mol, and compounds this size will probably not comprise the lignin as GC analysis would indicate their presence. This tailing can potentially be caused by the presence of compounds in the mixture that possess a very high affinity for the chromatographic stationary phase (i.e. compounds having a high number of polar side chains, relative to their overall molecular mass).

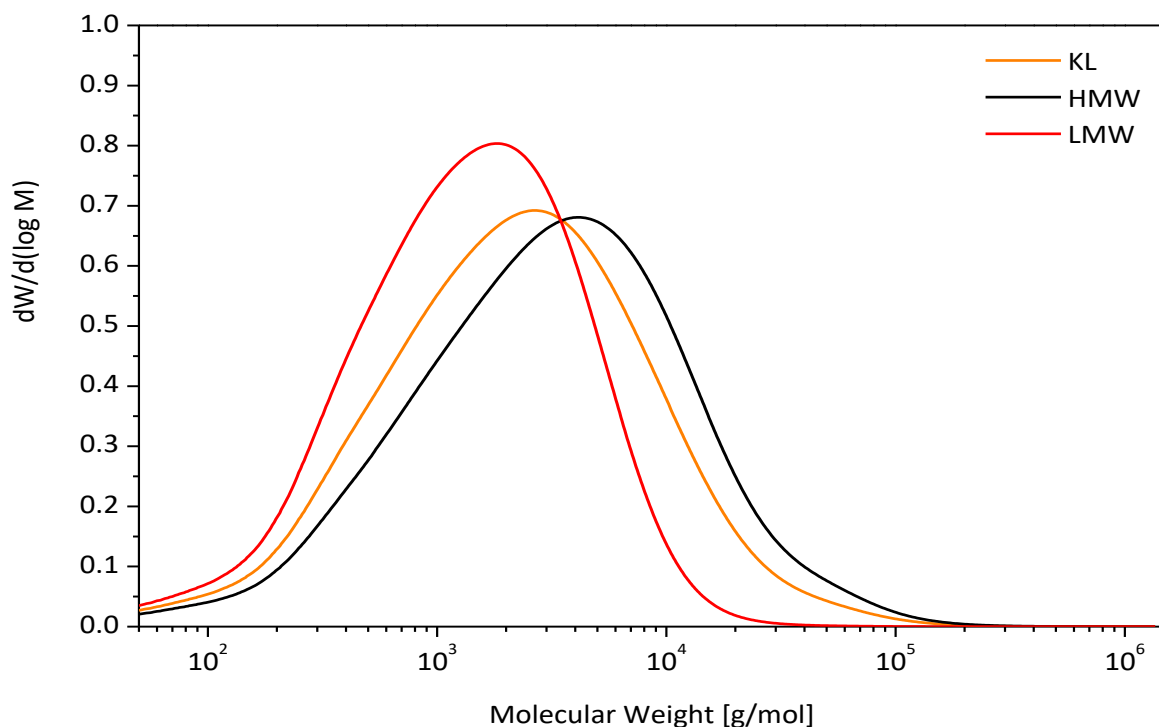


Figure 15: Molecular weight distribution of original KL and the MeOH soluble and insoluble fraction after extraction at 250 mg/mL measured via GPC.

Table 13: Average molecular weights and polydispersity of the KL after MeOH extraction as determined *via* GPC.

Sample	M_w [g/mol]	M_n [g/mol]	PDI [-]
KL	5,330	940	5.7
MeOH Insoluble Fraction High Molecular Weight (HMW)	7,460	1,170	6.4
MeOH Soluble Fraction Low Molecular Weight (LMW)	2,320	700	3.3

Integrating the chromatogram over $\log M$ leads to the summation curve and the derived histogram for m_i/m is given in Figure 16(a), for n_i/n in Figure 16(b). The tailing of the elution chromatogram seems to overestimate the weight fraction of the smaller compounds. If these were to comprise more than 50% of the molecules, the GC readouts in chapter 3.2.4 would show more monomers. Figure 16(b) shows, that the majority of the molecules has chain lengths between three and 20 C_9 -Units. This is shifted towards smaller molecules for the LMW fraction and towards higher for the HMW fraction, but these fractions still have the majority in this area. The value for M_i used for the calculation of n_i and n *via* equation (2-7) is taken from the results of the elemental analysis and the 2D HSQC in chapter 3.2.6. The value for m_i/m for C_9 -Units +100 is 5.3 wt%, 8.9 wt.%, and 0.4 wt.% for the fractions KL, HMW, and LMW, respectively. They have been categorised into (100,200], (200,500], and (500,1000] and contribute in total 0.4% for n_i/n for the HMW fraction. The detailed values are given in Table A 1.

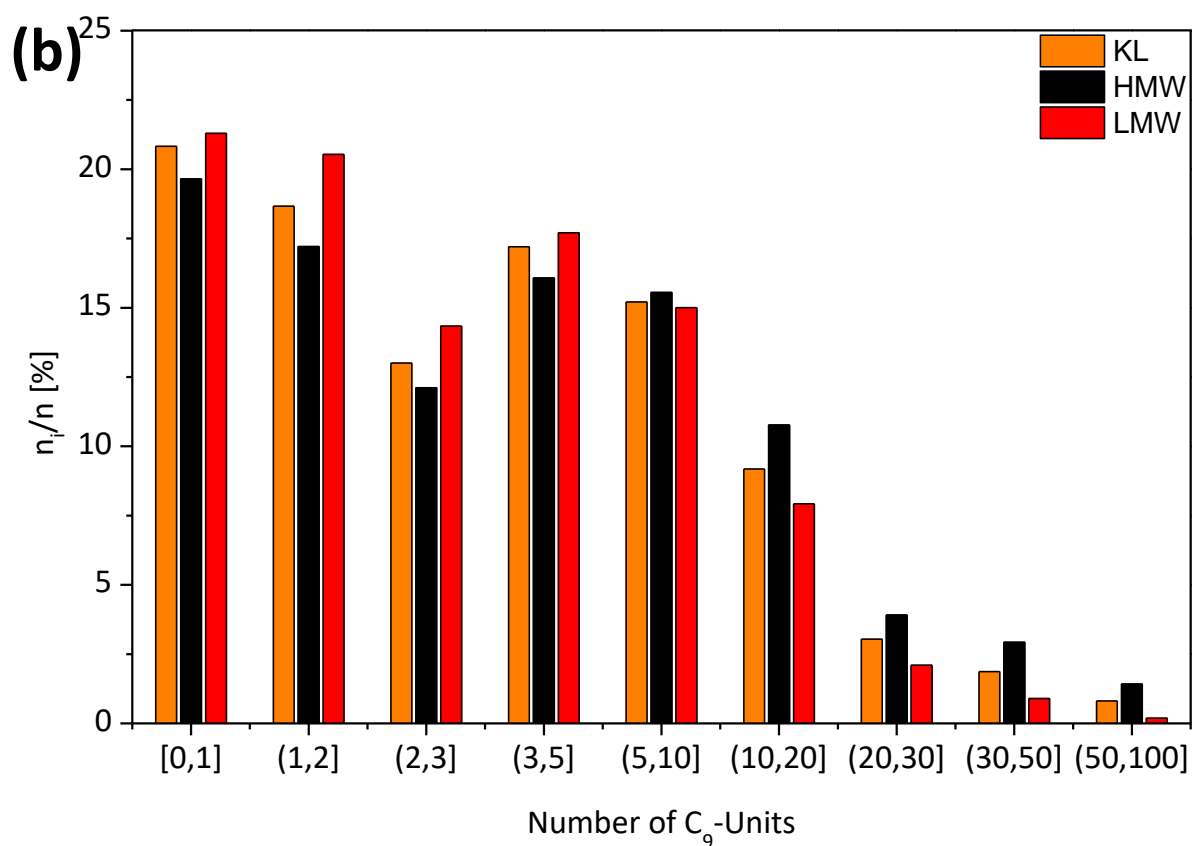
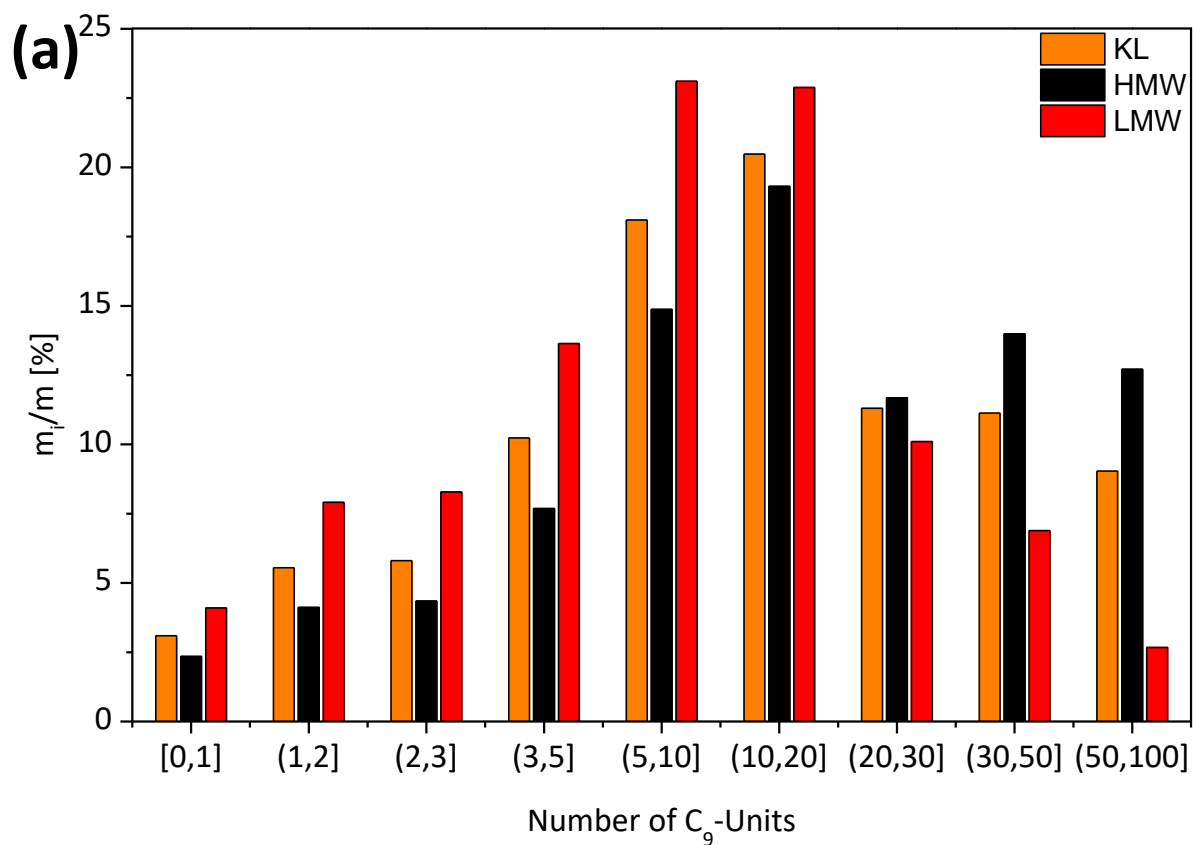


Figure 16: (a) m_i/m and (b) n_i/n for specific chain length of KL, HMW, and LMW. The values are generated from the GPC data and the value used in the calculation of n_i is taken as mean value from the ranges (e.g. 15 for 15-20).

3.2.2 Elemental Analysis (EA)

Elemental analysis of the three fractions is given in Table 14. The analysis indicates an increase of carbon and decreases in sulphur content in the MeOH soluble fraction. The change in oxygen results from being calculated by difference. It seems that more of the sulphur is bound in larger aromatic structures not being dissolvable in MeOH at the given concentration. Jiang *et al.*¹⁰⁵ and Mörck *et al.*⁶⁹ experienced the same increase in carbon content in the lower molecular weight fractions, while no differences in sulphur content between the fractions could be seen in the work of Jiang *et al.*, where Mörck *et al.* saw an increase in the lower molecular weight fractions. The Domtar KL analysed by Jiang *et al.*¹⁰⁵ and Hu *et al.*¹¹⁵ had nitrogen contents of *ca.* 0.1%, while in the lignin used in this study nitrogen was not detected.

Table 14: Elemental analysis of KL, LMW, and HMW

Fraction	C [%]	H [%]	O ^a [%]	N [%]	S [%]
KL	62.13	5.74	30.39	n.d. ^b	1.74
LMW	64.55	5.79	28.22	n.d.	1.44
HMW	61.59	5.67	30.88	n.d.	1.86

^a calculated by difference; ^b not detected

When using the results from the EA and doing an elemental based mass balance on carbon and sulphur (the change in hydrogen is too small and oxygen is calculated by difference), this leads to a theoretically dissolved amount of 19 wt.% (equation(A 1) to (A 3)). This value confirms the 20 wt.% determined *via* the mass balance.

3.2.3 Thermogravimetric Analysis (TGA/DTG/DSC)

Thermogravimetric analysis of the three fractions (KL, HMW, LMW) is shown in Figure 18(a). At 600 °C the LMW has a residue of 45.4%, while HMW and Lignin have 52.3 and 50.1%, respectively. The corresponding DTG is given in Figure 18b showing a monomodal distribution for all fractions with maxima at 352, 361, and 363 °C for the LMW, KL, and HMW fraction.

Table 15: Decomposition temperature (T_d), maximum in DTG, and residual mass at 600 °C of the Domtar KL and the MeOH extracted fractions.

Fraction	T_d^a [°C]	Maximum in DTG [°C]	Residual mass at 600 °C [%]
KL	299.7	359.7	50.1
HMW	297.3	363.0	52.3
LMW	272.7	352.7	45.4

^a temperature at 10% weight loss

Jiang *et al.* did a TGA of the Domtar lignin with the same parameters.¹⁰⁵ Their residual mass for the unextracted lignin was 45.2%, i.e. *ca.* 5% less than in this work. Their fraction F1 (the highest molecular weight fraction) had a residual mass of 46.6%, also significantly less than the 52.3% in this work. The low molecular weight fractions cannot be compared due to the very different composition (Table 10). The decomposition temperature (T_d : defined at 10% weight loss) in the study of Jiang *et al.* was at 277 °C for the unextracted lignin, where this value is

at 300 °C in this work. It seems that the difference in residual mass is due to more volatile low molecular weight compounds in the study of Jiang *et al.* being present. Saito *et al.* extracted with MeOH from a different KL. While the residual mass in the TGA was determined at 1000 °C and is thus not comparable to the numbers in this work, the temperatures for T_d are very similar (Table 8). Yoshida *et al.* also extracted subsequently from a softwood KL.¹¹³ The 10% weight loss was at 306 °C for the unfractionated lignin (Table 7).

Additionally, TGA was conducted at the ICTP-CSIC in Madrid as preparation for the DSC. These were performed up to 800 °C and show a peak in the DTG at *ca.* 700 °C, which only appears in KL and HMW (Figure A 3). The DSC of the three fractions is given in Figure 17 and the resulting values for the glass transition temperatures in Table 16. While KL and LMW exhibit a clear glass transition at 147 and 121 °C, respectively, the HMW fraction only shows a small endothermic event at 159 °C and continues with a comparable increase in c_p afterwards.

Table 16: Glass transition of the KL, HMW, and LMW fractions determined via DSC.

Sample	Onset [°C]	Midpoint [°C]	End [°C]	Height [W/g]	Delta c_p [J/(g K)]
KL	139.53	146.91	157.20	0.02458	0.2952
HMW	156.56	159.10	161.18	0.02106	0.2528
LMW	115.98	121.02	134.37	0.03966	0.4760

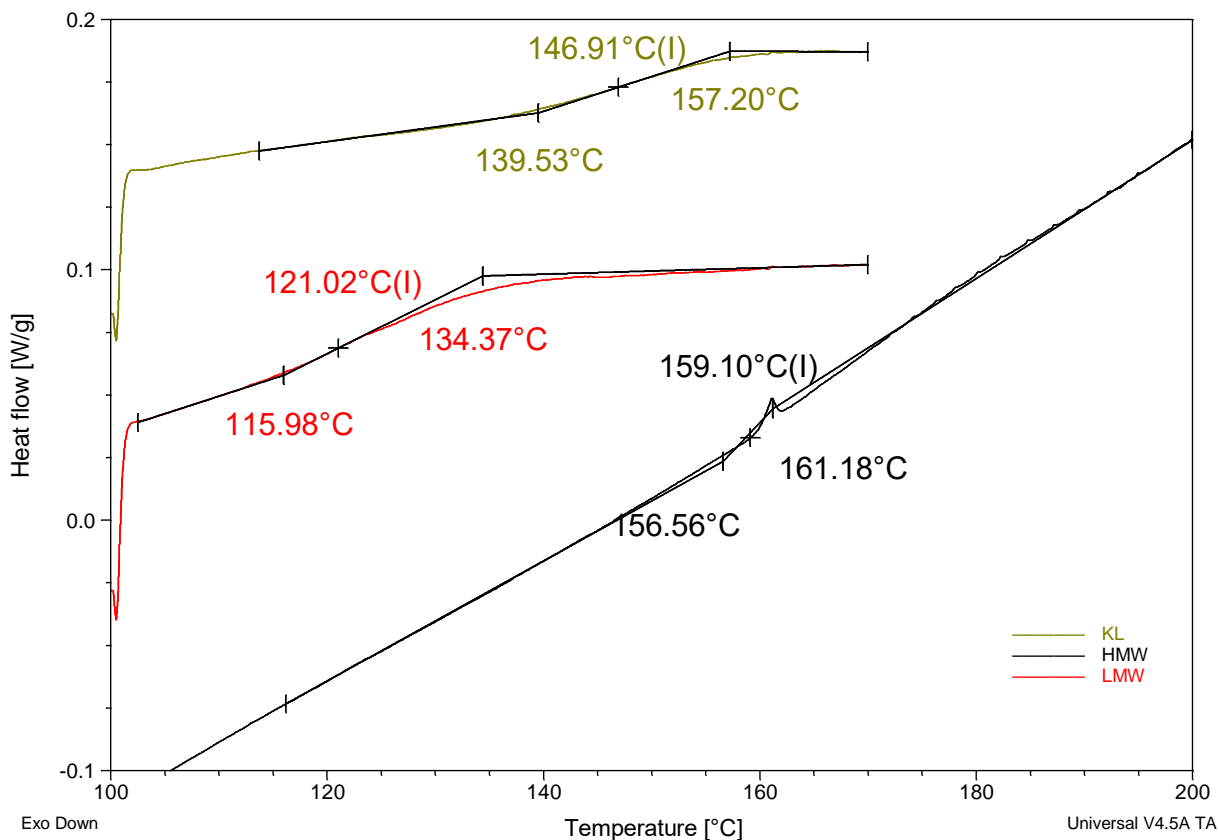


Figure 17: DSC traces of the fractions KL, HMW, LMW. Glass transition temperatures were determined via the TA Universal software within the indicated limits.

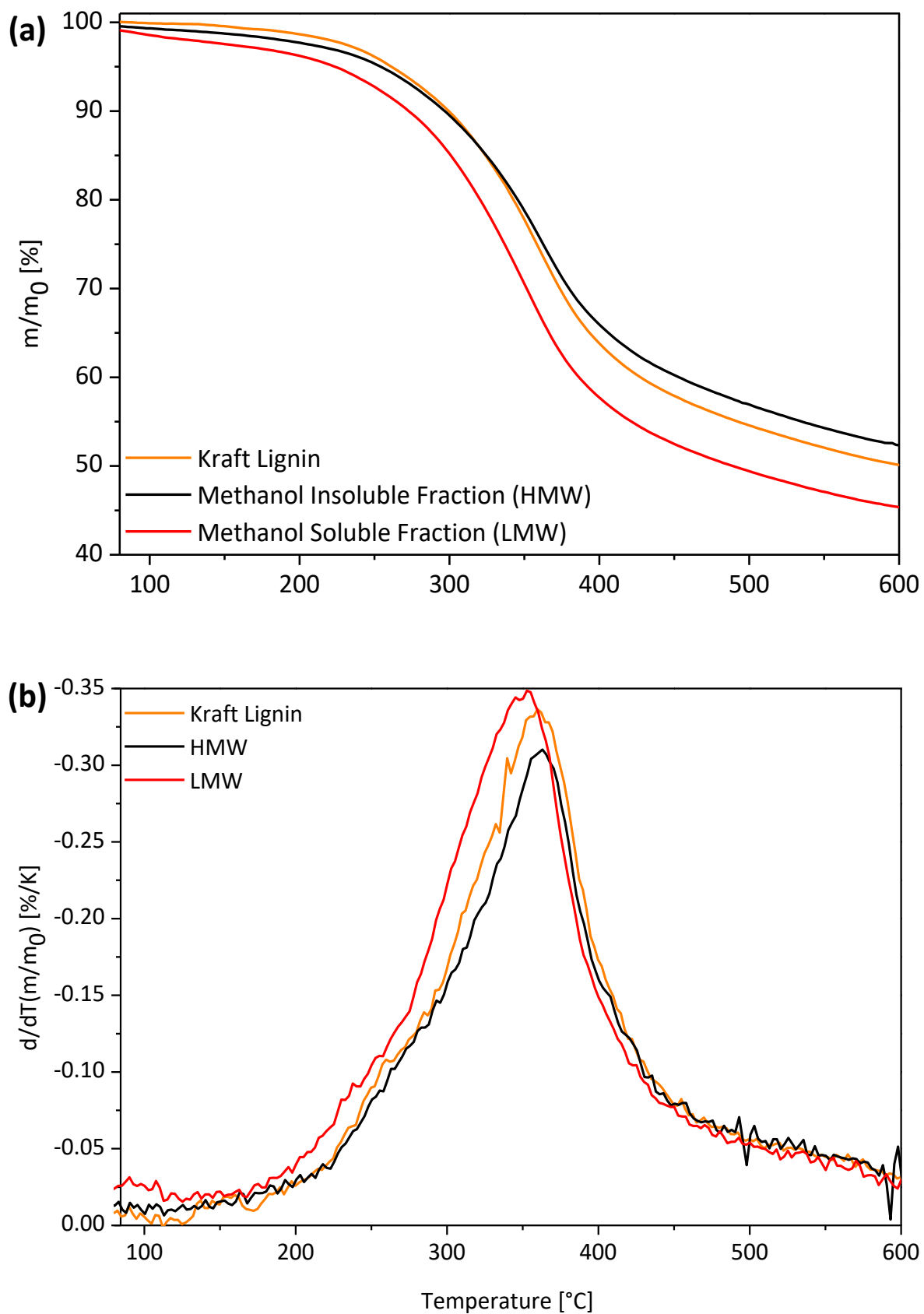


Figure 18: Thermogravimetical analysis plots of KL and the MeOH insoluble (HMW) and soluble (LMW) fractions (a) and their respective derivatives (b).

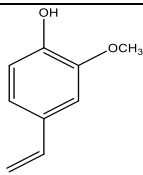
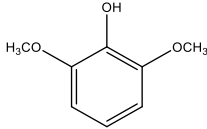
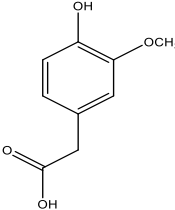
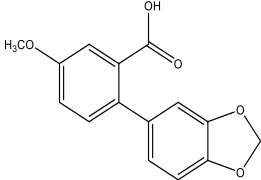
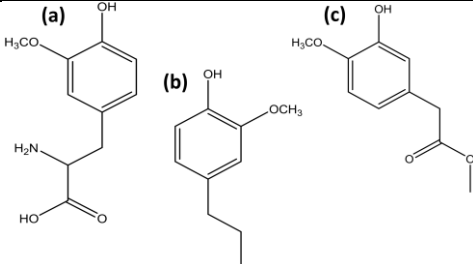
3.2.4 Gas Chromatography (GC)

The separation after extraction is performed *via* centrifugation and decantation, leaving a MeOH wet solid as HMW. This also means that some of the low molecular weight compounds will be found in the undissolved fraction. To estimate this effect 50 mg/mL of dried solids from each fraction (KL, HMW, LMW) were dissolved in acetone (no total solubility for KL and HMW) and analysed *via* GC-FID. The major compounds detectable *via* GC in the KL are described in Table 18. Vinyl guaiacol and homovanillic acid are calibrated, while the dimeric compounds are identified *via* the NIST database (v2.0f, 2009) and are not unambiguous. A complete GC-MS chromatogram of 30 wt.% KL in MeOH with all compounds identified *via* the help of the database is found in the appendix (Figure A 5 and Table A 2). From these data, it can be concluded, that the compounds of dimeric or trimeric aromatic nature contain many oxygen atoms, have numerous side chains, and have no ether bonds between aromatics. The Hansen solubility parameters of MeOH are given in Table 17 and MeOH has strong hydrogen bonding and pronounced dipole parameters. Aromatics have generally very low dipole and hydrogen bonding parameters, i.e. they are insoluble in MeOH. The group-contribution theory¹¹⁹ gives the possibility of calculating δ and δ_d (thereby, implicitly giving the value of $\delta_p + \delta_h$) *via* an empirical equation out of the functional groups (here: aromatic backbone plus side chains) of a component. This shows that aromatics are only soluble in solvents with high ($\delta_p + \delta_h$) values, if sufficient functional groups and side chains are present.

Table 17: Hansen solubility parameters of different compounds.¹⁰²

Compound	Δ [MPa] ^{1/2}	δ_d [MPa] ^{1/2}	δ_p [MPa] ^{1/2}	δ_h [MPa] ^{1/2}
MeOH	29.61	15.13	12.27	22.30
Toluene	18.32	18.16	1.40	2.00

Table 18: Major monomeric and dimeric compounds in the untreated KL.

$t_{\text{retention}}$ [min]	Compound	Structural Formula
25.396	Vinyl guaiacol	
26.384	Syringol (internal standard, 1 mg/mL)	
33.760	Homovanillic acid	
52.187	4-Methoxy-4', 5'-methylenemethoxybi- phenyl-2-carboxylic acid	
55.775	(a) 3-hydroxy-o-methyltyrosine (b) 4-Propylguaiacol (c) Methyl 4-hydroxy-3-methoxyphenylacetate	

When calculating the total dissolved amount by using syringol as internal standard, the ratio gives $\frac{A_{\text{total}} - A_{\text{syringol}}}{A_{\text{syringol}}} = 5.34$. Since the FID signal is proportional to the amount of carbon atoms, this value is only accurate when the sum formula of the measured compounds is a linear combination of the formula of syringol ($\text{C}_8\text{H}_{10}\text{O}_3$). This is certainly not the case, but it is a usable approximation. Since the concentration of the internal standard (syringol) was 1 mg/mL, it can be assumed that *ca.* 5 mg/mL of the lignin could be detected by GC. I.e., some 10 wt.% of the KL are monomers and dimers. Figure A 4(b)+(c) show the GC FID chromatogram of 50 mg/mL LMW and HMW dissolved in acetone, respectively. The LMW has a higher solubility and 25 wt.% are GC detectable. The colour of the HMW solution is only lightly yellow, while the other two were dark black. The peaks only show residual amounts of monomers and dimers, the sole large peak is the internal standard. Less than 1 wt.% were detected by GC.

3.2.5 ^{13}C Cross Polarisation Magic Angle Spinning (CP MAS) NMR

^{13}C CP MAS NMR analysis of the KL, LMW, and HMW is presented in Figure 19, with resonance/chemical shift assignment provided in Table 20. A coarse description of the resonances and chemical shift regions in ^{13}C NMR is provided in Table 19 and a more detailed resonance description in Table 20. ^{13}C analysis is a powerful tool also for quantitative means. Kringstad and Mörck published a detailed definition of the ^{13}C spectrum of KL from different cooking stages in comparison to milled wood lignin from spruce.¹²⁰ Mörck *et al.* provided also ^{13}C NMR spectra of acetylated lignin, differentiating between phenolic- and aliphatic-OH groups appearing as three distinct resonances for primary and secondary aliphatic acetyl groups and aromatic acetyls.¹²¹

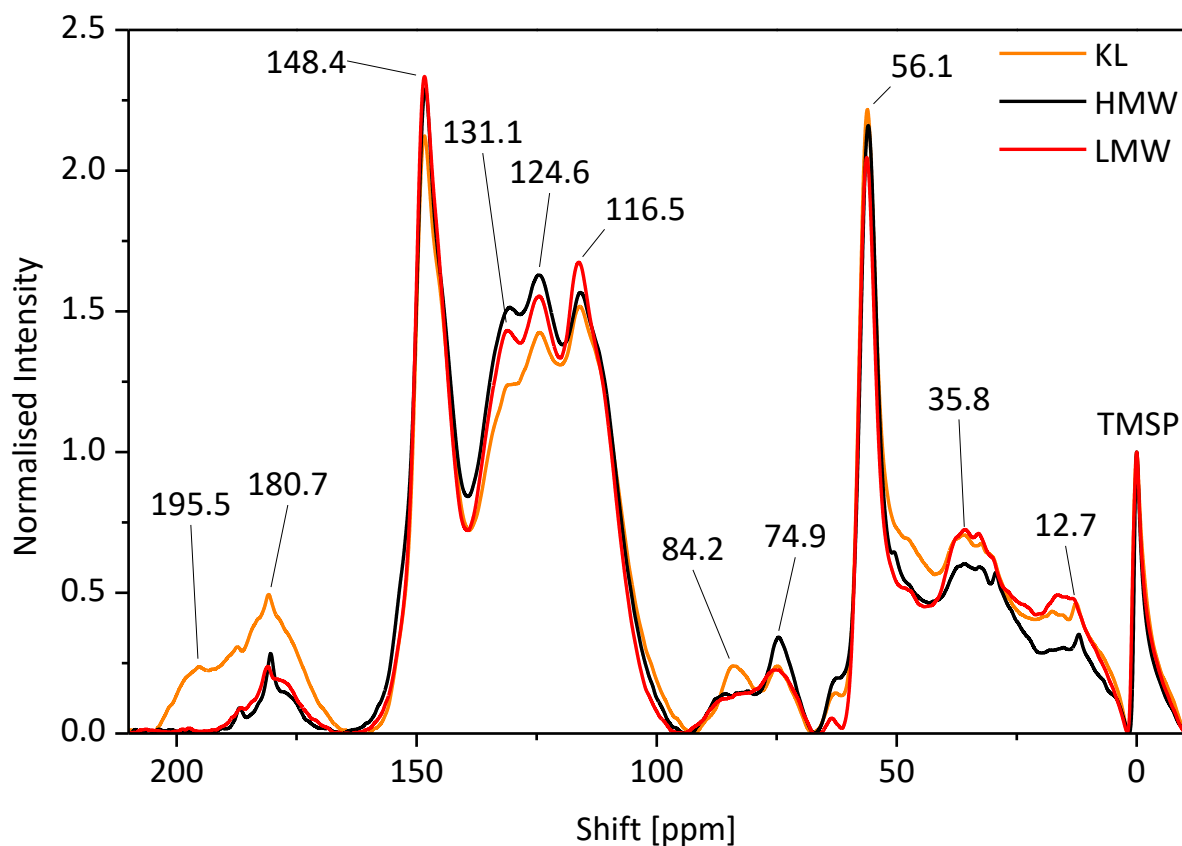


Figure 19: ^{13}C CP MAS NMR spectra of KL, MeOH soluble fraction (LMW) and MeOH insoluble fraction (HMW).

Table 19: Chemical shift assignments for the ^{13}C CP MAS NMR spectra of KL, MeOH soluble fraction (LMW) and MeOH insoluble fraction (HMW).

Range of chemical shift [ppm]	Description	Examples
210 – 150	Carboxylic acids, aldehydes, and ketones	C_1 in vanillin, C_β in homovanillic acid
150 – 100	Aromatic ring structures	$\text{C}_{(1-6)}$ in guaiacol
100 – 50	Ring structures and oxygenated side chains (e.g. sugars and methoxy groups)	$\text{C}_{(1-5)}$ in xylan, $-\text{OCH}_3$, $\text{C}_{(\alpha/\beta)}$ in aryl ethers
50 – 0	Aliphatic side chains	$-\text{CH}_2-$, $-\text{CH}_3$,

The lignin contains significant amounts of carboxylic acids and aldehydes, which could already be assumed from the GC analysis. The ^{13}C NMR shows that these end groups not only appear in the mono- and dimeric fraction, since there is no difference between the LMW and HMW fraction. It has to be noted that 9 wt.% of TMSP were added to the sample.

This compound has, beside the $-\text{Si}-(\text{CH}_3)_3$ groups, three more carbon atoms which add to the spectrum (Figure 20). Two will be found in the aliphatic side chains region ($-\text{CH}_2-$ at 30 ppm) and one in the carboxylic acid region ($-\text{COO}^- \text{Na}^+$ at *ca.* 170 ppm). The chemical shift region of $\delta_{13\text{C}} > 160$ ppm of the original KL is integrated *ca.* four times larger compared to LMW or HMW. The remaining spectrograms are comparable in shape and size, while it has to be hinted at some differences. The resonance at $\delta_{13\text{C}} = 131.1$ ppm representing the C_1 in guaiacyl is less pronounced in the KL while at 84.2 ppm a resonance with increased intensity is clearly visible in that fraction, which corresponds to the C_β in β -aryl ethers. In the range of $\delta_{13\text{C}} = 72.8 - 75.7$ ppm lie the C_{2-4} carbon atoms of xylan, meaning that some hemicellulosic sugars are still present. The $\delta_{13\text{C}} = 56.1$ ppm resonance represents the guaiacylic methoxy groups (syringylic units are not present) and the aliphatic aide chains can be found on lower chemical shifts. The resonance at *ca.* $\delta_{13\text{C}} = 35$ ppm is (probably) corresponding to the two $-\text{CH}_2-$ groups of the TMSP.

Table 20: Chemical shift assignments for the ^{13}C NMR analysis of lignin.

Chemical shift [ppm]	Assignment (with the data from Kringstad and Mörck, 1983) ¹²⁰
190+	G-CHO, G-CH=CH-CHO,
175 – 185	-COOH
148.4	C_3 in guaiacyl
131.1	C_1 in guaiacyl
124.6	C_5 in guaiacyl, substituted (C_5' p, o'-stilbenes)
116.5	$\text{C}_5\text{G-CH=CH-}$, G-CH, G- CH_2-
84.2	C_β in β -aryl ethers
72.8 - 75.7	C_{2-4} xylan
56.1	$-\text{OCH}_3$
35.8	mainly $-\text{CH}_2-$ in guaiacyl side chains
12.7	$-\text{CH}_3$
0	TMSP

12 mg of TMSP were added to 120 mg of lignin. M_{TMSP} is 127.27 mg/mmol and the resonance at $\delta_{13\text{C}} = 0$ ppm is corresponding to the $-\text{Si}-(\text{CH}_3)_3$ groups. I.e. the signal corresponds to $n_{\text{is}} = 3 \frac{12 \text{ mg mmol}}{127,27 \text{ mg}} = 0.282$ mmol of carbon atoms, where the subscript *is* refers to *internal standard*. Resonances at $\delta_{13\text{C}} = 148.4$ and 56.1 ppm represent the carbon atoms in the guaiacyl ring where the methoxy group is bound to and the carbon atom of the methoxy group, respectively. Taking these values as a measure for the total number of guaiacyl subunits, it gives *ca.* 0.64 mmol in 120 mg of sample. With a molar mass of 124.14 mg/mmol this represents 77 mg or *ca.* 65 wt.% of the KL. This value is comparable in all three fractions, but the resolution of resonances in the ^{13}C CP MAS is not good enough to differentiate in more detail. When 65% is the mass of guaiacyl units in the KL, the remaining 35%

make up for the remainder, i.e. side chains. With a mass of 124 g/mol per guaiacol this leads to a mass of 190 g/mol of one guaiacylic ring with attached side chains.

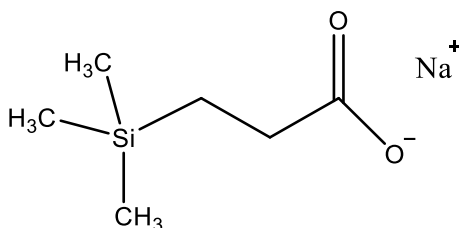


Figure 20: Chemical structure of TMSP. Internal standard used at ^{13}C CP MAS NMR.

3.2.6 ^1H and 2D Heteronuclear Single Quantum Correlation (HSQC) NMR

^1H NMR spectra is provided in Figure 21 with corresponding chemical shift assignment in Table 21. The differences in the identified regions are defined in Table 21 and provided in Figure 22. The values are normalised on the DMSO- d_6 region. The three fractions do not show large differences when considering the total integrated areas, while the specific peaks are more pronounced in the LMW fraction. ^1H NMR spectra were recorded concurrently with the HSQC data acquisition. This analysis also presents stronger signals for the LMW fraction, attributed to a higher solubility of this fraction in the DMSO. Since the areas from the ^1H are all comparable and no visible residue was found after solubilisation, it is more probable that the LMW fraction has less condensed compounds. This would lead to a higher number of C-H bonds compared to C-C bonds in condensed aromatic rings. Since only C-H correlations are visible in HSQC, this would explain a higher total number of signals in the LMW fraction. Figure A 6 shows the ^1H areas in more detail and Figure A 8, Figure A 9, and Figure A 10 show the 2D HSQC.

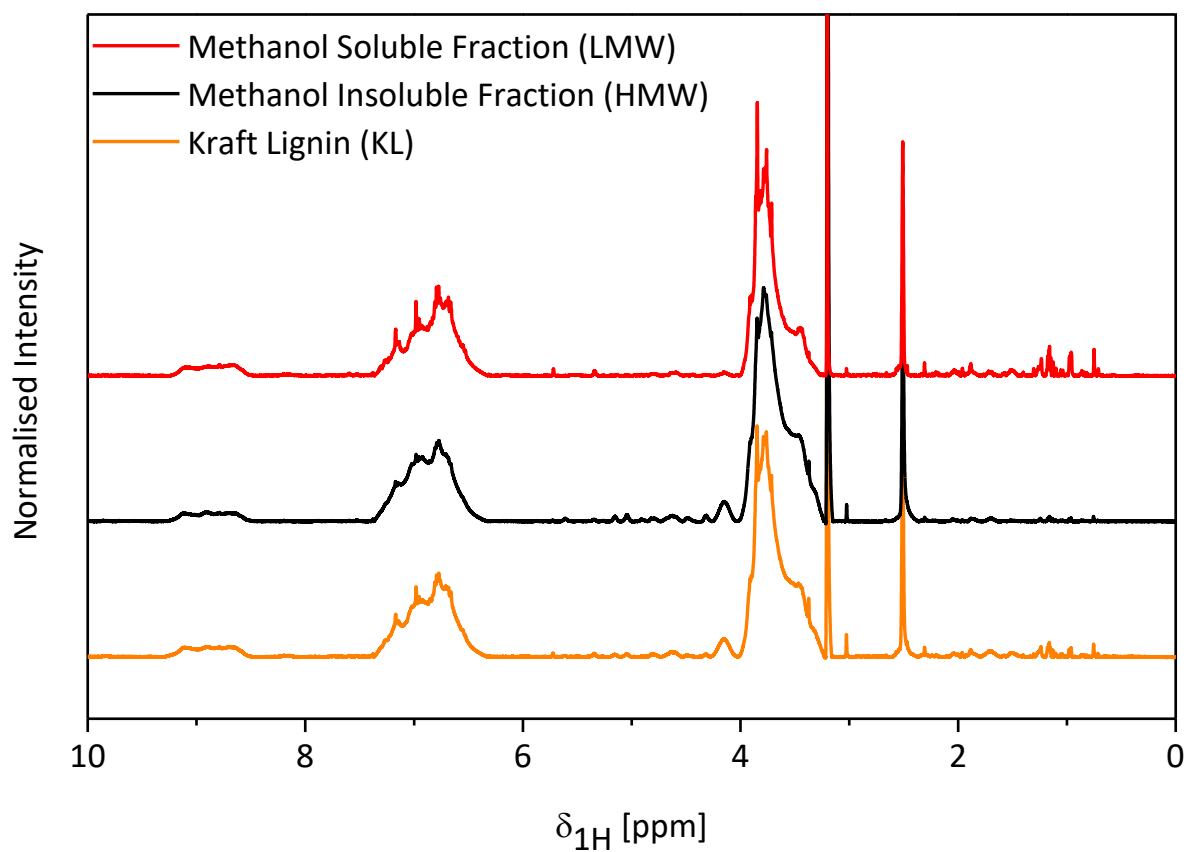
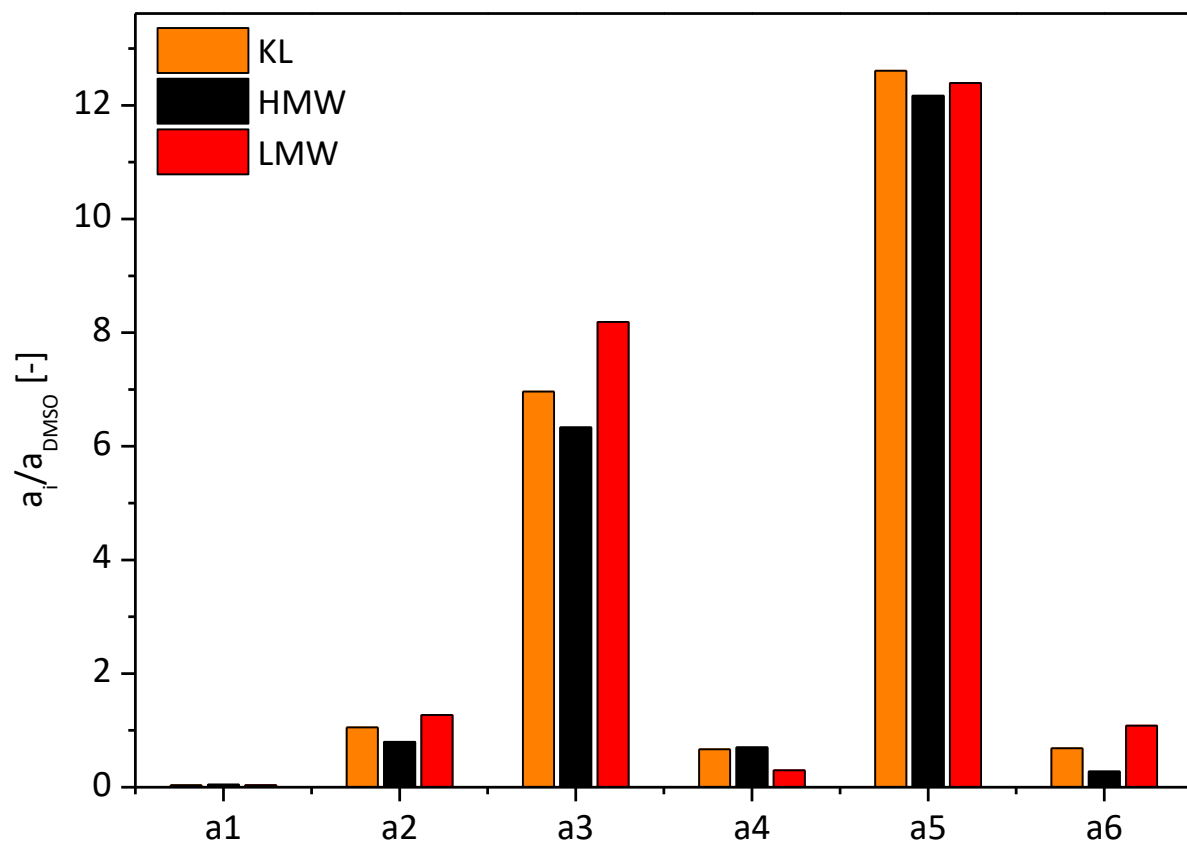
Figure 21: Liquid ^1H NMR spectra of KL, MeOH soluble and MeOH insoluble fraction in $\text{DMSO-}d_6$ Figure 22: Integrated ^1H NMR spectra of KL, MeOH soluble and MeOH insoluble fraction in $\text{DMSO-}d_6$ (as normalised to the standard).

Table 21: Chemical shift assignments for the ^1H NMR spectroscopic analysis of lignin.

Chemical shift regions ^{122,123} [ppm]	Assignment	Chemical Shift		Assignment
		#	$\delta^1\text{H}$ [ppm]	
a1 (10.10 to 9.35)	Formyl			Benzaldehyde units ¹²⁴
a2 (9.35 to 8.00)	Nitrogen substituted phenols			C-H in phenols with adjacent ester substitute
a3 (8.00 to 6.00)	Aromatic and vinyl	1	7.16	C ₂ -H ₂ in G-units ¹²⁵
		2	6.98	C ₆ -H ₆ in G-units ¹²⁵
		3	6.8 to 6.6	C ₅ -H ₅ in G-units ¹²⁵
		4		
a4 (6.00 to 4.05)	Aliphatic oxygenated and aromatic side chains		4.75 to 4.85	C _{α} -H _{α} β -O-4
			4.60 to 4.75	C _{β} -H _{β} in β -O-4
			4.62	C _{α} -H _{α} in resinol units (β - β) ¹²⁴
			4.60	C _{α} -H _{α} in (β -5, α -O-4)
		5	4.15	C ₁ -H ₁ in xylan C _{γ} -H _{γ} in resinol units (β - β) ¹²⁴
			4.05	-OH of CH ₃ OH in DMSO ¹²⁶
a5 (4.05 to 3.20)	Methoxyl	6	3.85	CH ₃ in Ar-OCH ₃
		7	3.76	
		8	3.72	
		9	3.47	C _{β} -H _{β} in phenylcoumaran
		10	3.37	
a6 (3.20 to 0)	Aliphatics		3.20	-CH ₃ in CH ₃ OH in DMSO ¹²⁶
		11	3.03	C ₂ -H ₂ in xylan, C _{β} -H _{β} in β - β resinol
			2.52	D ₃ C-(O=S)-CD ₂ H in DMSO- <i>d</i> ₆
			2.40 to 2.50	-CH ₂ - in ethylcatechol; CH ₃ in aceto-vanillone
		12	2.31	
			2.21	-CH ₃ in 4-methylcatechol
			1.11	-CH ₃ in ethylcatechol

Area a1 ranging from $\delta_{1\text{H}} = 10.10$ to 9.35 ppm

The first area corresponds to signals related to ^1H atoms in formyl groups. These have the highest shift, since they are the least shielded protons, the electrons being drawn towards the oxygen. The resonances observed in this area are only visible at very large magnification (Figure A 6(a)), but it can be seen that the compounds present in the KL end up in the LMW fraction with only a weak resonance at $\delta_{1\text{H}} = 9.86$ ppm in the HMW fraction and a small buckle down towards 9.79 ppm. These resonances are assigned to signals related to benzaldehydes (e.g. vanillin). These seem to be of lower molecular weight and are dissolved in the MeOH.

Area a2 ranging from $\delta_{1\text{H}} = 9.35$ to 8.00 ppm

The total area is larger in LMW fraction while this area shows no significant differences between the LMW and HMW fraction in the details of the spectral features (Figure A 6(b)). Resonances at $\delta_{1\text{H}} = 9.11$ and 8.89 ppm are slightly more pronounced in the HMW fraction and the LMW fraction has a very small additional resonance at $\delta_{1\text{H}} = 8.17$ ppm. These spectral features are not observed in 2D HSQC NMR.

Area a3 ranging from $\delta_{1H} = 8.00$ to 6.00 ppm

This region is associated with resonances related to aromatic and vinyl groups. The LMW fraction spectrum presents a more clearly resolved resonance with a corresponding larger area (Figure 22 and Figure A 6(c)). Resonances in the chemical shift region originate from protons directly attached to the aromatic ring or other π -bonds and are thus also visible in 2D HSQC. The larger area in the LMW fraction is probably due to the less condensed state of this fraction resulting in more Ar-H bonds. Condensed structures with fused rings will only contribute with their outer rings where protons are attached, leading to a smaller total area. Resonances at *ca.* $\delta_{1H} = 6.98$ ppm, 6.77 ppm, and 6.66 ppm belong to the $C_{2,5,6}$ -H $_{2,5,6}$ guaiacyl units. A clear assignment is difficult, since the literature is ambivalent and shifts depend on solvent and structure in the vicinity of the proton. Feng *et al.* assign the G_2 (C_2 -H $_2$ in guaiacyl) to a shift of $\delta_{1H} = 6.98$ ppm and puts the $G_{5,6}$ at 6.80 ppm.¹²⁷ Mainka *et al.* put the G_2 unit at $\delta_{1H} = 7.12$ ppm, G_6 at 6.93 ppm and G_5 at 6.6 to 6.8 ppm.¹²⁵ It makes sense that G_2 experiences the strongest de-shielding, since it is neighbouring the *p*-position of the guaiacylic structure and the methoxy group. G_6 is next to the *p*-position and, the either free or occupied, G_5 . G_5 is the position the most prone to condensation, i.e. the G_6 resonance at $\delta_{1H} = 6.93$ ppm can be watched for shifts as an indicator for further condensation.

The HSQC shows distinct areas for G_2 , G_5 , and G_6 (Figure 23, Figure A 8(d), Figure A 9(d), and Figure A 10(d)) and that the three areas are overlapping for the 1H shift. Table A 3 gives data on signal assignment from various literature sources. Since the three guaiacyl carbons give signals over a broad range, it can be assumed that a large heterogeneity of compounds is present. Quantification *via* HSQC is difficult and requires high signal to noise ratios and the correct settings for the NMR,¹²⁸ but a rough estimation can be performed. The G_5 position has the largest area followed by G_2 and G_6 . This is also true for the HMW and LMW fraction, meaning that condensation and/or attachment of side chains as e.g. $-CH_3$ and $-CH_2-CH_3$ mainly occurs at the 2 and 6 positions. Employing equation (2-10) and using the molecular weight of one C_9 -unit given in Table 23 an approximation for the free G_2 , G_5 , and G_6 positions can be performed. The absolute numbers in Table 22 have to be treated with care and their values are unexpectedly low. The areas of the three guaiacyl positions are not totally distinguishable and the precision of the calibration *via* the solvent is unknown. Nevertheless, they show a rather condensed state of the lignin and that, after extraction, most of the condensed rings situate in the HMW fraction. Additionally, alkylation leads to decreased signals in these areas which is most pronounced for the LMW fraction (compare Table 24). Since the LMW fraction shows the highest values, alkylation seems to play a minor role compared to condensation.

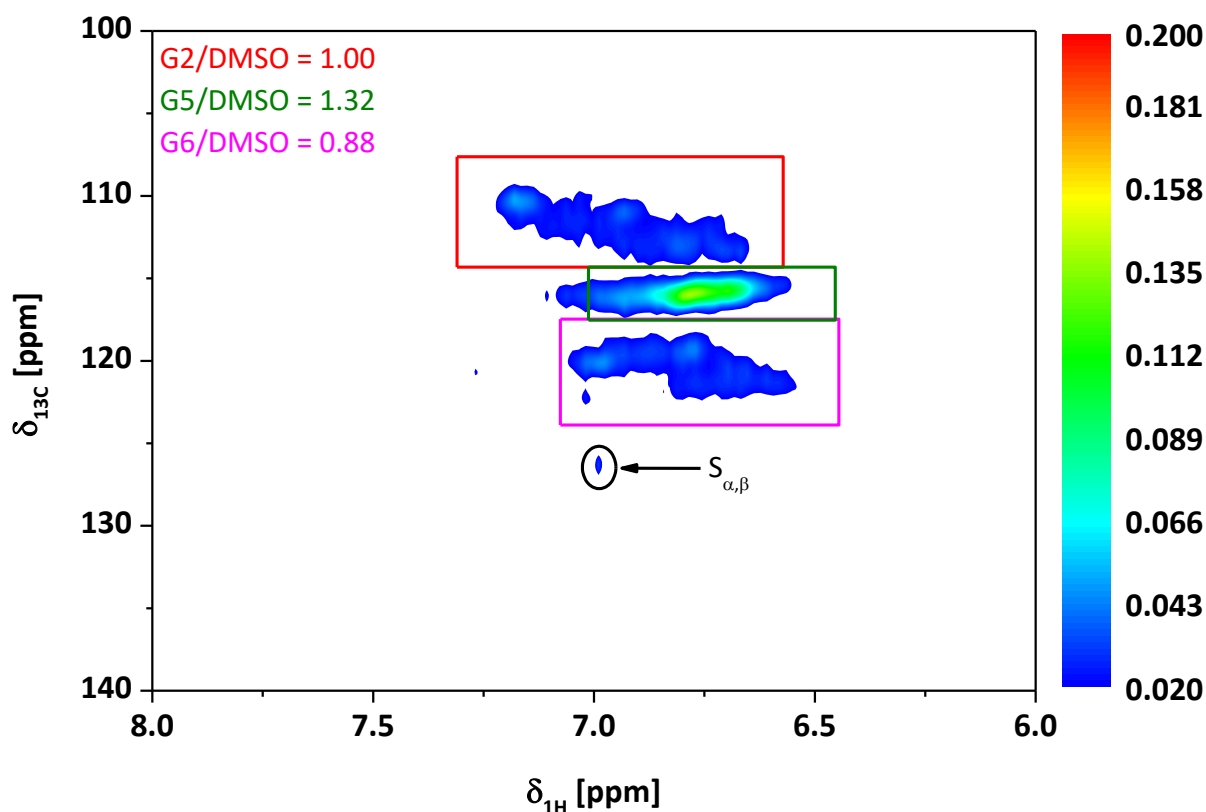


Figure 23: 2D HSQC NMR spectra of the aromatics region of HMW. The areas of G2, G5, and G6 are colour-coded and given as relative areas to the DMSO-*d*₆ solvent.

Table 22: Free G2, G5, and G6 positions per aromatic ring in KL, HMW, and LMW fractions.

Fraction	G ₂	G ₅	G ₆
	<i>per 100 C₉-unit</i>		
KL	8.82	11.51	7.74
HMW	6.77	8.94	5.96
LMW	20.11	21.69	16.69

With the G₅ position as the least occupied in the guaiacyl rings, condensation reactions *via* formaldehyde (FA) as described by Chakar and Ragauskas seem to be minor pathways.¹²⁹ This pathway would also produce Ar-CH₂-Ar units and the CH₂-group should be clearly visible at $\delta_{1H} = 3.4$ to 3.5 ppm and $\delta_{13C} = 35$ to 40 ppm.¹³⁰ These areas are empty in the HSQC of all three fractions and also do not show any signals in the solids' fractions after base catalysed processing at 300 °C. Only the oil fractions do show signals for *ortho-para* and *para-para* linkages, this will be discussed in detail in chapter 4.2.2.

Area a4 ranging from $\delta_{1H} = 6.00$ to 4.05 ppm

This region corresponds to oxygenated aliphatics such -CH and -OH groups as found in sugars or alcohols. The area for the HMW fraction is clearly larger while also more distinct resonances for this fraction are visible (Figure A 6d). The most striking difference is the resonance at $\delta_{1H} = 4.15$ ppm - this corresponds to the C₁-H₁ proton in xylan, showing that some of the hemicellulose is still present and is not dissolvable in MeOH. Also, the majority of other resonances are more prominent in the HMW fraction in this area - $\delta_{1H} = 5.35$, 5.15 , and 5.04 ppm. The

HSQC does not show any significant features in this area, i.e. majority of resonances are associated with C-OH bonds.

Area a5 ranging from $\delta_{1H} = 4.05$ to 3.20 ppm

The majority of the resonances in this region are associated with $-\text{OCH}_3$ groups in guaiacyls. Strong spectral features from $\delta_{1H} = 3.71$ to 3.85 are related to guaiacyl peaks and are more defined in the LMW fraction while flattened out in the HMW fraction. This indicates a larger variety in the HMW fraction with peaks being smeared over the region. The HSQC clearly presents resonances associated with methoxy groups - $\delta_{13C} = 55$ to 57 ppm and $\delta_{1H} = 3.5$ to 4.0 ppm. The second largest chemical shift area is centred at $\delta_{13C} = 60.5$ ppm and between $\delta_{1H} = 3.75$ to 3.25 ppm corresponding to the C-H₁ and C-H₂ of the γ -position in β -O-4 linkages (Figure A 8(b), Figure A 9(b), Figure A 10 (b) and Table A 3). With the DMSO as an internal standard and *via* the equations (2-9), (2-10) and (A 4) to (A 6) the amount of methoxy groups and β -O-4 linkages can be estimated. In combination with the values for the elemental analysis from Table 14, a C₉-formula can be established (Table 23).

Table 23: C₉-formula and β -O-4 content of the MeOH extracted lignin

Fraction	C ₉ -formula	MeO [wt.%]	M _{C9} [g/mol]	β -O-4 per 100 C ₉
KL	C ₉ H _{9.45} O _{3.14} S _{0.09} (OCH ₃) _{0.25}	4.32	178.50	2.69
HMW	C ₉ H _{9.60} O _{3.24} S _{0.11} (OCH ₃) _{0.21}	3.70	179.65	2.44
LMW	C ₉ H _{9.03} O _{2.71} S _{0.08} (OCH ₃) _{0.37}	6.53	174.33	4.04

Using a C₉-formula is common for lignin and performed in various sources for different kinds of lignin.^{115,131} While it is useful for native lignin comprising of phenylpropanoid units, the condensed structure of technical lignin renders it questionable, since the backbone units of these lignin will most probably have less than nine C-atoms (Figure 5).

The value between two and four for the β -O-4 linkages lies within the range for KLS in the literature (Table 10), while the amount of methoxy groups is *ca.* half the value reported.^{115,132} Table 23 shows that the amount of methoxy groups and β -O-4 linkages in the LMW fraction is significantly higher than in the other two fractions. For the methoxy groups it can be explained by assuming that here no condensed structures are present, meaning that nearly all aromatic rings have a $-\text{OCH}_3$ moiety. The larger percentage for the β -O-4 linkages is less easy to explain. This fraction will have fewer linkages per aromatic unit; since it consists mainly of dimers (please refer to GC analysis in section 3.2.4). And this would mean that for 100 aromatic rings, 50 linkages are present. When one oligomer with 100 units is present there would be 99 linkages. This means that four β -O-4 linkages per 100 aromatic units in dimers would mean that 8% of the linkages are β -O-4. This is very improbable from the results of the GC-MS analysis (Table A 2) and also from the fact that most of the ether linkages are assumed to be cleaved during Kraft pulping.^{12,13,15,59} It is assumed that the area used for the determination of the β -O-4 linkages *via* HSQC contains the two B_γ protons (Figure A 7c) and no other C-H correlations. The literature gives a broad range for the ¹H shift ranging from 3.30 to 3.57 ppm for the first proton and from 3.63 to 4.12 ppm for the second (compare Table A 3). This large range hints at structural differences, meaning that the γ -position of the structure

given in Figure A 7c is not the only feature found in this area. The amount of β -O-4 linkages is thus not a representation of only these linkages and probably contains other moieties.

Area a6 ranging from $\delta_{1H} = 3.20$ to 0 ppm

This chemical shift region is associated with unsubstituted aliphatics, present in the structure mainly as side chains attached to aromatics. Figure 21 and Figure 22 show that the majority of these compounds are in the LMW fraction. Mattsson *et al.* gave a definition for defining these side chains *via* their ^1H and ^{13}C shift.¹³³ Most of the peaks appear between a shift of $\delta_{1H} = 0.75$ to 1.30 ppm in the ^1H NMR (Figure A 6(f) – e.g. the HSQC presents the majority of its resonances in the $\text{CH}_x \beta$ position), corresponding to the ^1H shift between $\delta_{1H} = 1.00$ and 1.90 ppm (Figure A 8(b), Figure A 9(b), Figure A 10(b)). Table 24 summarises the amounts of CH_2 and CH_3 groups in α -position per 100 C_9 units and gives a trend for the groups in β and $\gamma+$ positions.

Table 24: Aliphatic side chains per 100 C_9 units of the original KL and the MeOH insoluble (HMW) and soluble (LMW) fraction

Fraction	$\text{CH}_2 \alpha$	$\text{CH}_3 \alpha$	$\text{CH}_x \beta$	$\text{CH}_x \gamma+$
	<i>per 100 C_9 units</i>		<i>a_i/a_{DMSO}</i>	
KL	1.90	0.35	0.27	0.10
HMW	0.53	0.07	0.04	0
LMW	7.46	1.05	1.21	0.38

As predicted *via* the group contribution theory for the Hansen solubility parameters, there is a strong increase in the LMW fraction and a decrease in the HMW fraction. Most compounds are $\text{CH}_x \beta$ moieties, which can simply be linked *via* a $\text{CH}_2 \alpha$ forming an ethyl group or appear at the end of different chains as for guaiacylacetone (Table A 2 #6).

3.2.7 Attenuated Total Reflection Fourier Transform Infrared (ATR FT-IR)

The ATR FT-IR can provide fast and easy insight into the chemical structure of the lignin fractions without having to dissolve the solids and with much shorter measuring times. Problematic is the less good resolution, i.e. a clear interpretation is difficult since most spectral bands overlap each other. The complete spectrum is given in Figure A 11 and an overview of the fingerprint region in Figure 24. A detailed assignment for the wavenumbers of the spectra can be found in Table A 4. It has to be pointed out that most spectral bands are overlapping generating no clear signals of one specific functional group or bond.¹³⁴ The most pronounced bands are 6, 7, 10, 11, 12, and 14, which all belong to ring modes of guaiacyl units (G-units). Bands 3, 4, and 5 belong to C=O stretches and –COOH groups. Band 8 is a combination of the CH deformation in OCH_3 groups and CH in-plane modes of aromatics. Band 9 represents aliphatic C-H stretches in CH_3 (excluding $-\text{OCH}_3$) additional to phenolic-OH stretches. 13 is assigned to secondary alcohols and esters in aliphatics. Band 15 is the out-of-plane deformation of ethylenes and 16 is a general aromatic CH out-of-plane mode. Band 17 and 18 are CH out-of-plane modes special for G-units at C_2 , C_5 , and C_6 .

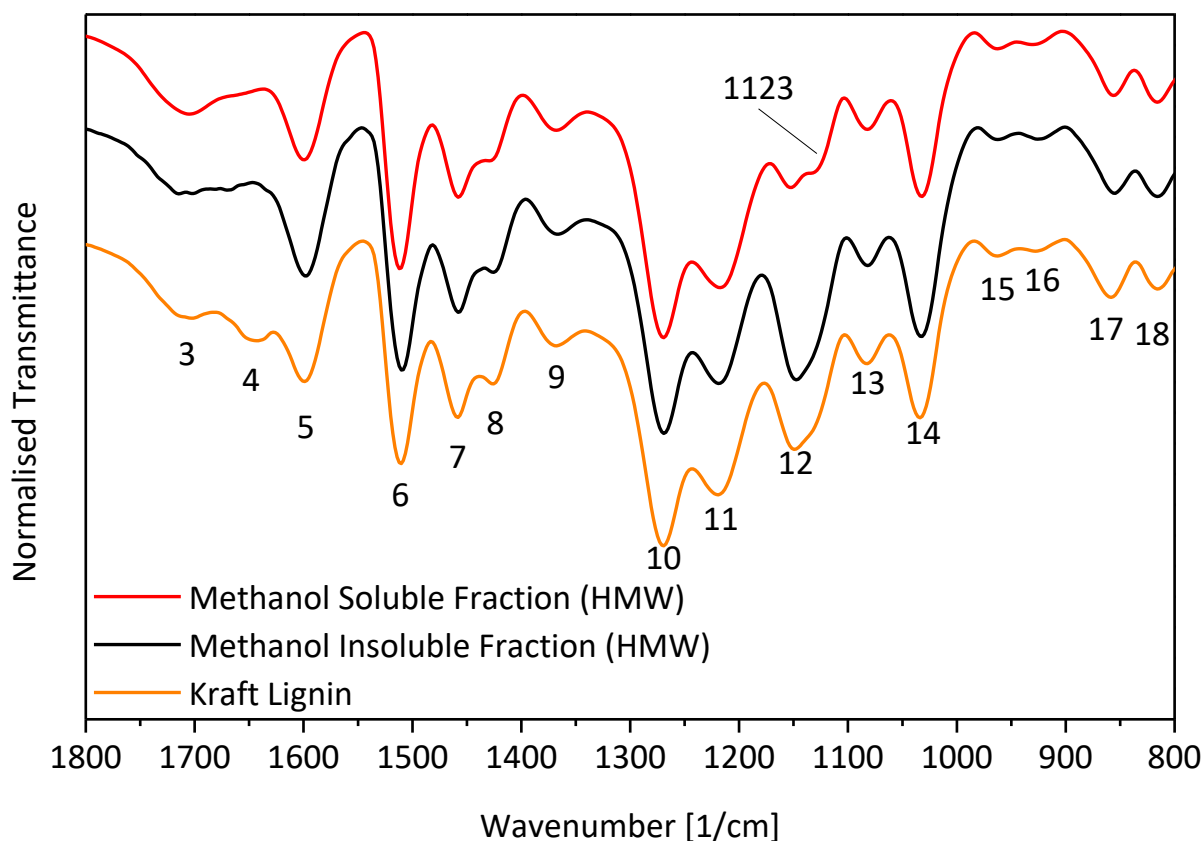


Figure 24: Fingerprint region of the ATR FT-IR spectra of KL, MeOH insoluble fraction (HMW), and MeOH soluble fraction (LMW).

In the HMW fraction bands 3 and 4 are less defined corresponding to the C=O stretch. Here, the KL has three defined FTIR spectral bands, confirming the larger area of the ^{13}C CP MAS at $\delta_{13\text{C}} > 190$ ppm. Band 12 is less pronounced in the LMW fraction, which leads to a clear appearance of a peak at 1123 cm^{-1} , which can be seen as a small shoulder in the KL and HMW spectra. Band 12 corresponds to the C-H stretch in guaiacyl rings but cannot be taken as a sole indicator for a lesser number of G-units. The band at 1123 cm^{-1} is also an aromatic ring absorbance. Bands at 5, 6, 7, 10, 11, 12, 14, 17, and 18 are all directly related to G-units, i.e. that they would have to be influenced if the amount of total guaiacylic rings was different. Band 8 is also less pronounced in the LMW fraction which corresponds to OCH_3 groups in aromatics.

3.2.8 Summary & Conclusions

Summarising the findings on the MeOH extraction it can be seen, that the low molecular weight compounds have successfully been extracted from the lignin. Ca. 20 wt.% of the lignin are removed and form a fraction (LMW) with a significantly lower molecular weight, less thermal stability, and more aliphatic side chains. The high molecular weight fraction (HMW) has, opposing to the LMW fraction, a higher molecular weight and reduced amounts of aliphatic side chains. The structure itself is more condensed, thereby giving in total fewer signals in the 2D HSQC. EA shows a higher carbon and lower sulphur amount for the LMW fraction. In combination with the findings of the NMR analyses, this leads to a significant higher amount of methoxy groups and $\beta\text{-O-4}$ linkages in the LMW fraction. I.e., these occur more frequently in the lower molecular weight units and increase solubility of units with equivalent weight. Thermal stability for the HMW fraction is higher when heating to $600\text{ }^\circ\text{C}$ but the

temperature for 10% mass loss is slightly lower. This is probably caused by residual hemicellulose (xylans) which accumulated in the HMW fraction and has a decomposition temperature between 200 and 300 °C. Furthermore, the compounds mainly evaporating at 700 °C are transferred into the HMW fraction. KL and LMW have a T_g at 147 and 121 °C, respectively (mid-point). The HMW fraction does not show a clear glass transition, but a small endothermic event at 159 °C. Thus, the LMW fraction could serve as plasticiser for the HMW fraction. GC shows, that monomers in the KL mainly consist of vinyl guaiacol, acetovanillone, and propyl guaiacol and dimers are connected *via* C-C bonds. In total 10 wt.% of the original KL are GC detectable, i.e. monomers and dimers. The results from the GPC underpin these findings for the KL, while also giving some seven percent monomers and dimers for the HMW fraction. The GC did not detect any significant amounts of compounds in this fraction, as this is the MeOH indissoluble part. This leads to the conclusion, that some larger compounds have a more extended retention time in the GPC's column than the pullulan standards with comparable molecular weight. In the case of monomers and dimers, the calibration was performed with single mono- and disachharides. Some highly polar compounds with larger molecular masses are detected as monomers, while other small unpolar molecules will be interpreted as larger ones.

Chemical structure does not appear very different between the two extracted fractions as indicated by ^{13}C CP MAS NMR, 2D HSQC, and ATR FT-IR. ^{13}C NMR gives a molecular weight of one guaiacyl unit with attached side chains of *ca.* 190 g/mol, while the combination of EA and 2D HSQC results indicate the mass of one C_9 -Unit to be approximately 180 g/mol. The amount of C-H correlations in guaiacyl units is significantly larger in the LMW fraction, hinting at a less condensed structure. As expected, the LMW fraction exhibits a larger amount of side chains as detected by ^1H NMR and 2D HSQC. ATR FT-IR does not indicate significant differences between the fractions.

4 Base Catalysed, Hydrothermal Treatment of Lignin

4.1 Theory and Prior Art

Among the array of thermochemical methods investigated thus far for the conversion of lignin and associated residues, base catalysed depolymerisation (hereon referred to as BCD) has been envisioned as a possible approach for the production of small aromatic (e.g. phenolic monomer) compounds.^{77,135–144} A base catalysed process is defined as a process where a Brønsted or Lewis base is present in a liquid solvent. The nucleophile, be it an HO^- or any other electron donator, attacks the reactant and alters its electronic structure by withdrawing, in most cases, a proton. The BCD process relies on the use of an alkali and mainly Brønsted basicity. Deprotonation of phenolic-OH groups and other aromatic components of the lignin structure are proposed to alter the electronic structure of these structural moieties and in turn improve its solubility in H_2O . It has been reported previously that a minimum of 31 phenolic-OH groups per 100 phenyl propane units is necessary for solubilisation of lignin in aqueous alkali media.¹⁴⁵ The concurrent reaction pathway is influenced by solvent choice, catalyst type, and temperature. The latter parameter is particularly interesting (coupled with pH) as it not only enhances reaction rate but can also alter the characteristics of the reaction solvent (e.g. ionic product and dipole moment of H_2O).¹⁴⁶ This approach has been described for numerous biomass-derived model compounds,^{60,61,63,66,147,148} and is also the underlying mechanism of the Kraft pulping process (e.g. where wood chips are cooked in $\text{NaOH}/\text{Na}_2\text{S}$ mixtures at $T = 170\text{ }^\circ\text{C} / t = 2\text{ h}$).¹³ Regarding an introduction to prior art and background on the development of this approach to lignin conversion, BCD has been investigated by a number of groups over the last 20 years, and is receiving revived interest in recent years. Thring have previously investigated the conversion of Alcell lignin with NaOH (aq), with liquid phase products obtained in yields of $\leq 30\%$.¹⁴⁹ BCD has also been envisioned as pre-treatment step to produce a product mixture more suitable for further processing (e.g. catalytic hydrodeoxygenation for gasoline-range aromatic fuel production).^{150–155,155,156}

Most BCD processes focus on the yield of low molecular weight compounds (i.e. monomers and dimers). These can, in theory, be brought to market as substitutes for phenols and derivatives (e.g. phenyl formaldehyde).⁸⁸ The production capacities of phenol were at *ca.* 10 Mt/a in 2016¹⁵⁷ allowing for the addition of some 100 kt/a of substitute without having a strong impact on prices. Phenol prices are in the range of 800 – 1,200 \$/t, meaning there is no significant margin allowing for a sophisticated purification process. As already stated in the first chapter an easy to implement process for a Kraft mill would be a base catalysed process. Since this process generates oligomers as a major fraction, it is necessary to describe this fraction and evaluate its suitability as resource for downstream processing. The focus of this chapter lies on the assessment of existing base catalysed processes and, from these, derivation of suitable conditions for the optimisation of the oligomeric fraction. Under basic conditions, guaiacylic units (i.e. aromatics with a free ortho position) undergo condensation reactions with addition of FA (Figure 25).¹²⁹

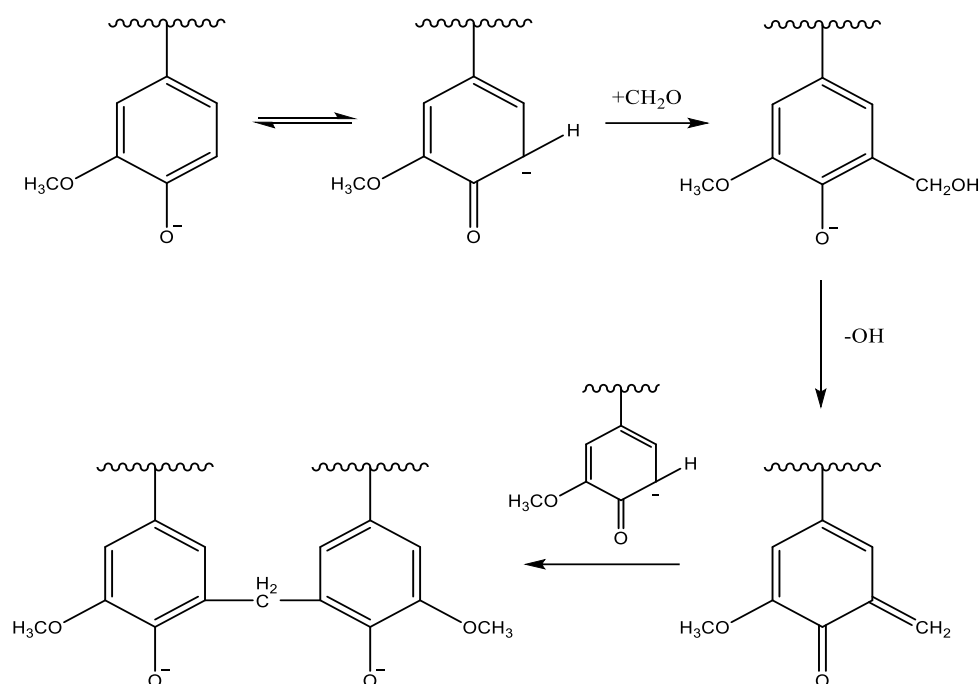


Figure 25: Condensation reaction mechanism of guaiacylic lignin units with formaldehyde (FA) as proposed by Chakar and Ragauskas.¹²⁹

4.1.1 A General Mechanistic Description of BCD

Regarding a mechanistic description of BCD, Gierer describes it as a process similar to transformation of lignin moieties during Kraft pulping.⁵⁹ Gierer *et al.* have reported on the depolymerisation of β -O-4 and α -O-4 model compounds based on treatment in 2 M NaOH (aq) and a mixture of NaOH (0.875 M (aq)) and Na₂S (0.129 M (aq)) to simulate the white liquor conditions found typically in the Kraft process.^{60,61,63} Reactions were conducted at 170 °C for 2 h and resulted in moderate to complete cleavage of the β -O-4 compounds with both alkalis. It was reported that the cleavage of the α -O-4 linkage is only achieved upon addition of Na₂S.⁶⁰ The reaction pathway to cleavage of the β -O-4 linkage in the presence of either HO⁻ or HS⁻, proceeds initially *via* nucleophilic attack and subtraction of a proton from the phenolic-OH end group, thereby altering the electronic structure (Figure 4). As a consequence, it is proposed that an ether bond is then broken at the C _{α} position, resulting in the formation of a quinone methide intermediate. In NaOH (aq), the C _{β} is subsequently deprotonated to an enol ether which is, to a large extent, stable under alkali conditions. The addition of Na₂S (and in turn sulphide anions) to the reaction results in the addition of sulphur at the C _{α} / quinone methide structure, which leads to displacement of the aroxyl substituent at the C _{β} position, leading to the formation of an epi-sulphide intermediate and a phenolic-OH group.⁵⁹ Typically, these initial mechanistic studies were performed under conditions relevant to the Kraft pulping process.^{59–61,63}

4.1.2 Reactions of Lignin under Basic, Hydrothermal Conditions

Clearly the strength of the employed base will play a critical role. In this context, Miller *et al.* reported on the use of different bases and showed that stronger bases (e.g. KOH, NaOH) are able to produce higher yields of low molecular weight species than weaker bases (e.g. LiOH).^{142,143,158} As already mentioned, phenolic compounds with free *ortho*-positions undergo condensation reactions in alkali media when FA is present.¹²⁹ Miller *et al.*

showed that the -OMe groups of lignin model compounds are transformed into -OH groups and MeOH under basic hydrothermal conditions (e.g. Figure 26 – model conversion of anisole to phenol and MeOH).¹⁴³

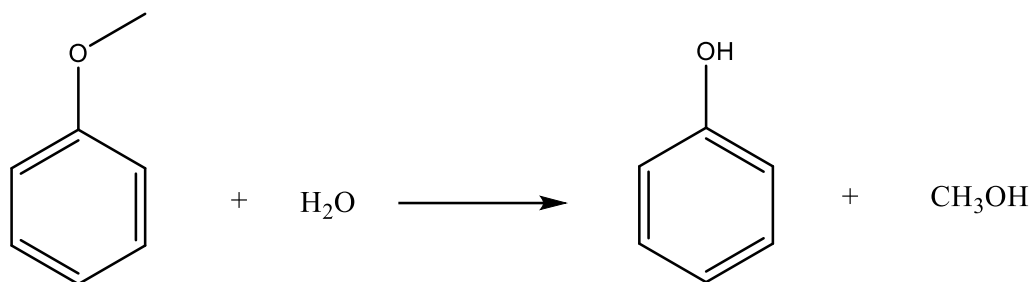


Figure 26: Reaction of anisole under hydrothermal basic conditions into phenol and MeOH

When employing syringol (i.e. where both *ortho*-positions are occupied) it has been reported that under BCD conditions, the products directly polymerise (10 wt.% KOH (aq), T = 290 °C, t = 30 min).¹⁴³ As will be discussed later, this was also observed during the course of this doctoral work for reactions of 1 wt.% syringol in 1 M NaOH (aq) at T = 250 °C (based on sampling at different time intervals under batch processing). If polymerisation of syringol also takes place *via* the *ortho*-position, the present -OMe group must therefore be activated under basic hydrothermal conditions. Furthermore, beside solvent and alkali choice, reaction temperature is an important parameter. It has been reported that between 230 and 260 °C, propanoid side chains undergo scission, whilst in the interval 275 to 330 °C, the C-C and β-β bonds undergo cleavage.¹⁵⁹ Under these conditions increased repolymerisation and condensation are also observed, as seen by the increased yield of insoluble components after reaction (compare citations in Table 25). An overview of reactions performed with lignin in NaOH (aq) is provided (Table 25). Further details regarding the results of these reactions are provided in the Appendix (Table A 5, Table A 6, and Table A 7).

Table 25: Overview of reactions performed with lignin in NaOH (aq).

Source Reference	Lignin	Concentration [wt.%]		Temperature [°C]	$t_{\text{retention}}$ [min]	Process
		NaOH	Lignin			
#1 135	KL (Indulin AT, mixed softwood)	5	10	270, 290, 315	13, 23, 43	continuous (102 mL)
#2 77	OL (acetosolv, formosolv, aceto/formosolv)	4	5	300	80	batch (V not given)
#3 136	4 different corn stover enzymatic lignin, 1 KL	2, 4	10	270, 300, 330	40 (+ 8-12 min preheating)	batch (50 mL)
#4 137	Hemp and softwood lignin (FIRSST process, Ref.: 160)	5	10	300, 310, 320, 330	45 min (including heat up time)	batch (15 mL)
#5 138	KL (softwood)	4.6, 5.0, 5.4, 6.6	20	200, 250, 300, 350	30, 45, 60, 90, 120, 180, 240	batch (100 mL)
#6 139	OL and two types of hydrolytic lignin	10	10	165, 210, 290, 350	15, 60 (+ 45 to 60 min heat up time)	batch (500 mL)
#7 140	OL	2 to 5	2.5, 5, 10	240, 260, 280, 300, 320, 340	2.5, 5, 10, 15	continuous (V not given)
#8 141	OL (beech wood saw dust -> hardwood) sulfur containing technical lignin	1, 3, 5	5	OL: 250, 300, 350 technical lignin: 300, 320, 340	5, 10, 15	continuous (ca. 120 mL)
#9 143	OL from mixed hardwood (Alcell process)	1 to 10	10	290, 310, 330	5, 10, 15, 30, 45, 60	Batch (15 mL) only mass balances on ether solubles
#10 144	OL (olive tree pruning)	4	5	300	40	batch (V not given)

Base catalysed processes based on lignin feeds typically produce low molecular weight compounds at maximum yields of 20% (Table 25). The usage of capping agents has been investigated with the aim to prevent the undesired repolymerisation by capping the reactive sites, thereby inhibiting further reactions. Roberts *et al.* have employed H_3BO_3 , whilst Toledano applied H_3BO_3 and phenol in different concentrations.^{140,144} Yuan *et al.* performed reactions in $\text{H}_2\text{O}:\text{CH}_3\text{CH}_2\text{OH}$ with phenol as a capping agent, whilst Madzhidova *et al.* have used anthraquinone in an 8 wt.% NaOH (aq).^{161,162} Okuda *et al.* have conducted the BCD of lignin in $\text{H}_2\text{O}:\text{phenol}$ mixtures, under supercritical conditions (at 400 °C).¹⁶³ Here the reaction was based on a lignin that was completely soluble in THF (unfortunately the concentration was not reported).¹⁶³ When using pure H_2O or phenol, THF insolubles were produced leading to THF solubility, after $t_{\text{retention}} = 60$ min, of 82% and 87%, respectively. In the $\text{H}_2\text{O}:\text{phenol}$ (1.8:2.5 w/w) mixture, 99% of the products remained soluble in THF, while the M_w was decreased from 2,100 to 420 (i.e. 20% of its original value).¹⁶³ When using H_3BO_3 , Roberts *et al.* found that an acid:lignin weight ratio of 2:1 lead to optimal results at a NaOH: H_3BO_3 ratio of 0.75:1.¹⁴⁰ This resulted in an increase in oil yield to 52%. This increase was proposed to be the consequence of the acid forming esters with phenolic-OH groups, thus inhibiting repolymerisation.¹⁴⁰ Whilst the oil yield increased, boron however was found to be incorporated into the product (and in turn has to be removed depending on the end application), and its regeneration would be of interest given it is consumed stoichiometrically in the process. Toledano *et al.* also reported on an increase in oil yield when using a 2:1 H_3BO_3 :lignin ratio, of > 50% (i.e. from ca. 20% without a capping agent).¹⁴⁴ Contrary to Roberts *et al.*, an increase in oil yield for reactions performed with a 0.75:1 or 1:1 ratio, was not observed. When application of capping agent is able to increase the yield of low molecular weight compounds to > 50 wt.%, it means that repolymerisation is taking place under basic conditions and it also means that the reaction conditions are suitable to cleave the majority of the bonds.

The use of KL is interesting as it has already undergone a base catalysed conversion process, rendering the resulting KL devoid of or featuring limited amounts of α -O-4 and β -O-4 structural linkages. The review of Rinaldi *et al.* is of particular reference to the reader, with the authors summarising that one out of seven β -ether linkages survives the Kraft process.¹⁵ Similarly, OL has reduced amounts of β -ether linkages, dependent on the severity of the employed process.¹⁵ 2D HSQC NMR spectroscopy analysis indicate that β -O-4 linkages still constitute the majority of detectable linkages with ca. six per 100 aromatic units.¹²⁸ Linkages as 4-O-5 or 5-5 (Figure 3) cannot be detected *via* HSQC NMR analysis, due to a lack of C-H bonds. It can be assumed that these linkages comprise the majority of KL, as G_2 , G_5 , and G_6 are still relatively abundant.^{124,133,164} Interestingly the G_5 position is often the predominant of these three structures. This is in contrast to the suggested condensation reactions with FA as crosslinker leading to *ortho-ortho* Ar-CH₂-Ar structures. This mechanism is also described by Chakar and Ragauskas as alkali promoted condensation of phenolic units.¹²⁹ Constant *et al.* analysed different lignin *via* ³¹P NMR spectroscopy and quantified the corresponding contributions of 5-substituted phenols.¹²⁸ The comparison of the spectra of Indulin Kraft and soda P1000 lignin indicated that KL has significantly reduced resonance intensities in this region.¹²⁸

When comparing previously reported results, it is important to consider both the process conditions employed and, perhaps more significantly, the type of lignin feed. In many reports OL has been used, produced under a wide range of conditions and solvents.^{76,77,81,139-141,143,144} Table 25 provides an overview of reactions performed

under hydrothermal conditions with NaOH as the base. Beside the feed, sample workup after the reaction also influences the nature of the product (Table A 5). When conducting an organic extraction from the aqueous phase after acidification, different compounds are extracted as the pH is lowered to 7 as compared to pH 1. While this does not influence the amount of monomeric phenolics, as these are dissolvable in pH 1 aqueous phase, it does influence the mass balance. Finally, the definition of yields and conversion plays a role. While the latter does not influence the outcome of the reaction, it influences the interpretation. Table A 5 provides an overview on the definitions of specific fractions. In this context, Erdocia *et al.* have reported on the dissolution of the solid residue after acidification of the aqueous product mixture in THF and declared the dissolvable fraction as unconverted lignin and the insoluble as coke.⁷⁷ This implies that it can be clearly differentiated between products from polymerisation/condensation (coke), depolymerised compounds (dissolvable in pH 1 (aq)), and the unconverted fraction (and in turn, ease the derivation of process reaction kinetics).

When trying to derive clear quantifiable information from the BCD of lignin, it can only be said that a low pH dissolvable fraction is produced, which can be defined as an oil. This oil phase comprises between 5 and 20 wt.% of the original lignin. The remaining fraction is insoluble at low pH and termed the solids fraction. This is of lower molecular weight than the original lignin (Table A 7). In this chapter, particular focus is placed on the insoluble oligomeric fraction and its characterisation. Furthermore, its suitability as a carbon fibre precursor will be discussed.

4.2 Results & Discussion

4.2.1 Runs #B1-5

Yields of the runs separated into pH 10 solids, pH 7 solids, pH 2 solids, and oil are presented (Figure 27). The corresponding standard deviations and the underlying data are presented in Figure A 12 and Table A 8. The differences in density before and after reaction are negligible and density is on average 1.048 g/mL. With a total feed mass of 580 g generating a volume of 553 mL with a concentration of 112 mg/mL of lignin. In 200 mL product solution, there should be 21.68 g of dissolved lignin derivatives, which is taken as 100% for yield calculations. Evolution of a gas phase could not be detected; this was further confirmed by batch experiments in a closed reactor ($t = 30 \text{ min}$, $T = 300 \text{ }^\circ\text{C}$).

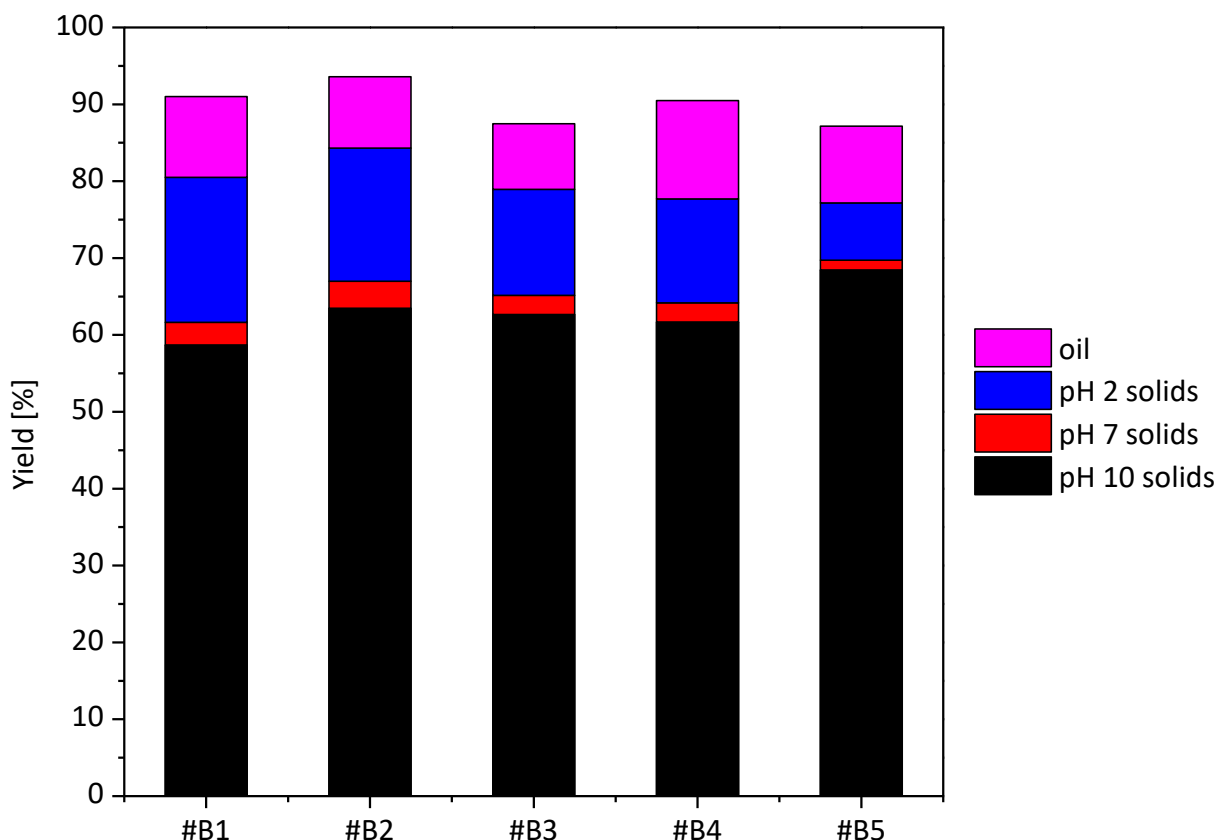


Figure 27: Yields of the different fractions of the reactions #B.

Solid yields were found in the range of 80% for all reactions, while oil yields were *ca.* 10%. Literature reports indicated yields from 35 to 93% for solids, although it should be noted that the definition of what constitutes a solid product often differs and some mass balances are not closed (Table A 6).^{76,77,135–141,143,144} Likewise regarding liquid yields, literature reports values in the range of 5.5 to 23%, with this variability presumably related to the use of different feedstocks and different conditions. An elemental mass balance can be performed using the results of the elemental analysis; this will be discussed the respective section.

Table A 8 provides data concerning the pH before and after reaction. The feed solutions have a starting pH of *ca.* 13.5, meaning that the lignin is deprotonated and thereby made soluble, while the protons set free neutralise some of the HO⁻ ions. After reaction, the pH is *ca.* 12.5, meaning that more protons are dissociated in the course of the reaction. A pH of 14 for a 1 M NaOH (aq) is assumed. This dropped to 13.5 after the addition of 60 g of the HMW fraction into 500 mL, meaning that *ca.* 680 mmol/L of HO⁻ are protonated. Based on the collected molar mass data (Table 23), it was calculated that *ca.* 640 mmol/L of C₉ units are added to the solution, and that roughly one functional group per C₉ unit was therefore deprotonated. In the course of the reaction the pH changed to 12.5, meaning that a further 280 mmol/L of HO⁻ were transformed into H₂O. These protons could be liberated during bond cleavage or by incorporation of oxygen atoms from HO⁻ into the lignin.

Gel Permeation Chromatography (GPC)

The results of the GPC are given in numbers in Table 26 and graphically in Figure 28 and Figure 29, starting point for the summation of the elution chromatogram is 10 min. The values for M_w of the pH 10 solids are comparable between the feed types and do not show large differences (#B1 excluded). pH 2 solids show a larger variation, while also some variation occurs within the group of runs #B1 to #B3 which were all performed under identical conditions. M_w is larger in all pH 2 fractions compared to pH 10 fractions, which is unexpected, since the solubility of large aromatics should be higher at higher pH due to the higher degree of deprotonation. This difference is shown in more detail in the corresponding histograms for the C_9 -Units (Figure 30). Molecular weight for the C_9 -Units is based on EA analyses. pH 10 fractions were found to have a higher content below three C_9 -Units as compared to the pH 2 solids, while the values between three and ten are comparable. Above ten units, the pH 2 solids have higher m_i/m values. The number of C_9 -Units with > 100 constituents (Table A 9), also shows relevant values only for pH 2 solids. A comparison between pH 10 and pH 2 solids from the repetition runs #B1, #B2, and #B3 (regarding their m_i/m and n_i/n values), indicated good data reproducibility (Figure A 13). Literature mainly shows a decrease in molecular weight during base catalysed processes with lignin (Table A 6). Definite numbers vary and Toledano *et al.* even indicate an increase for their hardwood OL cooked at $T = 300\text{ }^\circ\text{C}$ for 40 min.¹⁴⁴ Schmiendl *et al.* describe the change of M_w and M_N graphically indicating a slight decrease over temperature and $t_{\text{retention}}$ between 300 and 340 °C and 5 to 15 min.¹⁴¹

Table 26: Molecular weight distribution data for #B reactions. Comparison between feed types and solids precipitated at different pHs.

Run	Feed			pH 10 solids			pH 2 solids		
	M_w [g/mol]	M_N [g/mol]	PDI [-]	M_w [g/mol]	M_N [g/mol]	PDI [-]	M_w [g/mol]	M_N [g/mol]	PDI [-]
#B1	7,460	1,170	6.4	2,710	600	4.5	3,430	740	4.6
#B2				1,920	450	4.2	2,770	670	4.1
#B3				2,040	490	4.1	4,320	900	4.8
#B4	2,320	700	3.3	1,650	440	3.8	2,150	590	3.6
#B5	5,330	940	5.7	1,960	520	3.8	2,370	650	3.7

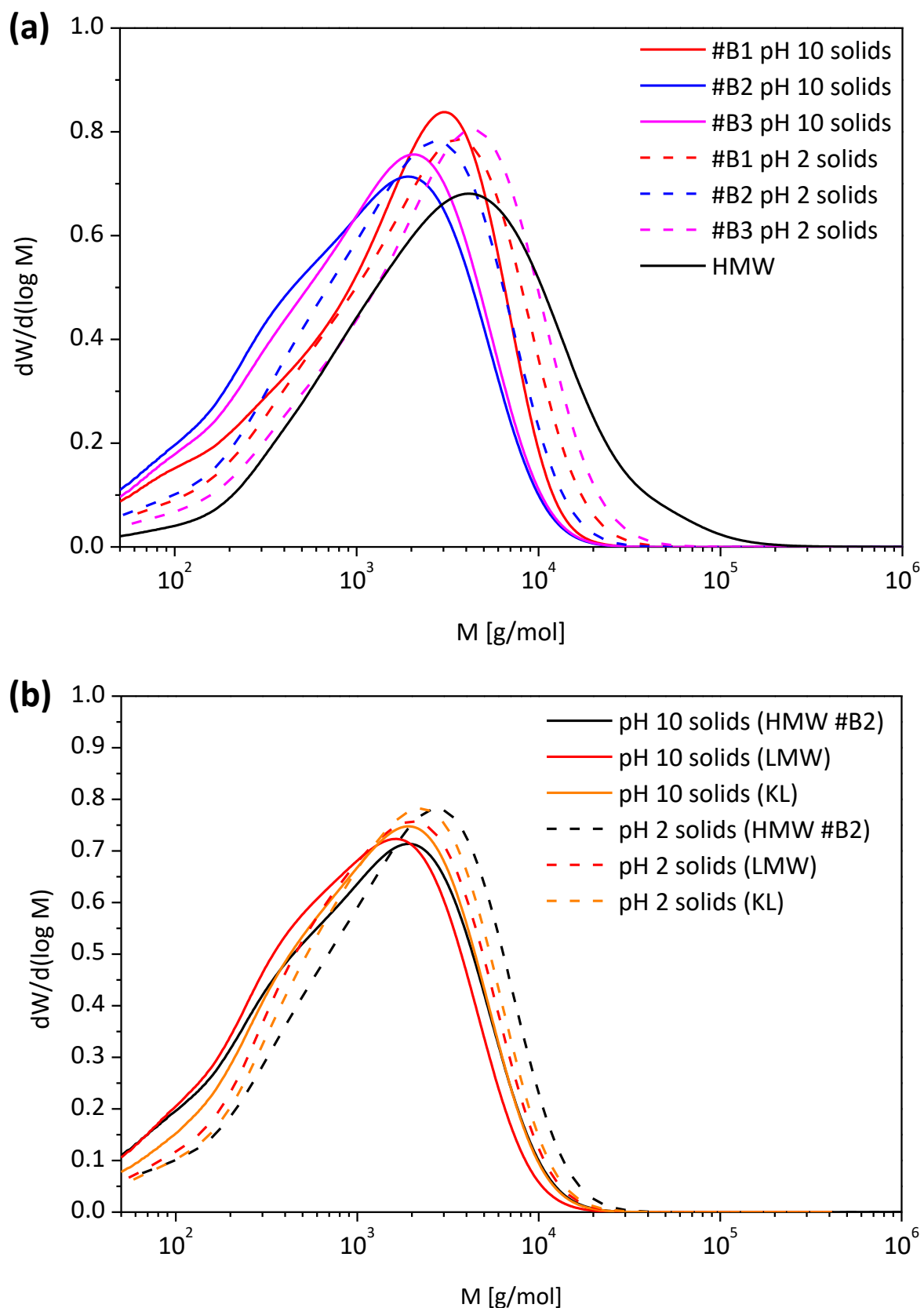


Figure 28: GPC analysis of precipitated solids after reaction at $T = 300\text{ }^\circ\text{C}$ / tretention = 16 min. (a) the three reactions with HMW as feed compared to HMW and (b) comparison between the precipitates resulting from the three feed types HMW, LMW, and KL.

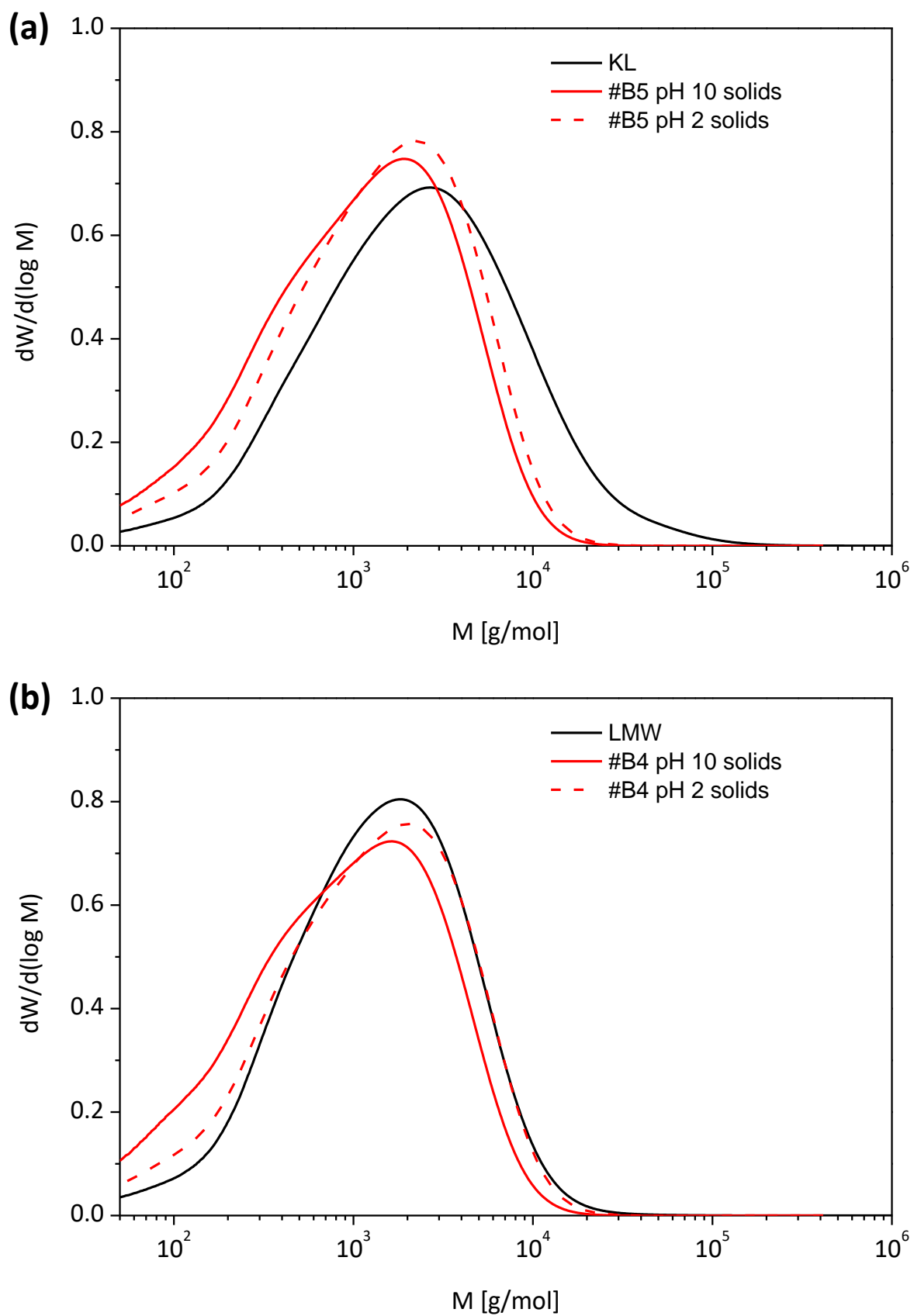


Figure 29: GPC analysis of precipitated solids after reaction at $T = 300\text{ °C}$ / $t_{\text{retention}} = 16\text{ min}$ in direct comparison to the feed. (a) KL as feed, (b) LMW as feed.

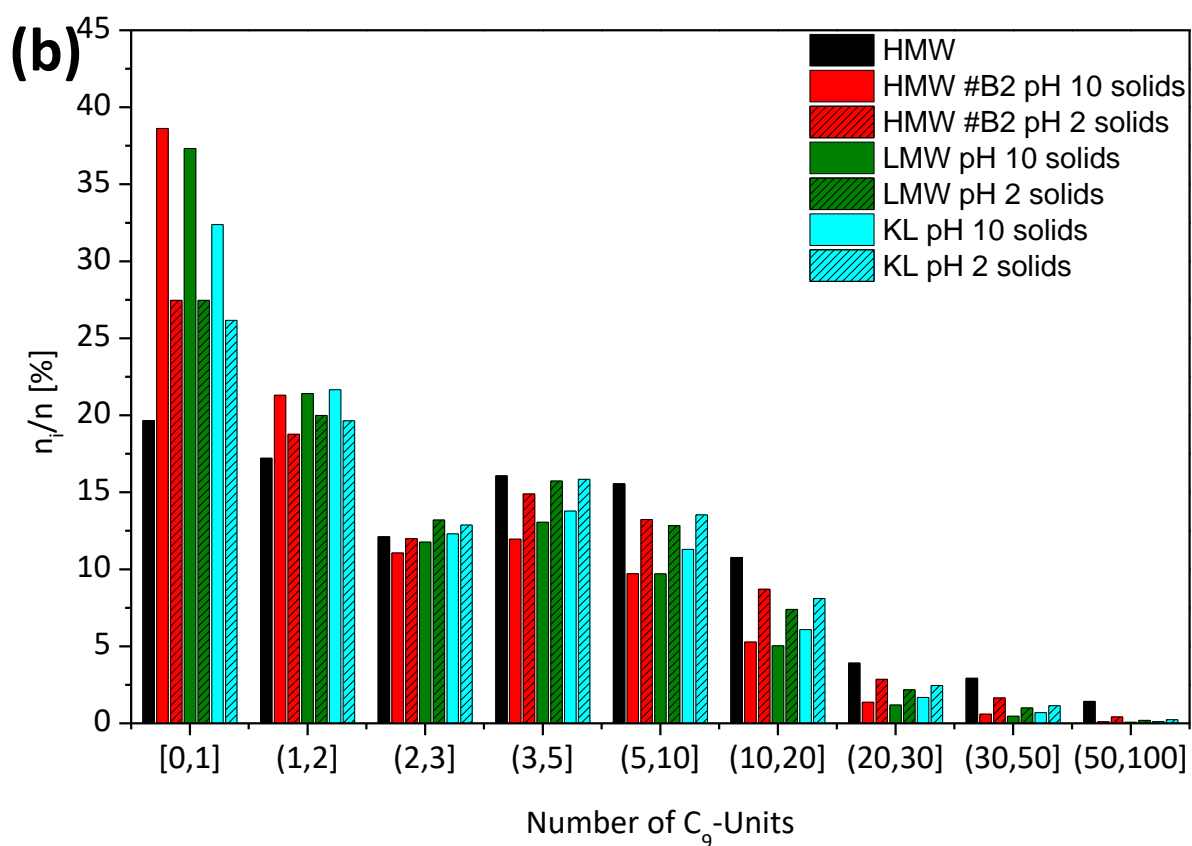
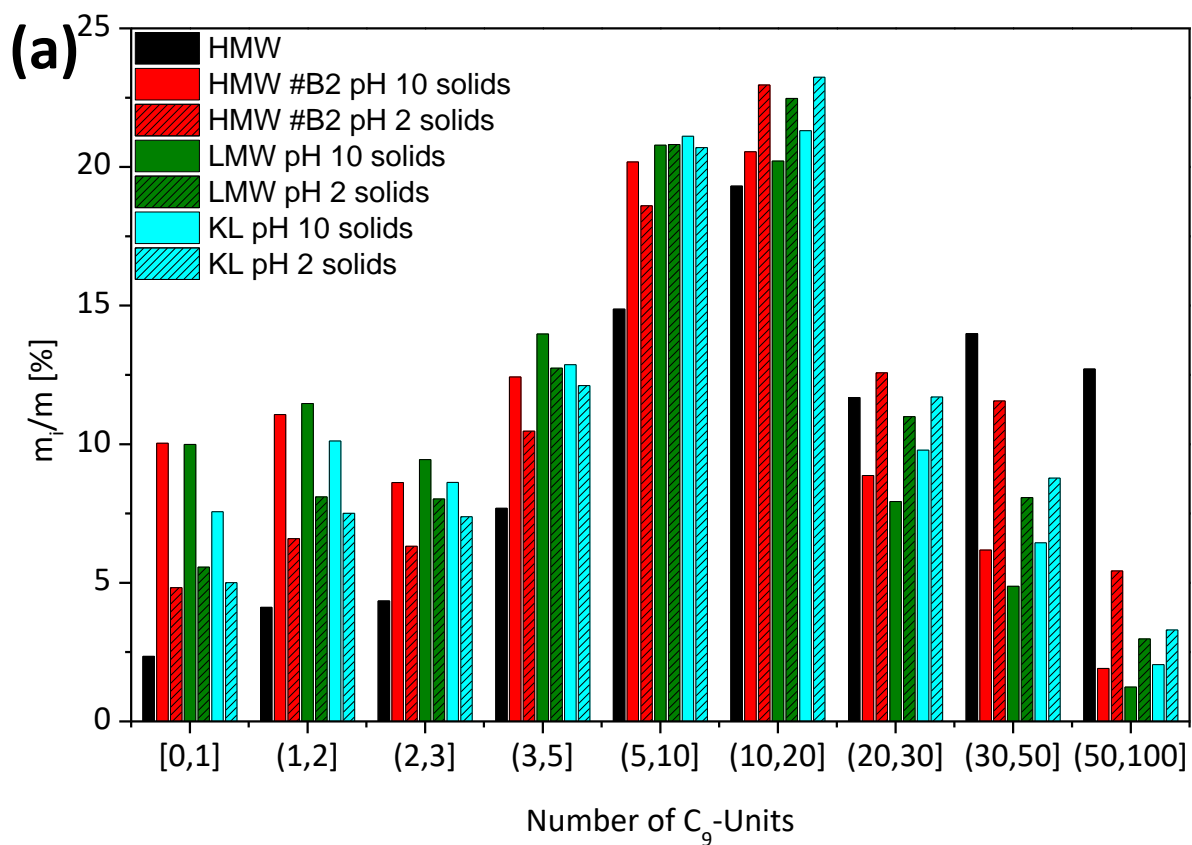


Figure 30: (a) m_i/m and (b) n_i/n for specific chain length of runs #B2, #B4, and #B5 with HMW, LMW, and KL as feed, respectively. The values are generated from GPC data and chain length for M_i calculation is the mean value of the respective number range.

Elemental Analysis (EA)

Regarding EA data (Table 27), a significant decrease in sulphur by roughly two thirds in all fractions was observed. Since no gas phase evolved, the sulphur is either in the oil phase or in the pH 2 aqueous phase. An increase in carbon content and a decrease in hydrogen can be observed. The increase in carbon content is comparable to observation in previous reports (Table A 6). This relative increase is caused by the decrease in sulphur and, mainly, oxygen. Based on a hydrogen content of 5.7 wt.% in the HMW fraction and 5.0 wt.% in the pH 10 solids, as well as 5.2 wt.% in the pH 2 solids and using respective mass fractions (Table A 8; 62% for pH 10 solids and 17% for pH 2 solids), a loss of *ca.* 600 mmol/L (hydrogen) was observed, assuming the hydrogen content of the remaining 21% is constant. This is twice the amount that was calculated by change in pH.

Table 27: Elemental analysis of the #B reactions. Comparison between feed types and solids precipitated at different pHs. The elemental composition of the feed types is added for easier comparison.

Run	pH 10 solids				pH 2 solids			
	C [%]	H [%]	O ^a [%]	S [%]	C [%]	H [%]	O ^a [%]	S [%]
#B1	63.95	4.93	30.58	0.54	67.24	5.26	27.03	0.47
#B2	63.11	5.05	31.40	0.44	67.48	5.20	26.82	0.50
#B3	62.94	5.03	31.57	0.46	64.87	5.09	29.65	0.39
#B4	65.56	5.21	28.68	0.55	67.95	5.35	26.14	0.56
#B5	65.08	5.26	29.20	0.46	66.11	5.21	28.21	0.47
Feed	C [%]		H [%]		O ^a [%]		S [%]	
KL	62.13		5.74		30.39		1.74	
HMW	61.59		5.67		30.88		1.86	
LMW	64.55		5.79		28.22		1.44	

^a calculated by difference

From the collected data (Table 27), the C₉-Formulae can be derived for the #B runs and their respective feeds (Table 28). The C₉-Units of the pH 2 solids are *ca.* 10 g/mol smaller, which is mainly due to a reduction in oxygen content. With the yield of the specific fractions and EA data, a mass balance for C, H, O, and S is calculated. The lost mass and its elemental composition are presented (Table 29). For the pH 7 solids and the oil, no elemental analysis was performed. The elemental composition of the pH 7 solids was estimated as average of pH 10 and pH 2 and the oil composition was assumed as that of catechol, i.e. C₉H₉O₃ → C = 65.47 wt.%, H = 5.45 wt.%, O = 29.08 wt.%. The amount of lost hydrogen and sulphur is relatively constant. The amount of lost sulphur also mirrors the amount of sulphur in the feed, i.e. higher amount for the HMW, lower for KL, and lowest for LMW. The carbon content varies a lot, leading to significant changes in the molecular formula. It can be assumed, that some of the products are MeOH and H₂S. The latter should appear in the form of (HS)⁻ and will be released as gas during acidification. The general formula of CH_{2.x}O_{0.5} and the fact that the compounds should be either escape as gas during acidification or be dissolvable in pH 2 aqueous phase hints at C₁₋₄ organic alcohols and acids. These are probably generated from demethoxylation (e.g. MeOH), removal of side chains, and ring cleavage. Miller *et al.* have previously reported that anisole can react stoichiometrically with phenol and MeOH under hydrothermal conditions at T = 290 °C, with addition of NaOH (n_{Na}:n_{anisole} = 1:1).¹⁴³

Table 28: C₉-Formulae of the #B runs and the three fractions from MeOH extraction (The latter are presented without the methoxy groups for better comparison to the #B runs / Values are derived from the elemental analysis).

Run	pH 10 solids		pH 2 solids	
	C ₉ -Formula	M _{C9} [g/mol]	C ₉ -Formula	M _{C9} [g/mol]
#B1	C _{9.00} H _{8.33} O _{3.23} S _{0.03}	169.02	C _{9.00} H _{8.46} O _{2.72} S _{0.02}	160.75
#B2	C _{9.00} H _{8.65} O _{3.36} S _{0.02}	171.27	C _{9.00} H _{8.33} O _{2.69} S _{0.02}	160.18
#B3	C _{9.00} H _{8.64} O _{3.39} S _{0.02}	171.73	C _{9.00} H _{8.48} O _{3.09} S _{0.02}	166.63
#B4	C _{9.00} H _{8.59} O _{2.96} S _{0.03}	164.87	C _{9.00} H _{8.51} O _{2.60} S _{0.03}	159.07
#B5	C _{9.00} H _{8.74} O _{3.03} S _{0.02}	166.09	C _{9.00} H _{8.52} O _{2.88} S _{0.02}	163.50
Feed	C ₉ -Formula			M _{C9} [g/mol]
KL	C _{9.00} H _{9.99} O _{3.30} S _{0.09}			173.97
HMW	C _{9.00} H _{9.95} O _{3.39} S _{0.10}			175.50
LMW	C _{9.00} H _{9.70} O _{2.95} S _{0.08}			167.45

Table 29: Elemental analysis data regarding the composition and molecular formula of the lost mass for reactions #B.

Run	Total lost mass [g]	C [g]	H [g]	O ^a [g]	S [g]	Molecular formula
#B1	1.94	0.55	0.23	0.85	0.31	C _{1.00} H _{5.02} O _{1.16} S _{0.21}
#B2	1.40	0.32	0.19	0.56	0.32	C _{1.00} H _{7.21} O _{1.32} S _{0.38}
#B3	2.72	1.30	0.27	0.82	0.33	C _{1.00} H _{2.45} O _{0.48} S _{0.09}
#B4	2.07	1.06	0.22	0.56	0.22	C _{1.00} H _{2.51} O _{0.40} S _{0.08}
#B5	2.78	1.14	0.25	1.09	0.30	C _{1.00} H _{2.59} O _{0.72} S _{0.10}

^a calculated by difference

Thermogravimetric and Differential Thermogravimetric Analysis (TGA/DTG)

Thermogravimetric analysis (TGA) indicates that all five reactions lead to a strong increase in thermal stability of the respective products (Figure 31, Figure A 14 and Figure A 14). Unfortunately, as can be seen, the complete removal of H₂O from all the samples was found to be difficult, making determination of T_d not possible. Furthermore, pH 10 solid sample of run #B2 appeared to be contaminated in some way. From the TGA data, the solid residue at 600 °C and DTG peaks of the samples were determined. All samples have a significant higher residue even though they seem to have lost *ca.* 10% as H₂O (and maybe some other low volatiles) during heat-up to 150 °C. The pH 10 solids have a bimodal DTG profile with one prominent decomposition event at *ca.* 280 °C and a second at 410 °C, while the decomposition profile of the pH 2 solids sample is extremely broad, with a non-discrete maximum at *ca.* 390 °C for runs with the HMW fraction as feed. This and the higher thermal stability of the pH 2 solids correspond to a higher molecular weight determined *via* GPC. The pH 2 solids seem to be mainly devoid of the compounds evaporating at *ca.* 280 °C in pH 10 solids, which have a lower molecular weight and a lower solubility in H₂O with a pH ≤ 10. Results from EA show that these compounds have a lower C/O ratio, since the carbon content is lower in the pH 10 solids (Table 27).

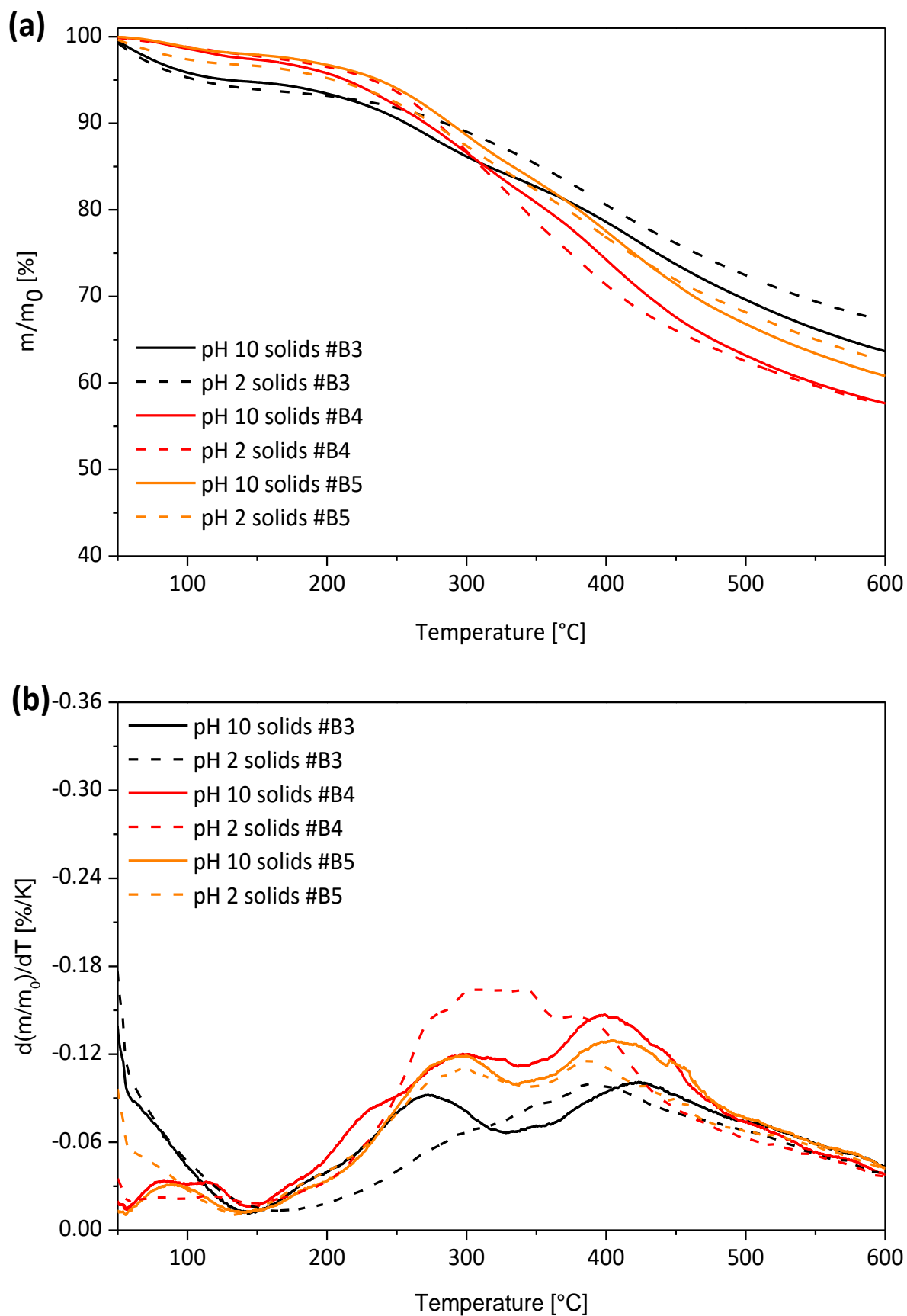


Figure 31: TGA and DTG plots of the pH 10 and pH 2 solids of reactions #B3 (HMW), #B4 (LMW), and #B5 (KL)

Table 31: Monomer yields of the #B runs determined via GC-FID.

Reaction	Oil yield ^a [%]	GC detectables ^b / GC calibrated [%]	Compounds yield ^c [%]				
			<i>Catechol</i>	<i>Guaiacol</i>	<i>Vanillin</i>	<i>4-methyl catechol</i>	<i>Aceto vanillone</i>
#B1	10.51	21.21/16.94	6.29	3.16	2.63	0.82	3.95
#B2	9.29	59.32/50.34	24.71	6.58	5.26	6.09	6.51
#B3	8.54	56.47/46.18	23.59	6.10	4.35	5.43	5.56
#B4	12.80	32.41/26.13	12.37	4.26	2.83	3.05	3.05
#B5	9.91	35.82/28.00	12.15	0.92	4.43	4.35	5.55

^a percentage of total; ^b total mass estimated by total GC-FID area and catechol/syringol response factor;

^c percentage of total oil

All yields of reaction #B1 are significantly lower than those of #B2 and #B3, while the total amount of oil is comparable (Table 31). Using the LMW fraction (#B4) as feed generated a 25% higher yield of oil, while the amount of GC detectables is nearly halved, meaning that more dimers are produced. The chromatograms of runs #B1, #B2, #B4, and #B5 are presented (Figure A 15), showing a comparable product profile for GC detectable compounds. When using the unextracted lignin as feed (#B5) the total amount of oil is comparable to the amount of the HMW fraction, while again more dimeric compounds are present.

¹³C Cross Polarisation Magic Angle Spinning (CP MAS) NMR

¹³C CP MAS NMR spectrum of reaction #B1 product presents resonances at $\delta_{13C} > 170$ ppm, attributed mainly to the TMSP COO⁻ group (Figure 33). The aromatic region between $\delta_{13C} = 160$ and 100 ppm and methoxy groups at $\delta_{13C} = 56$ ppm show a significant decrease in intensity. The signals in the side chain region for oxygenated aliphatics between $\delta_{13C} = 100$ and 56 ppm are removed, while those in the region below $\delta_{13C} = 56$ ppm are decrease, also the other two TMSP associated resonances are to be found. The maxima for the HMW fraction at $\delta_{13C} = 148.4$ and 124.5 ppm are slightly shifted and less resolved and the methoxy resonance at $\delta_{13C} = 56$ ppm is reduced to 13%, hinting at demethoxylation and condensation. Figure A 16(b)+(c) give the comparisons between KL and LMW fraction before and after reaction. The general trend is the same as for the HMW fraction, as in Figure 33. It is interesting to note that the total area is lowest for the reaction #B5 with KL as feed and resonances $\delta_{13C} > 170$ ppm are shifted and different in proportion compared to the other analyses. Figure A 16(a) compares the three runs with HMW fraction as feed and #B3 has a very bad signal to noise ratio, while its total scans were also 3,600. The pH 10 solids of #B1 and #B2 show very good congruency. In summary, the ¹³C CP MAS NMR spectra show a strong decrease in guaiacyl units and general in resonance intensity/area in the aromatics region, hinting at condensed rings giving less intense signals. Mainka *et al.* performed ¹³C CP MAS NMR analysis at different stages during CF production from hardwood KL.¹⁶⁵ The spectrum after oxidative stabilisation resembles that of the lignin fractions after base catalysed, hydrothermal treatment.

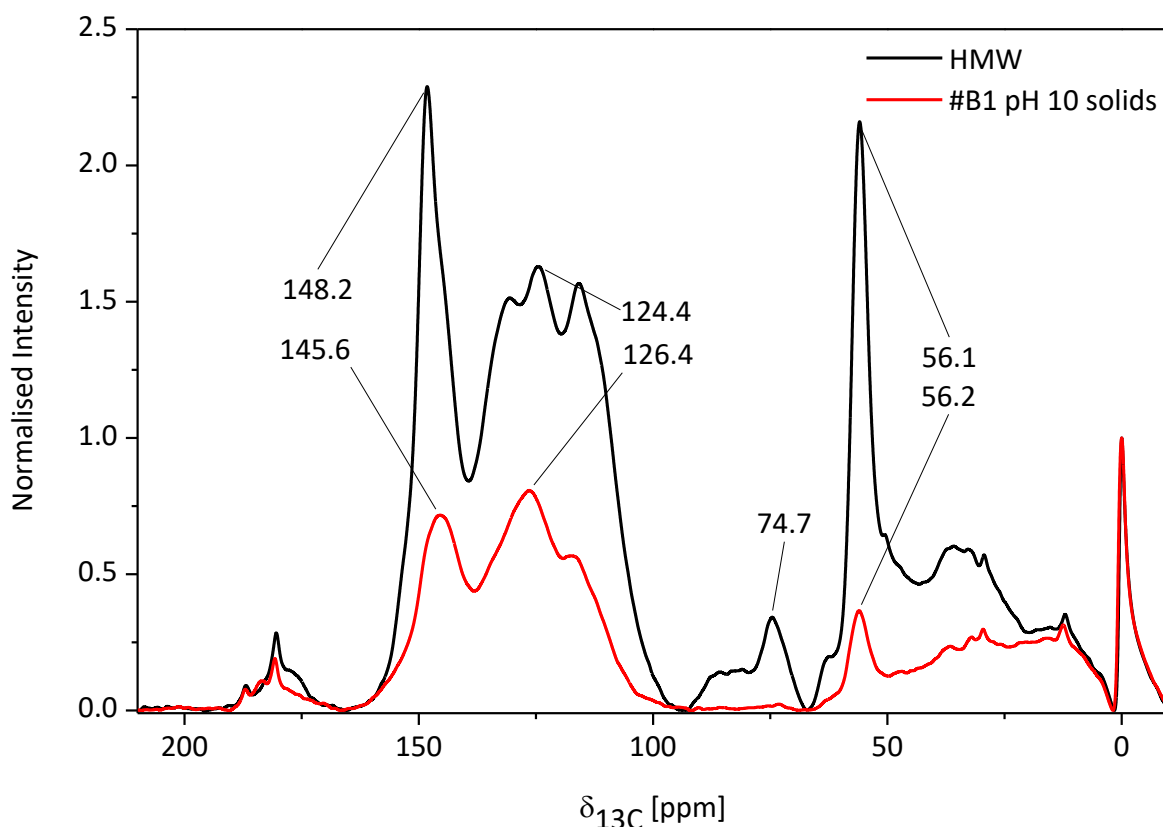


Figure 33: ^{13}C CP MAS NMR spectra of the pH 10 solids of reaction #B1 compared to the HMW fraction.

Attenuated Total Reflection Fourier Transform Infrared (ATR FT-IR) Spectroscopy

ATR FT-IR of the solids from the reaction of run #B shows some significant differences when compared to the feed. Figure 34 shows the FT-IR spectra of the pH 10 and pH 2 solids of run #B3 compared to the feed, the HMW fraction. Band 3 at 1705 cm^{-1} representing C=O bonds is clearly more pronounced in the pH 10 solids, hinting at an increase in aldehyde groups in this fraction. The pH 2 solids do not have this increase in absorbance, which is one of the few differences in the infrared spectrum between the pH 10 and pH 2 solids. Absorbance at 1600 cm^{-1} , (Band #5) representing the symmetric aryl ring stretch, is slightly stronger, while the absorbance of the asymmetric aryl ring stretch (#6) and the asymmetric CH deformation (#7) at 1510 cm^{-1} and 1458 cm^{-1} , respectively, are strongly reduced. In the pH 10 and pH 2 solids no clearly resolved spectral feature at 1426 cm^{-1} (#8) corresponding to the asymmetric CH deformation in $-\text{OCH}_3$ is visible. The latter shifts the minima in absorbance between #8 and #9 to slightly higher wavenumbers. #9 at 1367 cm^{-1} is again more pronounced, which is the aliphatic CH stretch excluding $-\text{OCH}_3$, but including some aromatic skeletal vibrations. #10 is a general aryl ring breathing mode at 1270 cm^{-1} and is in all samples the strongest absorption. At 1220 cm^{-1} C=O stretches can be found and this mode absorbs stronger in the pH 10 and pH 2 samples, which is in-line with the stronger absorption for #3. #12 is nearly completely gone and #14 is strongly reduced, both representing guaiacyl ring modes. #13 represents CO in secondary alcohols and aliphatic esters, which could refer to C-OH bonds in side chains of β -O-4 bonds or other inter unit connections, these are also reduced to a small shoulder. #15 and #16 are vinyl and aromatic CH out-of-plane vibrations, respectively. The vinyl stretch is removed, while the aromatic one is constant. #17 and #18 are supposed to be CH out-of-plane vibrations specifically of guaiacyl units. The absorption of these bands

in Figure 34 shows an increase. Figure A 17(b) shows here some deviations between the three HMW runs with #B3 having the strongest absorption. But also, when assuming a weaker absorption, the value will still be bigger or equal to that of the HMW feed, which is contrary to the findings of the previous bands as well to the ^{13}C CP MAS NMR which indicate a decrease in guaiacyl moieties. Figure A 17(a) show congruent results hinting at a good reproducibility of the runs. On the other hand, the results of #B4 and #B5 shown in Figure A 17(b) are not too different from each other and #B3, indicating in general a comparable absorption spectrum between the solids produced, independent from the feed used.

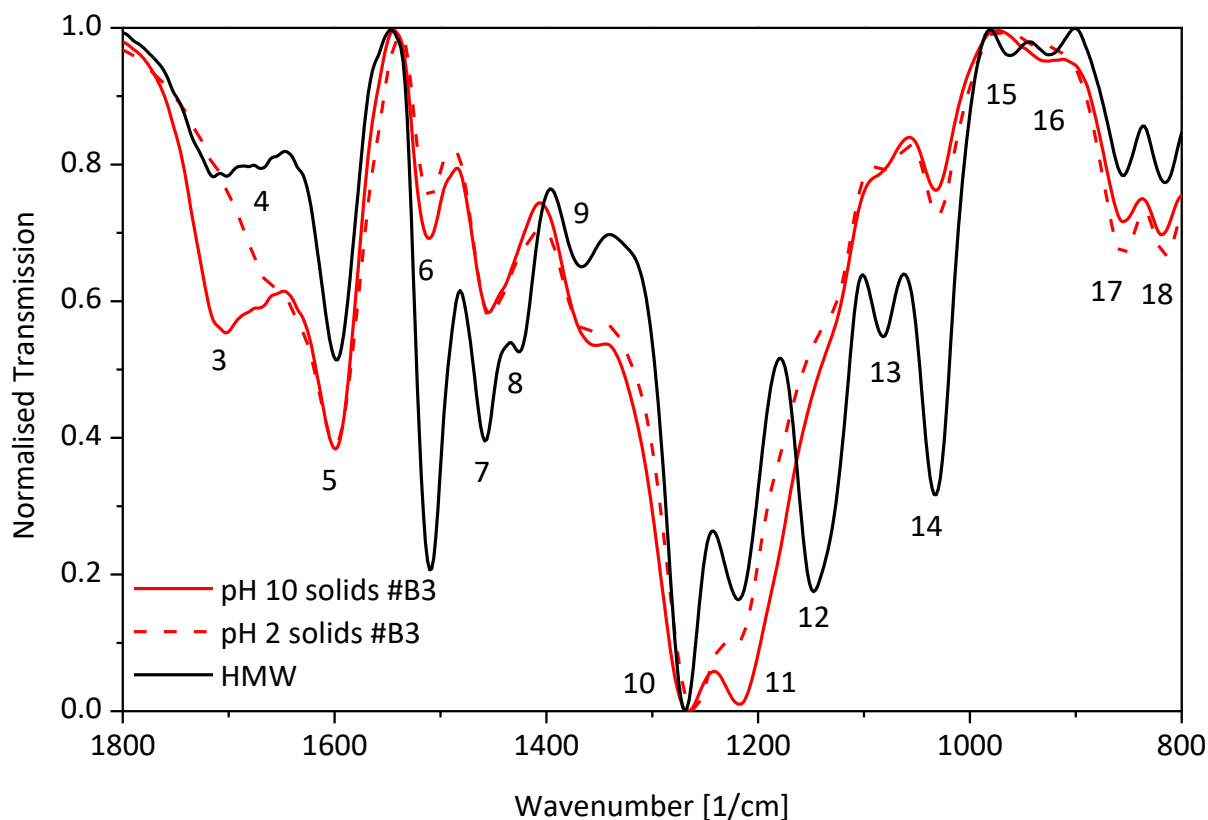


Figure 34: ATR FT-IR spectra of the HMW fraction and the pH 10 and pH 10 solids of reaction #B3.

Summary & Conclusions

After reaction, all solutions have a pH of roughly 12.5. *Ca.* 60-70% of solids are precipitated when going down to pH 10 and only further 15-20% between pH 10 and pH 2. The solids precipitated between pH 10 and pH 7 is negligible (*ca.* 2-3%). Oil yields are *ca.* 10%, reaching a maximum of 12.5% when the LMW fraction is employed as feed. The corresponding molecular weight distribution of the precipitated solids resembles that of the LMW fraction, meaning that KL and HMW presumably undergo a degree of depolymerisation. EA indicates an increase in carbon and a decrease in H, O, and S. While the amount of sulphur and hydrogen decrease significantly, compared to their original value by *ca.* 65 and 10%, respectively and do not differ between the pH 10 and pH 2 fractions. Carbon and the oxygen contents are influenced by the pH. The pH 10 fractions experience only a slight increase in carbon content by 1-2% and the pH 2 fractions by up to 8%. This leads to no change in oxygen content for the pH 10 solids and a small decrease for the pH 2 solids. As *ca.* 10 wt.% of the mass is unaccounted for, these

compounds were described indirectly over elemental mass balancing. This leads to an average composition of $\text{CH}_{2.5}\text{O}_{0.5}\text{S}_{0.1}$ for reactions #B3, #B4, and #B5, which is also comparable with the results of the #K runs. Reactions #B1 and #B2 show very different molecular formula with increased amounts of H, O, and S. This is due to reduced amounts of carbon, since the total amount of hydrogen and sulphur in this fraction is constant over all five reactions. Oxygen is calculated by difference, meaning fluctuations in this compound are a direct result of fluctuations in carbon content. A possible explanation for this behaviour could be the fact, that the reactor was newly built, and during the first runs the catalytical influence of the steel alloy was still of greater importance, leading to coke layers on the surface of the reactor wall. This also inhibits the influence for later reactions. All solids produced in the reactions have a higher thermal stability, and the pH 2 solids are more stable than the pH 10 solids. Brodin *et al.* describe a comparable increase in thermal stability and the shift of the DTG peak towards higher temperatures during the oxidation of lignin under air for 60 min at 250 °C. ^{166}H proton NMR indicates a clear reduction by *ca.* 60% of the signals in the aromatics region from ^{13}C CP MAS NMR shows a reduction in the aromatics area from $\delta_{13\text{C}} = 160$ to 100 ppm by roughly 60%, complete removal of side chains region between $\delta_{13\text{C}} = 100$ and 60 ppm and a strong reduction for the methoxy groups at $\delta_{13\text{C}} = 56$ ppm by more than 85%. ATR FT-IR underpins the reduction in guaiacyl units.

4.2.2 Runs #K1-5

The yields of the runs #K1-5 are shown in Figure 35. Differentiation between pH 2 and pH 10 solids is presented in Figure A 18, showing problems with the precipitation procedure especially for #K5. Table A 11 gives detailed values for the pH, density, and mass fractions of the reactions. Reaction #K3 was performed under the same conditions as reactions #B1-3. Comparing the yields, some clear differences arise. The total mass balance differs by *ca.* 15%. This is due to total solids being roughly 10% less and a decrease in oil yield by 5%. The latter is effectively only half of the amount of the reactions from the #B runs. Also, the distribution between pH 10/pH 2 solids changed from 63/17 to 27/43, i.e. from 3.7 to 0.6. The latter can be related to problems with the pH probe.

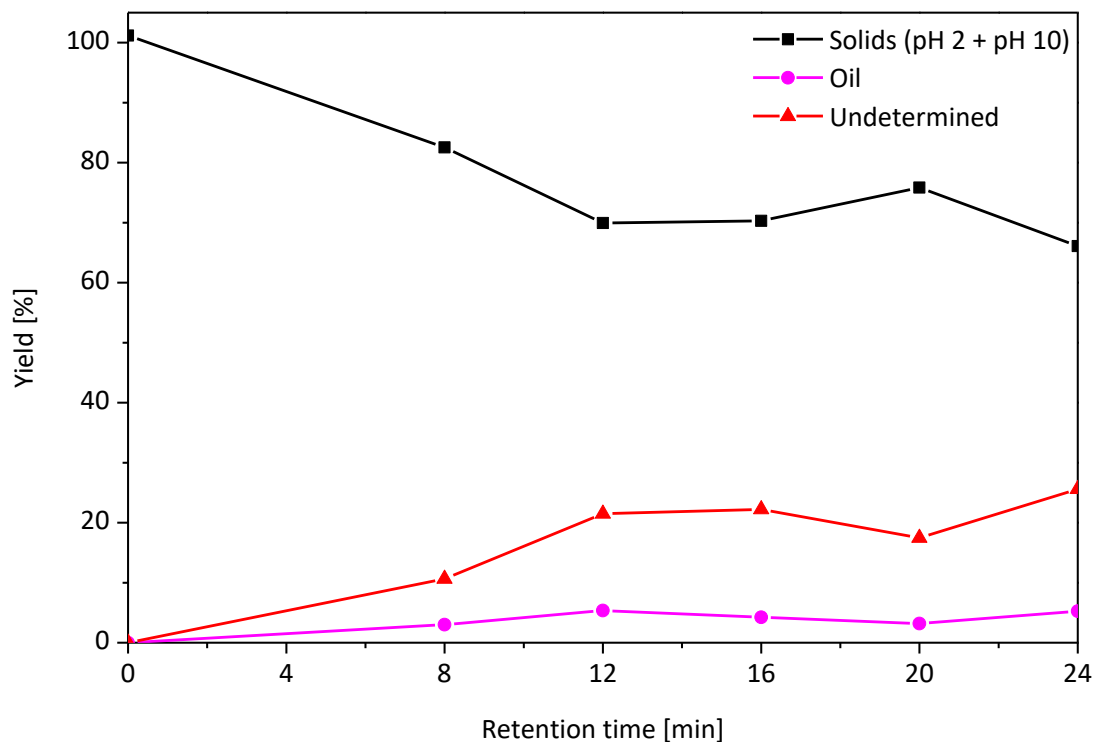
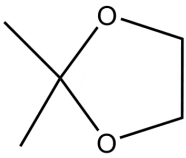
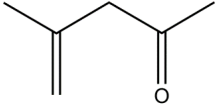
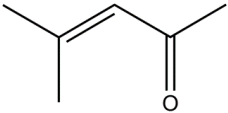
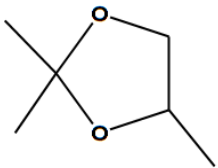
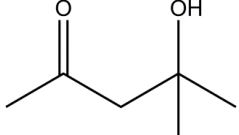
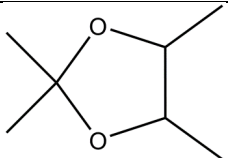
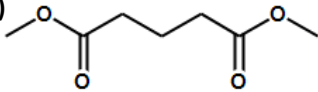
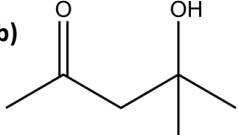


Figure 35: Yields of solids, oil, and undetermined compounds of the kinetic runs #K1-5.

Nevertheless, the number of undetermined compounds rose to *ca.* 20-25%, which cannot be explained by gas evolution or coke formation, since no gas was detected and after all reactions solids in the reactor and filters amounted to less than 0.2 g (compared to 60 g of total lignin pumped through the reactor). In order to quantify the quality of the product separation procedure, 60 g of HMW fraction was dissolved in 1 M NaOH (aq) and precipitated without doing a reaction. Total mass balance was 101.19% (Table A 11). This only leaves compounds dissolvable in aqueous phase at pH 2 and non-dissolvable in EtOAc, i.e. highly polar low molecular weight compounds as organic acids and small alcohols. Furthermore, these compounds must have a higher volatility than H₂O, since the extracted aqueous phase was dried under ambient conditions over five days and the remains were extracted with acetone. The acetone was let to evaporate at ambient conditions for one more day and the compounds were determined gravimetrically as well as *via* GC-MS-FID. The fraction gave in total the same amount as the oil phase, i.e. *ca.* 5% and consisted mainly of the compounds presented in Table 32. Data was acquired directly after sample production and then repeated after ten days. It was found, that the amounts of compounds #2, #3, and #5 increased significantly. Compounds #2 and #3 are generated *via* the acid catalysed self-aldol condensation of acetone with compound #7 as intermediate. Anteunis and Rommelaere showed that compounds #1 and #6 can be synthesised *via* acetone and 1,2-ethanediol or meso-2,3-butanediol, respectively.¹⁶⁷

Table 32: Compounds detected via GC-FID analysis of the pH 2 (aq) solution (after being extracted with ethyl acetate).

$t_{\text{retention}}$ [min]	Compound	Structural formula	a_i/a_{Syringol}	
			1 day	10 days
#1 3.40	1,3-Dioxolane, 2,2-dimethyl- (71.9%)		0.028	0.047
#2 5.23	4-Penten-2-one, 4-methyl-		0.007	0.095
#3 7.38	3-Penten-2-one, 4-methyl- (Mesityl oxide) (61.1%)		0.018	1.493
#4 9.25	1,3-Dioxolane, 2,2,4-trimethyl (65.4%)		0.375	0.320
#5 9.38	2-Pentanone, 4-hydroxy-4- methyl (73.0%)		0.037	0.443
#6 10.41	1,3-Dioxolane, 2,2,4,5-tetrame- thyl (74.9%)		0.491	0.508
#7 13.93	a) Dimethyl glutarate (18.1%) b) 2-Pentanone, 4-hydroxy-4- methyl (10.8%)	(a)  (b) 	0.088	0.094

These findings lead to the conclusion, that most of this fraction stems from the solvent acetone and does thus not explain parts of the lost mass.

The decrease in density would also explain a small deviation since the value for 100% is calculated on the feed density. With a difference of 6 mg/mL and a loading of *ca.* 10 wt.% this would explain 0.5% of the mass, i.e. this effect is rather negligible. The remaining 15-20% are supposed to be high volatile organics. Quantitative HPLC or IEC can give more information on these compounds. Elemental mass balancing will give further insight into the composition of these compounds. Other groups also experienced non-closable mass balances.^{77,135,137,143,144} Beauchet *et al.* used as well a continuous reactor with softwood KL (Indulin AT) and attributed the difference in mass to the evolution of a gas phase.¹³⁵ Schmiel *et al.* describe formation of MeOH and the influence of base concentration on its formation but do not give numbers on the total amount.¹⁴¹ Since their mass balance is *ca.* 90% closed and no gas phase was detected, some 10% of these compounds can be assumed.

For all five kinetic runs a titration curve was recorded and compared to the titration of the HMW fraction (Figure 36). The untreated HMW fraction clearly has a higher buffer capability in the upper pH range down to *ca.* 8. At this point, the curve combines with the other curves by a steeper slope. The untreated lignin seems to have a higher affinity for protons in the upper pH range without leading to precipitation. Reaching a pH of 10 requires roughly twice the number of protons when precipitation the HMW fraction of untreated lignin compared to the compounds after base catalysed treatment.

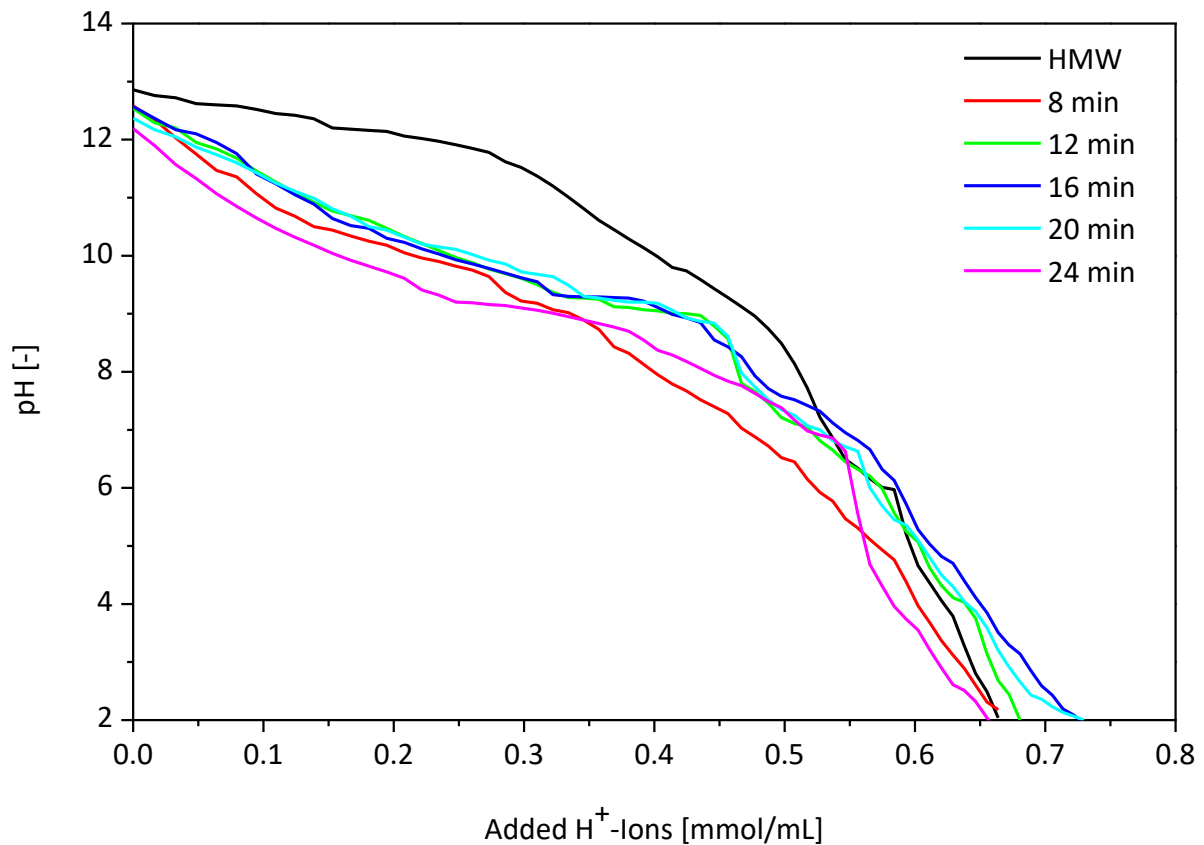


Figure 36: Titration curves of the kinetic runs #K1-5 and the HMW fraction.

Gel Permeation Chromatography (GPC)

GPC was only performed for the runs #K1-3, i.e. for $t_{\text{retention}} = 8, 16, \text{ and } 24$ min, but additionally for the oil fractions. Starting point of the summation was 13 min. Figure 37 shows the diagrams and Table 33 the corresponding values of all three reactions.

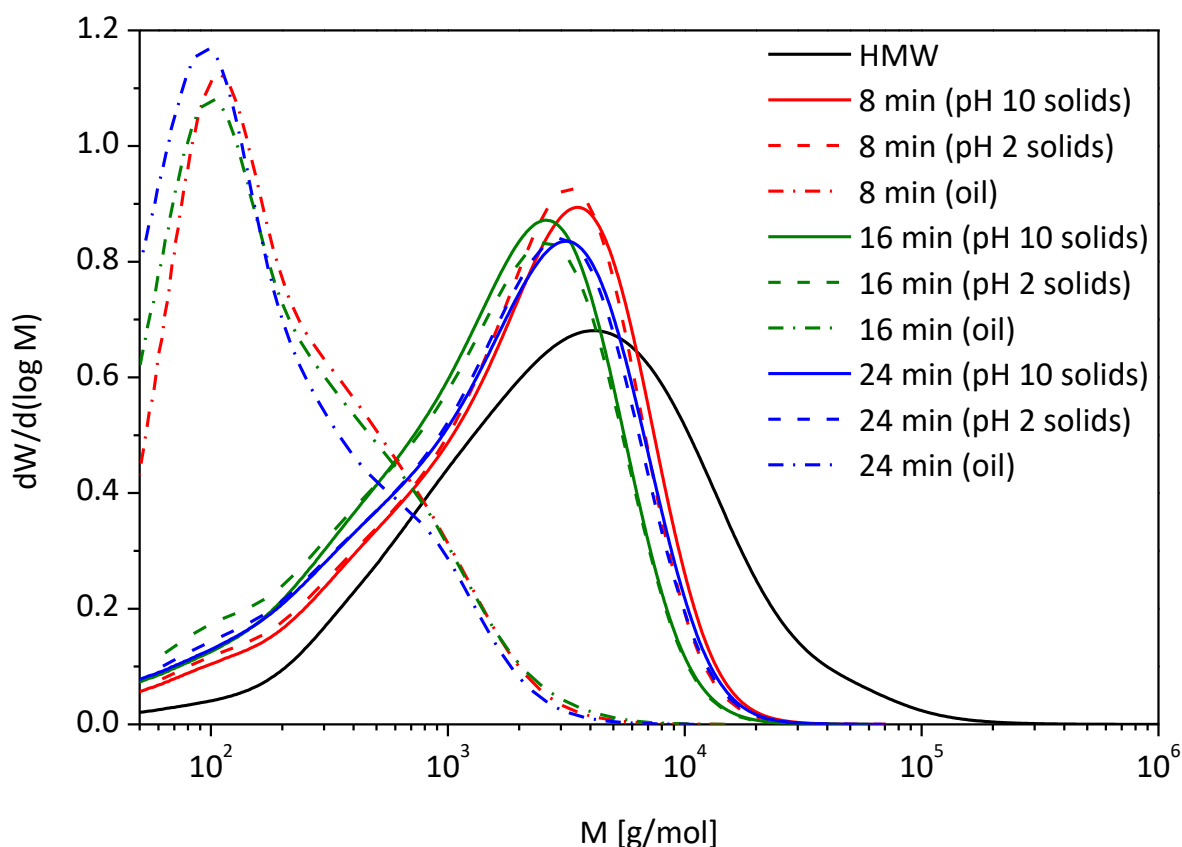


Figure 37: GPC analysis of the pH 10, pH 2, and oil fractions of the runs at $t_{\text{retention}} = 8, 16,$ and 24 min.

Table 33: Molecular weight distribution data for the #K1-3 reactions.

$t_{\text{retention}}$ [min]	pH 10 solids			pH 2 solids			Oil		
	M_w [g/mol]	M_n [g/mol]	PDI [-]	M_w [g/mol]	M_n [g/mol]	PDI [-]	M_w [g/mol]	M_n [g/mol]	PDI [-]
8	3,020	710	4.2	2,800	680	4.1	360	150	2.4
16	2,380	600	3.9	2,210	520	4.3	360	140	2.6
24	2,660	610	4.4	2,650	590	4.5	310	130	2.4

There is neither a large difference between pH 2 and pH 10 solids, nor between the different $t_{\text{retention}}$. The reduction in M_w is *ca.* 60-65% compared to the HMW fraction. The M_w of the oil phase lies in the range of dimers, while M_n hints at monomers. The histograms for the pH 10 and pH 2 solids are presented in Figure 38 and for the oil fractions in Figure 39. Only the pH 2 solids at $t_{\text{retention}} = 16$ min present different values, especially for smaller chains. The strongest change is again in molecules larger than 50 monomeric units with the strongest decrease for m_i/m and an increase for all fractions ≤ 30 units. The values for the 16 min pH 2 solids are unusually small and the 24 min samples seem to have an increased amount of 30+ units, which could be a hint at a starting repolymerisation. This trend is also supported by the 100+ C_9 -Units (Table A 12), where a slightly higher value for the 24 min samples was measured. The amount of mono- and dimeric compounds seems again overestimated, since MeOH extraction from the pH 10 and pH 2 solids and concurrent analyses *via* GC-FID did not present any peaks. The histograms for the oil fraction are generated under the assumption that catechol is the repeating unit of the chains, i.e. a value of 110 g/mol is used for M_i (Figure 39). The numbers for m_i/m for the monomers are in

good accordance with the values determined for GC detectable compounds (Table 38). The trend for the oil phase shows an increase of mono- and dimers with increasing $t_{\text{retention}}$. The GPC shows that 15 - 20 wt.% of the oil fractions consist of compounds with chain lengths > 5 . For the GPC analyses a column with polar polyhydroxy methyl methacrylate stationary phase was used and the pullulan standards are also highly polar. It is possible that the compounds detected in the oil phases corresponding to molecular weights of 500+ g/mol are small, less polar hydrocarbons (e.g. linear C_{3-6} organic alcohols and acids) that are still dissolvable in pH 2 (aq), but have less interaction with the column's stationary phase.

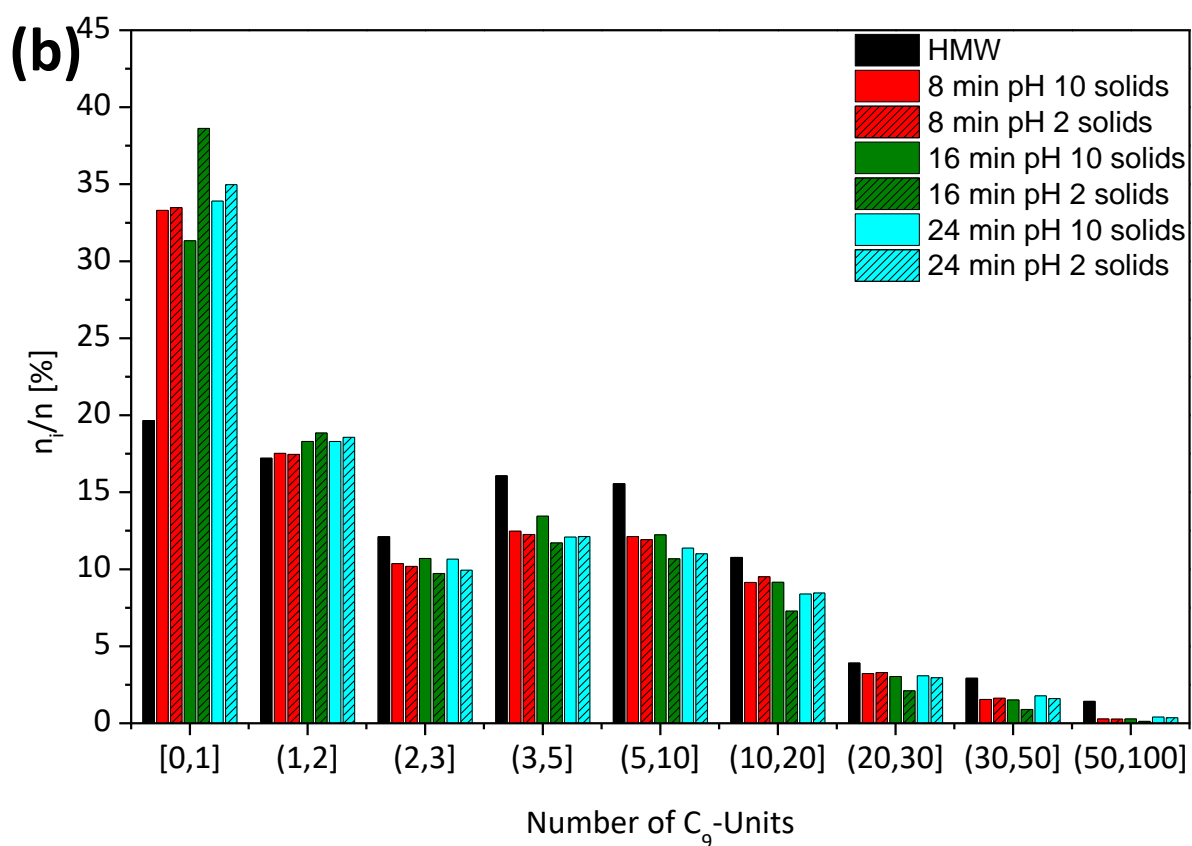
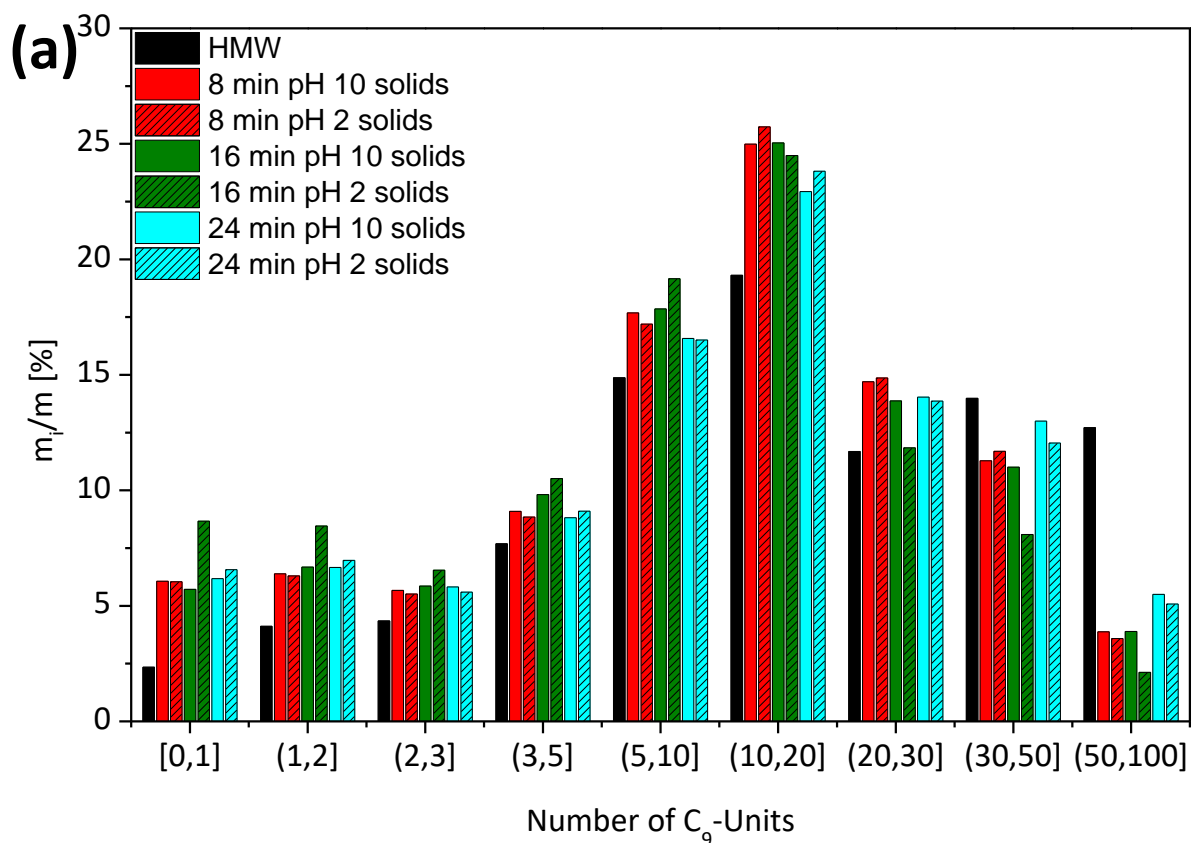


Figure 38: (a) m_i/m and (b) n_i/n for specific chain length of the solid fractions runs #K1, #K2, and #K3 at retention = 8, 16, 24 min, respectively. The values are generated from the GPC data and chain length for M_i calculation is the mean value of the respective number range

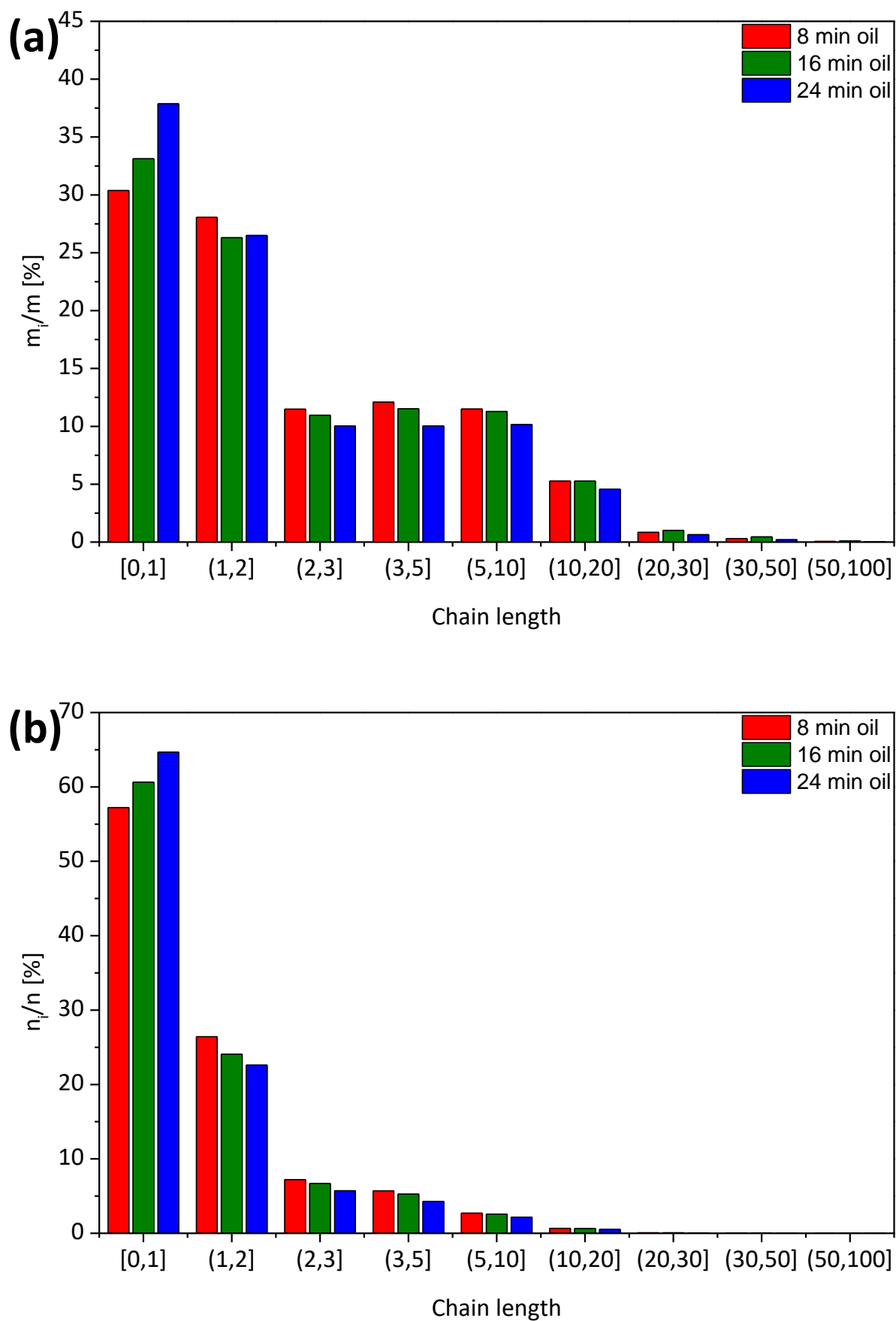


Figure 39: (a) m_i/m and (b) n_i/n for specific chain length of the oil fractions of runs #K1, #K2, and #K3 at tretention = 8, 16, 24 min, respectively. The values are generated from the GPC data and chain length for M_i calculation is the mean value of the respective number range.

Elemental Analysis (EA)

Table 34 shows the elemental composition of the pH 10 and pH 2 solids. As in the reactions of the #B runs an increase of carbon from *ca.* 60 to 70% can be seen. Figure 40 gives the change in elemental composition as a function of $t_{\text{retention}}$, where it can be seen that the change in carbon content commences in the range of 8 to 16 min. Removal of hydrogen and sulphur is completed at $t_{\text{retention}} \geq 8$ min. Regarding mass balance data for C, H, O, and S has been collected (Table 34). When subtracting H_2S , the molecular formula of the lost mass is $\text{CH}_2\text{O}_{0.7-1}$ which is in the range of alcohols such as 1,3-propanediol. The assumption, that the -OMe groups are transformed into MeOH accounts for *ca.* 6% of the C, 12% of the H, and 8% of the O (Table A 13). Here, it is assumed that MeOH is stable under the applied conditions (e.g. based on previously reported observations by Miller *et al.*¹⁴³). The amount of -OMe groups was determined based on the results of 2D HSQC NMR analysis (please see Sections 3.2.6 and 4.2.2, respectively).

Table 34: Elemental Analysis of the #K reactions. Comparison between feed types and solids precipitated at different pHs. The elemental composition of the feed types is added for easier comparison.

$t_{\text{retention}}$ [min]	pH 10 solids				pH 2 solids			
	C [%]	H [%]	O ^a [%]	S [%]	C [%]	H [%]	O ^a [%]	S [%]
8 (#K1)	59.37	4.93	35.12	0.58	64.92	4.91	29.55	0.62
12 (#K4)	68.91	5.21	25.31	0.57	70.68	5.24	23.64	0.44
16 (#K3)	71.40	5.26	22.92	0.42	64.40	4.83	30.32	0.45
20 (#K5)	69.48	4.90	25.23	0.39	64.97	4.84	29.80	0.39
24 (#K2)	69.95	5.11	24.12	0.82	70.54	5.09	23.97	0.40
Feed	C [%]		H [%]		O ^a [%]		S [%]	
HMW	61.59		5.67		30.88		1.86	

^a calculated by difference

Table 35: Elemental analysis and proposed molecular formula of the lost mass for the reactions #K.

$t_{\text{retention}}$ [min]	Total lost mass [g]	C [g]	H [g]	O ^a [g]	S [g]	Molecular formula
8	3.03	1.91	0.31	0.52	0.29	$\text{C}_{1.00}\text{H}_{1.93}\text{O}_{0.20}\text{S}_{0.06}$
12	5.25	2.00	0.37	2.56	0.32	$\text{C}_{1.00}\text{H}_{2.21}\text{O}_{0.96}\text{S}_{0.06}$
16	5.40	2.45	0.41	2.20	0.33	$\text{C}_{1.00}\text{H}_{2.01}\text{O}_{0.67}\text{S}_{0.05}$
20	4.38	2.08	0.39	1.58	0.34	$\text{C}_{1.00}\text{H}_{2.23}\text{O}_{0.57}\text{S}_{0.06}$
24	6.03	2.42	0.43	2.86	0.32	$\text{C}_{1.00}\text{H}_{2.12}\text{O}_{0.89}\text{S}_{0.05}$

^a calculated by difference

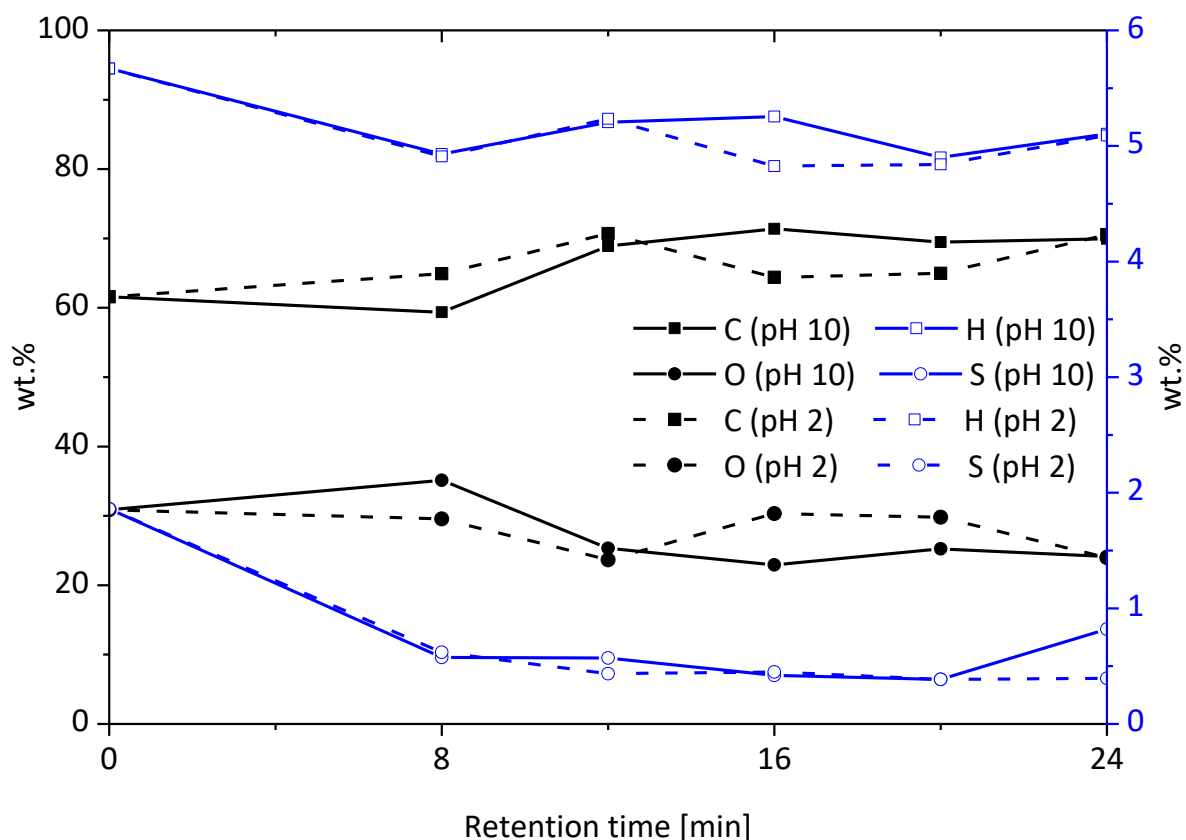


Figure 40: Elemental composition as a function of $t_{\text{retention}}$ for pH 10 and pH 2 solids of the #K runs.

H and S content of the project does not alter when $t_{\text{retention}} > 8$ min. The former reduces from 5.7 to 5.1%, the latter from 1.9 to 0.5%. Since O is calculated by difference, the increase in C content results in a decrease of O from 31% to 24%. The increase in C content is presumed to be related to a decrease in the presence of other compounds, since the only C source is the lignin itself. The decrease in H and S may account for *ca.* 2%, whilst the remaining 8% may result from deoxygenation - supported by elemental analysis of the lost mass.

Thermal Analysis (TGA/DTG/DSC)

TGA and DTG analyses of the pH 10 and pH 2 solids are presented with increasing $t_{\text{retention}}$ in Figure 42 and Figure 43. Compared to the analyses of the KL, HMW, and LMW fractions, the temperature range was extended to 900 °C. From the TGA, an increase from 52 to *ca.* 63% of solid residue after BCD compared to the feed, as already observed for #B runs (Figure 42). The data presented in Table 36 indicate an increase in solid residue with increasing $t_{\text{retention}}$ at 895 °C from 52.5% at 8 min to 58.4% at 24 min for the pH 10 solids and from 48.4% to 54.6% for the pH 2 solids. The DTG profile for the pH 10 and pH 2 solids presents a broader decomposition behaviour and weight loss in general (Figure 43). The broad profile feature in the DTG of the pH 10 solids / $t_{\text{retention}} = 8$ min centred at *ca.* 70 °C is attributed to residual solvent. The greatest mass loss occurs in the interval $T = 300$ to 500 °C with a shoulder at 240 - 290 °C and a maximum at 380 - 400 °C. As for the #B runs the pH 10 solids show a bimodal decomposition profile where $T = 200$ to 450 °C, whilst for pH 2 solids higher loss of mass in the T range below the main decomposition event at *ca.* 380 °C was observed. The pH 10 solids show a peak at *ca.* 700 °C,

which is most pronounced for $t_{\text{retention}} = 8$ min (Figure 43(a)). These compounds were MeOH insoluble and accumulated in the HMW fraction after extraction. At $t_{\text{retention}} = 8$ min, pH 2 solids do not show this broad peak (Figure 43(b)), while here a peak at higher T is observed.

Table 36: TG residue data and corresponding DTG peak positions for the pH 10 and pH 2 solids fractions of the #K runs.

$t_{\text{retention}}$ [min]	Feed		pH 10 solids		pH 2 solids	
	Residue ^a [wt.%]	DTG peaks [°C]	Residue ^a / Residue ^b [wt.%]	DTG peaks [°C]	Residue ^a / Residue ^b [wt.%]	DTG peaks [°C]
8	52.3	270 ^c /363	63.9/52.5	380/710 ^d	60.1/48.4	297/401/815 ^d
12			59.3/52.8	250 ^c /375/730 ^c	60.2/53.8	250 ^c /374/ 606 ^c /735 ^c
16			64.5/56.5	298/730 ^c	62.3/49.4	177 ^f /315 ^c / 382/845 ^f
20			63.4/52.0	306 ^c / 430-490 ^e /610 ^c	64.9/56.0	288 ^c /730 ^c /852
24			66.9/58.4	275/424/ 530 ^c /750 ^c	62.1/54.6	600 ^c /738 ^c

^a at 600 °C; ^b at 895 °C; ^c shoulder, ^d high rate of loss at elevated temperatures, ^e broad peak, ^f unusual large peak

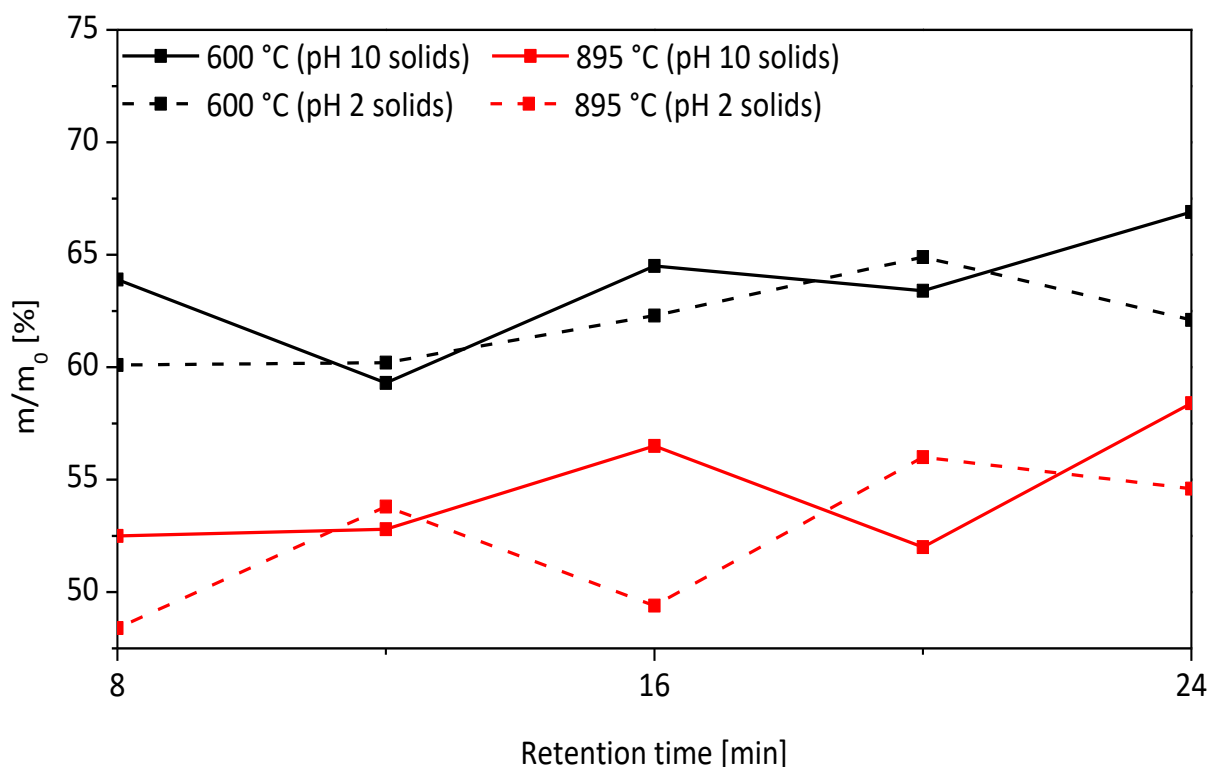


Figure 41: Solid residue of the pH 10 and pH 2 solids from reactions #K as a function of t_{retention}.

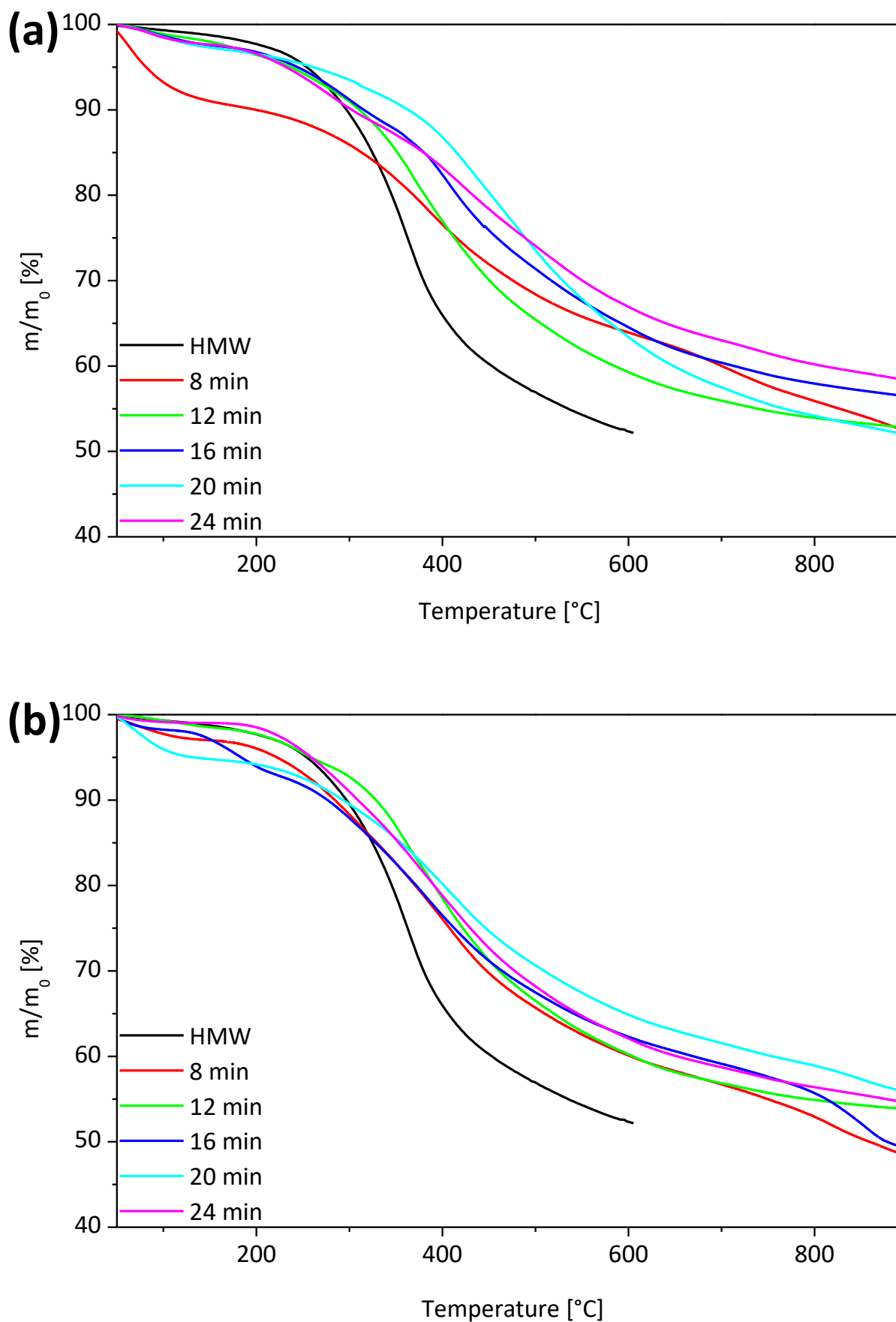


Figure 42: TG (mass loss as a function of increasing T) analysis of the pH 10 solids (a) and pH 2 solids (b) compared to the HMW fraction, relating to increasing tretention.

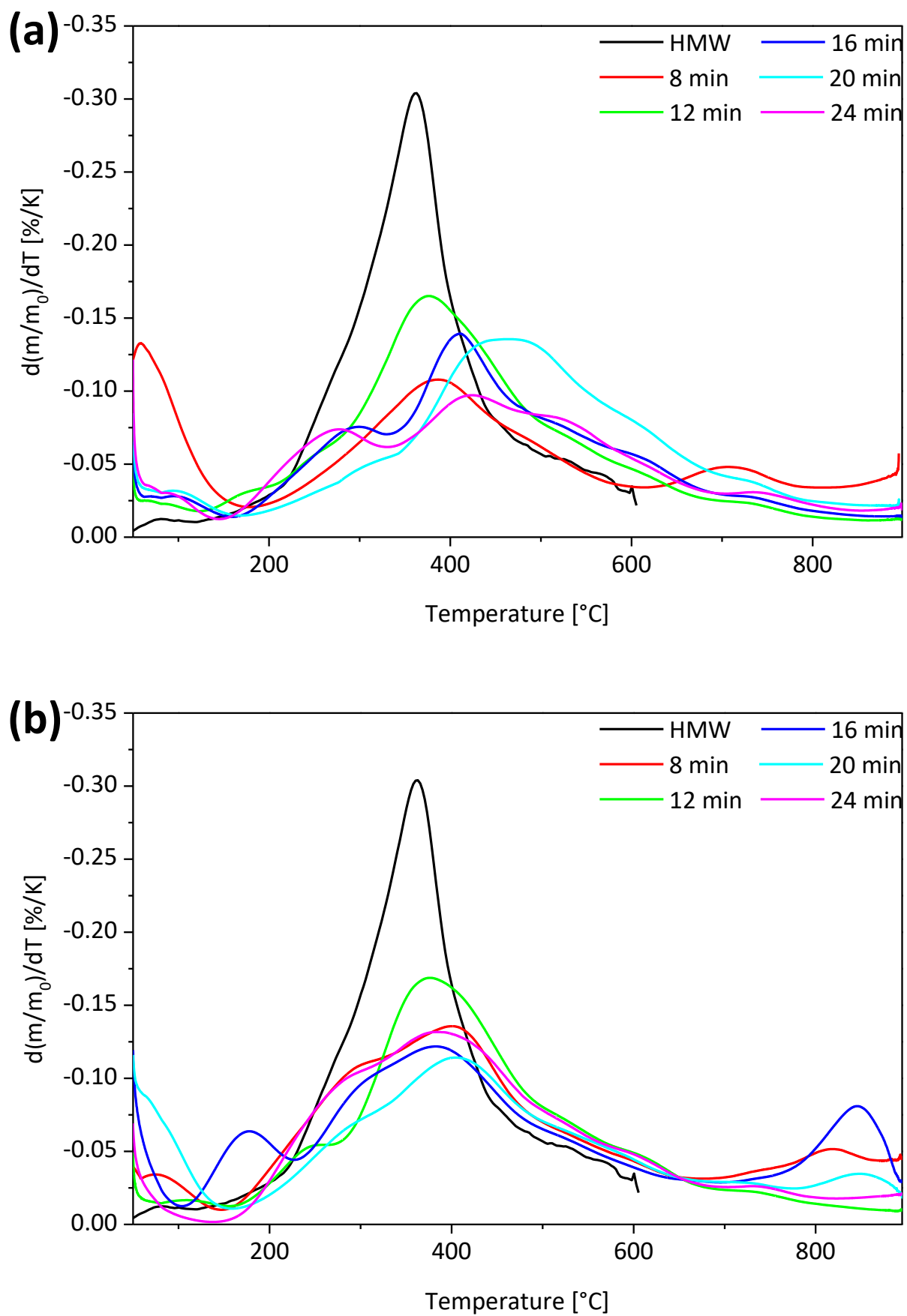


Figure 43: DTG (mass loss as a function of increasing T) analysis of the pH 10 solids (a) and pH 2 solids (b) compared to the HMW fraction, relating to increasing $t_{\text{retention}}$.

DSC was performed for the runs #K1, #K3, and #K2 at $t_{\text{retention}} = 8, 16, \text{ and } 24$ min, respectively. For the 24 min run, there was too few sample of the pH 10 fraction. Additionally, the 16 min pH 2 solids were mixed with the LMW fraction (1:1 w:w) to see if this fraction can serve as plasticiser. The DSC traces are shown in Figure 44. A clear glass transition cannot be determined for the samples after the base catalysed process.

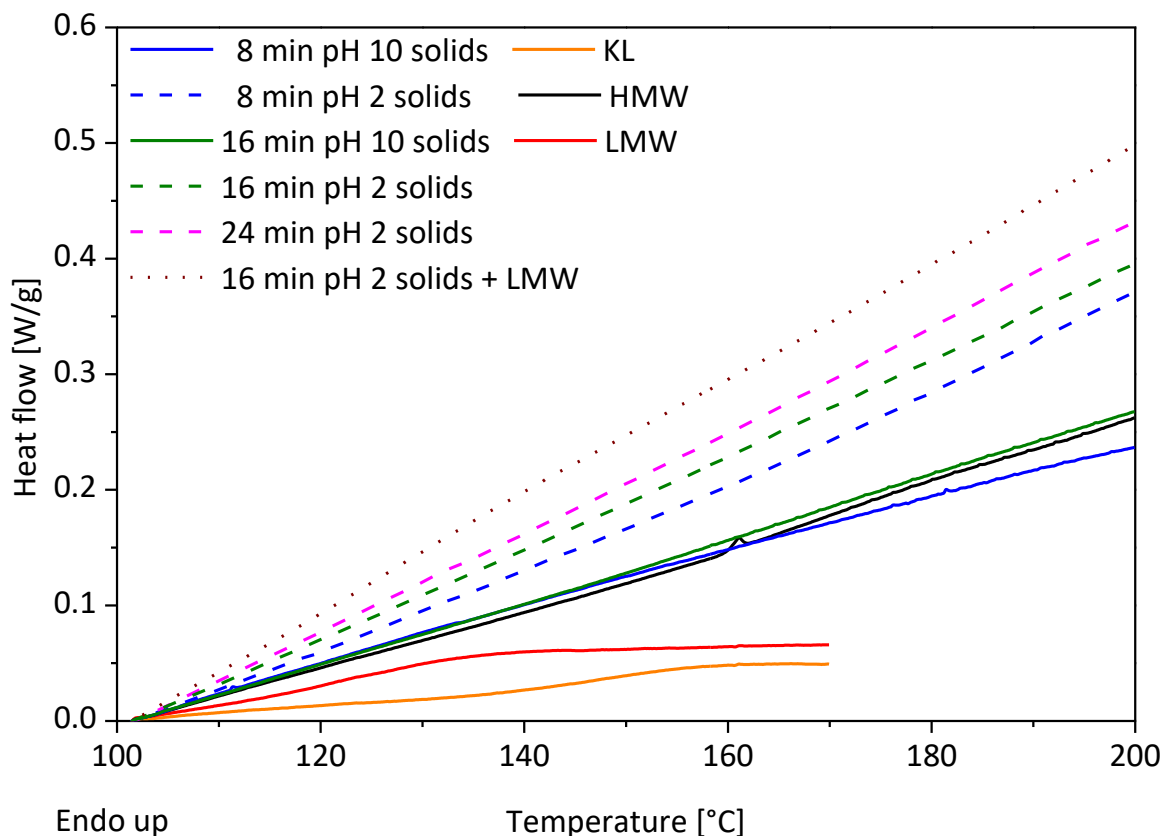


Figure 44: DSC traces of the #K runs $t_{\text{retention}} = 8, 16, \text{ and } 24$ min compared to the KL, HMW (feed); and LMW fractions.

DSC analysis of the precipitated solids indicated a linear increase in c_p over temperature (Figure 44). Assuming a linear constant slope for the DSC curves (except KL and LMW) between 110 °C and 180 °C, as well as excluding any influences from the machine, a change in c_p per Kelvin can be calculated (Table 37). The HMW fraction and the pH 10 solids lie in the range of 0.03, the pH 2 solids between 0.044 and 0.052 increasing with $t_{\text{retention}}$ and the sample of the 16 min pH 2 solids with LMW has the highest value with 0.06 J/(g K²). These results underpin the higher thermal similarity of the pH 10 solids with the feed compared to the pH 2 solids. The exact reason for the increase in apparent heat capacity over temperature of all reaction products is unknown. The behaviour resembles that of an amorphous polymer during glass transition, as the KL and LMW fractions. This transition is caused due to the amorphous sections becoming more mobile, which also increases their capability to absorb heat. The precipitated solids, as well as the HMW fraction, seem to experience an increase in mobility without reaching the final rubbery state and directly going into decomposition. The DTGs in Figure 43 show, that above 200 °C the mass loss increases for all samples, while the 16 min pH 2 solids have a strong peak already at 170 °C.

Table 37: Change in isobaric specific heat (c_p) over temperature for the solids of reactions #K.

Sample	Heat flow at 110 °C [W/g]	Heat flow at 180 °C [W/g]	$d/dT c_p$ [J/(g K ²)]
HMW	0.02164	0.20888	0.032
8 min pH 10 solids	0.02365	0.1946	0.029
8 min pH 2 solids	0.02715	0.28455	0.044
16 min pH 10 solids	0.02250	0.21366	0.033
16 min pH 2 solids	0.03167	0.31278	0.048
24 min pH2 solids	0.03493	0.34070	0.052
16 min pH 2 solids + LMW	0.04219	0.39484	0.060

Gas Chromatography (GC)

The evolution of four calibrated compounds in the oil fraction of #K runs as a function of $t_{\text{retention}}$ was investigated (Figure 45). Catechol and its derivatives are accumulating while guaiacol derivatives as vanillin and acetovanillone are slightly decreasing being probably a precursor for the catecholic compounds. The accumulation of catechol and derivatives is also described in the literature for base catalysed processes (Table A 6). The GC detectable amount of 4-methylcatechol is significantly higher than that of 3-methylcatechol, suggesting that the methyl group at the *para*-position prevents further methylation and probably originates as a residual group after demethoxylation of guaiacylic compounds with functional group at the *para*-position, such as vanillin or acetovanillone (Table 38).

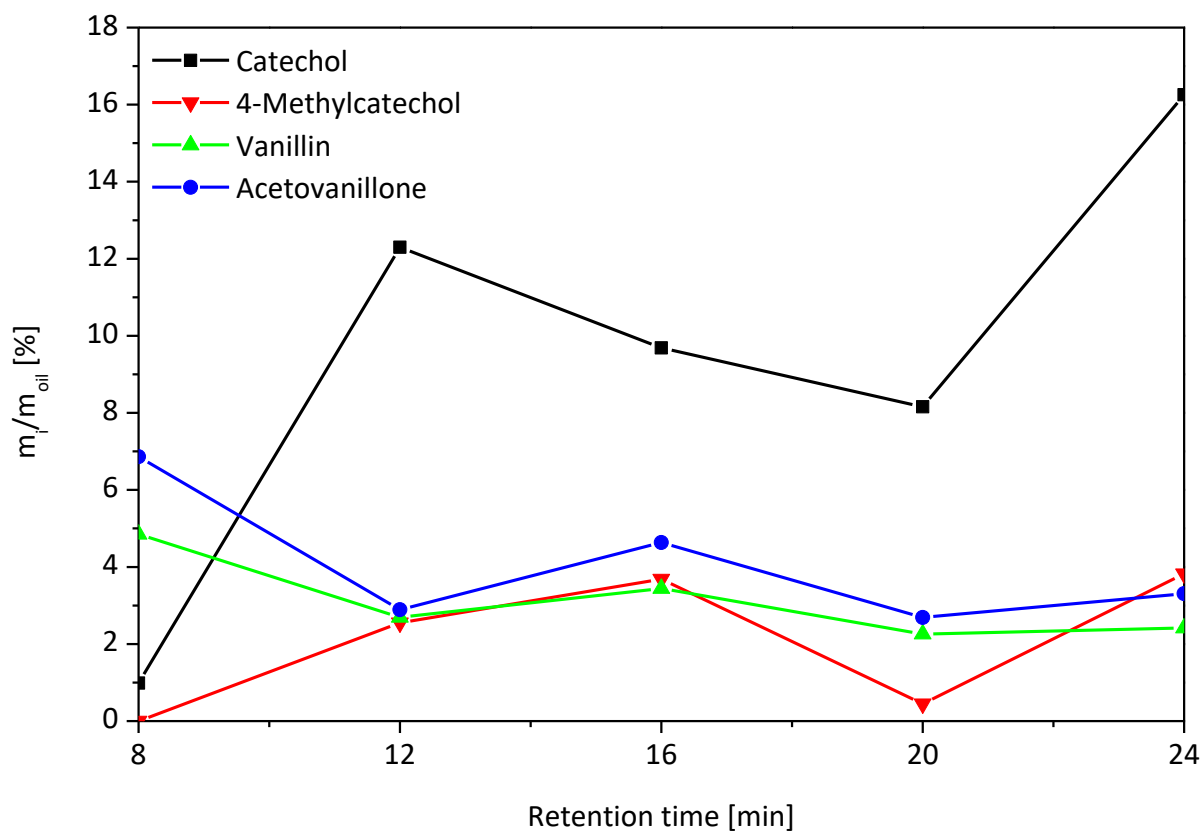
Figure 45: Main GC detectable compounds in the oil fractions of the #K runs as a function of $t_{\text{retention}}$.

Table 38: Oil yield, GC detectables, and monomeric compounds yield of the retention dependent runs #K.

$t_{\text{retention}}$ [min]	Oil yield ^a [%]	GC detectables ^b / GC calibrated [%]	Compounds yield ^c [%]					
			<i>Aceto- vanillone</i>	<i>Vanillin</i>	<i>Guaiacol</i>	<i>Catechol</i>	3- Methyl- catechol	4-
8	3.01	22.25/13.25	6.86	4.85	0.49	0.99	0.06	--
12	5.35	33.53/24.54	2.89	2.69	3.53	12.30	0.57	2.55
16	4.23	29.43/21.81	4.64	3.44	0.10	9.68	0.27	3.68
20	3.19	44.39/29.76	2.69	2.26	3.10	8.16	--	0.45
24	5.26	32.23/26.88	3.31	2.42	0.41	16.26	0.67	3.82

^a percentage of total; ^b total mass estimated by total GC-FID area and catechol/syringol response factor; ^c percentage of total oil

¹³C Cross Polarisation Magic Angle Spinning (CP MAS) NMR Spectroscopic Analysis

A ¹³C CP MAS NMR spectrum was only acquired for first run where $t_{\text{retention}} = 8$ min, since the device was unavailable afterwards. Characterisation of the pH 10 solids after $t_{\text{retention}} = 16$ min was used for comparison from the #B runs. Figure 46 presents the spectra of the aforementioned samples. In general, the interpretation is the same as for the samples of the #B runs. Removal of the side chain region, strong decrease in the methoxyl peaks as well as in the aromatics region. When looking at the results of the 8 min and the 16 min runs it appears that the side chains between $\delta^{13}\text{C} = 80$ to 60 ppm are completely removed during the first 8 min. The decrease of the peaks in the aromatic region and of the methoxy groups is only slightly stronger in the 16 min sample for the pH 10 solids compared to the 8 min sample. The pH 2 solids of the 8 min run gave unexpectedly strong signals. This was also observed for the 2D HSQC runs as well as for the ¹H NMR spectra acquired in DMSO.

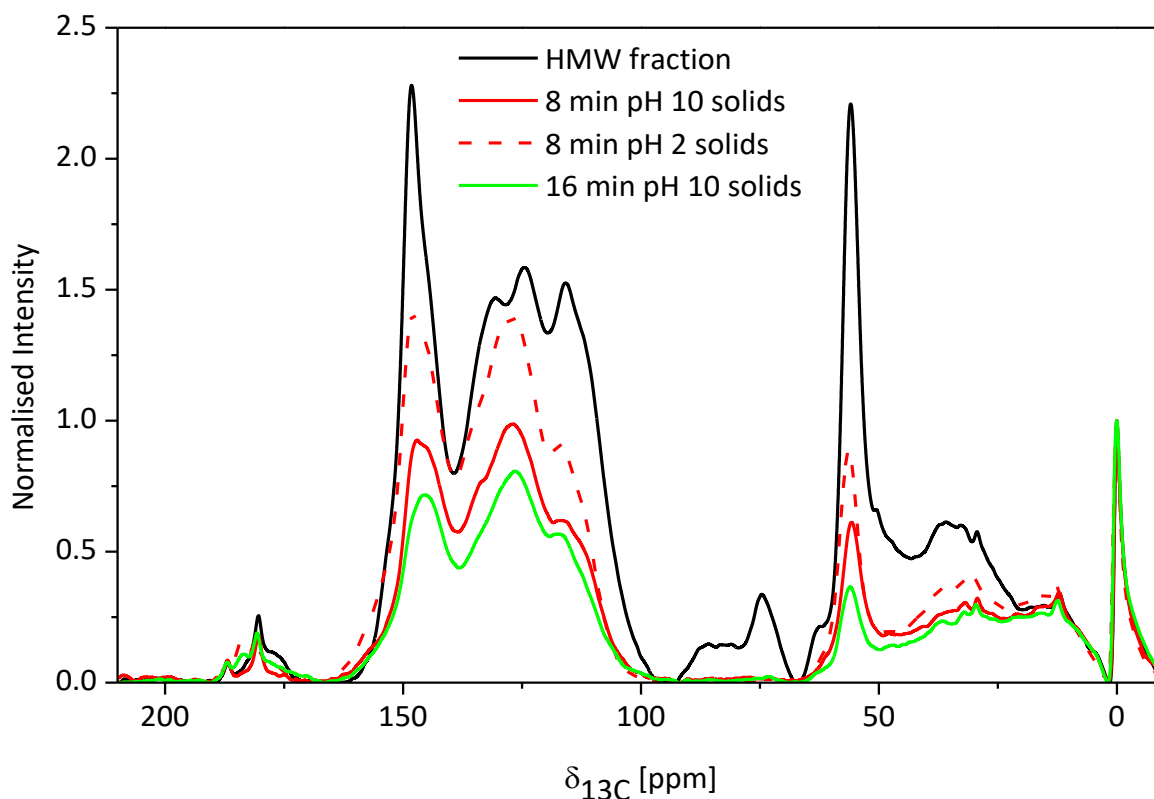


Figure 46: Solid state ^{13}C CP MAS NMR spectra of the #K1 pH 10 and pH 2 solids (8 min) and #B1 pH 10 solids (16 min).

^1H and 2D Heteronuclear Single Quantum Correlation (HSQC) NMR Spectroscopy

As in Chapter 3.2 the results from the NMR in $\text{DMSO-}d_6$ will be discussed by separation of the ^1H NMR spectra into the six distinct areas (i.e. as described in Table 21). Figure 47 presents the ^1H NMR spectra of pH 10 and pH 2 solids at $t_{\text{retention}} = 8, 16,$ and 24 min. These are also shown in Figure A 19 in more detail for further discussion. The spectra of the corresponding oil fractions are presented in Figure 48. Figure 49 compares the DMSO normalised areas of the pH 10 solids, pH 2 solids, and the oil fractions and Figure 50 and Figure 51 show the complete 2D HSQC spectra with designated sub-areas. It has to be mentioned that the intensity of the pH 2 solids peaks is in general stronger than those of the HMW fraction or pH 10 solid. This includes a stronger noise level compared to the $\text{DMSO-}d_6$ peak, which can be seen in the 2D HSQC NMR spectra in Figure 51, where the lower threshold had to be set higher in order to remove the noise from the spectra.

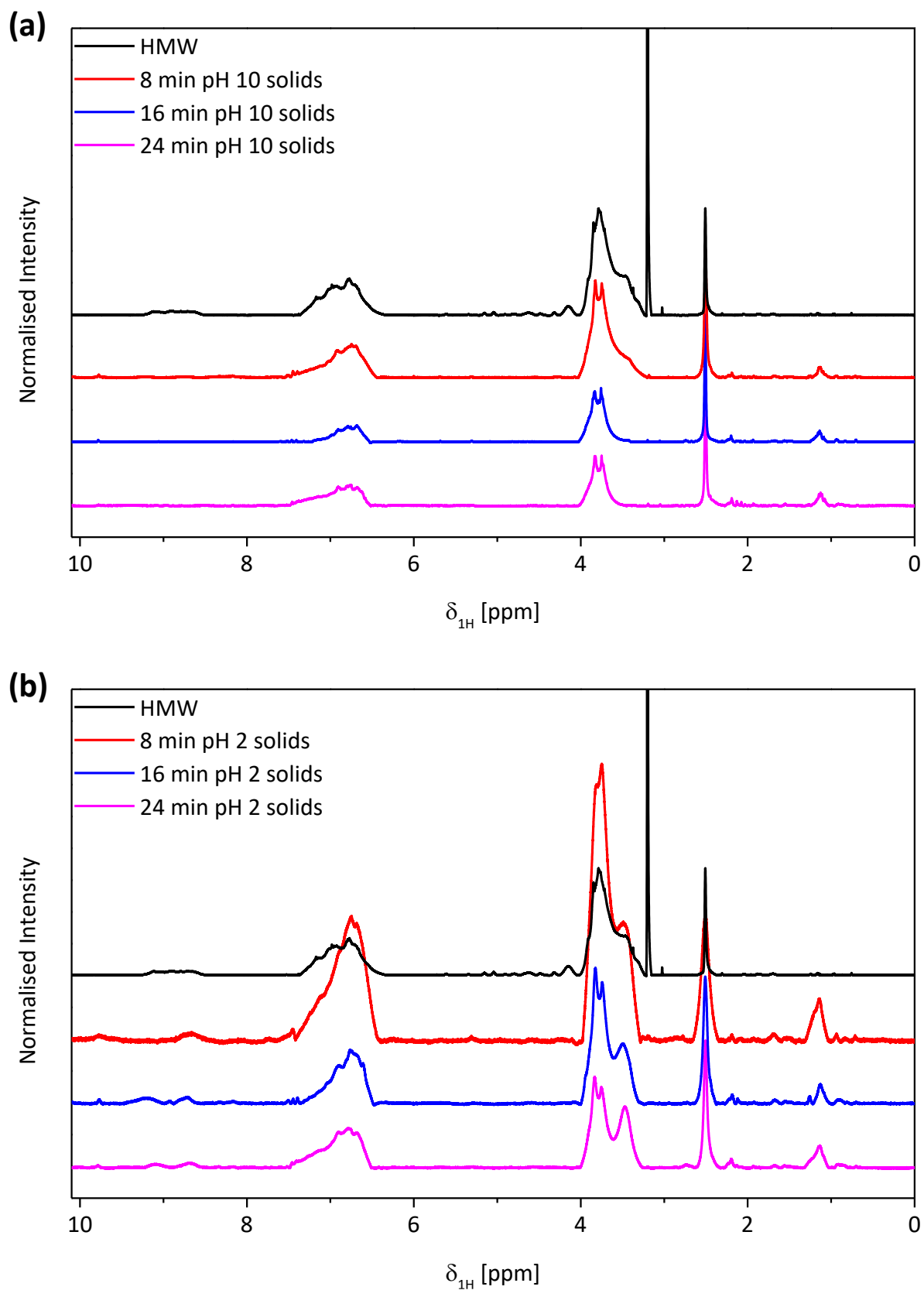


Figure 47: Liquid phase ¹H NMR spectra of the HMW fraction and the solids precipitated at treatment = 8, 16, and 24 min. (a) pH 10 solids and (b) pH 2 solids in DMSO-*d*₆.

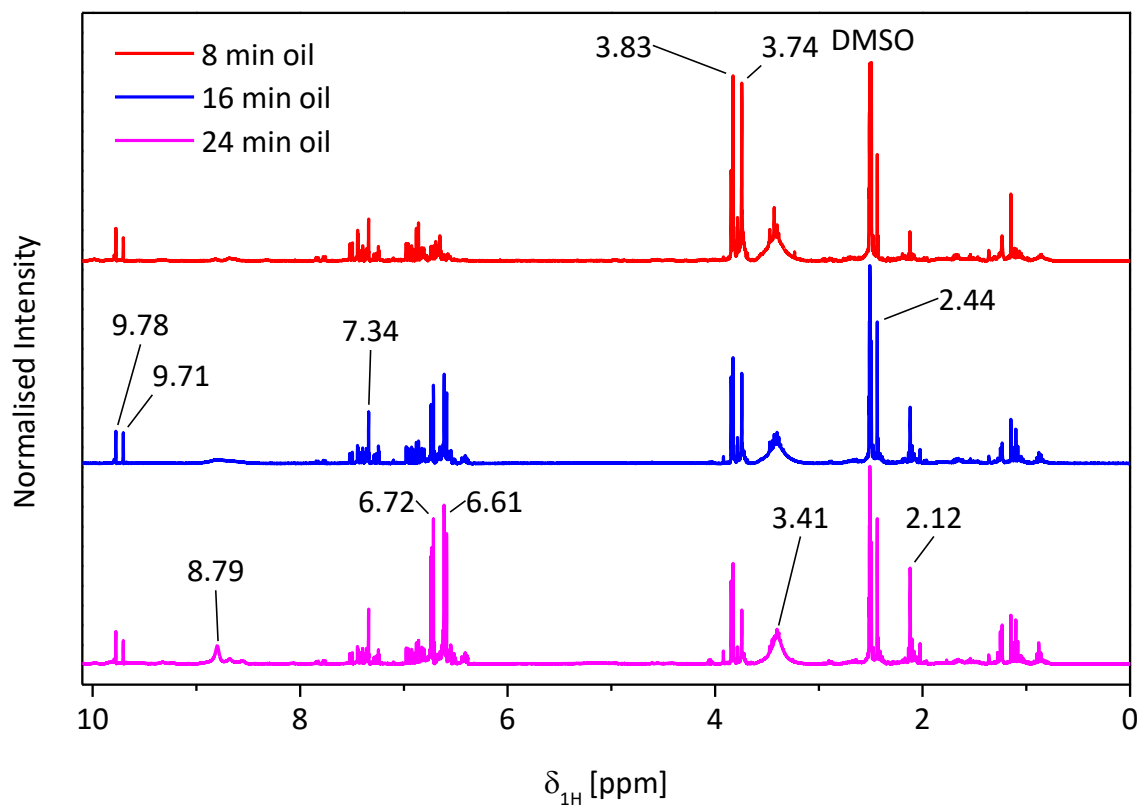


Figure 48: Liquid phase ¹H NMR spectra of the oil fractions recovered at tretention = 8, 16, and 24 min.

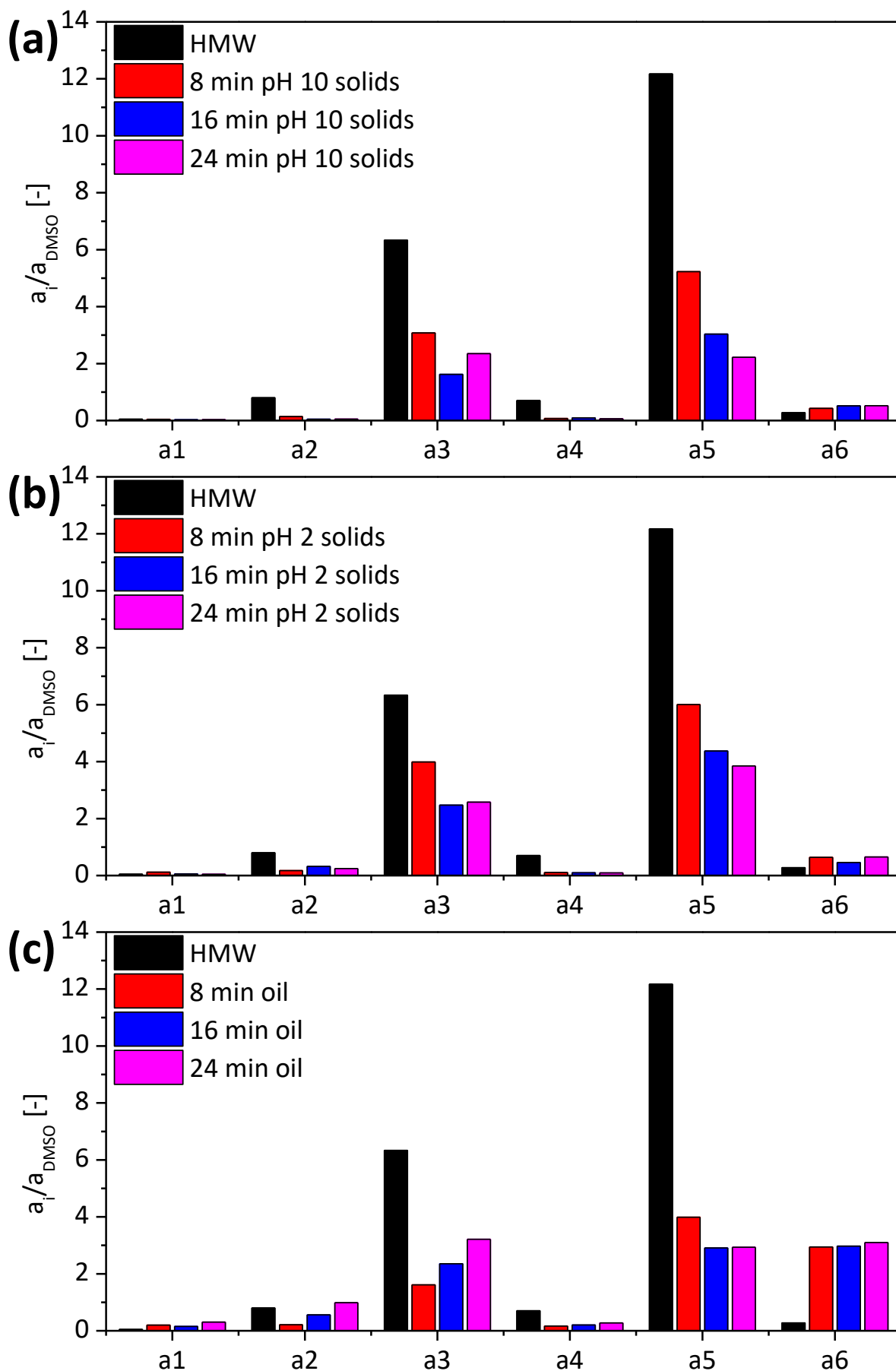
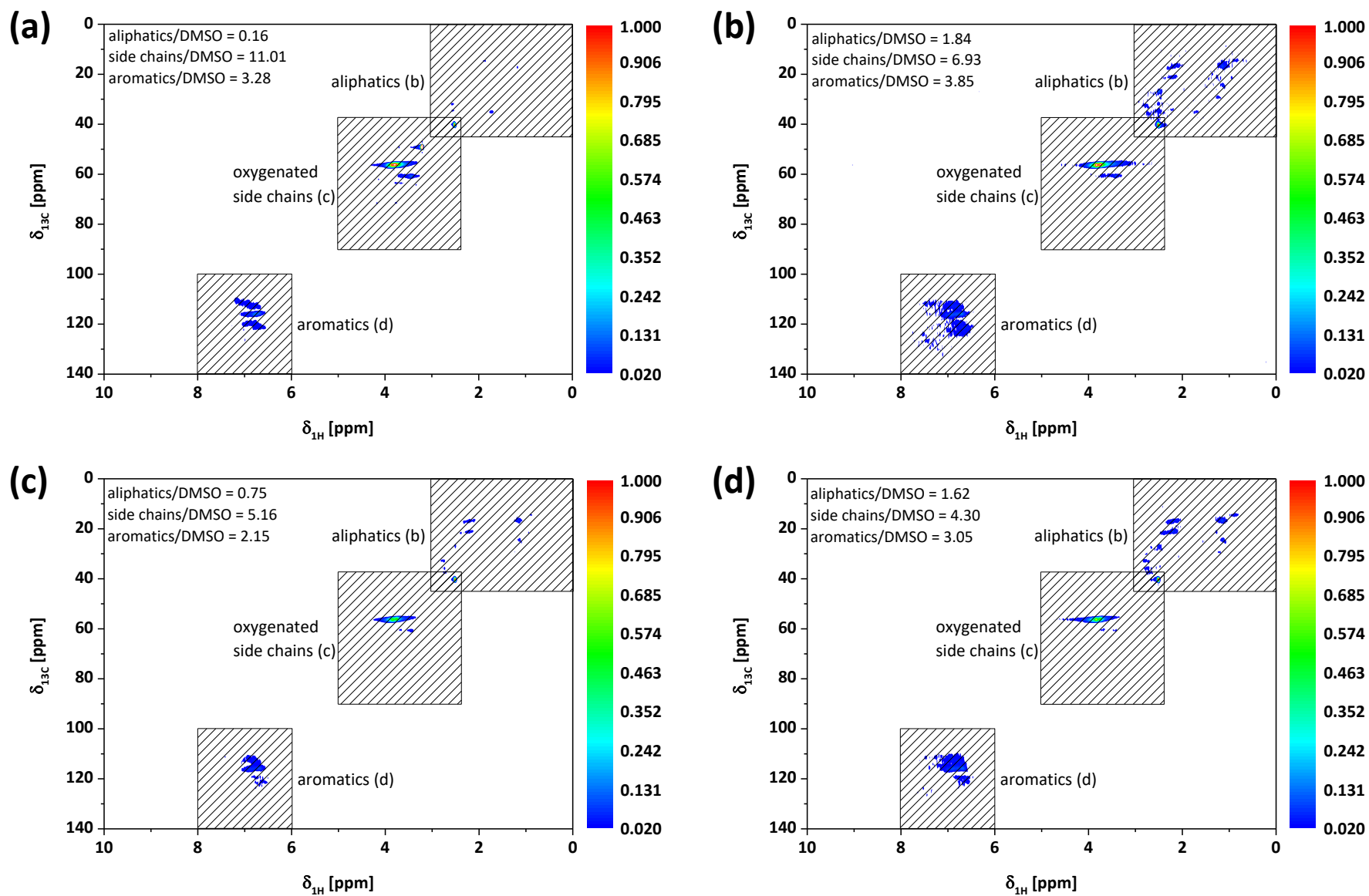
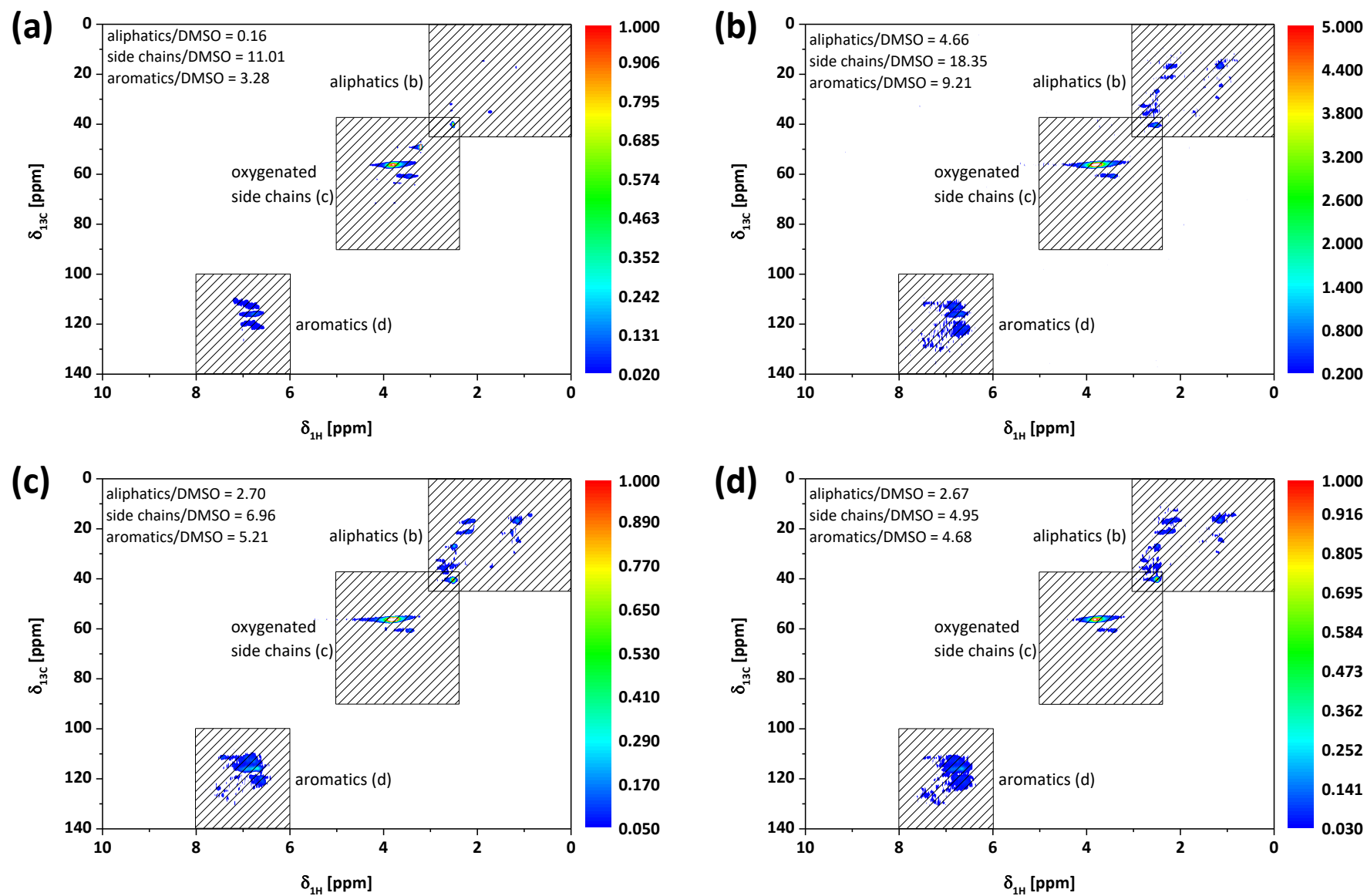


Figure 49: DMSO-normalised area integration of the ^1H NMR spectra for (a) pH 10 solids, (b) pH 2 solids, and (c) the oil fractions

Figure 50: 2D HSQC NMR spectra overview: (a) HMW fraction; pH 10 solids at $t_{\text{retention}} =$ (b) 8 min; (c) 16 min; (d) 24 min.

Figure 51: 2D HSQC NMR spectra overview: (a) HMW fraction; pH 2 solids at $t_{\text{retention}} =$ (b) 8 min; (c) 16 min; (d) 24 min

Area a1 ranging from $\delta_{1H} = 10.10$ to 9.35 ppm (Figure A 19(a)+(b)).

There is only one significant resonance in this area - at $\delta_{1H} = 9.78$ ppm. This peak is correlated to the COH of benzaldehyde units. It is non-existent in the feed and strongest at $t_{\text{retention}} = 8$ min, thereon decreasing with increasing $t_{\text{retention}}$. Figure 48 presents the spectra of the oil fractions, where a second peak at $\delta_{1H} = 9.71$ ppm is visible. The intensity of the two peaks is constant over $t_{\text{retention}}$. The peaks are also visible in the 2D HSQC shown in Figure 52(a). Here, the $\delta_{1H} = 9.78$ ppm is larger than the peak at $\delta_{1H} = 9.71$ ppm and increases towards longer $t_{\text{retention}}$ (Figure 52(b)).

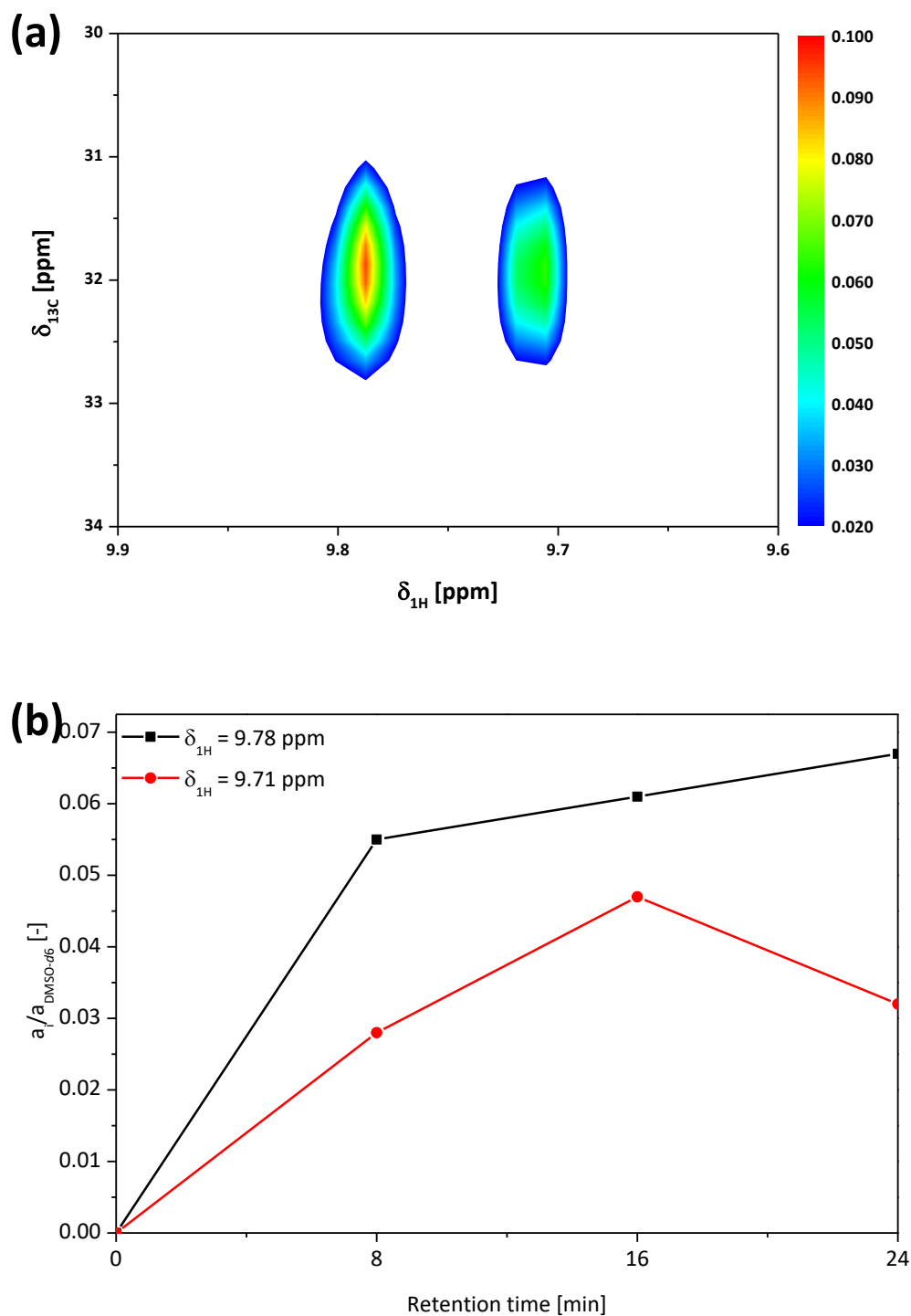


Figure 52: (a) 2D HSQC NMR spectrum of the oil fraction at $t_{\text{retention}} = 16$ min. Zoomed on the area for the benzaldehyde groups. (b) Relative area of the two peaks compared to the DMSO-*d*₆ peak as a function of $t_{\text{retention}}$.

Area a2 ranging from $\delta_{1H} = 9.35$ ppm to 8.00 ppm (Figure A 19(c)+(d))

The pH 10 solids show a clear decrease compared to the HMW fraction, while the pH 2 solids still show signals in this area. The oil fractions (Figure 48) of 8 and 16 min only show a broad small hill in this area, while the spectrum at $t_{\text{retention}} = 24$ min shows a distinct resonance at $\delta_{1H} = 8.79$ ppm.

Area a3 ranging from $\delta_{1H} = 8.00$ ppm to 6.00 ppm (Figure A 19(e)+(f))

Resonances corresponding to the aromatics area and show an increase at $\delta_{1H} = 7.4$ ppm which is most pronounced for the 8 min samples and is reduced again over $t_{\text{retention}}$. The 2D HSQC spectra in Figure A 24 and Figure A 25 show a more ambivalent situation. The areas defined as G₂, G₅, and G₆ are integrated and the results displayed in Figure 53(a)+(b). At $t_{\text{retention}} = 8$ min, a strong increase in the G₆ region accompanied with various peaks at higher δ_{1H} appear. The latter peaks correspond to C₂ and C₆ positions in benzaldehydes, as shown in the 2D HSQC spectra of the oil fractions in Figure A 29. The 2D HSQC of the oil fraction presents more distinct peaks for this area, where some could be identified as C₂-H₂ and C₆-H₆ in vanillin and acetovanillone, i.e. in benzaldehyde groups (Table A 14 - detailed compounds' limits). It seems that over the course of the reaction oligomeric benzaldehyde groups appear, which are removed after extended $t_{\text{retention}}$. This could be due to direct removal of the aldehydes, or by splitting off monomeric aldehydes. The formation of benzaldehydes under conditions employed in the Kraft process is described by Gierer and is supposed to take place *via* a retrograde aldol reaction.⁵⁹ From the 2D HSQC peaks a quantitative evaluation of the vanillin and acetovanillone concentration in the oil fraction was performed and compared to the GC-FID results. Figure 53(d) shows the data for vanillin and Figure 53(e) for acetovanillone. Both show a systematically stronger C₂-H₂ signal compared to the C₆-H₆ signal. The method used for deriving quantitative results out of the NMR data seems to overestimate the amount by a factor of *ca.* three. This can be explained by having a DMSO-*d*₆ not deuterated to 99.8% but to 99.93%.

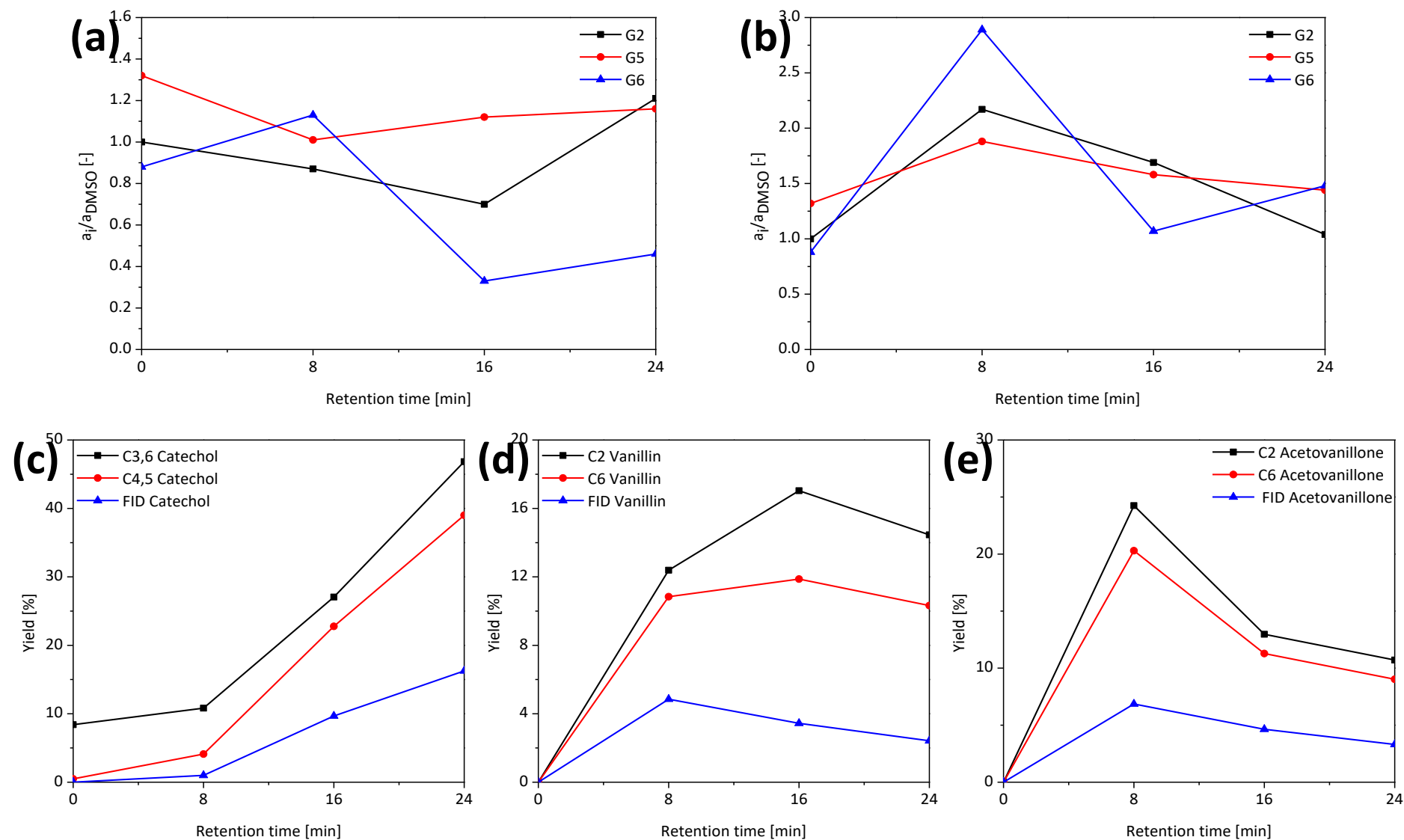


Figure 53: Trends of the G2, G5, and G6 C-H correlations as measured by 2D HSQC of the pH 10 solids (a) and pH 2 solids (b). (c), (d), and (e) show the yields of catechol, vanillin, and acetovanillone calculated *via* the 2D HSQC data compared to the values determined by GC FID.

Resonances at $\delta_{1H} = 7.2$ ppm correspond to the G_2 proton and are reduced in both the pH 10 and pH 2 solids. The 2D HSQC does not confirm these findings (Figure 53(a)+(b)). The G_2 and G_5 areas is relatively constant, while the G_6 position experiences a sharp drop in the pH 10 solids, while being constant in the pH 2 solids. The values at $t_{retention} = 8$ min of the pH 2 solids have to be used with caution, as all signals seem to be too large for an interpretation, additionally, it is important to keep in mind that these areas are named G_2 , G_5 , and G_6 but certainly not only contain the corresponding C-H correlations of guaiacyl units. From the data, it can be assumed that there are in total more unsubstituted G_5 and G_2 positions and that the G_6 position is more prone to alkylation or condensation. While the latter, i.e. the condensation, would be in contrast to the general process for the condensation reactions in phenyl formaldehyde, where the condensation takes place under basic conditions with formaldehyde as linking agent at the *ortho*-positions.¹²⁹

The δ_{1H} spectrum of the oil fractions i shows a strong increase over time, especially for the peaks at $\delta_{1H} = 6.72$ and 6.61 ppm (Figure 48). These two peaks directly correspond to the $C_{3,6}$ and $C_{4,5}$ positions in catechol (Figure A 29). They were used to calculate the amount of catechol in the oil fraction and the results were compared to the findings of the GC-FID. Figure 53(c) shows the results, which differ, as well as for vanillin and acetovanillone, at a factor of three. Again, the comparison is not absolutely equivalent. The GC-FID gives the calibrated yield of catechol, while the NMR shows the C-H correlations of the $C_{3,6}$ and $C_{4,5}$ positions. The latter include partially methylated catechol, especially 4-methylcatechol which has been detected *via* GC-FID in amounts of *ca.* 4 wt.% at $t_{retention} = 16$ and 24 min. This explains the systematically larger peaks of the $C_{3,6}$ correlation. This value is especially larger for the feed ($t_{retention} = 0$ min) and the 8 min samples, since other compounds contribute significantly to the signal.

Area a4 ranging from $\delta_{1H} = 6.00$ ppm to 4.05 ppm (Figure A 19(g)+(h))

This area corresponds to the side chains and inter unit linkages of the oligomeric fractions as well as links in residual sugars as xylenes. Figure A 19(g)+(h) show a complete removal of these features, which is confirmed by the 2D HSQC in Figure A 22 and Figure A 23.

Area a5 ranging from $\delta_{1H} = 4.05$ ppm to 3.20 ppm (Figure A 19(i)+(j))

Resonances from $\delta_{1H} = 3.9$ to 3.7 ppm mainly belong to the methoxy groups of the guaiacyl units. The broad peak of the HMW fraction is split into two resolved peaks at $\delta_{1H} = 3.81$ and 3.75 ppm. These are also visible as two separate peaks in the 2D HSQC in Figure A 22 and Figure A 23. Figure 54 gives an overview on the evolution of the methoxy groups and the signal assigned to the β -O-4 linkages and Table 39 gives the C_9 -formulae, methoxy groups content, C_9 -molecular weight, and β -O-4 per 100 C_9 units. Both groups, methoxy and β -O-4, are decreasing as a first order reaction regarding their own concentration (Figure 55). Assuming a simple first order reaction with $\frac{d}{dt} c_i = kt$, where c_i is the concentration of either the methoxy or the β -O-4 groups, a linear fit with intercept set to zero leads to the respective k-values presented in Figure 55, indicating a *ca.* three times faster removal of β -O-4 groups compared to the methoxy groups. While the reduction of methoxy groups is significant it is less strong than expected by the ^{13}C CP MAS NMR analysis (Figure 46), where a 90% reduction at $t_{retention} = 16$ min is indicated. This was also already true for the aromatics region between $\delta_{13C} = 150$ and 100 ppm. The peak at $\delta_{13C} = 148$ ppm corresponds to the G_3 position where the MeO group is attached and is thus not visible in HSQC.

But the $\delta_{13C} = 124$ to 116 ppm peaks lie in the G_2 , G_5 , and G_6 region and are at least partially visible in HSQC. One possibility could be that the amount of these C-H correlations is reduced to a lesser extent than other aromatic C-bonds. These C-H linkages are not making up the majority of the signals in 13C NMR, and their reduction therefore contributes only to a small amount to the observed decrease in the 13C spectrum. In the 1H NMR for the HMW fraction there is a slight shoulder at $\delta_{1H} = 3.45$ ppm (Figure A 19(i)+(j)). This is only marginally visible for the 8 min pH 10 solids and completely disappears after 16 min. In the pH 2 solids the peak at $\delta_{1H} = 3.45$ ppm experiences an increase. In the 2D HSQC no peak at this position appears, except for β -O-4 linkages, and these decrease over time (Figure 54). Interestingly there is a clear pair of peaks at this region for the oil phases. These are visible in the 1H NMR in Figure 48 for all three $t_{retention}$ and decrease over time. The 2D HSQC of the oil phases show Ar-CH₂-Ar linkages corresponding to this δ_{1H} shift (Figure 35). These are two distinct peaks at $\delta_{1H}/\delta_{13C} = 3.46/35.9$ ppm, which belongs to *ortho-para*, while the one at $\delta_{1H}/\delta_{13C} = 3.43/40.8$ ppm belongs to *para-para* connections.¹³⁰ If these linkages were the reason for the peak in the pH 2 solids, their 2D HSQC spectrum should have shown peaks for the corresponding areas.

Table 39: C₉-formula and β -O-4 content of the #K reactions after 8, 16, and 24 min.

Fraction		C ₉ -formula	MeO [wt.%]	M _{C9} [g/mol]	β -O-4 per 100 C ₉
HMW		C ₉ H _{9.60} O _{3.24} S _{0.11} (OCH ₃) _{0.21}	3.70	179.65	2.44
8 min	pH 10	C ₉ H _{8.71} O _{3.92} S _{0.03} (OCH ₃) _{0.13}	2.24	184.76	0.98
	pH 2	C ₉ H _{7.49} O _{2.86} S _{0.03} (OCH ₃) _{0.33}	5.75	172.51	2.93
16 min	pH 10	C ₉ H _{7.77} O _{2.10} S _{0.02} (OCH ₃) _{0.09}	1.83	152.90	0.35
	pH 2	C ₉ H _{8.11} O _{3.18} S _{0.02} (OCH ₃) _{0.12}	2.21	170.10	1.03
24 min	pH 10	C ₉ H _{7.74} O _{2.27} S _{0.04} (OCH ₃) _{0.07}	1.46	155.79	0.15
	pH 2	C ₉ H _{7.62} O _{2.23} S _{0.02} (OCH ₃) _{0.08}	1.64	154.63	0.70

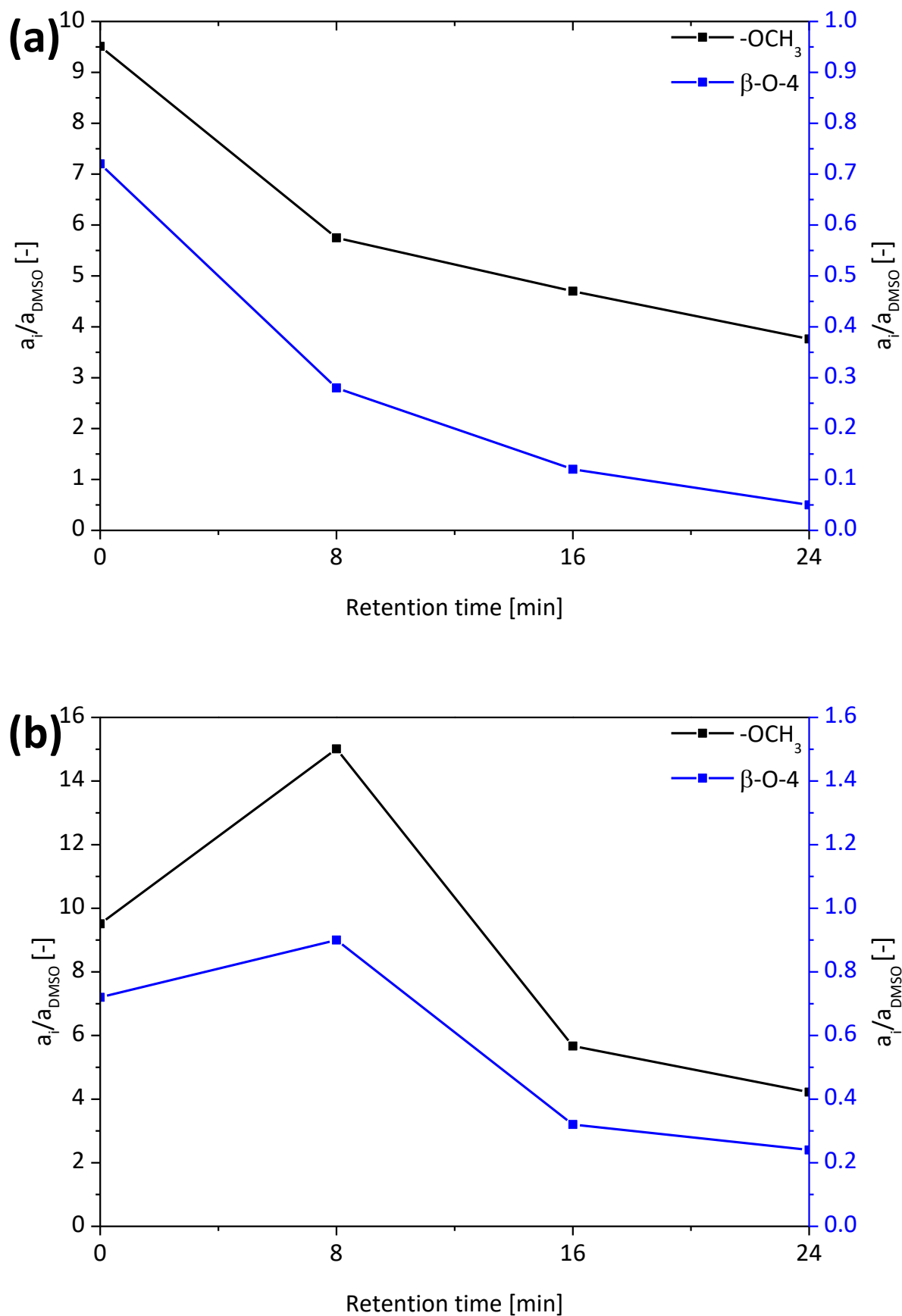


Figure 54: Relative areas of the 2D HSQC NMR spectroscopy analysis of the methoxy groups (-OCH₃) and the area assigned to the β -O-4 linkages. (a) pH 10 solids, (b) pH 2 solids. The values of the 8 min samples for the pH 2 solids are, as discussed in the text, unusually high.

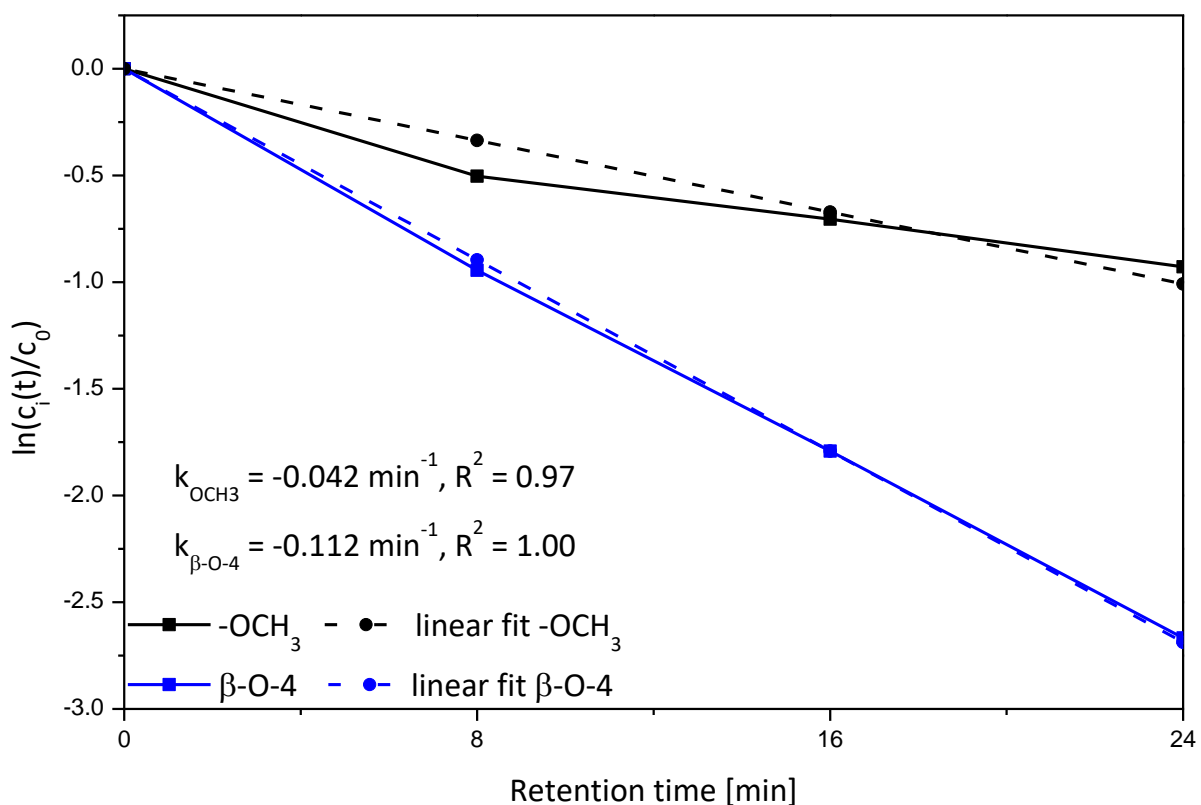


Figure 55: $\ln(c_i(t)/c_0)$ over $t_{\text{retention}}$ of the concentrations of the side chain groups of the pH 10 solids determined by 2D HSQC. The values for k are given in the figure along with the R^2 of the linear fit.

Area a6 ranging from $\delta_{1H} = 3.20$ ppm to 0 ppm (Figure A 19(k)+(l))

The resonance at $\delta_{1H} = 2.5$ ppm is the DMSO-*d*₆ peak and is used as level for normalisation. All other peaks down-field from this point are corresponding to the aliphatics of alkylated aromatics. It can be seen that there is a strong increase in the areas of $\delta_{1H} = 2.25$ to 2.00 ppm and 1.25 to 1.00 ppm. The former is mainly due to $-\text{CH}_2-$ and $-\text{CH}_3$ groups in α -position to aromatic rings, while the latter stems from β - and γ -position. The 2D HSQC (Figure A 20 and Figure A 21) undermines these findings. It is interesting that from both figures in Figure 56 it can be seen that alkylation after 8 min is stronger than after 16 min, while it afterwards increases again.

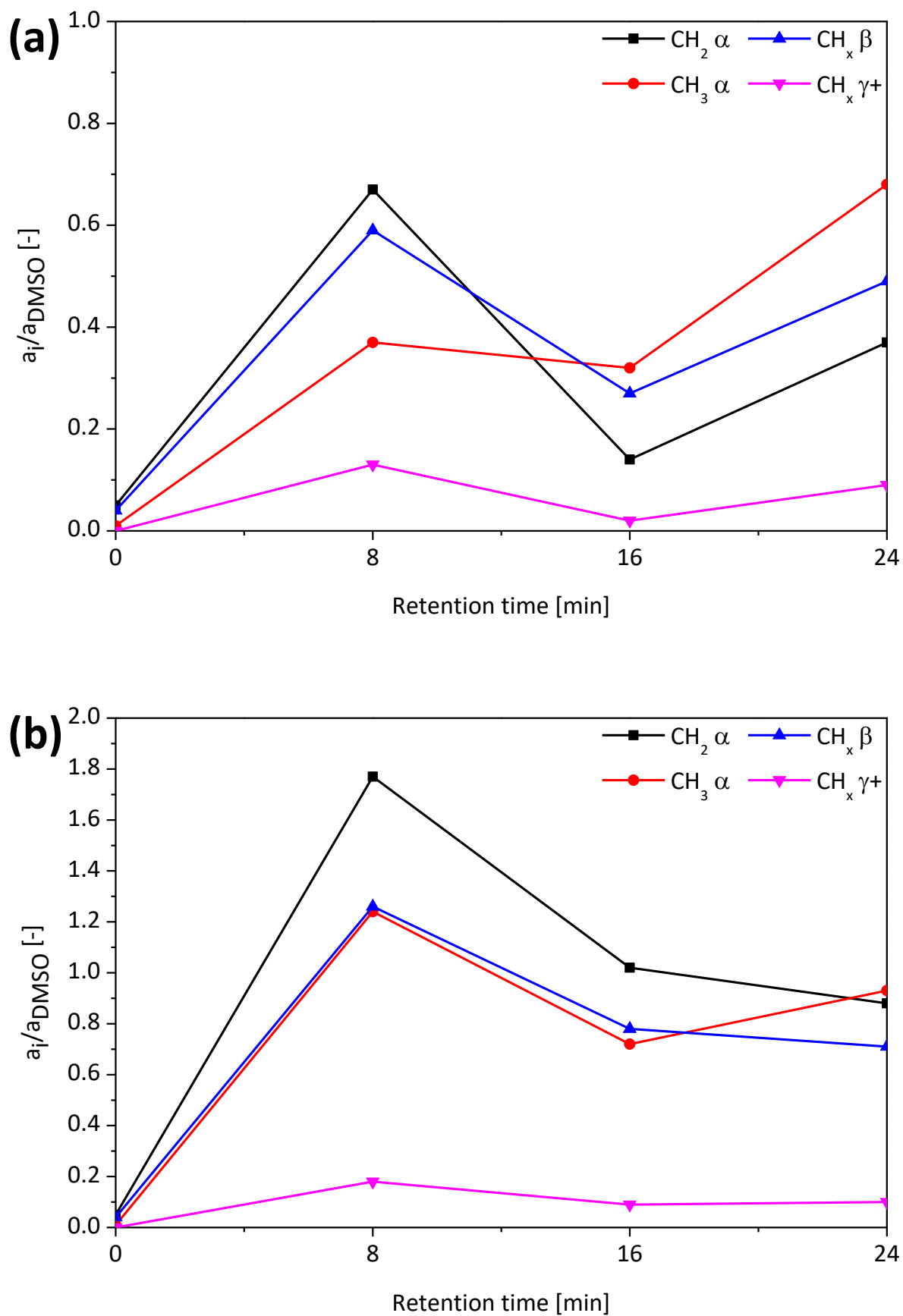


Figure 56: Evolution of the aliphatics region of the 2D HSQC NMR spectroscopy analysis of (a) pH 10 solids, (b) pH 2 solids.

The alkylation can also be observed for monomeric compounds, with the increase in 4-methylcatechol over time as the most prominent example. Gaylord Chemical produced DMS from 1961 to 2010 by using KL as methylating agent for sulphur in a high pH solution.¹⁶⁸ Nguyen *et al.* used KL from the LignoBoost® process at the Bäckhammar demonstration plant in a continuous reactor with K₂CO₃ as base over a ZrO₂ fixed bed reactor at near critical conditions.¹⁶⁹ They added phenol in roughly the same amount as lignin as co-solvent and char suppressing agent and found many alkylated phenols in the product oil. Alkylation of aromatic rings seems to be a dominant process during hydrothermal treatment of lignin under basic conditions. This also seems to increase the solubility of the oligomeric fractions in, e.g., MeOH. The solubility of some of the pH 10 and pH 2 solids in concentrations of 100 mg/mL was tested in MeOH and the samples were soluble between 75 and 90 wt.%. A lack of samples prevented a systematic analysis of this effect, but since the feed was the HMW fraction, i.e. the MeOH insoluble fraction, a significant increase in solubility can be seen. Probably most research groups in Table 25 experience an increase in solubility due to this effect, while they do not explicitly analyse solubility before and after.

Attenuated Total Reflection Fourier Transform Infrared (ATR FT-IR)

The ATR FT-IR of the solid fractions in Figure 57(a)+(b) do not show significant differences between the different $t_{\text{retention}}$. Differences are the same as for the #B runs and have been discussed in the corresponding chapter. Figure A 30 compares the pH 10 and pH 2 fractions of run #B3 and #K3, both with $t_{\text{retention}} = 16$ min. The only difference appears in the carbonyl area at *ca.* 1715 cm⁻¹, where the pH 10 solids of #B3 have a higher absorption compared to the pH 10 solids of #K3, while it is vice versa for the pH 2 solids. This hints at the compounds containing these carbonyl groups having a pK_s value close to 10.

The strong differences, that has been experienced for the pH 2 fraction at $t_{\text{retention}} = 8$ min during the NMR analyses were not visible in the FT-IR spectra. Quantitative prediction is, as already stated in the discussion of the #B runs, difficult *via* FT-IR. On the other hand, the spectra of the oil fractions do display the evolution of catechol quantitatively at 750 cm⁻¹. This peak represents *ortho*-substituted phenols and should therefore represent unsubstituted catechol and guaiacol. The spectra of the solids and the oil fractions have more in common than the spectra of the solids compared to the HMW fraction. The general chemical changes performed to the lignin seem to appear in all molecular weight fractions and separation by pH only marginally changes relative chemical composition. Nevertheless, the oil fraction has some characteristic differences as can be seen in Figure 57(d). The carbonyl peak at 1715 cm⁻¹ is more pronounced, which is in line with the results of the NMR analyses. The areas at 1489, 1460, and 1333 cm⁻¹ show less absorption and the dent at 1082 cm⁻¹ in the solids is non-existent in the oil, while here a dent at 1124 cm⁻¹ is visible. The peak at 750 cm⁻¹ indicates the *ortho*-substituted phenols and appears only in the oil fraction.

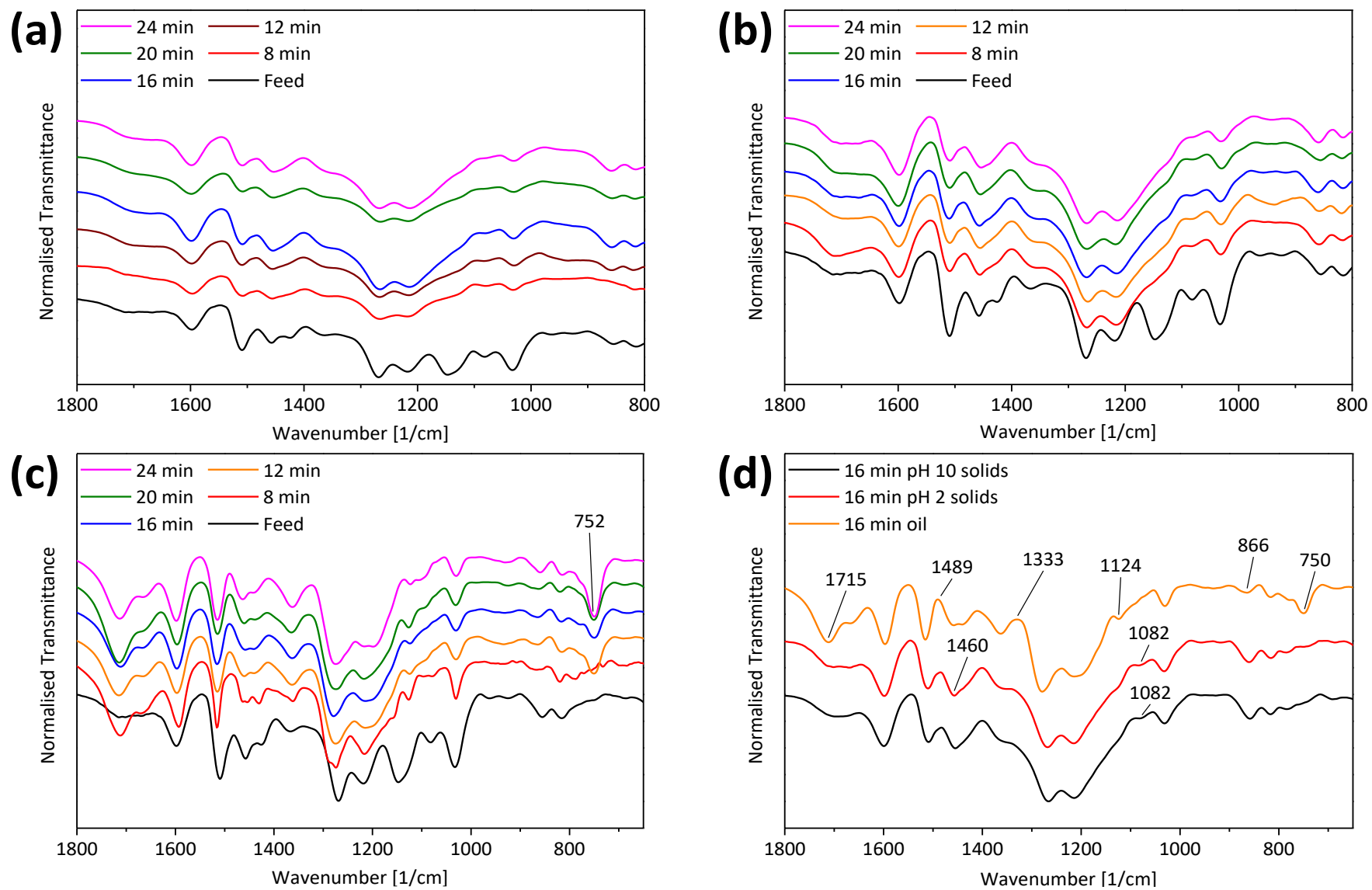


Figure 57: ATR FT-IR spectra of the #K reactions. (a) pH 10 solids; (b) pH 2 solids; (c) oil; (d) pH 10 solids, pH 2 solids, and oil of run #K3 at retention = 16 min.

Summary & Conclusions

Additionally, to the findings of the #B3 runs, where a higher thermal stability, a lower molecular weight, and a strong reduction in methoxy groups were the main findings for the solid precipitates, 2D HSQC, ^1H NMR, and DSC analyses show a more detailed picture. Molecular weight distribution and thermal stability seem not to change in a significant way as a function of $t_{\text{retention}}$, while changes on the molecular level do occur over time. Mass balance shows a loss of *ca.* 20-25 wt.% for all but at $t_{\text{retention}} = 8$ min, where the loss accumulates to 10 wt.%. Average C_9 -Unit mass is reduced from 180 to *ca.* 155 g/mol after 24 min at 300 °C. Elemental composition shows an increase in carbon content and reduction in H, O, and S, while from the original sulphur 2/3 are removed. C, H, O, S mass balancing over the fractions lead to the conclusion that the 20% lost compounds have a molecular formula in the range of $\text{CH}_2\text{O}_{0.7-1}\text{S}_{0.05}$, resembling that of C_{1-4} organic acids and alcohols partially with thiol groups. These products probably originate from ring cleavage and leaving groups of the base catalysed reactions. TGA shows a slight increase in residual solids over $t_{\text{retention}}$ at 600 and 900 °C. The DSC traces for the precipitated solids are devoid of a clear glass transition up to 200 °C. Also, a mixture consisting of the pH 2 solids at $t_{\text{retention}} = 16$ min and the LMW fraction (1:1, w:w) does not show a glass transition. ^1H and 2D HSQC NMR also show a significant increase in side chains after reaction. The ^1H NMR also indicates a significant decrease for the phenolic region from $\delta_{1\text{H}} = 9.35$ to 8.00 ppm and the aromatics region from $\delta_{1\text{H}} = 8.00$ to 6.00 ppm, which is in line with the results of the ^{13}C CP MAS NMR. 2D HSQC does not confirm this, giving comparable results for the C-H correlations of the HMW fraction and the precipitated solids at the G_2 , G_5 , and G_6 positions. This could either mean that the total amount of aromatic C-H correlations does not change significantly, or that quantification of these structures is not valid by the means employed. 2D HSQC NMR allows for quantitative description of the removal of the methoxy groups and $\beta\text{-O-4}$ linkages. Both decrease in a (pseudo) first order reaction with regard to concentration and the rate constant of the demethoxylation is *ca.* three times lower than that for the $\beta\text{-O-4}$ cleavage. Results of the ATR FT-IR are comparable to those of the #B runs and confirm in general the NMR spectra.

The oil fraction consists mainly of catechol and its alkylated derivatives, and guaiacyl units e.g. vanillin, acetovanillone, and homovanillic acid. The oil yield does not increase any further after 12 min and is at maximum *ca.* 5 wt.%. Catechol and derivatives are the main constituents after 12+ min and the concentration of catechol is directly proportional to $t_{\text{retention}}$. It seems a rather stable molecule under the applied conditions, meaning that hydroxy groups are less prone to removal compared the methoxy groups. The amount of catechol can also be monitored *via* FT-IR at a wavenumber of 752 cm^{-1} .

The results lead to the conclusion, that an increase in $t_{\text{retention}}$ does influence the precipitated solids, as an increased demethoxylation and cleavage of ether linkages can be observed, while thermal properties and molecular weight distributions are less affected. Over the different $t_{\text{retention}}$ investigated in this study, no hints at extensive condensation or polymerisation reactions could be observed. The lack of a glass transition means, that a plasticiser has to be found if the solids are to be used for melt spinning.

4.3 Techno-Economic Evaluation of a Continuous Base Catalysed Depolymerisation of Lignin in a Kraft Mill

In this section, a preliminary techno-economic evaluation of the BCD process described in previous chapters is provided in the context of its potential implementation in a Kraft mill. Based on the gathered process data, a price for the product can be obtained with an assumed ROI before taxes of 15%. The BCD process uses chemicals, equipment, and conditions that should be either present in a Kraft pulp mill or can be easily acquired and installed with existent know-how. The KL utilised in this study was that provided by a Domtar pulp mill (Plymouth, North Carolina, USA) as precipitated *via* the LignoBoost® process (as installed at the mill in 2015). It is assumed that the LignoBoost® plant can provide a 75 t/d feed, containing *ca.* 26 wt.% of H₂O. Table 40 provides the general make-up data for the simulation and assumptions concerning prices for commodities and energy.

Table 40: General data for the simulation of the process

Assignment		Definition/Symbol	Value
Feed mass flow		\dot{m}_{feed}	75 t/d
Lignin H ₂ O content		$\frac{\dot{m}_{\text{H}_2\text{O}}}{\dot{m}_{\text{lignin}} + \dot{m}_{\text{H}_2\text{O}}} / \omega_{\text{H}_2\text{O},1}$	0.26
Lignin H ₂ O content after drying		$\frac{\dot{m}_{\text{H}_2\text{O}}}{\dot{m}_{\text{lignin}} + \dot{m}_{\text{H}_2\text{O}}} / \omega_{\text{H}_2\text{O},2}$	0.05
Lignin lower heating value		LHV _{lignin}	15 MJ/kg
MeOH per lignin for extraction		$\frac{\dot{m}_{\text{lignin}}}{\dot{V}_{\text{MeOH}}}$	250 kg/m ³
Ratio of fractions after extraction		$\frac{\dot{m}_{\text{HMW}}}{\dot{m}_{\text{LMW}}}$	7/3 = 2.33
τ _{retention}	MeOH extraction	τ _{MeOH}	15 min
	CO ₂ precipitation	τ _{CO2}	30 min
	H ₂ SO ₄ washer	τ _{H2SO4}	5 min
Loss of MeOH		$\frac{\dot{m}_{\text{MeOH,out}}}{\dot{m}_{\text{MeOH,circuit}}}$	0.01
Compounds the HMW fraction is reacted into		$\dot{m}_{\text{product}} + \dot{m}_{\text{H}_2\text{O solubles}}$	
Mass of CO ₂ needed to precipitate 1 kg of product		$\frac{\dot{m}_{\text{CO}_2}}{\dot{m}_{\text{product}}}$	0.5
Amount of lignin precipitated with CO ₂ after reaction		$\frac{\dot{m}_{\text{product}}}{\dot{m}_{\text{product}} + \dot{m}_{\text{H}_2\text{O solubles}}}$	0.8
Prices	Feed / Lignin	p _{feed}	400 €/t
	MeOH	p _{MeOH}	250 €/t ¹⁷⁰
	CO ₂	p _{CO2}	90 €/t ²⁸
	NaOH	p _{NaOH}	320 €/t ¹⁷¹
	H ₂ SO ₄ (96%)	p _{H2SO4}	200 €/t ¹⁷²
	Heat	p _{heat}	0.01 €/kWh ^a
	Electricity	p _{elec}	0.04 €/kWh ¹⁷³
	H ₂ O	p _{H2O}	0.35 €/t ^b

^a LHV natural gas 10.5 kWh/m³, price natural gas 2.50 USD/MJ¹⁷⁴, efficiency steam production 0.8;

^b estimation from industry partners

4.3 Techno-Economic Evaluation of a Continuous Base Catalysed Depolymerisation of Lignin in a Kraft Mill

The process is in detail shown in Figure 58 and the corresponding mass and heat flows in Table A 15 and Table A 16, respectively.

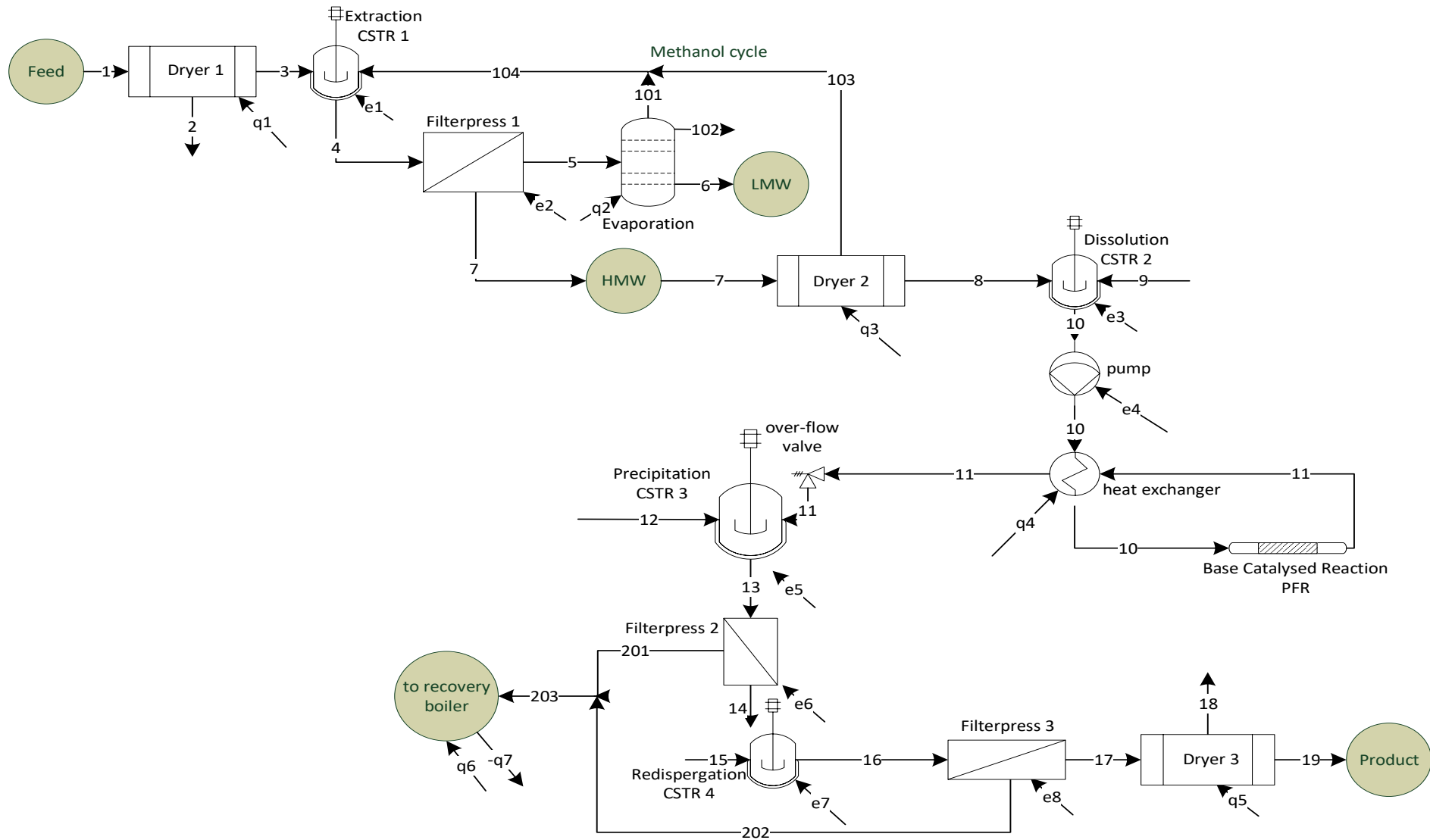


Figure 58: Process flow sheet with mass and energy flows.

In a first step, the lignin is dried to 5 wt.% residual H₂O and then extracted *via* MeOH in a continuous stirred tank reactor (CSTR 1). The dispersion is filtered and the retentate dried to remove and recover the MeOH (Dryer 2). From the permeate, the MeOH is removed and fed back into the process. Stream 102 gives *ca.* 100 kg/h of H₂O that would accumulate in the MeOH. It has to be seen which amount of H₂O in the MeOH is acceptable and to what level a removal is technically and economically feasible. Since the feed already contains H₂O, the MeOH does not have to be completely H₂O free. The LMW fraction (MeOH soluble) is determined as secondary product and contains 5 wt.% residual H₂O. After drying the HMW fraction is dispersed and dissolved at 10 wt.% in a 1 M NaOH solution. This results in roughly 16 m³/h, which will be brought *via* a piston membrane pump to 180 bar and pumped through a plug flow reactor (PFR) with $t_{\text{retention}} = 10$ min. T is set at 325 °C, and two serial tube bundle heat exchangers with DN250 tubes and a length of 5800 mm each are used for the heat transfer. The PFR is a simple bundle heat exchanger kept at reaction T. The hot liquid at the exhaust is used to heat the feed and an efficiency of 90% is assumed. The pressure in the PFR is kept at 180 bar with an overflow valve. The product is precipitated with CO₂ in CSTR 3, filtered and re-dispersed in CSTR 4, where it is washed with a pH 2.5 H₂SO₄ solution composed to have 10 wt.% solids. After washing, a last filtration and drying step are included. The precipitation and washing procedure is comparable to the LignoBoost® process and enables the usage of similar equipment and already present know-how. The permeate of the washing solution and low pH H₂O is fed to the recovery cycle of the pulp mill and contains 324 kg/h of H₂O solubles originating from the lignin. Additionally, 588 kg/h of NaOH and 323 kg/h of CO₂ will be fed into the recovery process. These will be dissolved as Na⁺ and HCO₃⁻-Ions. A recovery rate for the NaOH of 95% is assumed,¹¹ while the CO₂ and H₂SO₄ are considered to be not recoverable. Additionally, 1% of the MeOH is considered to be lost. Stream 203, which leads into the recovery boiler, contains *ca.* 25 m³/h of H₂O. The process will be charged the necessary heat of evaporation for this amount of H₂O with an efficiency of 90%, while the LHV of the H₂O solubles will be accounted for.

Table 41: Net chemicals usage in the base catalysed process implemented into a Kraft mill.

Usage	NaOH	CH ₃ OH	CO ₂	H ₂ SO ₄
[kg/h]	31.1	73.2	324.1	1.8
[kg/t _{product}]	24.0	56.5	250.0	1.4

From these data, prices for the equipment of the unit operations were acquired from different companies and are presented (Table 42). In order to generate a first estimation of the costs based on this data, a factor of 4.5 for the inside battery limits (ISBL) costs is used, which results in costs of 18.54 M€, or *ca.* 20 M€. For the investment, a construction time of two years and capital costs of 10% are assumed. The capital stems 50% from equity with 15% ROI and 50% from debt with an assumed interest rate of 5%. In the first year 40% of the capital is used, in the second 60%. Depreciation is set linear over ten years and 100% plant utilisation is established at 8,000 h/a. Further fix costs are personnel, taxes and insurance with 1.5%, overhead with 1.5%, and repairs and maintenance with 3% of the fixed capital costs (Table A 17). Additionally, generalia (G+A) and R&D with 3% and 2% of the product price, respectively, are accounted for.

4.3 Techno-Economic Evaluation of a Continuous Base Catalysed Depolymerisation of Lignin in a Kraft Mill

Table 42: Prices for the main components of the different unit operations described in the flow sheet in Figure 58.

Equipment	Material/Comments	Price [€]
Dryer 1 ¹⁷⁵	Belt dryer Entry air: $m_{H_2O}/m_{air} = 0.5\%$ temperature: 80	400,000
CSTR 1 ¹⁷⁶	X6CrNiMoTi17-12-2 (1.4571, 316Ti) 2.3 m ³ / 15 min retention	15,000
Filter press 1 ¹⁷⁷	FP 1200 (4.1 m ³)	350,000
Dryer 2 ¹⁷⁵	Belt dryer with ex protection Entry air: $m_{H_2O}/m_{air} = 0.5\%$ temperature: 80	1,500,000
CSTR 2 ¹⁷⁶	X6CrNiMoTi17-12-2 (1.4571, 316Ti) 4.0 m ³ / 15 min retention	15,000
Membrane Pump ¹⁷⁸	Typ: TKM900R "Bauform 3" single acting piston	200,000
Heat exchanger ¹⁷⁹	Tube: Pure nickel Shell: X6CrNiMoTi17-12-2	300,000
PFR ¹⁷⁹	Tube: Pure nickel Shell: X6CrNiMoTi17-12-2 2x DN250 L: 5800 mm	250,000
CSTR 3 ¹⁷⁶	X6CrNiMoTi17-12-2 (1.4571, 316Ti) 8.0 m ³ / 30 min retention	25,000
Filter press 2 ¹⁷⁷	FP 1200 (4.1 m ³)	350,000
CSTR 4 ¹⁷⁶	X6CrNiMoTi17-12-2 (1.4571, 316Ti) 1.1 m ³ / 5 min retention	15,000
Filter press 3 ¹⁷⁷	FP 1200 (4.1 m ³)	350,000
Dryer 3 ¹⁷⁵	Belt dryer Entry air: $m_{H_2O}/m_{air} = 0.5\%$ temperature: 80	350,000
Sum		4,120,000

Table 43 shows variable and fix costs per tonne of product. The relative fix costs apply for a utilisation of 8,000 h/a. The greatest impact on the cost is the feed, followed by depreciation and heat. The price for the feed of 400 €/t was provided by Domtar and was their price for 1 tonne of lignin in 2014. Since there is no real market for softwood KL from LignoBoost® plants, it is difficult to define a price. Energy optimisation regarding heat integration is also an important factor regarding potential cost reductions. Possibilities have to be elucidated for each installation site. Depreciation is company specific and has to be regarded in each specific frame.

4.3 Techno-Economic Evaluation of a Continuous Base Catalysed Depolymerisation of Lignin in a Kraft Mill

Table 43: Yearly absolute and relative variable and fix costs per tonne of product without by-product credits at an average utilisation of 8,000 h/a.

Variable costs			Fix-costs		
Type	[€/t _{product}]	[%]	Type	[€/t _{product}]	[%]
Feed	964	62	Personnel	54	3
CO ₂	45	3	Depreciation	179	12
NaOH	15	1	Taxes, insurance, overhead	54	3
H ₂ SO ₄	<1	<1	Maintenance	54	3
H ₂ O	7	<1			
CH ₃ OH	14	1			
Heat	159	10			
Electricity	4	<1			
Sum	1209	78		341	22

Four scenarios have been defined, where the by-product credits of the LMW fraction are varied. Scenario 1 is assumed to be the most probable one at the beginning, since no market for the LMW fraction must be established.

1. Sold for 400 €/t, which is the price of the feed.
2. Has zero value.
3. Sold for 800 €/t, which is assumed as price for a substituent in phenyl formaldehyde.
4. Sold for the same price as the main product, when serving as a plasticiser.

Table 44 gives a detailed listing of the product values for all four scenarios. When assuming by-product credits for the LMW fraction in the amount of the purchasing price, the product must be priced at 1,628 €/t for achieving an ROI of 15%.

4.3 Techno-Economic Evaluation of a Continuous Base Catalysed Depolymerisation of Lignin in a Kraft Mill

Table 44: Product value and cost overview in correlation with by-product value (see scenarios 1 to 4).

	Capacity 10,370 t/a			
	Scenario 1	Scenario 2	Scenario 3	Scenario 4
Invest [€]	18,540,000	18,540,000	18,540,000	18,540,000
Battery limits	18,540,000	18,540,000	18,540,000	18,540,000
Off-sites	0	0	0	0
Production costs [€/t]				
Raw materials	964	964	964	964
By-product credits	-214	0.00	-429	-612
Utilities	244	244	244	244
Variable costs	994	1,209	780	597
Operating labour	54	54	54	54
Maintenance (3%/a of invest)	54	54	54	54
Total direct costs	1,102	1,316	887	704
Taxes & insurances, overhead (3%/a of invest)	54	54	54	54
Plant cash costs	1,155	1,369	941	757
Depreciation (10%/a of invest)	179	179	179	179
Plant gate costs	1,334	1,548	1,120	936
G+A, sales, research (5% of product value)	81	94	68	57
Production costs	1,415	1,643	1,188	993
15% ROI before taxes	268	268	268	268
Product value	1,628	1,889	1,366	1,142

Table 45 gives the necessary product prices for scenario 1 when different plant utilisations are used and the ROI is fixed at 15%. At utilisations of 50% and 75% the price has to be raised to 1,744 €/t and 1,976 €/t, respectively.

4.3 Techno-Economic Evaluation of a Continuous Base Catalysed Depolymerisation of Lignin in a Kraft Mill

Table 45: Product value and cost overview for a by-product value of 400 €/t in correlation with plant utilisation.

	Capacity 10,370 t/a		
Plant utilisation [%]	100	75	50
Invest [M€]	18,540,000	18,540,000	18,540,000
Battery limits	18,540,000	18,540,000	18,540,000
Off-sites	0	0	0
<u>Production costs [€/t]</u>			
Raw materials	964	964	964
By-product credits	-214	-214	-214
Utilities	244	244	244
Variable costs	994	994	994
Operating labour	54	71	107
Maintenance (3%/a of invest) ^a	54	54	54
Total direct costs	1,102	1,119	1,155
Taxes & insurances, overhead (3%/a of invest)	54	721	107
Plant cash costs	1,155	1,191	1,262
Depreciation (10%/a of invest)	179	238	358
Plant gate costs	1,334	1,429	1,620
G+A, sales, research (5% of product value)	81	87	99
Production costs	1,415	1,516	1,719
15% ROI before taxes	268	268	268
Product value	1,628	1,744	1,976

^a scales with utilisation

$$NPV = -I + \sum_{t=0}^t \frac{cash\ flow_t}{(1+i)^t} + L(1+i)^{-t} \quad (4-1)$$

Equation (4-1) defines the net present value (NPV) of an investment. I is the investment at time zero, t is the respective period, $cash\ flow$ is defined as $(revenue - costs)$ in t , i is the interest on capital, and L the remaining value of the investment at time t . The remaining value is assumed to be zero in the calculations. With the defined interest on capital employed of 10% and a targeted ROI of 15%, the NPV for 100, 75, and 50% plant utilisation is given in Figure 59. For this graph, scenario 1 is chosen. The investment is split into two equal sized parts and starts at year zero. Even with a utilisation of 50% an NPV of zero can be achieved after 21 years.

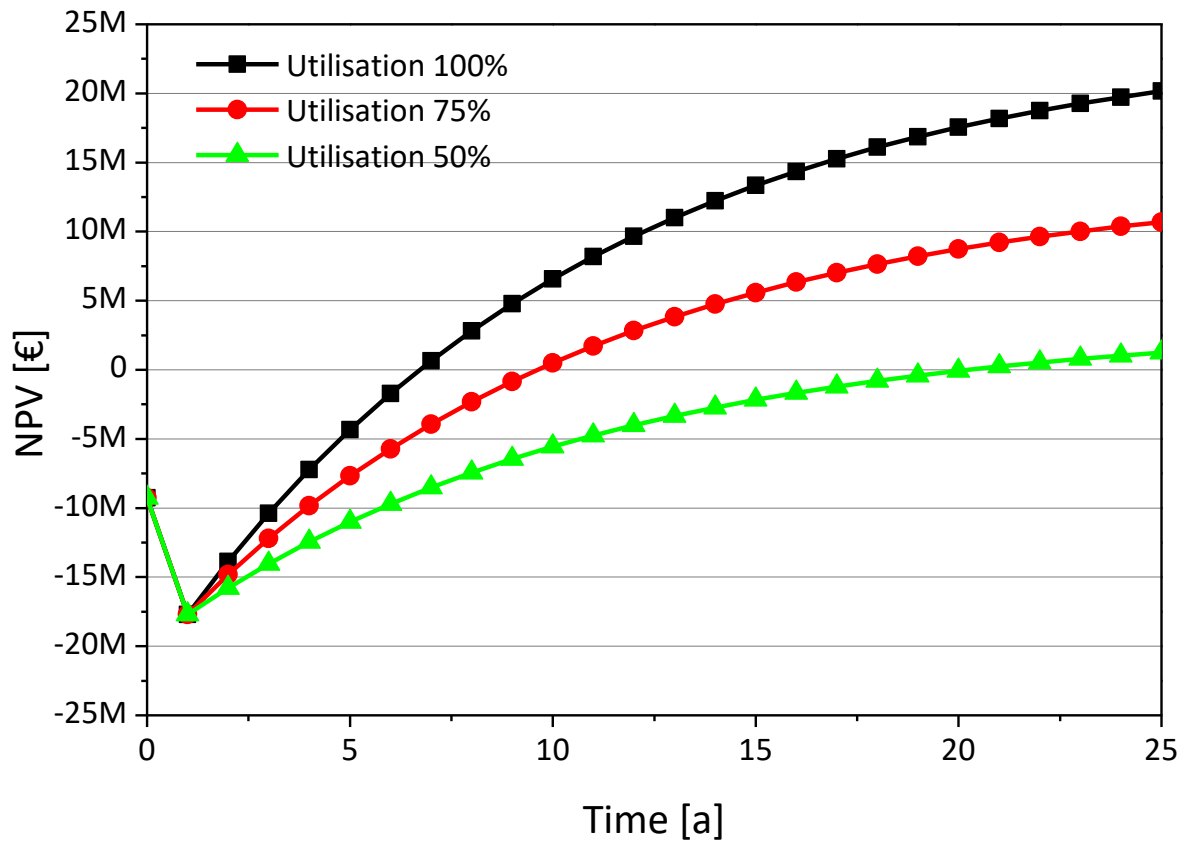


Figure 59: NPV for scenario 1 (by-product sold for 400 €/t) at different plant utilizations. An interest rate of 10% on capital employed is assumed.

In summary, 1,700 €/t seems an economically necessary pricing for the product. The main variable cost drivers are feed (62%) and energy (10%). 1,700 €/t for a carbon fibre precursor is considered reasonable, however at this point the costs for spinning are not accounted for. It has also to be considered that the material is only composed of 70% C, meaning that additional weight loss will occur during carbonisation. The precursor can be considered less expensive than traditional carbon fibre precursors such as PAN (ca. 15,000 \$/t), with its suitability for spinning and final performance eventually define price. The price can be lowered if a reasonable usage for the by-product can be found. When used as plasticiser, it can be as low as 1,150 €/t- Furthermore, product costs per tonne can be decreased *via* economy of scale. When assuming a 600,000 t/a pulp mill with an average cellulose yield of 50%, and a lignin content of 30% 360,000 t of lignin are removed from the fibres. With 75% as a maximum amount of usable lignin, this will lead to 810 t/d. The actual plant has a size of 55.5 t/d, meaning that one order of magnitude for scale-up seems realistic.

5 Hydrodeoxygenation of Lignin Model Compounds

5.1 Theory and Prior Art

Hydrodeoxygenation (HDO) of lignin was originally considered as route to increasing its heating value with regard to liquid fuel applications.^{150,153,180–185} One tonne of oil equivalent (toe) has an energy content of 41.868 MJ/kg while the heating value of lignin is at about 25 MJ/kg (e.g., Nguyen *et al.* reported a HHV of 27.7 MJ/kg for the KL produced at the LignoBoost® demonstration plant in Bäckhammar, Sweden).¹⁶⁹ Reducing the O content of lignin would therefore increase the heating value. In this context, Shabtai *et al.* have filed several patents regarding the upgrading of biomass-derived aromatics into high octane gasoline additives.^{150,152,153,183,184} Most of these processes use a heterogeneous noble metal catalyst and H₂ for the removal of O from the aromatics of the lignin structures (e.g. leading to a variety of products).^{27,186,187} As was discussed earlier, hydrothermal BCD of lignin (e.g. KL) can lead to the production of mainly alkylated bifunctional phenols such as catechol and 3-, or 4-methylcatechol (see Chapter 4). Furthermore, different kinds of guaiacylic units will be found in the product mixture (Table A 6). The application of heterogeneous catalysts for the selective transformation of these compounds into a more homogeneous mixture can be a feasible approach. As such a process has to be selective for the removal of side-chains with controllable kinetics, so that it is capable of producing a narrow range of products. Hydration and hydrogenation of aromatic compounds under hydrothermal conditions with and without catalysts open up this possibility. Pepper and Lee reported in 1969 the use of different catalysts for hydrogenation of lignin, mainly with the goal of structure elucidation.⁵¹ Here Raney-Ni, 10% Pd-C, 5% Rh-C, 5% Rh-alumina, 5% Ru-C, and 5% Ru-alumina were used for the conversion of pre-extracted spruce wood meal. Reactions were performed in a dioxane:H₂O mixture (1:1/v:v) at 195 °C over 5 h with an initial p(H₂) of 35 bar. Using a 5% Rh-C catalyst gave a ca. 25% yield of CHCl₃ solubles with a high methoxy-content. These are considered to originate from the lignin and were soluble in diethyl-ether by up to 70%. Gas-liquid chromatography indicated propyl guaiacol und dihydroconiferyl alcohol as the main components. These reports indicate the possibility of catalytic hydrogenation regarding the “refining” of lignin (e.g. to substituted aromatics), and the process resembles the idea of the *lignin-first-processes*, where the biomass decomposition aims at producing aromatics from lignin in a first step and subsequently takes care of the sugars.¹⁵ Tanksale *et al.* have analysed the hydrolysis of sugars under hydrothermal conditions *via* a 3.26 wt% Pt/Al₂O₃ catalyst at temperatures between 185 and 220 °C.¹⁸⁸ The sugars are decomposed producing mainly CO₂ and H₂. The suggested reaction mechanism indicates that H-consuming reactions take place, cleaving at high rate and selectively the C-O bonds. While these reactions are undesired when H₂ and CO₂ are the primary products, they can be exploited when fast and selective C-O bond cleavage is required. Tanksale *et al.* also suggested that at a high number of metal sites, C-C bond cleavage might also be possible. In another report, Nagy *et al.* used, among others, Raney-Ni and Pt-C for the hydrothermal treatment of OL at 175 °C for 20 h at a p(H₂) of 50 bar.⁷³ The results showed an increase in CH₃CH₂OH solubility and in H/C

ratio. The latter results from the removal of oxygen, while the content with 25.5 wt.% is only slightly lower compared to the feed with 27.8 wt.%. Runnebaum *et al.* have performed reactions with lignin model compounds in the gas phase over a 1 wt.% Pt/ γ -Al₂O₃ catalyst at T = 300 °C.¹⁸⁹ In this report, guaiacol, anisole, 4-methylanisole, and cyclohexanone were used as model compounds and evaporated at 0.015 to 0.030 mL/min into a gas stream of 100 mL/min consisting of a 3/7 mixture of H₂/N₂. In this work, rate constants were determined for the different reaction pathways, with the authors indicating that hydrogenolysis was the major pathway. In this context, guaiacol is proposed to be split mainly into catechol and phenol at a ratio of *ca.* 3:2 while generating MeOH and CH₄ as side products. Valenzuela *et al.* have demonstrated the possible production of H₂ from southern pine sawdust under hydrothermal conditions in the presence of a Pt/Al₂O₃ as catalyst.¹⁹⁰ Reactions were performed in an autoclave at T = 225 °C/t = 3 h, with addition of 1 to 5% 2 M sulphuric acid. CO₂ was found to be the major product in the gas phase, with H₂ accounting for 18% of the non-condensable gases. Zakzeski *et al.* have previously provided a detailed review on the catalytic conversion of lignin and model compounds.¹⁸⁷ Here, a reductive pathway based on guaiacylic units are highlighted, demonstrating the formation of catechol and phenol as intermediates. The stability of the alumina support however is an issue, as it is known that the amorphous γ -Al₂O₃ transforms into crystalline boehmite under hydrothermal conditions.^{191–193}

Based on this information and the previously reported investigations, by using suitable reaction conditions, it should be possible to push the reaction of guaiacylic units towards one of these products. Therefore, a detailed reaction network and associated kinetic parameters are necessary to be determined. In this chapter, reactions with guaiacol and syringol as feed will be considered under hydrothermal conditions, in the presence of a supported Pt catalyst. Addition of stoichiometric amounts of MeOH is considered to act as an internal H₂ source - *via* catalytic cleavage of MeOH – and as such directly available as adsorbed protons at the active metal site of the catalyst. This is proposed to give a handle on the reaction routes ultimately leading to the desired products catechol and phenol. Regarding catalysis, Pt supported on γ -Al₂O₃, ZrO₂, TiO₂, and activated carbon were investigated, while a Ni/C catalyst was also tested as a (more cost effective, sustainable) alternative. Pt/ZrO₂ showed the best results with regard to conversion, followed by Pt/C and Pt/ γ -Al₂O₃. Pt/TiO₂ and the Ni/C catalysts showed no significant conversion. Catalyst performance comparisons were conducted over t = 10 h, with liquid samples taken at hourly intervals. A simple reaction network is proposed and reaction rates are estimated and then fitted onto measured data.

5.2 Analytics and Methods

5.2.1 Batch Reactions

Chemicals & Catalysts

Chemicals are the same as in section 2.1.

All catalysts were prepared by an incipient-wetness impregnation method with further drying and calcination steps. Hexachloroplatinic acid hexahydrate (H₂PtCl₆·6H₂O) for the Pt-supported catalysts and nickel nitrate hexahydrate (Ni(NO₃)₂·6H₂O) for the Ni/C catalyst together with H₂O were distributed on the supporting material. The amount of H₂O depends on the absorbing capacity of each support. After the drying procedure at RT for 12

h the Pt/ γ -Al₂O₃, Pt/TiO₂, and Pt/ZrO₂ catalysts were put in an oven for 24 h at 80 °C. Subsequently, they were calcined for 3 h at 500 °C (Pt/ γ -Al₂O₃) and 550 °C (Pt/TiO₂, Pt/ZrO₂), respectively. The Pt/C catalyst was heated to 300 °C at 3 K min⁻¹, followed for an isothermal period of 2 h under N₂/H₂ (70 vol.% / 30 vol.%). Ni/C was reduced in a 10 mL/min N₂ flow at 450 °C for 2 h. The metal loading was 3 wt.% for the Pt-based catalysts and 10 wt.% for the Ni/C catalyst. The catalysts were sieved and the fraction between 200 and 400 μ m used for reactions.

Reactor Set-Up and Reaction Runs

The autoclave used was a Roth stainless steel (X6CrNiMoTi17-12-2 or AISI 316 Ti) autoclave (Article No.: 2094.1) equipped with a heating jacket and a magnetic stirrer. Since the temperatures exceeded 250 °C a glass covered stirring bar (Roth Art.-No.: PK62.1) instead of a Teflon[®] one was used. The autoclave was equipped with an electronic pressure indicator (Huba Control) and a thermocouple (Thermo Sensor). The readings of both were recorded and logged every 10 s with a datalogger. To be able to take liquid samples during the reaction, a sampling device was designed and constructed (Figure 60). This device enabled aliquots of the complete reaction mixture to be taken (including catalyst). The catalyst was sampled as well so as not to change the reactant/catalyst ratio in the autoclave. The sample volume removed was *ca.* 5 mL. To ensure a clear and liquid free capillary, 5 mL (an amount significantly higher than the volume of the installed capillary) was drawn and discarded before sampling.

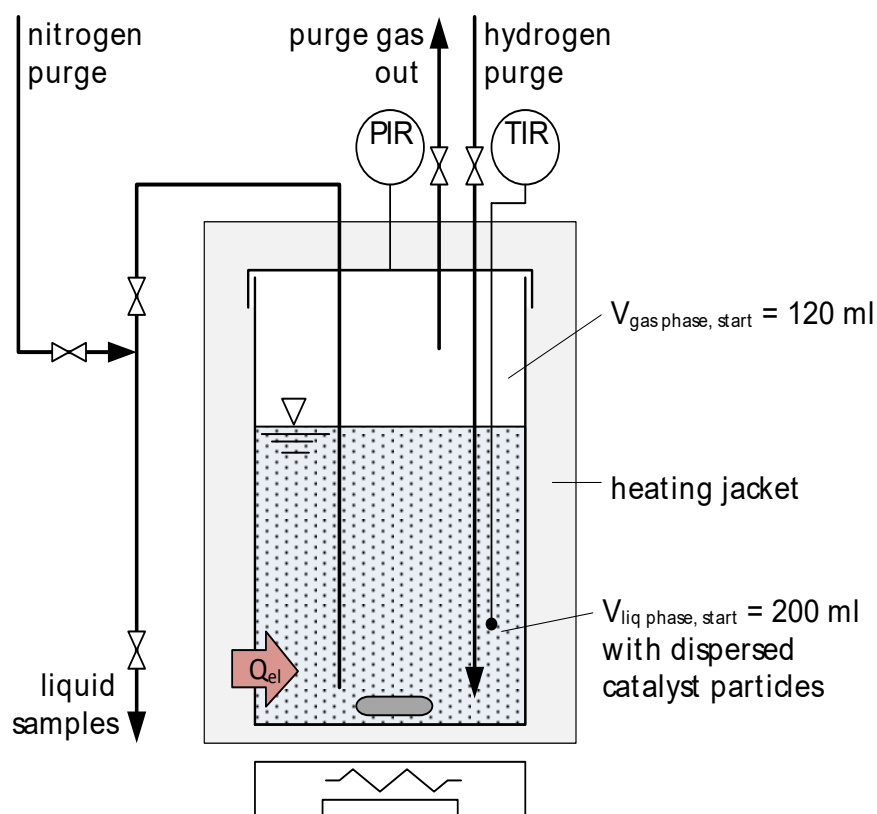


Figure 60: 250 mL batch reactor set-up. Sampling tube volume = 5 mL. The tube was purged after each sample extraction with N₂.

The gas phase was analysed *via* GC-TCD (please refer to Chapter 2.4.5). For total quantification, the reactor was flushed and pressurised with N₂ (5 bar) before every reaction. Based on pressure, volume, and relative amount of N₂ at the end of the reaction, the amount of every gas phase component was determined quantitatively. Since

the solubility of CO₂ in H₂O at STP is not negligible, the amount was calculated *via* its Henry constant from the partial pressure and added to the measured amount.

The standard aromatic compounds (i.e. syringol, guaiacol, catechol, and phenol) were dissolved in equi-molar amounts relative to 1.5 wt.% guaiacol (i.e. 0.24 mol/L). In the experiments where MeOH was added, the latter was added stoichiometrically with regard to the produced H₂ *via* its reformation, as compared to the total methoxy (MeO) groups (as defined as the number of H₂ molecules produced after complete conversion of MeOH should be the same number of MeO groups at the beginning of the reaction). Since the reformation of 1 mol MeOH with H₂O produces 3 moles of H₂ (Equation (5-1)), 1/3 of the molar amount of guaiacol (2/3 when using syringol) were added.



$$m_{\text{MeOH}} = \frac{n_{\text{MeO}} M_{\text{MeOH}}}{3 M_{\text{Aromatic}}} m_{\text{Aromatic}} \quad (5-2)$$

Where n_{MeO} is the number of MeO groups of the aromatic ring which are to be removed.

In the case of 1.50 g guaiacol, 0.13 g of MeOH was added prior to the reaction (Equation (5-2)) After having added all chemicals the catalyst was added to the reactor which was then closed and checked for gas tightness up to 60 bar with a N₂-H₂ mixture. A H₂ detector was used to check the test rig for leakages. Pressure was released and the reactor purged several times with N₂. Before starting the reaction, the N₂ pressure was increased to 5 bar. The reactor, including solvent, reactants, catalyst, and stirrer, was weighed before the reaction. It was then heated to reaction temperature (245 °C in most cases) within 60 min and the magnetic stirrer was set at 550 rpm. At predefined time intervals liquid aliquots were drawn from the reaction mixture *via* the custom-built sampling device. After 10 h, the heating jacket was turned off, the gas phase was sampled after cooling as described and the reactor was opened for sampling of the remaining liquid phase. The reactor with its contents and the liquid samples are again weighed after the reaction to check for any mass losses. The mass of the gas phase lost was considered to be insignificant.

All the catalyst particles were ground to a fine powder during the stirred reactions. Therefore, the sediment of reactor contents was a grey or black slurry and was filtered out after each test run. Before analysing the liquid phase with GC-MS and GC-FID, each aliquot was filtered using a 0.22 µm membrane syringe filter to remove any potential solid particles from the samples.

Kinetics Calculations

The reaction kinetics of the various reactions are described in form of a set of differential equations (Equations (5-3) to (5-10)). The respective reactions and their corresponding reaction rates have been tabulated in Table 46.

$$\frac{d}{dt}n_{\text{Guaiacol}} = -r_8 - r_9 - r_{10} - r_{11} \quad (5-3)$$

$$\frac{d}{dt}n_{\text{Catechol}} = r_8 + r_9 - r_{13} - r_{14} \quad (5-4)$$

$$\frac{d}{dt}n_{\text{Phenol}} = r_{10} + r_{14} - r_{15} \quad (5-5)$$

$$\frac{d}{dt}n_{\text{MeOH}} = r_8 + r_{10} - r_{12} \quad (5-6)$$

$$\frac{d}{dt}n_{\text{H}_2} = 3 r_{12} - r_9 - r_{10} - r_{13} \quad (5-7)$$

$$\frac{d}{dt}n_{\text{CH}_4} = r_9 \quad (5-8)$$

$$\frac{d}{dt}n_{\text{CO}_2} = r_{11} + r_{12} \quad (5-9)$$

$$\frac{d}{dt}n_{\text{Coke \& Poly}} = r_{11} + r_{14} + r_{15} \quad (5-10)$$

Table 46: Reactions and reactions' rates of the model compounds' reactions starting with Syringol and Guaiacol under hydrothermal conditions.

Reaction #	Stoichiometry	Reaction rate r_i
1	Syringol + H ₂ O $\xrightarrow{r_1}$ 1,2-BD, 3-MeO ^a + MeOH	$k_1 n_{\text{Syringol}}$
2	Syringol + H ₂ $\xrightarrow{r_2}$ 1,2-BD, 3-MeO + CH ₄	$k_2 n_{\text{Syringol}} n_{\text{H}_2}$
3	Syringol + H ₂ $\xrightarrow{r_3}$ Guaiacol + MeOH	$k_3 n_{\text{Syringol}} n_{\text{H}_2}$
4	1,2-BD, 3-MeO + H ₂ O $\xrightarrow{r_4}$ 1,2,3-THB ^b + MeOH	$k_4 n_{1,2\text{-BD},3\text{-MeO}}$
5	1,2-BD, 3-MeO + H ₂ $\xrightarrow{r_5}$ Guaiacol + H ₂ O	$k_5 n_{1,2\text{-BD},3\text{-MeO}} n_{\text{H}_2}$
6	1,2-BD, 3-MeO + H ₂ $\xrightarrow{r_6}$ Catechol + MeOH	$k_6 n_{1,2\text{-BD},3\text{-MeO}} n_{\text{H}_2}$
7	1,2,3-THB + H ₂ $\xrightarrow{r_7}$ Catechol + H ₂ O	$k_7 n_{1,2,3\text{-THB}} n_{\text{H}_2}$
8	Guaiacol + H ₂ O $\xrightarrow{r_8}$ Catechol + MeOH	$k_8 n_{\text{Guaiacol}}$
9	Guaiacol + H ₂ $\xrightarrow{r_9}$ Catechol + CH ₄	$k_9 n_{\text{Guaiacol}} n_{\text{H}_2}$
10	Guaiacol + H ₂ $\xrightarrow{r_{10}}$ Phenol + MeOH	$k_{10} n_{\text{Guaiacol}} n_{\text{H}_2}$
11	Guaiacol $\xrightarrow{r_{11}}$ Coke & Poly + CO ₂	$k_{11} n_{\text{Guaiacol}}$
12	MeOH + H ₂ O $\xrightarrow{r_{12}}$ 3H ₂ + CO ₂	$k_{12} n_{\text{MeOH}}$
13	Catechol + H ₂ $\xrightarrow{r_{13}}$ Phenol + H ₂ O	$k_{13} n_{\text{Catechol}} n_{\text{H}_2}$
14	Catechol $\xrightarrow{r_{14}}$ Coke & Poly	$k_{14} n_{\text{Catechol}}$
15	Phenol $\xrightarrow{r_{15}}$ Coke & Poly	$k_{15} n_{\text{Phenol}}$

^a 3-methoxy-1,2-benzenediol; ^b 1,2,3-trihydroxybenzene

It is assumed here that the reactions take place in a regime where only micro-kinetics is important, i.e. surface and pore diffusion is considered negligible. Weisz-Prater defined a dimensionless ratio (equation (5-11)) of reaction rate and diffusion, where the nominator contains reaction rate parameters and the denominator the diffusion parameters. When smaller than unity, reaction rate is supposed to be the rate determining step.

$$\Psi = L_C^2 \frac{n+1}{2} \frac{r_{cat}}{D_{i,s} c_{i,0}} \quad (5-11)$$

With L_c [cm] as characteristic length of the catalyst particle, r [$\text{mol g}^{-1} \text{s}^{-1}$] the observed reaction rate, ρ_{cat} [g cm^{-3}] the density of catalyst in the reaction space, $D_{i,s}$ [$\text{cm}^2 \text{s}^{-1}$] as the diffusion coefficient of compound i in solvent s , and $c_{i,0}$ [mol cm^{-3}] as the concentration of compound i at time zero. The catalyst particles are ground to a fine powder during the reaction, so $400 \mu\text{m}$ is a worst-case scenario. The diffusion coefficient of phenol in H_2O was chosen, which is strongly dependent on temperature. Plugatyr and Svishchev gave a value of *ca.* $10^{-8} \text{ m}^2 \text{ s}^{-1}$ for $250 \text{ }^\circ\text{C}$.¹⁹⁴ With these values and the fastest observed reaction rate in Table 49 of *ca.* 1 s^{-1} $\Psi = 0.16$, i.e. an influence of diffusion can be excluded. Since diffusion is already faster than kinetics, a calculation of the Sherwood number, *via* e.g. the Froessling equation, will be omitted.

In order to determine the adsorption capacity an experiment was performed with guaiacol and only a catalyst support (ZrO_2). Here, no reaction products occur and the difference between guaiacol at the beginning and after 2 h at $245 \text{ }^\circ\text{C}$ is considered to be the adsorption/desorption equilibrium at the defined conditions. An equi-molar mixture of guaiacol and catechol was also tested on the same support to estimate the competitive adsorption of these species. Deactivation of the catalyst will be described as coking as in equation (5-12) adjusted from Butt and Peterson.¹⁹⁵

$$\mathbf{k}_{\text{eff.}} = \mathbf{k}a = \mathbf{k} \left(1 - \frac{n_{\text{Coke \& Poly}}}{n_{\text{Coke \& Poly,max}}} \right) \quad (5-12)$$

Where $\mathbf{k}_{\text{eff.}}$ is the vector of the effective reaction rate constants, $n_{\text{Coke \& Poly,max}}$ is defined as the amount of Coke & Poly at equilibrium. Since the form of the coke is unknown, it is difficult to describe the usage or production of H_2 during the process. When assuming the coke consists of cyclic fused and saturated rings, hydrogen is produced when the side chains are removed and during condensation. The MeO group is also considered to produce CO_2 . Nevertheless, the coking mechanism is described as H_2 neutral in the reaction network, since this gives good results for the function fit, while a H_2 producing or consuming mechanism gives less positive results. All aromatic compounds are considered to be able to contribute to coking, and only one type of coke is formed. In order to adjust the parameters of the kinetics model a minimum value problem had to be solved. This was performed using MatLab® *via* the function *fminsearch*. Equation (5-13) gives the used expression for this problem. This function uses the simplex process of Nelder and Mead, which is linear and uses no derivatives giving a slow but numerically very stable solver.

$$f(k_1, k_2, \dots, k_n) = \exp \left(\sum_j \sum_i w_{j,i} |c_{j,i,\text{calculated}}(k_1, k_2, \dots, k_n) - \bar{c}_{j,i,\text{measured}}| \right) - 1 \quad (5-13)$$

Where $c_{j,i}$ is the concentration of component i at time j and $w_{j,i}$ is a weight factor for the respective component i at time j . Since finding of the absolute minimum is quite improbable, the starting values for finding a reasonable local minimum are very important. Here, realistic estimations for the kinetic constants provide assistance. It is assumed that the reaction rate of guaiacol with H_2O is one or two orders in magnitude lower than all reaction rates with respect to H_2 or MeOH reformation with water.

There are no concentrations available for the gas phase other than the final concentration at the end of the reaction. This last value was taken for the function fit. CH_4 and CO_2 appear only as products but do influence the calculation of the reaction rates. The ratio of CH_4/CO_2 indicates the ratio of the reactions of the MeO groups with

H₂ to OH groups to the reaction of the MeOH reformation, which, without MeOH addition, is a direct function of the reaction of the MeO groups with water. The MeOH reformation is the only internal H₂ source speeding up the reaction of MeO to OH groups and enabling new reaction routes, including the direct removal of MeO to yield MeOH. Since H₂ is an important reactant, its amount has to be modelled during the simulation. H₂ does appear, solubilised in the liquid phase, and bound to the active centres of the catalyst. While all three are in a dynamic equilibrium, only H₂ at the active centres is important for reaction rates. In the simple model, all H₂ is assumed to be available for the reaction, while the more complex model will give the possibility of H₂ ad- and desorption, allowing for a more realistic H₂ modelling. Solubility of gases in the liquid phase is ignored, since the Henry's constants at the given temperature are negligible for CO₂, CH₄, and H₂ in H₂O. Only the solubility of CO₂ in H₂O at ambient temperature is taken into account to determine the final amount of CO₂ after the reaction.

Conversion and yields are defined as follows:

$$\text{conversion}_{(G,S)} = X_{(G,S)} = 1 - \frac{n_{(G,S)}}{n_{(G,S),0}} \quad (5-14)$$

$$\text{yield}_i = y_i = \frac{n_i - n_{i,0}}{n_{(G,S),0}} \quad (5-15)$$

Where $n_{(G,S)}$ is the amount of guaiacol or syringol, and "0" indicates initial concentrations at the start of a test run. The amount of "Coke & Poly" is calculated by subtracting the number of moles of all detected aromatic rings in the product from the initial amount of guaiacol and syringol, respectively. This number gives no new information; it only displays the amount of "lost" aromatics, which is assumed to mainly polymerise and adsorb on the catalyst support.

$$Me_{gas} = \frac{n_{C,gas}}{(n_{MeO,0} X_{(G,S)}) + (n_{MeOH,0} X_{MeOH})} \quad (5-16)$$

Here, $n_{C,gas}$ gives the amount of molecules containing carbon atoms found in the gas phase divided by the amount of carbon atoms removed from the aromatic rings (MeO) and from the MeOH. A value over unity indicates ring destruction and the formation of larger hydrocarbons which are partially reformed into CO₂, CH₄, and H₂O. Me_{gas} is an indicator for ring splitting. It gives the ratio of carbon atoms found in the gas phase to the amount of carbon atoms at beginning of the reaction in methoxy groups and MeOH. If the value is larger than unity, some of the carbon stems from the benzoic rings.

5.2.2 Continuous Reactions

Deactivation of the catalyst was analysed under continuous test rig operation based on a plug flow reactor setup (see Chapter 2.3). The reactor was a simple stainless steel (X6CrNiMoTi17-12-2 or AISI 316 Ti) tube with $d_i = 12$ mm and length of 180 mm. Four thermocouples were attached alongside the reactor and the catalyst was kept in place with stainless steel nets.

Weight hourly space velocity (WHSV) is defined as the mass flow of reactant over the mass of catalyst in equation (5-17) and a dimensionless *Loading* value is defined, which is simply the *WHSV* multiplied with the time on stream τ .

$$WHSV [h^{-1}] = \frac{\dot{m}_{\text{Guaiacol}}}{m_{\text{Catalyst}}} \quad (5-17)$$

$$\text{Loading} [-] = WHSV \tau \quad (5-18)$$

The reactor was filled with DI-H₂O prior to reaction and retention time characteristics showed that after 35 min the first samples could be analysed.

5.3 Results & Discussion

Reactions were performed with different supports and the evaluation with respect to the calculated kinetical constants was performed for the Pt/ZrO₂ catalyst. Table 47 provides an overview of the conversion of guaiacol achieved over the investigated catalysts and in the case of Pt/ZrO₂ also with addition of MeOH. The obtained yields of catechol and phenol are also indicated. To extend the presented study, reactions were also performed with syringol as the model lignin feed compound (Table 47). The resulting gas phase products were also analysed (Table 48). Figure 61 shows the suggested reaction network for guaiacol under hydrothermal conditions.

Table 47: Conversion and yield of the liquid products of the reactions with Guaiacol (G) and Syringol (S) under hydrothermal conditions with different catalysts. Starting concentration 0.024 mol guaiacol in 200 mL H₂O, $t_{\text{retention}} = 10 \text{ h}$ / $T = 245 \text{ }^\circ\text{C}$.

Reactant + catalyst	Conversion	Yield				
		1,2-Benzenediol, 3-Methoxy	Guaiacol	Catechol	Phenol	Coke & Poly
(G) Pt/ZrO ₂	0.96	-	-	0.45	0.27	0.24
(G) Pt/ZrO ₂ + MeOH	0.90	-	-	0.30	0.45	0.14
(G) Pt/ γ -Al ₂ O ₃	0.43	-	-	0.31	0.07	0.06
(G) Pt/TiO ₂	0.34	-	-	0.00	0.00	0.34
(G) Pt/C ^a	0.84	-	-	0.46	0.04	0.31
(G) Ni/C	0.36	-	-	0.02	0.00	0.34
(G) ZrO ₂ ^b	0.00	-	-	0.00	0.00	0.00
(S) Pt/ZrO ₂	0.29	0.14	0.02	0.01	0.00	0.15
(S) Pt/ZrO ₂ + MeOH	0.74	0.09	0.05	0.19	0.10	0.36

^a Samples were measured after nine hours. ^b Only 0.012 mol of substrate was used in 98.5 mL of H₂O.

Table 48: Conversion and yield of the gaseous products of the reactions with Guaiacol (G) and Syringol (S) under hydrothermal conditions with different catalysts. Starting concentration 0.024 mol guaiacol in 200 mL H₂O, $t_{\text{retention}} = 10 \text{ h}$ / $T = 245 \text{ }^\circ\text{C}$.

Reactant + catalyst	Me _{gas}	Yield of specific gases				CH ₄ /CO ₂
		CO ₂	CH ₄	H ₂	Hydrocarbons ^a	
(G) Pt/ZrO ₂	1.26	0.45	0.61	1.07E-3	0.07	1.37
(G) Pt/ZrO ₂ + MeOH	0.92	0.63	0.71	1.53E-1	0.12	1.13
(G) Pt/ γ -Al ₂ O ₃	0.43	0.13	0.27	1.77E-2	0.01	2.13
(G) Pt/TiO ₂	0.02	0.01	0.01	2.14E-2	0.01	0.34
(G) Pt/C ^b	0.64	0.25	0.39	1.20E-3	0.01	1.57
(G) Ni/C	0.02	0.02	0.01	1.84E-2	0.00	0.21
(G) ZrO ₂ ^c	0.00	0.01	0.00	6.36E-3	0.00	0.00
(S) Pt/ZrO ₂	0.26	0.09	0.21	2.02E-2	0.02	2.44
(S) Pt/ZrO ₂ + MeOH	0.78	0.79	0.74	2.59E-1	0.02	0.94

^a Includes: ethene, ethane, propene, propane, butane, and 2-propanol. ^b Samples were measured after nine hours. ^c 0.012 mol of substrate was used in 98.5 mL of H₂O.

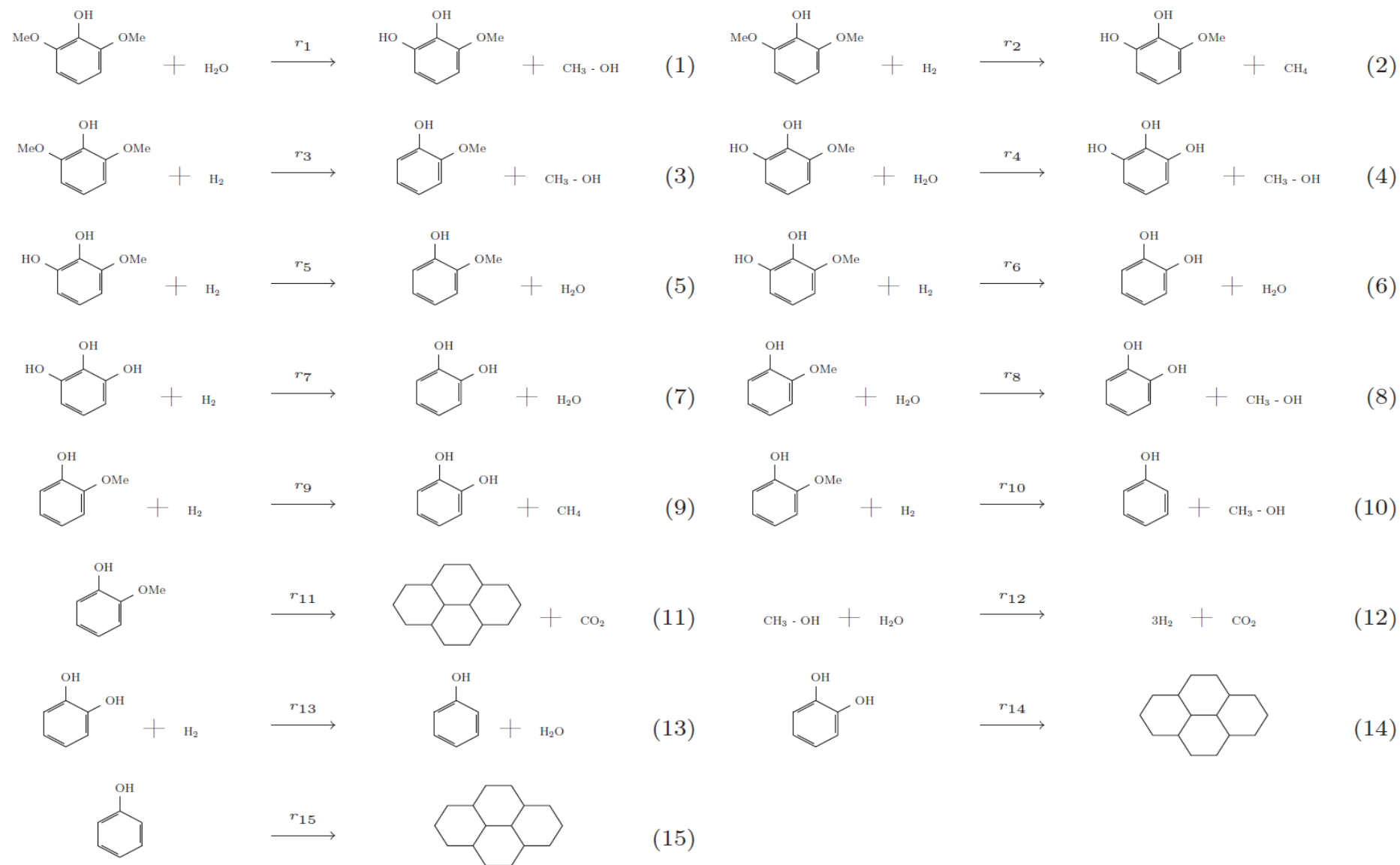


Figure 61: Reaction network for the hydrothermal decomposition of syringol and guaiacol with Pt/metal catalyst including the decomposition of MeOH.

5.3.1 Pt/ZrO₂

Guaiacol

Kinetic Studies

The use of the Pt/ZrO₂ catalyst provided the highest conversion and good selectivity towards the two desired products (Table 47). Addition of MeOH pushes the reaction further in favour of the formation of phenol and reduces coke formation, presumably linked to higher H₂ concentration.¹⁹⁵ Forming a ratio of coke & poly/conversion provided a value of 0.25 for the reaction with ZrO₂ without MeOH and a ratio of 0.16 with addition of MeOH. A control reaction involving only the ZrO₂ support resulted in no conversion of guaiacol. MeOH is produced as intermediate and small amounts appear between at $t = 30$ and 200 min. Analysis of the gas phase after 10 h indicates the presence of mainly CO₂ and CH₄ (Table 48). CO concentrations were below the detection limits of the GC-TCD (< 10 ppmv) in all test runs. The methoxy transfer ratio is 1.26, which means that some C atoms in the gas phase originate from aromatic rings in the liquid phase (i.e. a product of decomposition into smaller molecules). The value of 1.26 for Me_{gas} indicates that an additional 0.26 carbon atoms per guaiacol are transferred into the gas phase. With a remaining six carbon atoms, this makes *ca.* 4% of the aromatic rings. All other reactions present values below unity, which does not automatically mean that no ring scission appears. As reactions involving the addition of MeOH have a higher starting amount of methyl groups, the denominator in Equation (5-16) is larger. It cannot be differentiated between coke and liquid hydrocarbons that are not detectable *via* the method employed by the GC-FID. When considering the reaction network (i.e. as suggested in Figure 61), the main source of CO₂ is MeOH (12), while CH₄ is produced *via* the conversion of a -OMe to a -OH group with hydrogen (9). In the reactions without additional MeOH, reaction (8) acts as a source of this alcohol. This reaction is the initiating step and MeOH supplies three H₂ or six adsorbed protons. If all of this H₂ fuels reaction (9), the ratio of CH₄/CO₂ in the gas phase should be 3. Since also reaction (10) consumes H₂ but produces more MeOH, an oversupply of protons is potentially available. The ratio of CH₄/CO₂ can therefore be used as an indicator of r_9/r_{10} ratio, mirroring also the catechol/phenol ratio, provided r_8 and r_{13} are negligible. Additionally, all forms of coking/ring scission will interfere with this ratio.

It is also observed that the amount of H₂ in the gas phase is negligible for the reaction without MeOH addition and still very small for the reaction with MeOH. In the reactions with MeOH addition, the MeOH is not completely converted and the concentrations of all compounds are more or less constant after *ca.* 180 min. A minor amount of saturated hydrocarbon rings appears according to the GC-MS analysis. Additional products were also detected based on GC-MS analysis namely benzene, cyclopentanone, cyclohexanone, and 1,2-cyclohexadiol. MeOH conversion is *ca.* 70%, yield of H₂ in the gas phase is 0.15, suggesting that the ratio of used MeOH-H₂ (hydrogen produces *via* MeOH) per converted guaiacol is 0.61 and that internally produced H₂ does indeed play a role. Reactions (8) and (10) produce H₂ indirectly *via* in-situ production of MeOH.

This information is summarised as a set of differential equations (5-3) to (5-10). Solving the minimum value problem in equation (5-13) with this set of differentials gives the results in Figure 63 for the reaction without MeOH addition and Figure 64 with MeOH addition. Starting and final values for the constant k are provided in Table 49. The constants indicate that the reaction of guaiacol with H₂O must be slow compared to all reactions with H₂.

Guaiacol reacts to catechol and to phenol, while more slowly in the case of the latter. The k -values for the reactions with H_2 are approximately one order of magnitude larger in the reaction without MeOH addition. A test run with only MeOH and Pt/ZrO₂ gave a value for $k_{12} = 2 \times 10^{-4} \text{ s}^{-1}$, similarly to that of the reaction with MeOH addition. Formation of MeOH and H_2 is problematic in the reaction without MeOH addition. While the results show an increase in MeOH between 30 and 200 min (Figure 63), simulation indicates only a minor increase. When speeding up MeOH production in the beginning, too much H_2 will be produced and is not consumed, since coking has already led to deactivation. The mechanism for H_2 production/consumption seems incomplete. The results of the fit for reaction rate constants differ between the reaction with and without MeOH addition. Also, the starting values had to be set at different levels to achieve a good fit. This clearly indicates an imperfect model and unaccounted side reactions. Nevertheless, the prediction of aromatics in Figure 63 and Figure 64 is good, and the concentration of MeOH as well as the final amount of hydrogen is described quite well for the reaction with MeOH addition. The simulation for the reaction without MeOH addition in Figure 63 has problems to give good results for MeOH and hydrogen.

Table 49: Reaction rate starting and final parameters of minimum value problem for the reactions of guaiacol on Pt/ZrO₂ with and without MeOH addition.

	$k_{\text{start,Pt/ZrO}_2}$	$k_{\text{start,Pt/ZrO}_2_MeOH}$	$k_{\text{final,Pt/ZrO}_2}$	$k_{\text{final,Pt/ZrO}_2_MeOH}$
$k_8 \text{ [s}^{-1}\text{]}$	2.00×10^{-5}	1.00×10^{-5}	4.51×10^{-6}	4.15×10^{-6}
$k_9 \text{ [mol}^{-1} \text{ s}^{-1}\text{]}$	6.00×10^{-1}	5.00×10^{-2}	9.66×10^{-1}	4.94×10^{-2}
$k_{10} \text{ [mol}^{-1} \text{ s}^{-1}\text{]}$	3.00×10^{-1}	5.00×10^{-3}	5.06×10^{-1}	1.48×10^{-2}
$k_{11} \text{ [s}^{-1}\text{]}$	3.00×10^{-5}	3.00×10^{-5}	4.51×10^{-5}	1.05×10^{-5}
$k_{12} \text{ [s}^{-1}\text{]}$	1.00×10^{-3}	2.00×10^{-4}	3.52×10^{-3}	2.82×10^{-4}
$k_{13} \text{ [mol}^{-1} \text{ s}^{-1}\text{]}$	1.00×10^{-1}	5.00×10^{-2}	1.31×10^{-2}	4.24×10^{-2}
$k_{14} \text{ [s}^{-1}\text{]}$	2.00×10^{-5}	2.00×10^{-5}	4.94×10^{-5}	0
$k_{15} \text{ [s}^{-1}\text{]}$	1.00×10^{-5}	1.00×10^{-5}	9.17×10^{-6}	7.96×10^{-5}

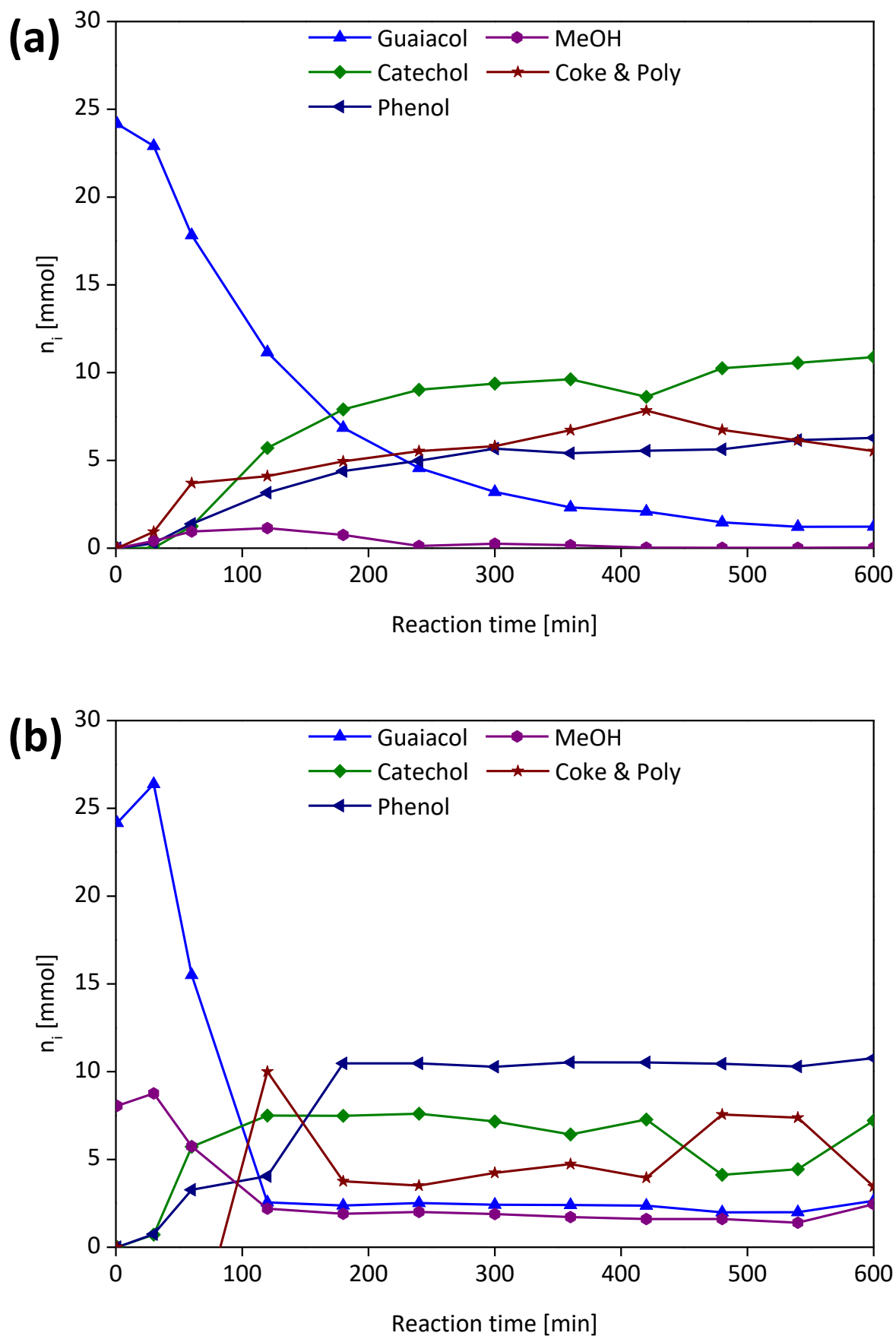
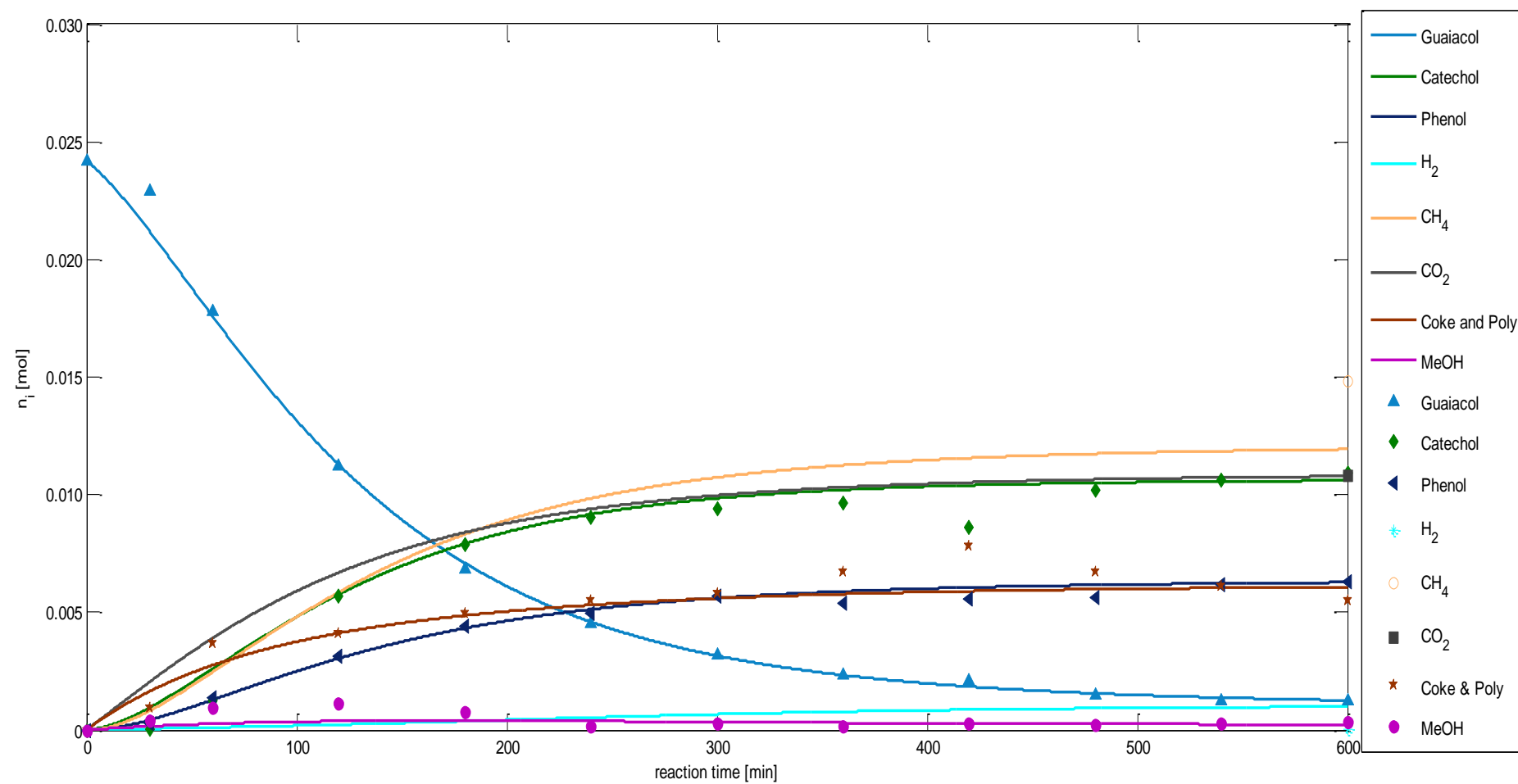


Figure 62: Progression of the reaction of guaiacol in water at $T = 245$ °C over Pt/ZrO₂; (a) without addition of MeOH, (b) with addition of MeOH.

Figure 63: Comparison between measured values and simulation results for the reaction of guaiacol with Pt/ZrO₂.

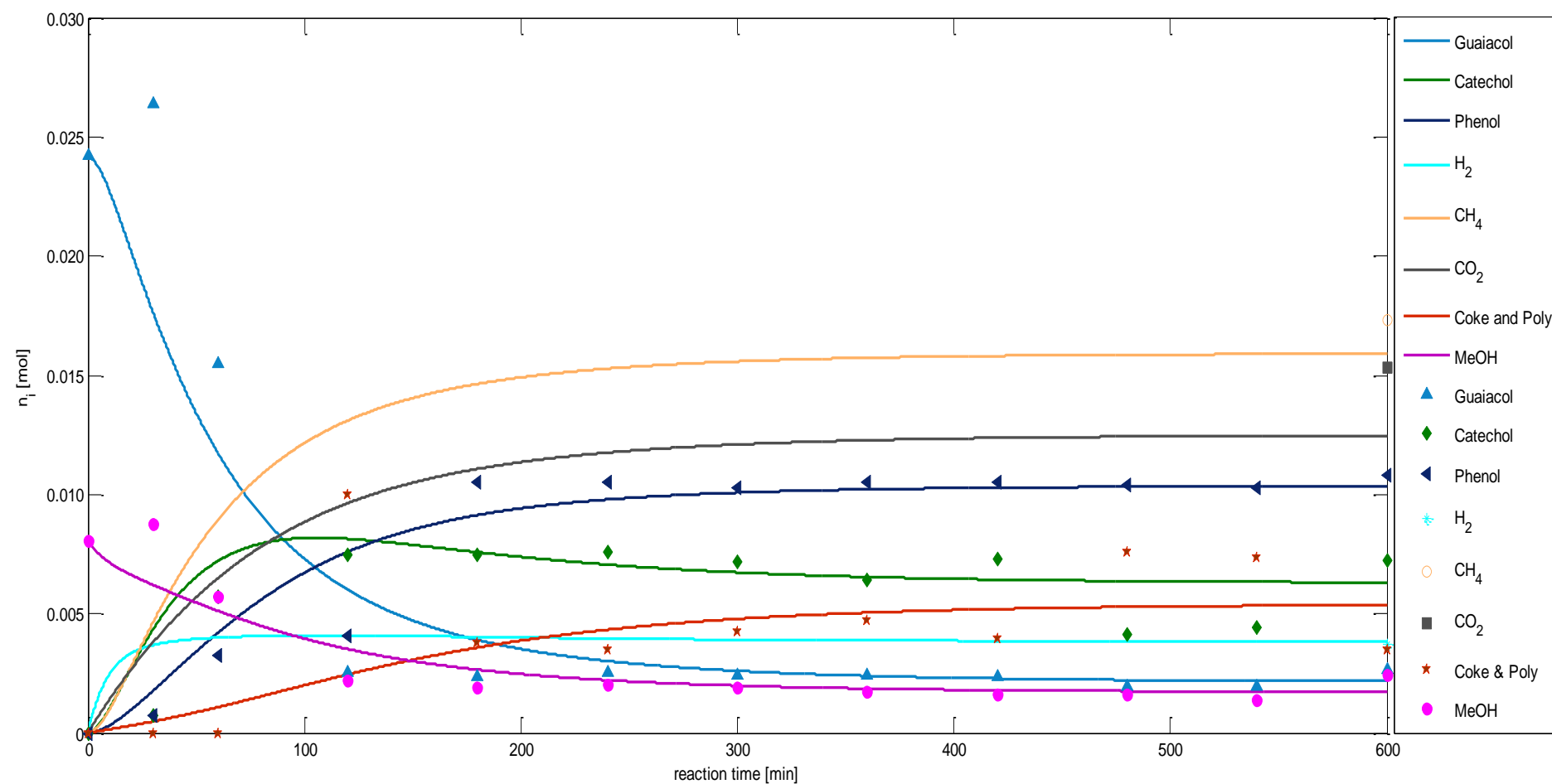


Figure 64: Comparison between measured values and simulation results for the reaction of guaiacol with Pt/ZrO₂, and addition of MeOH.

Catalyst Deactivation

The feed composition was the same, as in the reactions with MeOH addition, temperature was set at 250 °C, and pressure at 42 bar. Weight hourly space velocity is defined in (5-17) and set to 0.68 h⁻¹. This value was the highest possible, since 1.5 wt.% is the maximum solubility of guaiacol and 10 mL min⁻¹ the highest flow rate of the pump. After a loading (as defined in equation (5-18)) of 3.5 the test run for the fresh catalyst had to be interrupted for 1 week and was continued after that. The system was kept as is, meaning that the feed was kept in the reactor under ambient conditions. The spent catalyst after the complete first run was reactivated at 550 °C for 3 h under air flow applied *via* pressurised air in the plug flow reactor. Conversion of guaiacol for the fresh and reactivated catalyst is shown in Figure 65(a) and the yields of catechol, phenol, and coke & poly are presented in Figure 65(b).

Conversion is declining linearly over loading and a small but sharp drop is experienced after the interruption of one week at a loading of 3.5. The reactivated catalyst starts with the same conversion as the fresh one, but a faster deactivation takes place. This could be due to sintering of active Pt sites, thereby decreasing the active surface area. During reactivation, the overall temperature is set at 550 °C, but the oxidising of the coke is exothermic and small hot-spots will appear. Harris describes the sintering of Pt/Al₂O₃ under air flow and different retention times at 700 °C. In his findings, particle size after 0.5 h nearly doubled and tripled after 3 h.¹⁹⁶

The ratio of the yields of catechol and phenol is constant at a factor of *ca.* 1.7 and no coke & poly appears until the interruption, except for the initial analysis, where the amount of catechol is lower than expected. This could be due to the catalyst not being saturated with aromatics at this point and still some of the guaiacol adsorbs on the surface without the same amount of product being desorbed. After the pause, the yields drop very sharply from 65% to 30% for catechol and from 39% to 29% for phenol. The catechol to phenol ratio decreases to 1.5 and then increases to about three. The value of coke & poly increases accordingly, since the conversion does not experience this sharp drop, but continues to drop linearly (Figure 65(a)). This indicates no further deactivation of the catalyst during the pause, but a change in the reaction network. It is interesting, that until the loading of 3.5 the reaction produced nearly no coke and only catechol and phenol in a ratio of 1.7, while the batch reactions showed loss of compounds from the start. The catalyst still deactivates, while no further loss of compounds is detected. This means, that the coking must take place *via* already adsorbed species and that coking should continue when the catalyst is removed from the feed stream and treated under the same hydrothermal conditions in pure H₂O. The state in which no loss of aromatics is experienced seems to be a promising operating range.

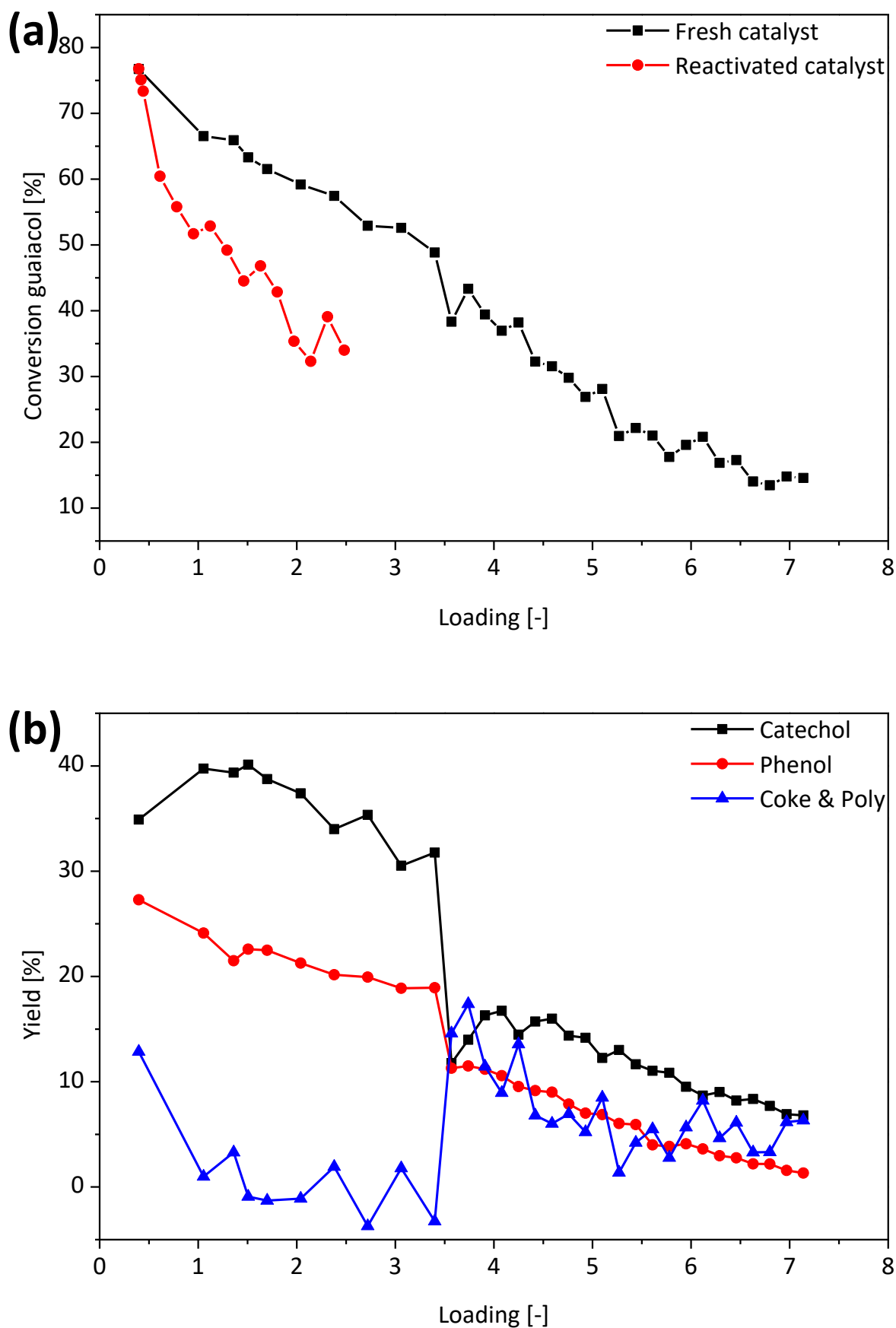


Figure 65: Continuous runs with guaiacol in water over Pt/ZrO₂ catalyst for determination of deactivation. (a) Conversion over loading of the fresh and reactivated catalyst and (b) yield of the main components catechol, phenol, and coke & poly for the runs with the fresh catalyst. At a loading value of 3.5 the run was interrupted for 1 week.

Syringol

The reactions with syringol are solely performed with the Pt/ZrO₂ catalyst and the complete reaction network is depicted in Figure 61. Figure 66(a) shows the reaction with 24 mmol/L syringol, and Figure 66(b) shows the same with 2/3 molar addition of MeOH. Without any addition of MeOH the syringol is reformed into 3-methoxy-1,2-benzenediol and Coke & Poly with a conversion of about 29%. The gas phase consists mainly of CH₄ with a yield of 21%, CO₂ with 9%, as well as hydrogen and hydrocarbons with 2% each. Reformation into 1,2-benzenediol, 3-methoxy seems to happen to a small extent *via* reaction (1) in Figure 61 and then mainly *via* reaction (2) enabled by the MeOH which is reformed into CO₂ and 3 H₂. This leads to the ratio of *ca.* 3:1 for CH₄:CO₂. The yield of CH₄ is 21% and the yield of 1,2-benzenediol, 3-methoxy only 14%, indicating that the generation of coke & poly also starts with the same demethoxylation reaction. Production of guaiacol is enabled through reactions (3) and (5). Reaction (3) is a parallel reaction to (2) and fuels itself by generating MeOH. Even after ten hours the reaction seems not having come to a halt and conversion of syringol continues. Assuming the conversion of syringol and that of guaiacol to be a (pseudo) first order reaction, the reaction rate of guaiacol is one order of magnitude larger than that of syringol (Figure 67). Steric hindrance for adsorption is assumed by the author to be the reason for this, as the syringol molecule is bulkier than guaiacol.

The reaction with MeOH addition shows a conversion of 74% and more products with less side chains appear (Figure 66(b)). Again, the reaction comes to a halt quite fast (approx. 120 min) as in the reaction with guaiacol and MeOH addition. Since syringol has two methoxy groups, the amount of MeOH was set to 2/3 of the molar amount of syringol. MeOH conversion is 66% after ten hours and 55% after 180 min, i.e. that still some MeOH conversion takes place. The main product is catechol followed by phenol, 3-methoxy-1,2-benzenediol, and guaiacol with a ratio of 3.7 : 1.9 : 1.7 : 1. The amount of coke & poly is 4.6 : 1 compared to guaiacol and constitutes the majority of the products. Main gas yields are 0.79 for CO₂, 0.74 for CH₄, and 0.26 for H₂. As expected, the amounts of CO₂ and H₂ as main products for the MeOH reformation are significant larger than for the reaction without MeOH addition, while also the value for CH₄ increased threefold. The conversion of MeOH is 66%, meaning that only a yield 0.44 of the CO₂ can stem from MeOH added in the beginning. Assuming that the remaining 0.35 also originate from MeOH, which was produced *via* reaction (3) and (10) another 1.05 of hydrogen would have been produced. The total amount of hydrogen produced *via* MeOH reformation is 2.37, which bases on the simple assumption that all the CO₂ is generated by MeOH reformation. If true, and if one H₂ is used for the production of CH₄, an amount of hydrogen of 1.37 takes part in reactions unaccounted for. This is a quite large amount and another proof for an incomplete reaction network.

During the syringol reaction with MeOH addition, more side products appear. These include: 1,2,3-trimethylbenzene, 3-methylphenol, benzene, cyclopentanone, 2-methylcyclopentanone, cyclohexanone, 1,2-cyclohexadiol, and 2-cyclohexen-1-ol. The yields of these compounds lie below 1% and they are not implemented into the reaction network.

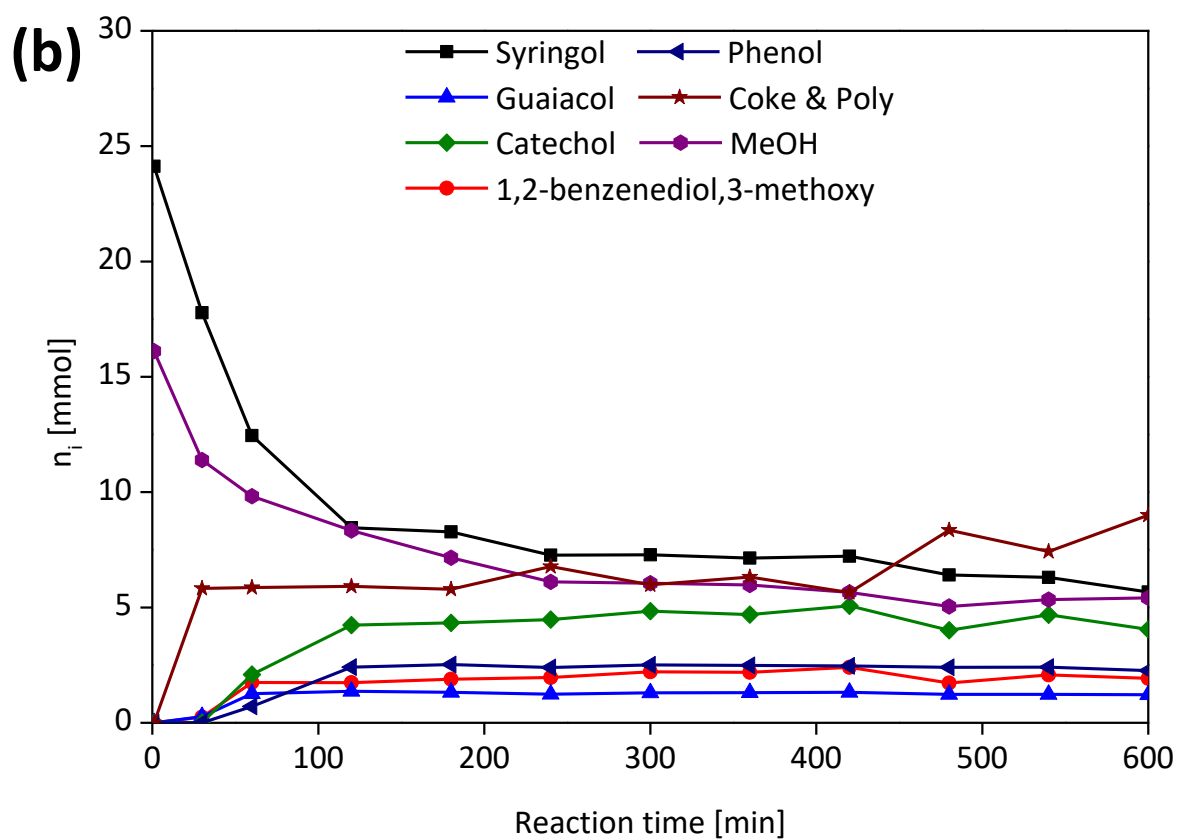
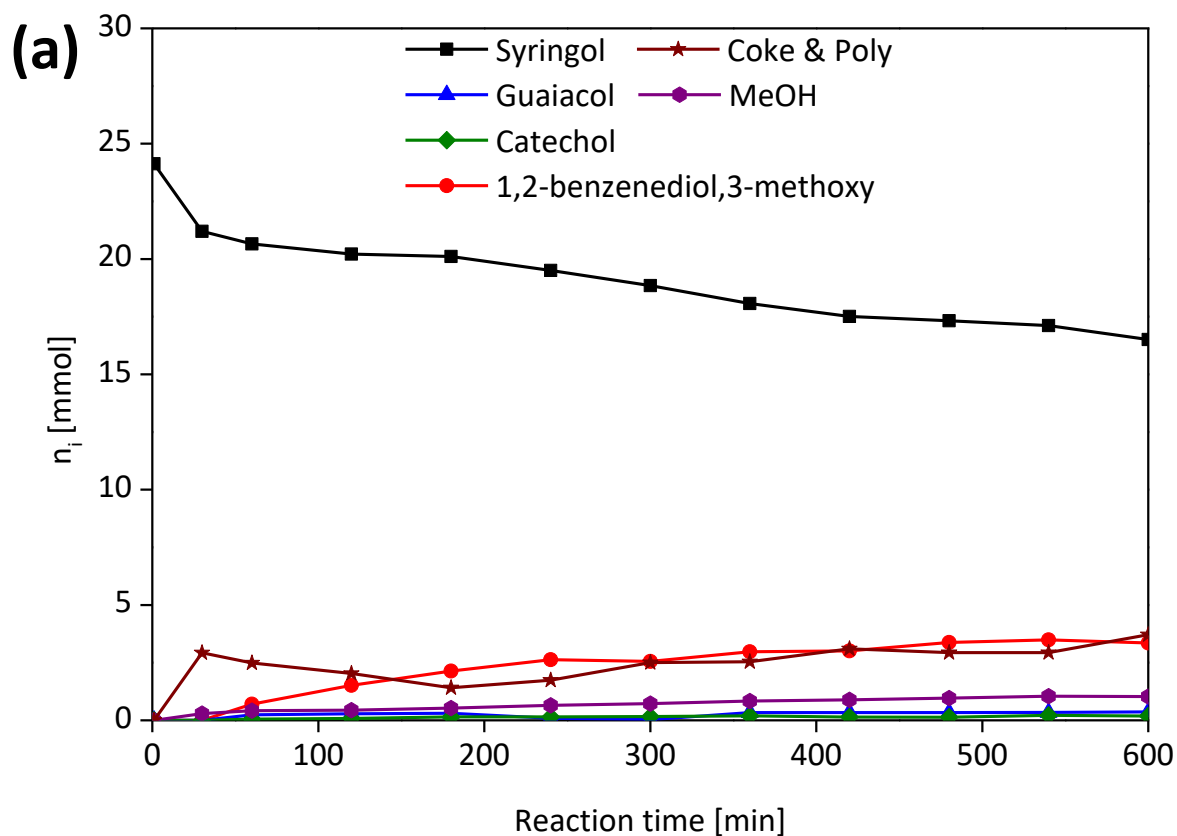


Figure 66: Progression of the reaction of syringol in H_2O at 245°C with Pt/ZrO_2 catalyst. (a) without addition of MeOH, (b) with addition of MeOH.

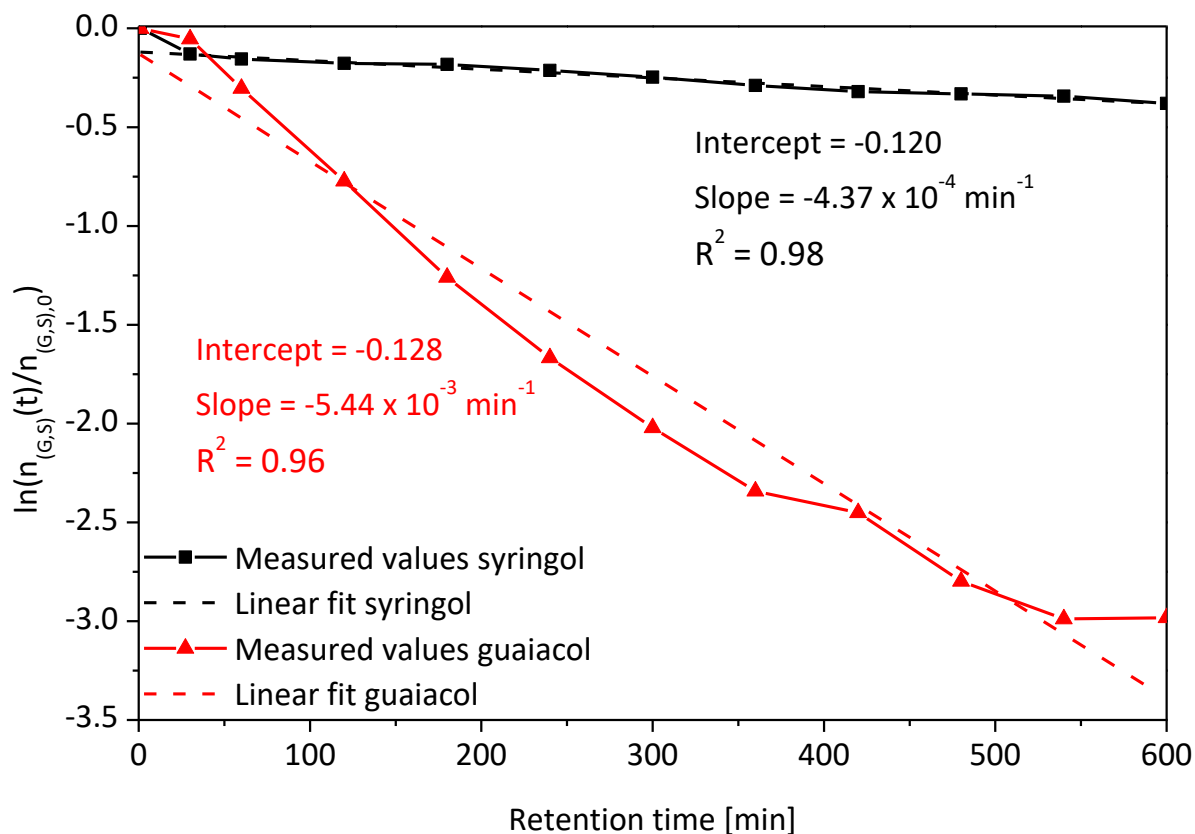


Figure 67: $\ln(n_{(G,S)}(t)/n_{(G,S)}(0))$ vs. $t_{\text{retention}}$ of the amount of guaiacol or syringol for the reaction over Pt/ZrO₂ at 245 °C in H₂O. For the linear regression of syringol, the first step is omitted, since it probably includes adsorption.

5.3.2 Pt/ γ -Al₂O₃

As described in Section 5.1, the alumina support is unstable under the hydrothermal conditions used for the reaction. It is known that the amorphous γ -Al₂O₃ incorporates water and is transformed into the crystalline boehmite which possesses a significantly smaller surface area. Moreover, the growing crystal structures cover the active platinum sites.^{191–193} This accounts for the low conversion (43%) compared to the ZrO₂ support. Catechol is the main product and the aromatics balance shows low adsorption and/or polymerisation. The reaction seems to come to a halt after about 300 min, as can be seen in Figure 68.

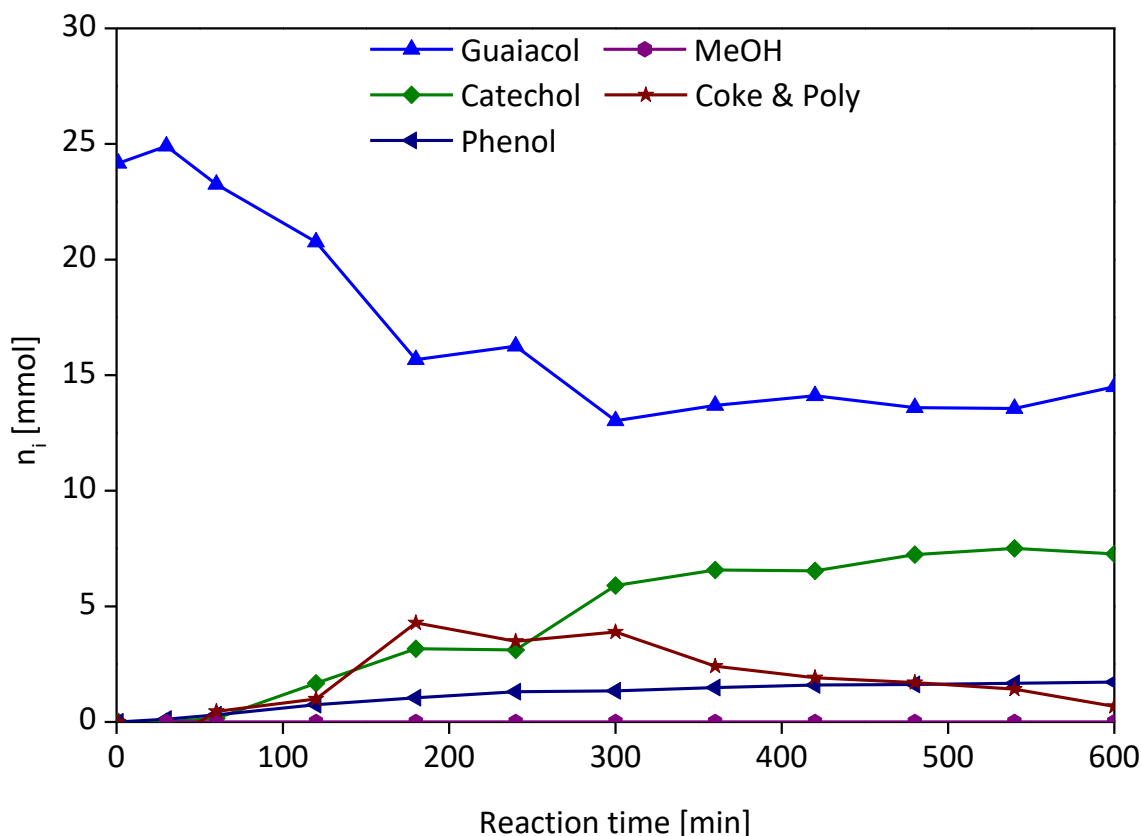


Figure 68: Progression of the reaction of guaiacol in water at 245 °C with Pt/ γ -Al₂O₃ catalyst.

The stability of the γ -Al₂O₃ support under hydrothermal conditions in an alkali CH₃CH₂OH/H₂O mixture was analysed by Jongerius *et al.*¹⁹⁷ Transformation of the support into boehmite was complete after only 4 h in water at 225 °C, reducing the BET surface area from 121 m²/g down to 35 m²/g. The addition of 0.13 mol/L guaiacol led only to a decrease from 158 to 76 m²/g after 15 h. Our catalyst had a starting surface area of 169 m²/g and ended up with 79 m²/g after 24 h with a guaiacol starting concentration of 0.12 mol/L. These results are in line with the findings of Jongerius *et al.*, and prove the inhibiting nature of mono aromatic compounds with two functional oxygen groups onto the transformation of γ -Al₂O₃ into boehmite.

Furthermore, Zakzeski *et al.* used a Pt/Al₂O₃ catalyst for the depolymerisation of different lignins in water/CH₃CH₂OH mixtures (1:1 v/v) in a batch autoclave.¹⁹² A co-catalyst (H₂SO₄, phosphotungstic acid hydrate, or NaOH) was used to increase the depolymerisation performance. The usage of the catalysts yielded significant amounts of different monomeric substances but did not lead to a purified monomeric mixture, as could have been expected by the findings of this paper. This can be attributed to a strong deactivation of the catalyst by coking. Our experiments show that this is very probable while inactivity due to steric hindrance cannot be excluded. Since the experiments of Zakzeski *et al.* were performed in a CH₃CH₂OH/H₂O mixture at 225 °C, a sufficient supply of H₂ *via* the reformation of CH₃CH₂OH with water should be provided. As stated previously, Jongerius *et al.* found that guaiacol and lignin inhibit or even prevent the transformation of γ -Al₂O₃ into boehmite.¹⁹⁷ This inhibition could be caused by the coking of the catalyst, which not only blocks the active centres, but also hinders the uptake of H₂O of the alumina.

5.3.3 Pt/TiO₂

The titania supported catalyst yields only trace amounts of the main conversion products catechol and phenol, while the amount of MeOH is not insignificant. 34% of the guaiacol disappeared from the liquid phase and seem to have formed coke on the support of the catalyst or just polymerised to larger compounds undetectable by the GC. The converted guaiacol seems to have adsorbed or polymerised, being unable to desorb and not forming aromatic monomers. The number of gaseous products is also negligible, meaning that the process of coking and polymerisation is not producing any gases.

5.3.4 Pt/C

The carbon support gave a lower conversion of guaiacol compared to ZrO₂ (Figure 69) but led more selectively to catechol. The amount of Coke & Poly is comparable to that of the ZrO₂ support. While relative to the conversion of guaiacol it is much higher. Interestingly the products catechol and phenol appear only after 120 min, while the fastest guaiacol reaction takes place during the first 30 min. It seems that a lot of the reactant adsorbs very fast on the catalyst prior to the start of a reaction and subsequent desorption.

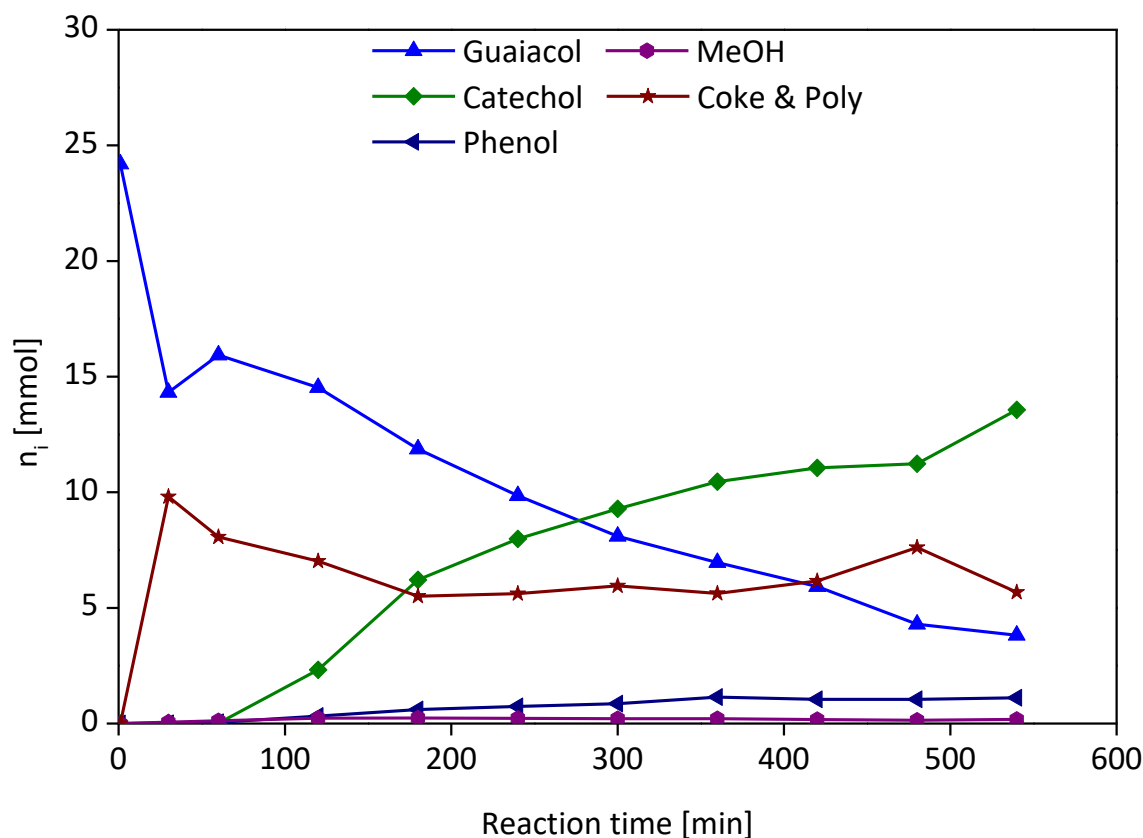


Figure 69: Progression of the reaction of guaiacol in water at 245 °C with Pt/ γ -Al₂O₃ catalyst.

5.3.5 Ni/C

The Ni/C catalyst gave similar results to Pt/TiO₂. While 36% of the guaiacol disappears; no significant amounts of the monitored products do appear. No further reactions and analyses were performed for this catalyst.

6 Summary & Outlook

As a general theme, the aim of this thesis was to develop a process that utilises industrial KL as feed and produces a precursor for carbon fibres that has more suitable characteristics than the original KL. Furthermore, the process should be cost effective and easily assimilable into an existing Kraft mill. The literature analysis in chapter 1.3 showed that carbon fibres from lignin suffer under the heterogeneity of the polymeric mixture and especially low molecular weight compounds that are not linked during thermal stabilisation of the spinned fibre. These compounds evaporate during stabilisation and, mainly, carbonisation, thereby tearing holes into the structure of the fibre. In most industrial applications, poly acrylonitrile (PAN) is used as precursor for carbon fibres. But also, mesophase pitch can be used; the latter resembling in its structure deoxygenated and condensed lignin. The process for treating the KL consists of an extraction step *via* MeOH and a subsequent rearrangement under basic hydrothermal conditions using NaOH (aq) as solvent and catalytical system (Figure 1). Furthermore, reactions with model compounds aiming at treating the oil phase after basic reaction are performed. These aim at homogenising the aforementioned phase in order for producing a feed-stream for the chemical industry.

It is possible to extract the low molecular weight compounds from KL *via* MeOH. The analysis of the HMW fraction shows a higher average molecular weight, higher thermal stability, and reduced amount of side chains per mass. Results of the subsequent base catalysed reaction did not show significant differences between using the three fractions KL, HMW, and LMW. The solids precipitated after base catalysed reaction show a molecular weight distribution comparable to that of the LMW fraction, while having an increased thermal stability. The mass loss at 600 °C under N₂ atmosphere is decreased from *ca.* 50% to 35-40%. DSC shows glass transition temperatures for the KL and LMW fraction at 147 and 121 °C, respectively. The solids precipitated from the product at pH 10 and pH 2 show no distinct glass transition, which is also true for the HMW fraction. Addition of LMW to the pH 2 fraction at $t_{\text{retention}} = 16$ min did not lead to a glass transition. I.e., the LMW fraction can serve as plasticiser for the HMW fraction, but not for the solids precipitated after base catalysed treatment. While the thermal properties of the solids are very promising, the lack of a glass transition makes it mandatory to find a more suitable plasticiser, if melt-spinning is to be used. Average C₉-Unit mass is reduced from 180 to *ca.* 155 g/mol after 24 min at 300 °C. Elemental composition shows an increase in carbon content and reduction in H, O, and S, while from the original sulphur 2/3 are removed. Mass balances of the reactions with different $t_{\text{retention}}$ showed, that *ca.* 20-25 wt.% of the feed are neither part of the solids nor the oil fraction after reaction. Since no gas phase evolved, these compounds will be in the pH 2 aqueous phase after extraction with ethyl acetate. C, H, O, S mass balancing over the fractions lead to the conclusion that the compounds have a molecular formula in the range of CH₂O_{0.7-1.5}, resembling that of C₁₋₄ organic acids and alcohols, some with thiol groups. These products probably originate from ring cleavage and leaving groups of the base catalysed reactions.

¹H proton NMR indicated a clear reduction by *ca.* 60% of the signals in the aromatics region from $\delta_{1\text{H}} = 8.00$ to 6.00 ppm, which is also confirmed by the ¹³C CP MAS NMR, where the total aromatics area from $\delta_{13\text{C}} = 160$ to 100 ppm is reduced by 60%. 2D HSQC does not confirm this, meaning that the amount of C-H correlations is not as strong affected. Solubility of the pH 10 and pH 2 solids in, e.g., MeOH is strongly increased compared to the

HMW fraction, which was by definition the MeOH insoluble fraction. 2D HSQC NMR and ATR FT-IR show a decrease in methoxy groups and β -O-4 linkages of 58 and 80%, respectively. Both degrade as a (pseudo) first order reaction in regard of their own concentration, while the rate constant of the methoxy groups is three times smaller than that of the β -O-4 linkages. Monitoring these groups gives a possibility for quantifying the conversion of the lignin during base catalysed hydrothermal treatment. The oil fraction gives *ca.* 5% yield when using the HMW fraction as feed and consists mainly of (alkylated) catechol and guaiacylic compounds in the monomeric range, which makes up 1/3 of the mass and 50% of the molecules.

Techno-Economical evaluation of the process shows that pricing of the potential product should be in the range of 1,600 €/t when an ROI of 15% is assumed. The potential price of the extracted LMW fraction is also an important factor for the profitability of the process. Since using this fraction as a plasticiser seems not possible, the second-best variant would be the usage as a phenol substituent in, e.g., phenyl formaldehyde resins. Investment of 20 M€ over two years are assumed. With 62%, the feed makes up the majority of the costs per tonne of product followed by depreciation (12%), and energy (11%). While depreciation can be dealt with via economy of scale, a focus on reduction of feed usage and price appears to be promising. Further heat integration is also a possible future research topic.

The catalytical systems analysed for the reformation of guaiacol and syringol under hydrothermal conditions lead to Pt/ZrO₂ as an optimal system. γ -Al₂O₃ is not stable under the conditions and Pt/TiO₂ showed no conversion. Activated carbon gives good results with mainly catechol as product, while the system would make a reactivation by calcination impossible. Ni/C did not show any conversions as pure ZrO₂ did not either. Reactions with the 3 wt.% Pt/ZrO₂ catalyst, showed that it is possible to control the reaction *via* stoichiometric amounts of MeOH. This MeOH is reformed into H₂ and CO₂, thereby providing hydrogen at the active centres of the catalyst. With addition of this *in situ* hydrogen, the reaction is pushed further down the reaction network, favouring direct demethylation by hydrogenolysis. This leads to higher amounts of phenol for reactions with guaiacol as feed and more catechol for the syringol reactions. Determining the rate constants *via* employing a minimum value problem shows good congruency for the evolution of the aromatic compounds, while prediction of MeOH and H₂ are less precise. The difference in calculated rate constants for the reactions without and with addition of MeOH, also gives rise to the assumption that the reaction network is incomplete. Especially evolution of the coke & poly fraction needs a more detailed reaction route. The deactivation of the catalyst was described in a continuous system, and shows no loss of compounds. Nevertheless, deactivation of the catalyst takes place, giving rise to the assumption that amount of coke for deactivation is negligible. The catalyst could be reactivated by calcination at 550 °C under air, which probably leads to sintering of the Pt particles. Using this catalytical system on the oil fraction of the base catalysed reaction could prove promising.

For future projects, the precipitation after reaction is supposed to be performed with CO₂. The generated solids are to be characterised *via* EA, TGA/DSC, and 2D HSQC NMR. Furthermore, specialists for carbon fibres should suggest parameters and analytical tools for the characterisation of the precipitated solids in regard of the usage as precursor. The results of the runs with different feeds after MeOH extraction did not yield significantly different products and using the KL as is for the base catalysed process would increase yield and reduce costs for the

extraction. When more specific parameters for a potential product are found, it makes sense to check an extraction improves the product. The *ca.* 20 wt.% of compounds in the pH 2 aqueous phase should be analysed in more detail. The use of ion exchange chromatography (IEC) could prove beneficial. The characteristics of the solids after base catalysed reactions resemble in regard of TGA and NMR stabilised lignin fibres after being stabilised in air at 250 °C for 60 min. Maybe a hydrothermal process for stabilising carbon fibres can save time and thereby costs. The equipment would of course have to be adapted for the high temperatures and pressure.

References

1. European Community (EC), *2020 climate & energy package* - http://ec.europa.eu/clima/policies/strategies/2020/index_en.htm, last accessed: 09. June 2016.
2. Environmental Protection Agency (EPA), *Standards of Performance for Greenhouse Gas Emissions From New, Modified, and Reconstructed Stationary Sources: Electric Utility Generating Units*, 2015.
3. United Nations, *Paris Agreement*, 2015.
4. P. J. Crutzen in *Earth system science in the anthropocene*, ed. E. Ehlers and T. Krafft, Springer, Berlin, New York, 2006, p 13.
5. bp, *BP Statistical Review of World Energy*, 2016.
6. G. A. Olah, A. Goepfert and G. K. S. Prakash, *Beyond oil and gas: The methanol economy*, Wiley-VCH, Weinheim, 2009.
7. T. Ward, B. Wilkison, J. Weishaar and G. Ruskowsky, *Methanol to Aromatics*, University of Wyoming, 2016.
8. K. Müller, F. Fabisch and W. Arlt, *Green*, 2014, **4**(1-6).
9. M. Schmied, P. Wüthrich, R. Zah, H.-J. Althaus and C. Friedl, *Postfossile Energieversorgungsoptionen für einen treibhausgasneutralen Verkehr im Jahr 2050: Eine verkehrsträgerübergreifende Bewertung*, 2014.
10. FAO - Food and Agriculture Organization of the United Nations, *pulp and paper capacities 2015 - 2020*, Rome, 2015.
11. H. Tran and E. K. Vakkilainen, *The Kraft Chemical Recovery Process*, 2007.
12. M. Ragnar, G. Henriksson, M. E. Lindström, M. Wimby, J. Blechschmidt and S. Heinemann in *Ullmann's encyclopedia of industrial chemistry*, Wiley Interscience, [Hoboken, NJ], 1999-2014.
13. P. J. Kleppe, *Tappi*, 1970, **53**(1), 35.
14. G. Gellerstedt, P. Tomani, P. Axegård and B. Backlund in *Integrated forest biorefineries: Challenges and opportunities*, ed. L. Christopher, Royal Society of Chemistry, Cambridge, 2013, p 180.
15. R. Rinaldi, R. Jastrzebski, M. T. Clough, J. Ralph, M. Kennema, Bruijninx, Pieter C. A. and B. M. Weckhuysen, *Angewandte Chemie (International ed. in English)*, 2016, **55**(29), 8164.
16. M. Björk, J. Rinne, K. Nikunen, A. Kotilainen, V. Korhonen, H. Wallmo and H. Karlsson in *NWBC 2015: The 6th Nordic Wood Biorefinery Conference Helsinki, Finland, 20-22 October, 2015*, VTT, Espoo (Finlande), op. 2015, p 185.
17. J. D. Gargulak and S. E. Lebo in *Lignin: Historical, biological, and materials perspectives*, ed. W. G. Glasser, R. A. Northey and T. P. Schultz, American Chemical Society; Distributed by Oxford University Press, Washington, DC, [Cary, NC], 2000, p 304.
18. M. J. Borgfeldt, *Anionic bituminous emulsions*(US3123569A), 1964.
19. S. Falkenhag and C. Bailey, *Dyestuff compositions containing lignin surfactants carboxy substituted*(US3841887A), 1974.
20. M. Dimitri, *Stabilized cleansing paste*(US3803041A), 1974.
21. H. H. Moorer and C. W. Sandefur, *Process for making combination wetting-dispersing agent*(US3986979A), 1976.
22. S. Y. Lin, *Lignin adducts*(US3956261A), 1976.
23. P. Dilling, *Ammonium lignosulfonates*(US4670482A), 1987.

24. P. Schilling and P. E. Brown, *Cationic and anionic lignin amines as flocculants*(US4781840A), 1988.
25. S. Y. Lin and L. H. Hoo, *Sulfonated ligno-aminodicarboxylates and process for making same*(US4728728A), 1988.
26. P. Dilling, *Method for preparing low electrolyte sodium lignosulfonates*(US4740590A), 1988.
27. J. D. Gargulak, S. E. Lebo and T. J. McNally in *Kirk-Othmer Encyclopedia of Chemical Technology*, ed. John Wiley & Sons Inc, John Wiley & Sons, Inc, Hoboken, NJ, USA, 2000.
28. P. Tomani, *Cell Chem Technol*, 2010, **44**(1-3), 53.
29. www.domtar.com/biochoice (last accessed November 2014).
30. P. Tomani, P. Axegard, A. Engström and H. Theliander, *LignoBoost: Lignin Extraction*, 2006.
31. M. C. Romano, V. Spallina and S. Campanari, *Energy Procedia*, 2011, **4**, 1168.
32. M. Li, A. D. Rao, J. Brouwer and G. S. Samuelsen, *Journal of Power Sources*, 2010, **195**(17), 5707.
33. E. Grol, *Energy Procedia*, 2009, **1**(1), 4307.
34. J. M. Klara, *Energy Procedia*, 2009, **1**(1), 3827.
35. R. Nagumo, S. Kazama and Y. Fujioka, *Energy Procedia*, 2009, **1**(1), 4089.
36. J. Kihlman in *NWBC 2015: The 6th Nordic Wood Biorefinery Conference Helsinki, Finland, 20-22 October, 2015*, VTT, Espoo (Finlande), op. 2015, p 402.
37. L. Kouisni, P. Holt-Hindle, K. Maki and Paleologou Michael, *Journal of Science & Technology for Forest Products and Processes*, 2012, **2**(4), 6.
38. <http://www.bioplasticsmagazine.com/en/news/meldungen/2016-04-08-Innovative-linin-extraction-plant-opened-in-Canada.php> (last accessed November 2016).
39. J. Velez and M. C. Thies, *Journal of Wood Chemistry and Technology*, 2015, **36**(1), 27.
40. M. A. Lake and J. C. Blackburn, *Cellulose Chemistry and Technology*, 2014, **48**(9-10), 799.
41. I. A. Pearl and D. L. Beyer, *J Am Chem Soc*, 1954, **76**, 6106.
42. S. B. Baker, T. H. Evans and H. Hibbert, *J Am Chem Soc*, 1948, **70**(1), 60.
43. S. B. Baker and H. Hibbert, *J Am Chem Soc*, 1948, **70**(1), 63.
44. C. P. Brewer, L. M. Cooke and H. Hibbert, *J Am Chem Soc*, 1948, **70**(1), 57.
45. J. M. Pepper and H. Hibbert, *J Am Chem Soc*, 1948, **70**(1), 67.
46. Bower Jr., John R., J. L. McCarthy and H. Hibbert, *J Am Chem Soc*, 1941, **63**, 3066.
47. A. B. Cramer, M. J. Hunter and H. Hibbert, *J Am Chem Soc*, 1939, **61**, 509.
48. M. J. Hunter, A. B. Cramer and H. Hibbert, *J Am Chem Soc*, 1939, **61**, 516.
49. Wright, George, F. and H. Hibbert, *J Am Chem Soc*, 1937, **59**, 125.
50. G. H. Tomlinson and H. Hibbert, *J Am Chem Soc*, 1936, **58**, 345.
51. J. M. Pepper and Y. W. Lee, *Can J Chemistry*, 1969(47), 723.
52. J. M. Pepper and Y. W. Lee, *Can J Chemistry*, 1970, **48**(3), 477-&.
53. J. M. Pepper, G. S. Sundaram and G. Dyson, *Can J Chemistry*, 1971, **49**(20), 3394-&.
54. J. M. Pepper and K. Jc, *Pulp Paper Mag Can*, 1972, **73**(9), 88-&.
55. Y. W. Lee and J. M. Pepper, *Tetrahedron Lett*, 1978(51), 5061.
56. J. M. Pepper and R. W. Fleming, *Can J Chem*, 1978, **56**(7), 896.
57. J. M. Pepper and P. Supathna, *Can J Chem*, 1978, **56**(7), 899.
58. J. S. Lupoi, S. Singh, R. Parthasarathi, B. A. Simmons and R. J. Henry, *Renewable and Sustainable Energy Reviews*, 2015, **49**, 871.
59. J. Gierer, *Wood Sci. Technol.*, 1980, **14**(4), 241.
60. J. Gierer, B. Lenz, N.-H. Wallin and H. M. Seip, *Acta Chem. Scand.*, 1964, **18**, 1469.
61. J. Gierer, L.-Å. Smedman, I. Falkehag, H. Halvarson and L. Nilsson, *Acta Chem. Scand.*, 1964, **18**, 1244.

62. J. Gierer, I. Norén, S. Lukkari, A. Block-Bolten, J. M. Toguri and H. Flood, *Acta Chem. Scand.*, 1962, **16**, 1713.
63. J. Gierer, I. Kunze, A. Evang, W. G. Terry, B. Sjöberg and J. Toft, *Acta Chem. Scand.*, 1961, **15**, 803.
64. J. Gierer, B. Alfredsson, B. Skrifvars, J. Schliack and L. Reio, *Acta Chem. Scand.*, 1957, **11**, 1516.
65. M. Alekhina, O. Ershova, A. Ebert, S. Heikkinen and H. Sixta, *Industrial Crops and Products*, 2015, **66**, 220.
66. J. W. Green, I. A. Pearl and F. C. Haigh, *IPST technical paper series*, 1977, **42**.
67. M. Kannangara, M. Marinova, L. Fradette and J. Paris, *Journal of Science & Technology for Forest Products and Processes*, 2012, **2**(4), 28.
68. M. Fasching, P. Schroder, R. P. Wollboldt, H. K. Weber and H. Sixta, *Holzforschung*, 2008, **62**(1), 15.
69. R. Mörck, H. Yoshida and K. P. Kringstad, *Holzforschung*, 1986, **40**, 51.
70. McDonogh and T. Joseph, *IPST technical paper series*, 1992(455).
71. R. Rinaldi in *Catalytic hydrogenation for biomass valorization*, ed. R. Rinaldi, Royal Society of Chemistry, [England], 2015, p 74.
72. M. Wang, M. Leitch and C. Xu, *European Polymer Journal*, 2009, **45**(12), 3380.
73. M. Nagy, K. David, Britovsek, G. J. P. and A. J. Ragauskas, *Holzforschung*, 2009, **63**(5), 513.
74. K. Barta, T. D. Matson, M. L. Fettig, S. L. Scott, A. V. Iretskii and P. C. Ford, *Green Chem.*, 2010, **12**(9), 1640.
75. A. Toledano, L. Serrano, A. M. Balu, R. Luque, A. Pineda and J. Labidi, *Chemsuschem*, 2013, **6**(3), 529.
76. A. Toledano, L. Serrano, A. Pineda, A. A. Romero, R. Luque and J. Labidi, *Appl Catal B-Environ*, 2014, **145**, 43.
77. X. Erdocia, R. Prado, M. Á. Corcuera and J. Labidi, *Biomass and Bioenergy*, 2014, **66**, 379.
78. K. Barta, G. R. Warner, E. S. Beach and P. T. Anastas, *Green Chem*, 2014, **16**(1), 191.
79. T. Klamrassamee, N. Laosiripojana, D. Cronin, L. Moghaddam, Z. Zhang and W. O. S. Doherty, *Bioresource Technology*, 2015, **180**, 222.
80. F. Weinwurm, A. Drljo, W. Waldmüller, B. Fiala, J. Niedermayer and A. Friedl, *Journal of Cleaner Production*, 2016.
81. X. Erdocia, R. Prado, J. Fernández-Rodríguez and J. Labidi, *ACS Sustainable Chem. Eng.*, 2016, **4**(3), 1373.
82. E. E. Harris, J. D'lanni and H. Adkins, *J. Am. Chem. Soc.*, 1938, **60**(6), 1467.
83. J. H. Lora, R. Katzen, M. Cronlund and C. F. Wu, *Recovery of Lignin*(US4764596), 1988.
84. M. Buchmann, M. Verges and M. Leschinsky in *NWBC 2015: The 6th Nordic Wood Biorefinery Conference Helsinki, Finland, 20-22 October, 2015*, VTT, Espoo (Finlande), op. 2015, p 78.
85. M. Baumeister and E. Edel, *Process and Reactor for the Continuous Digestion of Fibrous Plant Material*(EP0090969), 1985.
86. International Organization for Standardization, *Pulps -- Determination of Kappa Number 85.040*(ISO 302:2015), 2015. http://www.iso.org/iso/home/store/catalogue_ics/catalogue_detail_ics.htm?csnumber=66533 (last accessed November 2016).
87. J. Snelders, E. Dornez, B. Benjelloun-Mlayah, W. J. J. Huijgen, P. J. de Wild, R. J. A. Gosselink, J. Gerritsma and C. M. Courtin, *Bioresource Technology*, 2014, **156**, 275.
88. M. Delmas and B. Benjelloun Mlayah, *Phenolic resin obtained by polycondensation of formaldehyde, phenol and lignin*(WO 2014/206586).

89. M. L. Minus and S. Kumar in *Kirk-Othmer Encyclopedia of Chemical Technology*, ed. John Wiley & Sons Inc, John Wiley & Sons, Inc, Hoboken, NJ, USA, 2000.
90. A. A. Lysenko, V. A. Lysenko, O. V. Astashkina and O. I. Gladunova, *Fibre Chem*, 2011, **42**(5), 278.
91. D. Chung in *Kirk-Othmer Encyclopedia of Chemical Technology*, ed. John Wiley & Sons Inc, John Wiley & Sons, Inc, Hoboken, NJ, USA, 2000, p 1.
92. E. Frank, L. M. Steudle, D. Ingildeev, J. M. Spörl and M. R. Buchmeiser, *Angewandte Chemie (International ed. in English)*, 2014, **53**(21), 5262.
93. J. W. NEWMAN, **21**, 52.
94. L. S. Singer, *Fuel*, 1981, **60**(9), 839.
95. D. A. Baker and T. G. Rials, *J. Appl. Polym. Sci.*, 2013, **130**(2), 713.
96. S. Otani, Y. Fukuoka, B. Igarashi and K. Sasaki, *Method for producing carbonized lignin fiber*(US 3,461,082), 1969.
97. Y. Nordström, I. Norberg, E. Sjöholm and R. Drougge, *J. Appl. Polym. Sci.*, 2013, **129**(3), 1274.
98. P. Axegård, P. Tomani and H. Hansson, *Road map 2014 to 2025: Swedish lignin-based carbon fibre in composite materials of the future*.
99. www.ornl.gov/manufacturing.
100. R. Paul, X. Dai, A. Hausner, A. K. Naskar and N. C. Gallego in *Carbon Fibers and their Composites*, ed. The American Carbon Society, 2015.
101. OECD, *Test No. 118: Determination of the Number-Average Molecular Weight and the Molecular Weight Distribution of Polymers using Gel Permeation Chromatography*, OECD Publishing, 1996.
102. C. M. Hansen, *Hansen solubility parameters: A user's handbook*, Crc Press, Boca Raton, 2007.
103. C. Schuerch, *J. Am. Chem. Soc.*, 1952, **74**(20), 5061.
104. <http://www.methanol.org/wp-content/uploads/2016/07/Marc-Alvarado-Global-Methanol-February-2016-IMPCA-for-upload-to-website.pdf> (last accessed April 2017).
105. X. Jiang, D. Savithri, X. Du, S. N. Pawar, H. Jameel, H.-M. Chang and X. Zhou, *ACS Sustainable Chem. Eng.*, 2016.
106. Z. Strassberger, P. Prinsen, Klis, Frits van der, Es, Daan S. van, S. Tanase and G. Rothenberg, *Green Chem*, 2015, **17**(1), 325.
107. P. Yan, Z. Xu, C. Zhang, X. Liu, W. Xu and Z. C. Zhang, *Green Chem*, 2015, **17**(11), 4913.
108. T. Saito, J. H. Perkins, F. Vautard, H. M. Meyer, J. M. Messman, B. Tolnai and A. K. Naskar, *ChemSusChem*, 2014, **7**(1), 221.
109. K. Wang, F. Xu and R. Sun, *IJMS*, 2010, **11**(8), 2988.
110. R. Sun, J. Tomkinson and G. Lloyd Jones, *Polymer Degradation and Stability*, 2000, **68**(1), 111.
111. R. W. Thring, M. N. Vanderlaan and S. L. Griffin, *Journal of Wood Chemistry and Technology*, 1996, **16**(2), 139.
112. R. Mörck, A. Reimann and K. P. Kringstad, *Holzforschung*, 1988, **42**(2), 111.
113. H. Yoshida, R. Mörck, K. P. Kringstad and H. Hatakeyama, *Holzforschung*, 1987, **41**(3), 171.
114. T. Saito, R. H. Brown, M. A. Hunt, D. L. Pickel, J. M. Pickel, J. M. Messman, F. S. Baker, M. Keller and A. K. Naskar, *Green Chem.*, 2012, **14**(12), 3295.
115. Z. Hu, X. Du, J. Liu, H.-M. Chang and H. Jameel, *Journal of Wood Chemistry and Technology*, 2016, **36**(6), 432.
116. Z. Hu, T.-F. Yeh, H.-M. Chang, Y. Matsumoto and J. F. Kadla, *Holzforschung*, 2006, **60**(4).
117. K. M. Holtman, H.-M. Chang and J. F. Kadla, *Journal of agricultural and food chemistry*, 2004, **52**(4), 720.
118. Y. Ni and Q. Hu, *J. Appl. Polym. Sci.*, 1995, **57**(12), 1441.
119. E. Stefanis, L. Constantinou and C. Panayiotou, *Ind. Eng. Chem. Res.*, 2004, **43**(19), 6253.

120. K. P. Kringstad and R. Mörck, *Holzforschung*, 1983, **37**(5), 237.
121. R. Mörck and K. P. Kringstad, *Holzforschung*, 1985, **39**(2), 109.
122. M. Nagy, M. Kosa, H. Theliander and A. J. Ragauskas, *Green Chem*, 2010, **12**(1), 31.
123. P. C. Pinto, D. V. Evtuguin and C. Pascoal Neto, *Journal of agricultural and food chemistry*, 2005, **53**(20), 7856.
124. C. Fernandez-Costas, S. Gouveia, M. A. Sanroman and D. Moldes, *Biomass Bioenerg*, 2014, **63**, 156.
125. H. Mainka, O. Täger, E. Körner, L. Hilfert, S. Busse, F. T. Edelman and A. S. Herrmann, *Journal of Materials Research and Technology*, 2015, **4**(3), 283.
126. H. E. Gottlieb, V. Kotlyar and A. Nudelman, *J. Org. Chem.*, 1997, **62**(21), 7512.
127. J. Feng, J. Jiang, Z. Yang, Q. Su, K. Wang and J. Xu, *RSC Adv*, 2016, **6**(98), 95698.
128. S. Constant, H. L. J. Wienk, A. E. Frissen, P. d. Peinder, R. Boelens, D. S. van Es, R. J. H. Grisel, B. M. Weckhuysen, W. J. J. Huijgen, R. J. A. Gosselink and Bruijninx, Pieter C. A., *Green Chem*, 2016, **18**(9), 2651.
129. F. S. Chakar and A. J. Ragauskas, *Industrial Crops and Products*, 2004, **20**(2), 131.
130. X. Huang, T. I. Korányi, M. D. Boot and Hensen, Emiel J. M., *Green Chem*, 2015.
131. M. Alekhina, J. Erdmann, A. Ebert, A. M. Stepan and H. Sixta, *J Mater Sci*, 2015, **50**(19), 6395.
132. G. Gellerstedt, *Industrial Crops and Products*, 2015, **77**, 845.
133. C. Mattsson, S.-I. Andersson, T. Belkheiri, L.-E. Åmand, L. Olausson, L. Vamling and H. Theliander, *Biomass and Bioenergy*, 2016, **95**, 364.
134. O. Faix in *Methods in lignin chemistry*, ed. S. Y. Lin and C. W. Dence, Springer-Verlag, Berlin, New York, 1992, p 83.
135. R. Beauchet, F. Monteil-Rivera and J. M. Lavoie, *Bioresource Technol*, 2012, **121**, 328.
136. R. Katahira, A. Mittal, K. McKinney, X. Chen, M. P. Tucker, D. K. Johnson and G. T. Beckham, *ACS Sustainable Chem. Eng.*, 2016.
137. J.-M. Lavoie, W. Baré and M. Bilodeau, *Bioresource Technology*, 2011, **102**(7), 4917.
138. N. Mahmood, Z. S. Yuan, J. Schmidt and C. B. Xu, *Bioresource Technol*, 2013, **139**, 13.
139. Mariefel Valenzuela Olarte, *BASE-CATALYZED DEPOLYMERIZATION OF LIGNIN AND HYDRODE-OXYGENATION OF LIGNIN MODEL COMPOUNDS FOR ALTERNATIVE FUEL PRODUCTION*, PhD, Georgia, USA, 2011.
140. V. M. Roberts, V. Stein, T. Reiner, A. Lemonidou, X. Li and J. A. Lercher, *Chem. Eur. J.*, 2011, **17**(21), 5939.
141. D. Schmiedl, S. Endisch, D. Rückert, S. Reinhardt, G. Unkelbach and R. Schweppe, *Erdöl Erdgas Kohle*, 2012, **128**(10), 357.
142. J. E. Miller, L. R. Evans, A. A. Littlewolf and D. E. Trudell, *Batch Microreactor Studies of Lignin Depolymerization by Bases: 1. Alcohol Solvents*, 2002.
143. J. E. Miller, L. R. Evans, J. E. Mudd and K. A. Brown, *Batch Microreactor Studies of Lignin Depolymerization by Bases.: 2. Aqueous Solvents*, 2002.
144. A. Toledano, L. Serrano and J. Labidi, *Fuel*, 2014, **116**, 617.
145. R. Rinaldi, ed., *Catalytic hydrogenation for biomass valorization*, Royal Society of Chemistry, [England], 2015.
146. G. Brunner, *The Journal of Supercritical Fluids*, 2009, **47**(3), 382.
147. Virginia Marie Roberts, *Homogeneous and heterogeneous catalyzed hydrolysis of lignin*, PhD, Munich, 2008.
148. D. R. Dimmel and R. M. Kaylor, *IPST technical paper series*, 1995(552).
149. R. W. Thring, *Biomass and Bioenergy*, 1994, **7**(1-6), 125.

150. J. S. Shabtai and W. Zmierczak W., *Process for Conversion of Lignin to Reformulated Hydrocarbon Gasoline*(5,959,167), 1999.
151. D. K. Johnson, E. Chornet, W. Zmierczak W. and J. S. Shabtai, *Fuel Chemistry Division Preprints*, 2002, **47**(1), 380.
152. J. S. Shabtai and W. Zmierczak W., *Process for Conversion of Lignin to Reformulated Partially Oxygenated Gasoline*, 26(US 6,172,272 B1), 2001.
153. J. S. Shabtai, W. Zmierczak W., E. Chornet and D. Johnson, *PROCESS FOR CONVERTING LIGNINS INTO A HIGH OCTANE ADDITIVE*(US 2003/0100807 A1), 2001.
154. J. S. Shabtai, W. Zmierczak W. and E. Chornet, *Process for conversion of lignin to reformulated, partially oxygenated gasoline*(US6172272B1), 2001.
155. A. Vigneault, D. K. Johnson and E. Chornet, *Can J Chem Eng*, 2007, **85**(6), 906.
156. A. Vigneault, D. K. Johnson and E. Chornet in *Science in thermal and chemical biomass conversion*, ed. A. V. Bridgwater and D. G. B. Boocock, CPL Press, Speen, 2006, p 1401.
157. <https://mcgroup.co.uk/news/20140131/global-phenol-supply-exceed-107-mln-tonnes.html> (last accessed January 2017).
158. J. Miller, L. Evans, A. Littlewolf and D. Trudell, *Fuel*, 1999, **78**(11), 1363.
159. M. Brebu and C. Vasile, *Cell Chem Technol*, 2010, **44**(9), 353.
160. J.-M. Lavoie, E. Capek-Menard, H. Gauvin and E. Chornet, *Bioresource Technology*, 2010, **101**(13), 4940.
161. Z. Yuan, S. Cheng, M. Leitch and C. C. Xu, *Bioresource Technology*, 2010, **101**(23), 9308.
162. V. E. Madzhidova, G. N. Dalimova and B. K. Pulatov, *Khim Prir Soedin+*, 1996(5), 743.
163. K. Okuda, M. Umetsu, S. Takami and T. Adschiri, *Fuel Processing Technology*, 2004, **85**(8-10), 803.
164. J. Lofstedt, C. Dahlstrand, A. Orebom, G. Meuzelaar, S. Sawadjoon, M. V. Galkin, P. Agback, M. Wimby, E. Corresa, Y. Mathieu, L. Sauvanaud, S. Eriksson, A. Corma and J. S. M. Samec, *ChemSusChem*, 2016, **9**(12), 1392.
165. H. Mainka, L. Hilfert, S. Busse, F. Edelmann, E. Haak and A. S. Herrmann, *Journal of Materials Research and Technology*, 2015, **4**(4), 377.
166. I. Brodin, E. Sjöholm and G. Gellerstedt, *Journal of Analytical and Applied Pyrolysis*, 2010, **87**(1), 70.
167. M. Anteunis and Y. Rommelaere, *Bull. Soc. Chim. Belges*, 1970, **79**(9-10), 523.
168. F. G. Calvo-Flores, J. A. Dobado Jiménez, J. I. Garcia and F. J. Martín-Martínez, *Lignin and lignans as renewable raw materials: Chemistry, technology and applications*, John Wiley and Sons, Inc, Chichester, West Sussex, UK, 2015.
169. Nguyen, T. D. H., M. Maschietti, L. E. Amand, L. Vamling, L. Olausson, S. I. Andersson and H. Theiliander, *Bioresource Technol*, 2014, **170**, 196.
170. <https://www.methanex.com/our-business/pricing> (last accessed August 2017).
171. <https://www.alibaba.com/showroom/price-for-sodium-hydroxide.html> (last accessed August 2017).
172. https://www.alibaba.com/trade/search?fsb=y&IndexArea=product_en&CatId=&Search-Text=H2SO4 (last accessed August 2017).
173. D. Pescia and C. Reidl, *Comparing electricity prices for industry*, 2014.
174. <https://www.eia.gov/naturalgas/weekly/> (last accessed August 2017).
175. Theilen Maschinenbau GmbH, *Inquiry - dryer*, 2016.
176. Amrhein & Testi GmbH, *Inquiry - CSTR*, 2016.
177. MSE-Filterpressen GmbH, *Inquiry - filter press*, 2016.

178. Josef Emmerich Pumpenfabrik GmbH, *Inquiry - membrane pump*, 2016.
179. Apaco AG, *Inquiry - heat exchanger*, 2016.
180. M. Oshima, Y. Maeda and K. Kashima, *Process of Liquefaction of Lignin*(3105095), 1963.
181. Schuman, *Hydrogenation of Sulphite Liquors*(851709), 1970.
182. P. Urban and D. J. Engel, *Process for Liquefaction of Lignin*(4731491), 1988.
183. E. G. Baker and D. C. Elliott, *Method of Upgrading Oils Containing Hydroxyaromatic Hydrocarbon Compounds to Highly Aromatic Gasoline*(5180868), 1993.
184. J. S. Shabtai, W. Zmierczak W., E. Chornet and D. Johnson, *PROCESS FOR CONVERTING LIGNINS INTO A HIGH OCTANE BLENDING COMPONENT*(US 2003/0115792 A1), 2002.
185. J. Q. Chen and M. Blaise, *Aromatic Hydrocarbons from Depolymerization and Deoxygenation of Lignin*(US 2014/0250773 A1), 2014.
186. Fachagentur Nachwachsende Rohstoffe e.V., *Güzlöwer Fachgespräche - Stoffliche Nutzung von Lignin*, Bundesministerium für Ernährung, Landwirtschaft und Verbraucherschutz, Berlin, 2009, 238.
187. J. Zakzeski, Bruijninx, Pieter C. A., A. L. Jongerius and B. M. Weckhuysen, *Chem. Rev.*, 2010, **110**(6), 3552.
188. A. Tanksale, J. N. Beltramini and G. Q. Lu, *Dev. Chem. Eng. Mineral Process.*, 2006, **14**(1-2), 9.
189. R. C. Runnebaum, T. Nimmanwudipong, D. E. Block and B. C. Gates, *Catal Sci Technol*, 2012, **2**(1), 113.
190. M. B. Valenzuela, C. W. Jones and P. K. Agrawal, *Energ Fuel*, 2006, **20**(4), 1744.
191. A. L. Jongerius, *Catalytic Conversion of Lignin for the Production of Aromatics*, PhD, 2013.
192. J. Zakzeski, A. L. Jongerius, Bruijninx, Pieter C. A. and B. M. Weckhuysen, *ChemSusChem*, 2012, **5**(8), 1602.
193. K. Koichumanova, Vikla, A. K. K., de Vlieger, D. J. M., K. Seshan, B. L. Mojet and L. Lefferts, *Chemsuschem*, 2013, **6**(9), 1717.
194. A. Plugatyr and I. M. Svishchev, *The journal of physical chemistry. B*, 2011, **115**(11), 2555.
195. J. B. Butt and E. E. Petersen, *Activation, Deactivation, and Poisoning of Catalysts*, Academic Press, Inc., 1988.
196. P. HARRIS, *J Catal*, 1986, **97**(2), 527.
197. A. L. Jongerius, J. R. Copeland, G. S. Foo, J. P. Hofmann, Bruijninx, P. C. A., C. Sievers and B. M. Weckhuysen, *Acs Catal*, 2013, **3**(3), 464.
198. R. Samuel, M. Foston, N. Jaing, S. Cao, L. Allison, M. Studer, C. Wyman and A. J. Ragauskas, *Fuel*, 2011, **90**(9), 2836.
199. J. Rencoret, G. Marques, A. Gutiérrez, L. Nieto, J. I. Santos, J. Jiménez-Barbero, Á. T. Martínez and J. C. del Río, *Holzforschung*, 2009, **63**(6).

Appendix

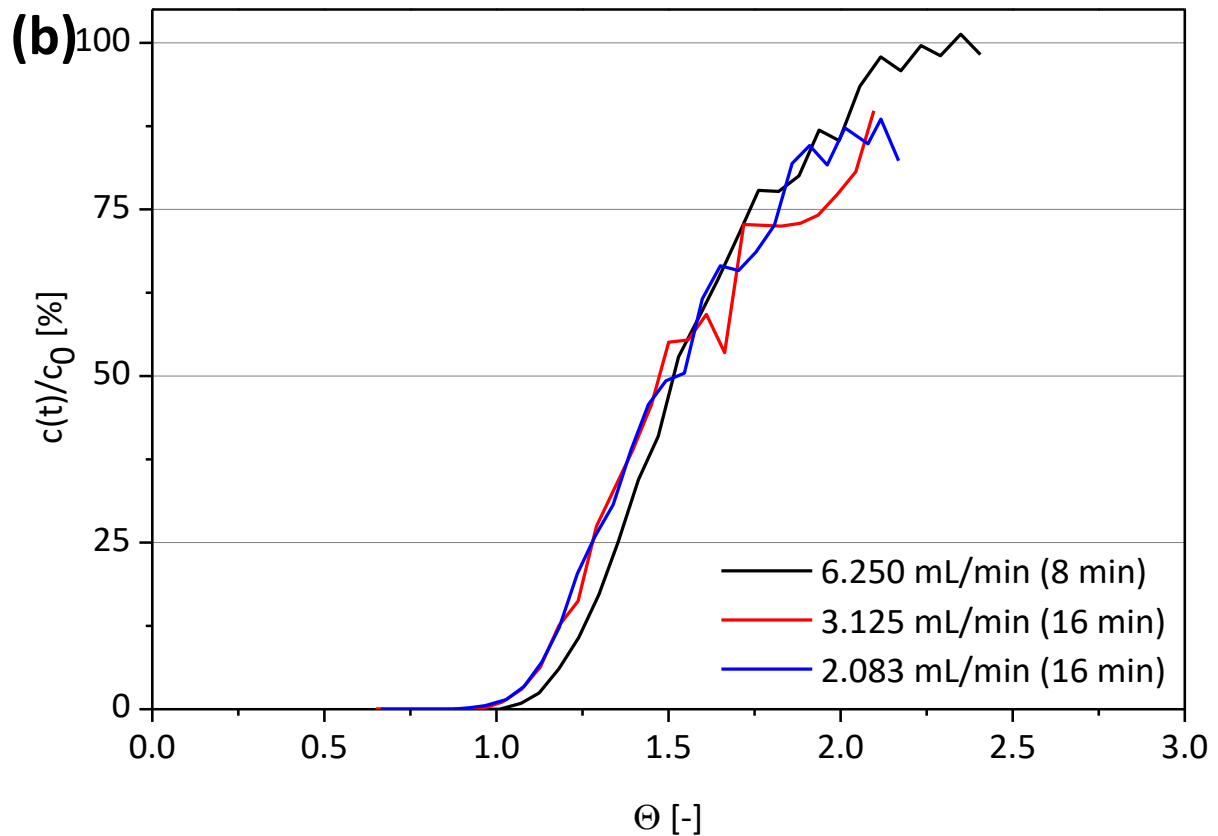
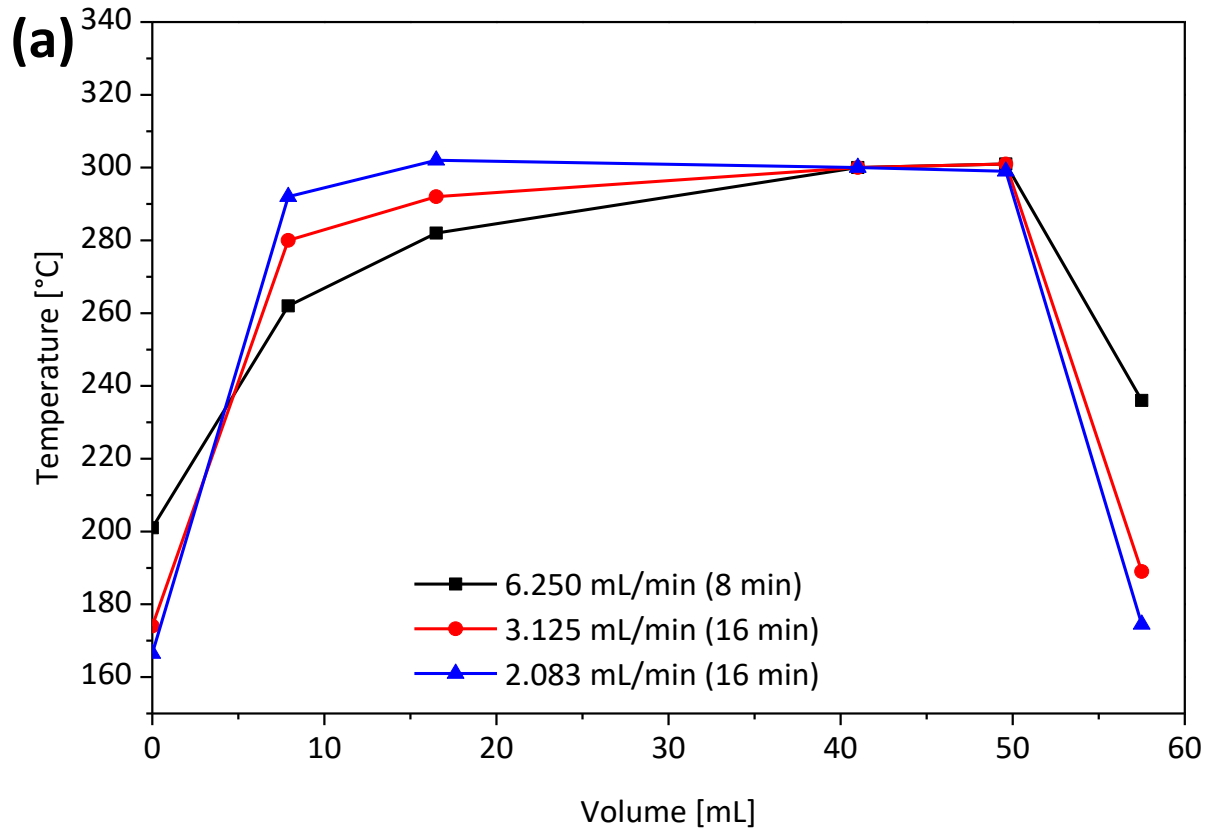


Figure A 1: (a) Temperature profile of the continuous flow reactor for three different flow rates. (b) $t_{\text{retention}}$ characteristics of the continuous test-rig.

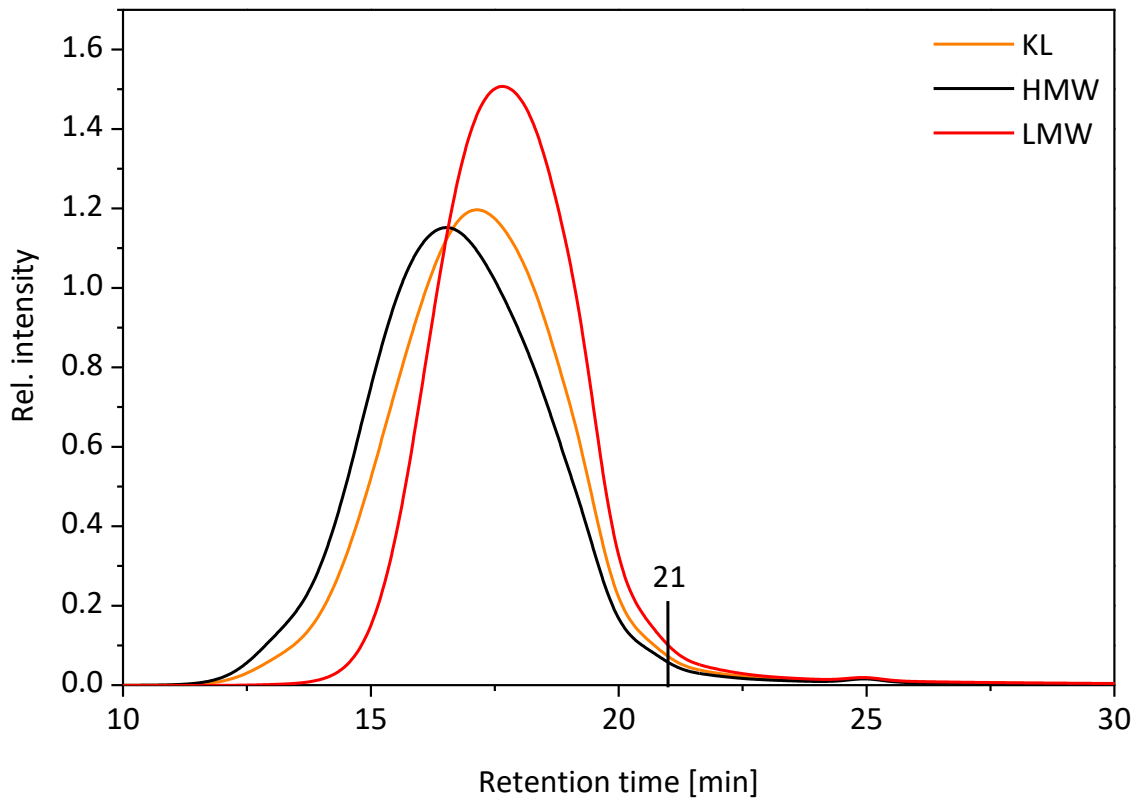


Figure A 2: GPC elution chromatogram for KL, HMW and LMW after MeOH extraction.

Table A 1: m_i/m and n_i/n for the fractions KL, HMW, and LMW for C_9 -Units > 100

Fraction		C ₉ -Units		
		{100,200}	{200,500}	{500,1000}
KL	m_i/m	3.5	1.5	0.2
	n_i/n	0.2	0.0	0.0
HMW	m_i/m	5.7	2.7	0.5
	n_i/n	0.3	0.1	0.0
LMW	m_i/m	0.3	0.1	0.0
	n_i/n	0.0	0.0	0.0

$$\omega_d = \frac{m_{\text{lignin,dissolved}}}{m_{\text{lignin}}} \quad (\text{A } 1)$$

$$\omega_u = \frac{m_{\text{lignin,undissolved}}}{m_{\text{lignin}}} = 1 - \omega_d \quad (\text{A } 2)$$

$$\min \left[(C\%_{\text{lignin}} - \omega_d C\%_d + (1 - \omega_d) C\%_u)^2 + (S\%_{\text{lignin}} - \omega_d S\%_d + (1 - \omega_d) S\%_u)^2 \right] \quad (\text{A } 3)$$

Minimum value problem for the mass balance after extraction *via* the results from the elemental analysis. Subscripts *d* and *u* correspond to dissolved and undissolved, respectively. *C%* and *S%* are the percentages of carbon and sulphur from the elemental analysis.

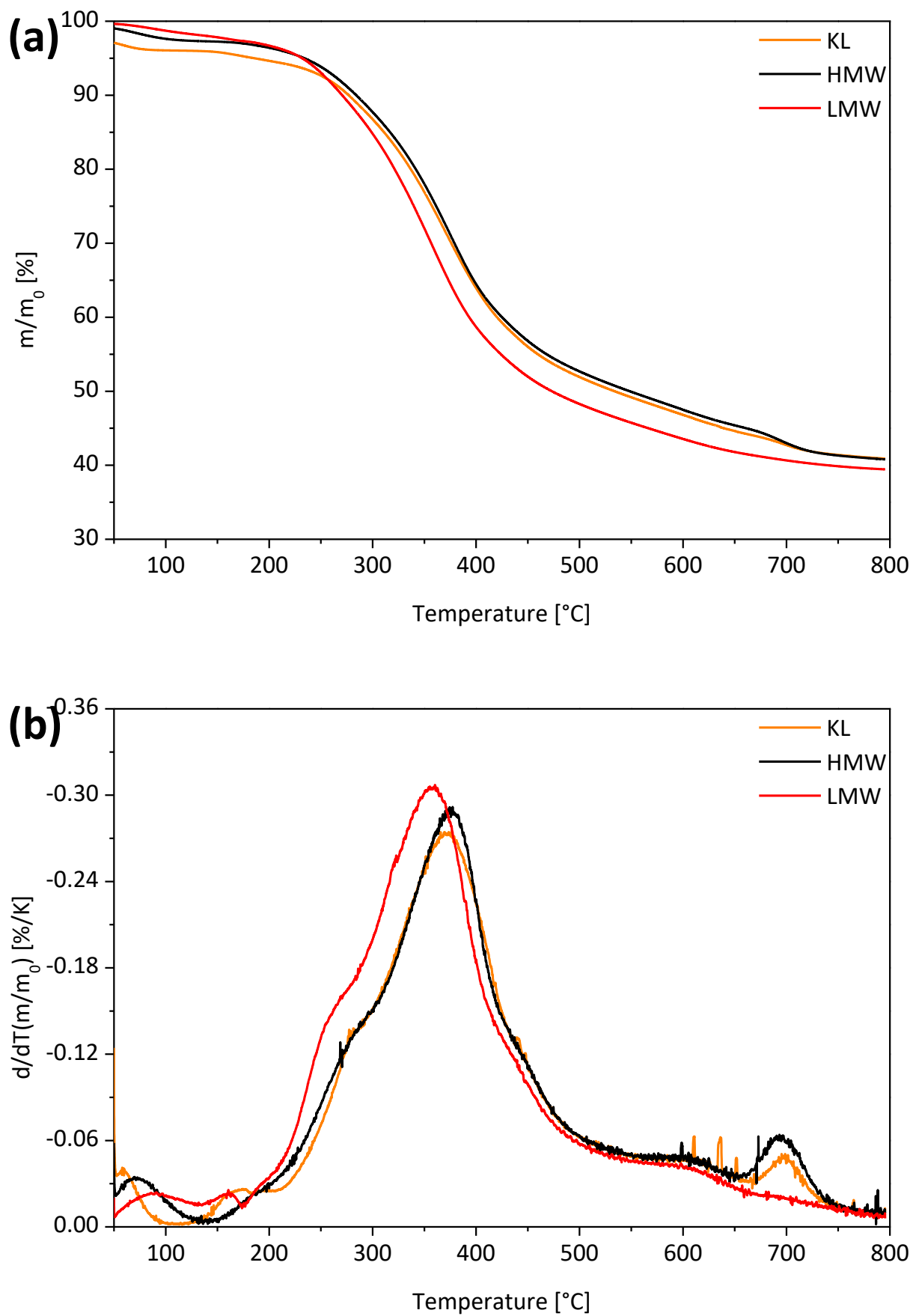


Figure A 3: (a) TGA and (b) DTG of KL, HMW, LMW performed up to 800 $^{\circ}\text{C}$, showing a peak at 700 $^{\circ}\text{C}$ in the KL and HMW fractions.

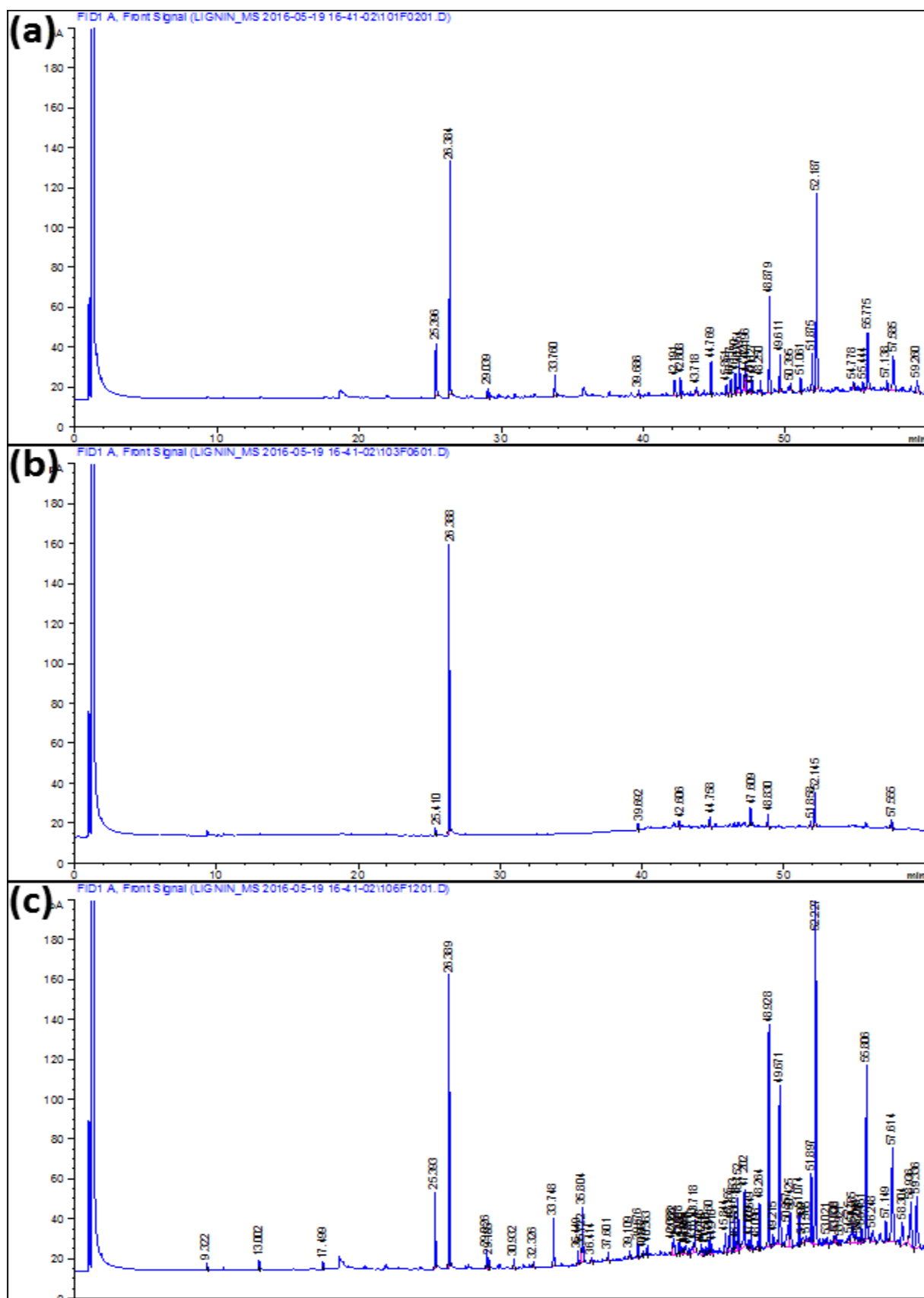


Figure A 4: GC-FID chromatograms of KL (a), MeOH soluble fraction (b), and MeOH insoluble fraction (c). Of each fraction 50 mg/mL were dissolved in acetone.

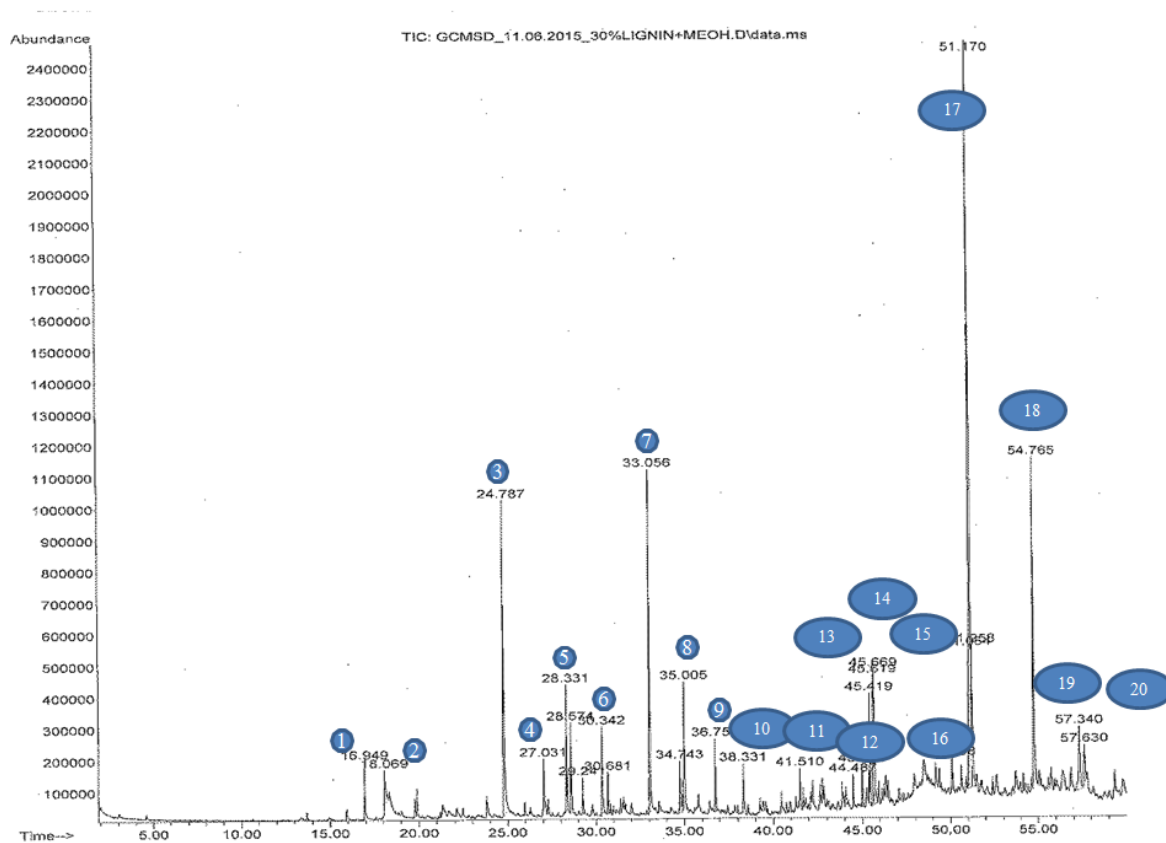
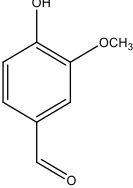
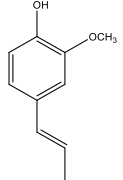
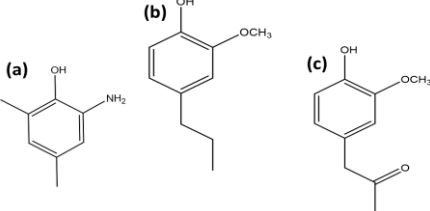
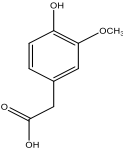
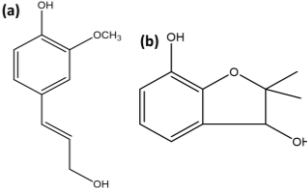
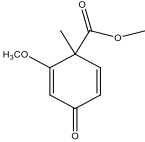
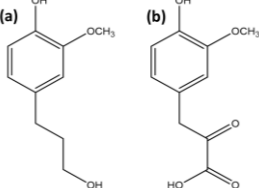
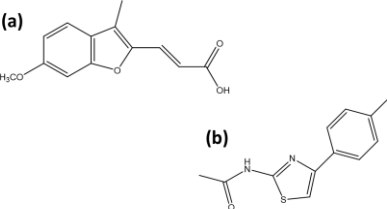
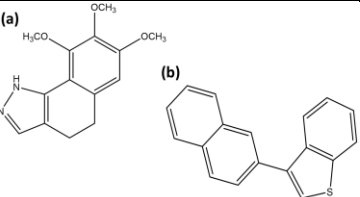
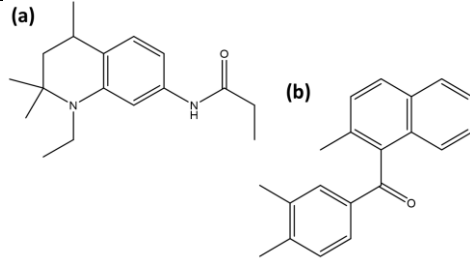
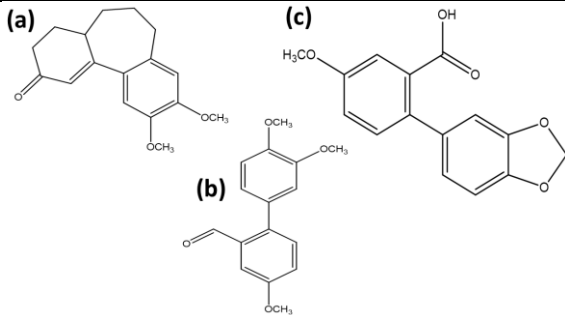
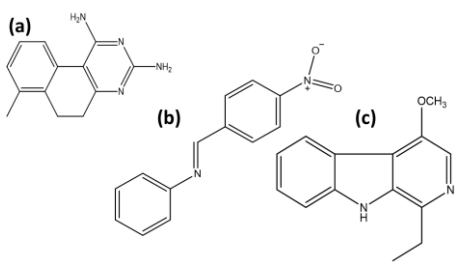
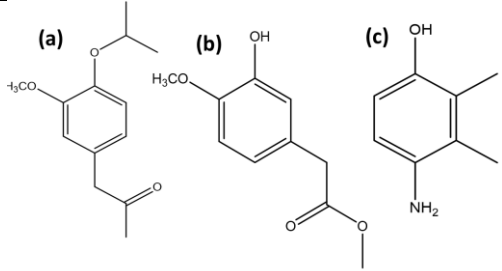
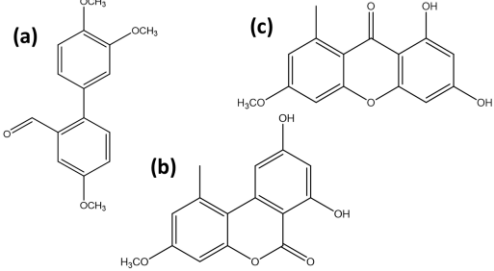
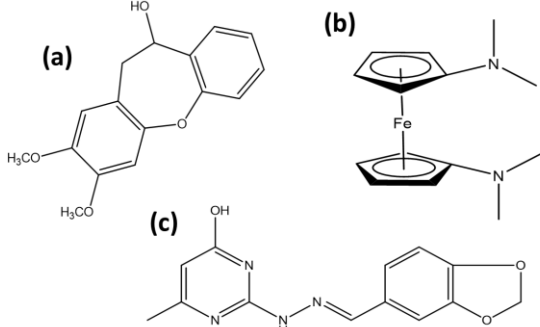


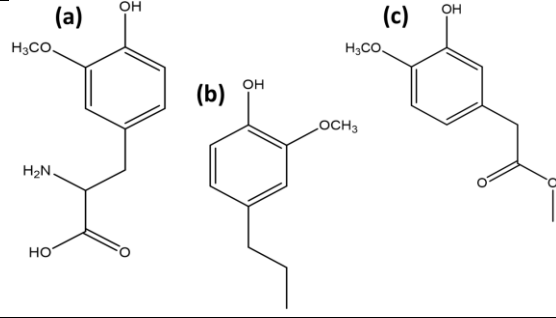
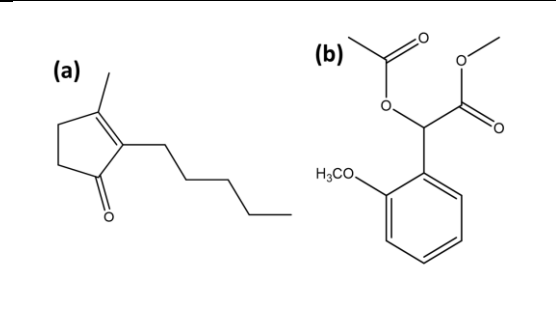
Figure A 5: GC-MS of 30 wt.% KL dissolved in MeOH. The GC detectable compounds represent *ca.* 10% of the lignin (v.s.).

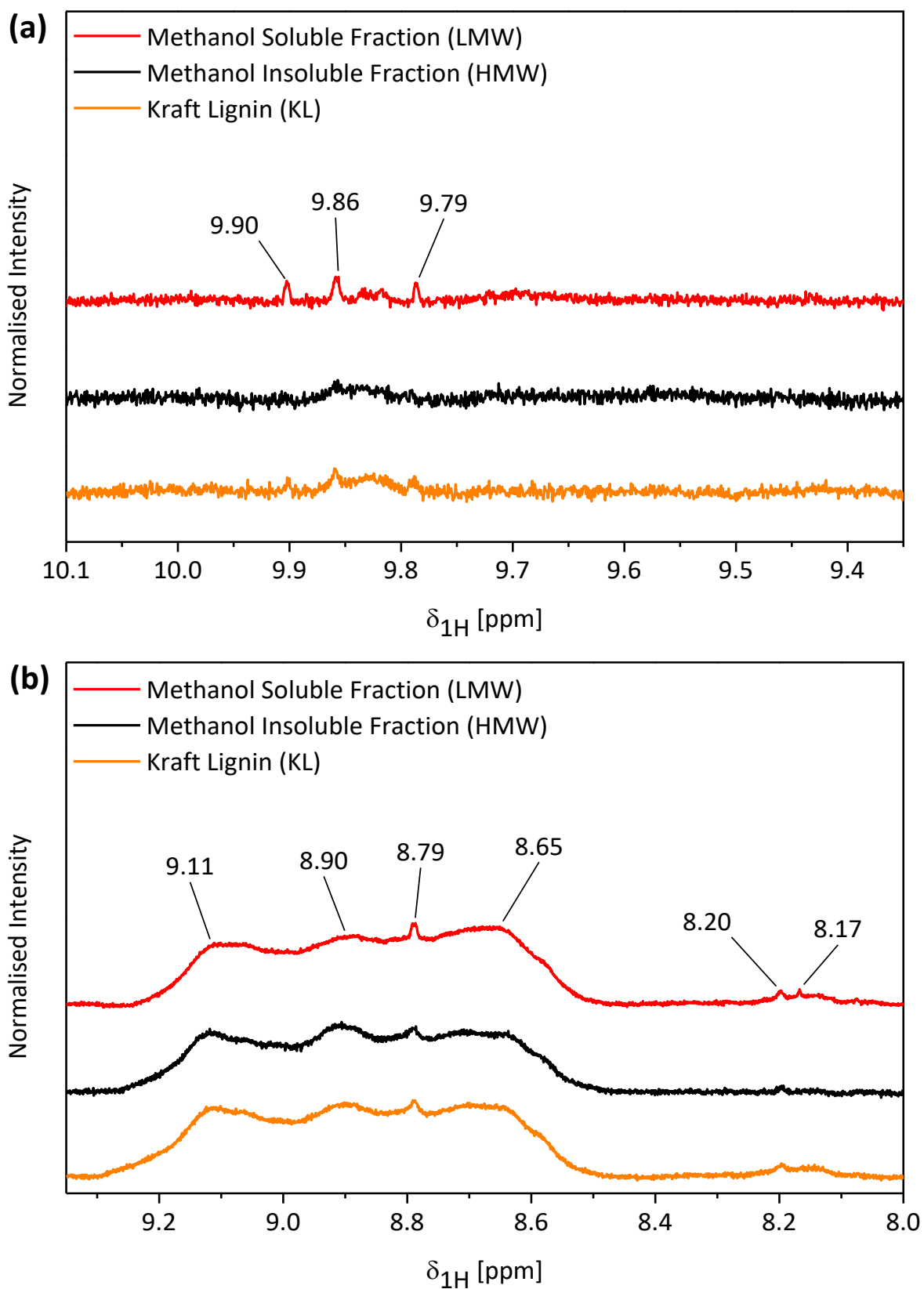
Table A 2: Major compounds of the chromatogram from (Figure A 5) defined via the NIST database. Note: Some of the compounds are definitely known (#2), some have a high probability to be similar (#17), and some are very improbable (#18, ferrocene).

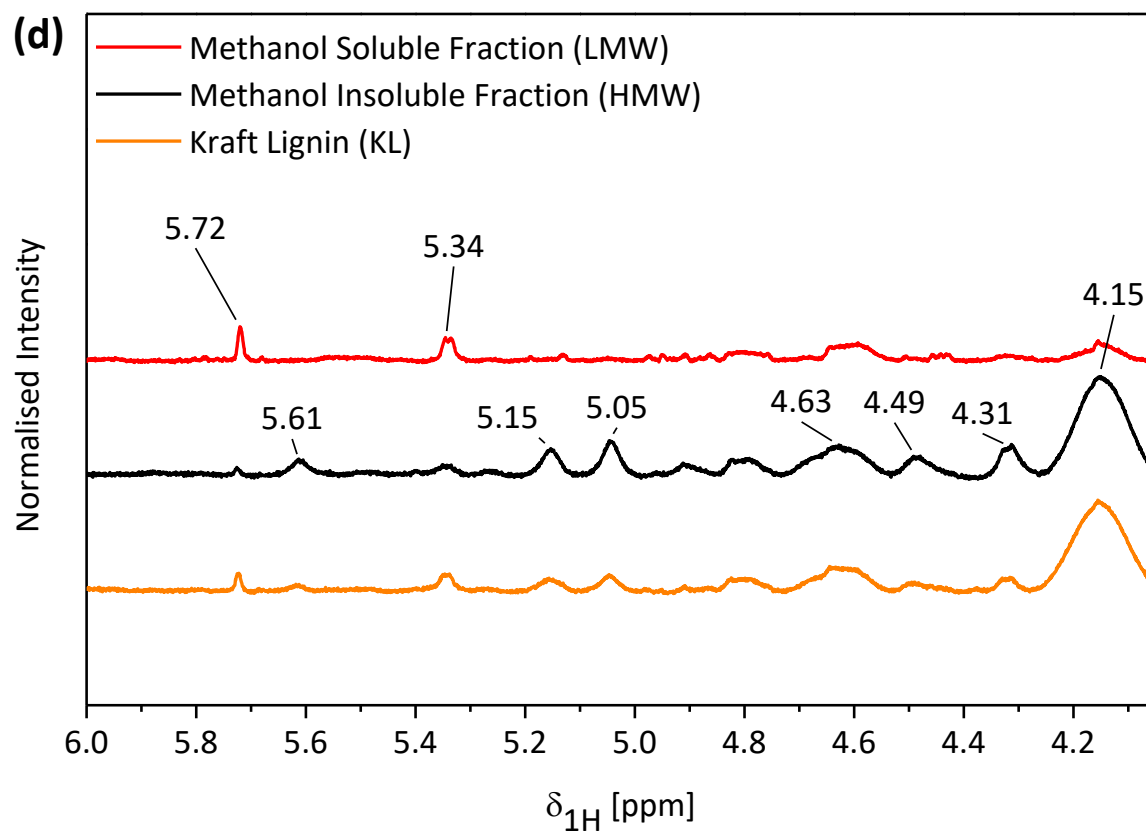
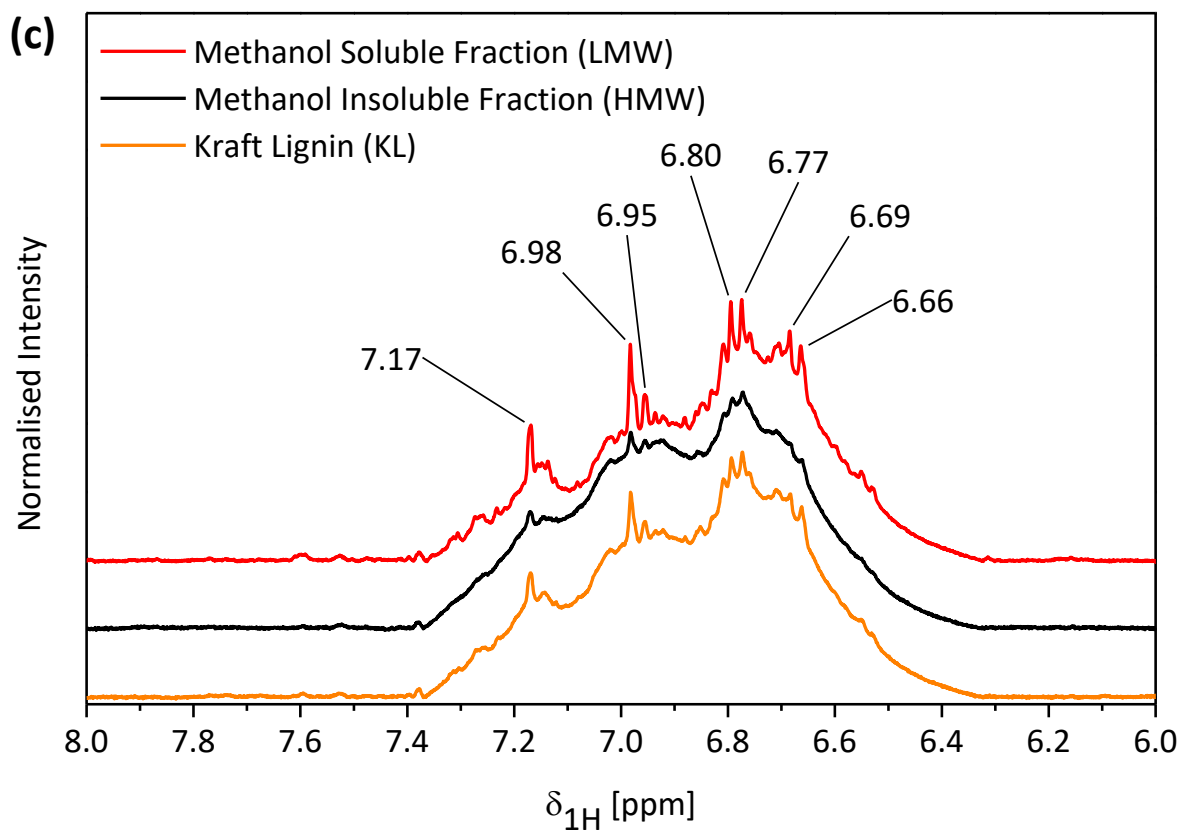
#	Compound (probability %)	Chemical Structure
1 16.949 1.22	2-Cyclopenten-1-one, 2-hydroxy-3,4-dimethyl	
2 18.067 1.17	Guaiacol (100, calibrated)	
3 24.787 9.84	Vinylguaiacol (100, calibrated)	

4 27.031 1.87	Vanillin (94)	
5 28.330 2.89	Isoeugenol (94)	
6 30.343 2.44	(a) 2-Amino-4,6-dimethylphenol (64) (b) 2-Methoxy-4-Propylphenol (56) (c) Guaiacylacetone (50)	
7 33.057 8.53	Homovanillic acid (81)	
8 35.004 3.44	(a) Coniferylalcohol (95) (b) 2,3-Dihydro-2,2-Dimethyl Benzofuran-3,7-diol (47)	
9 36.754 1.53	2,5-Cyclohexadiene-1-carboxylic acid, 2-methoxy-1-methyl-4-oxo-, methyl ester (95)	
10 38.331 1.31	(a) Homovanillyl alcohol (64) (b) Guaiacol, Pyruvic Acid (59)	
11 41.512 0.88	(a) 3-(6-Methoxy-3-methyl-2-benzofuranyl) acrylic acid (58) (b) 2-(4-p-Tolyl-thiazol-2-yl)-acetamide (52)	
12 45.004 1.03	(a) 7,8,9-Trimethoxy-4,5-dihydro-1H-benzotriazole (42) (b) 3-(2-Naphtyl) benzo[b]thiophene (38)	

13 45.417 2.36	(a) N-[(1-Ethyl-1,2,3,4-tetrahydro-2,2,4-trimethylquinolin)-7-yl]propanamide (87) (b) Naphthalene, 2-methyl-(3,4-dimethylbenzoyl) (72)	
14 45.617 3.07	(a) 3,4,4a,5,6,7-Hexahydro-9,10-dimethoxy-2-oxo-2H-dibenzo(a,c)cycloheptene (70) (b) 1,1'-Biphenyl-3,4,4'-trimethoxy-6'-formyl- (62) (c) 4-methoxy-4',5'-methylendioxybiphenyl-2-carboxylic acid (52)	
15 45.668 4.51	(a) 7-methyl-5,6-dihydrobenzo[f]quinazoline-1,3-diamine (58) (b) (4-Nitro-Benzylidene)-Phenyl-Amine (52) (c) 1-Ethyl-4-methoxy-9H-pyrindo[3,4-b]indole (Crenatine) (50)	
16 51.053 3.55	(a) 1-(3-methoxy-4-propan-2-yloxyphenyl)propan-2-one (47) (b) Methyl 4-hydroxy-3-methoxyphenylacetate (43) (c) 4-Amino-2,3-xylenol (43)	
17 51.169 26.35	(a) 1,1'-Biphenyl-3,4,4'-trimethoxy-6'-formyl- (64) (b) 1-Methyl-3-methoxy-7,9-dihydroxy-6H-dibenzo[b,d]pyran-6-one (59) (c) 1,3-Dihydroxy-6-methoxy-8-methyl-9H-xanthen-9-one (59)	
18 51.258 3.89	(a) 2,3-Dimethoxy-10,11-dihydrodibenzo[b,f]oxepin-10-ol (83) (b) Ferrocene, 1,1'-bis(dimethylamino) (58) (c) 1,3-benzodioxole-5-carbaldehyde (4-hydroxy-6-methyl-2pyrimidinyl)hydrazone (38)	

19 54.766 7.78	(a) 3-hydroxy-o-methyltyrosine (43) (b) 4-Propylguaiacol (38) (c) Methyl 4-hydroxy-3-methoxyphenylacetate (38)	
20 57.341 3.12	(a) 3-Methyl-2-pentyl-2-cyclopenten-1-one -> Dihydrojasmone (30) (b) Methyl 2-acetyloxy-2-(2-methoxyphenyl)acetate (22)	





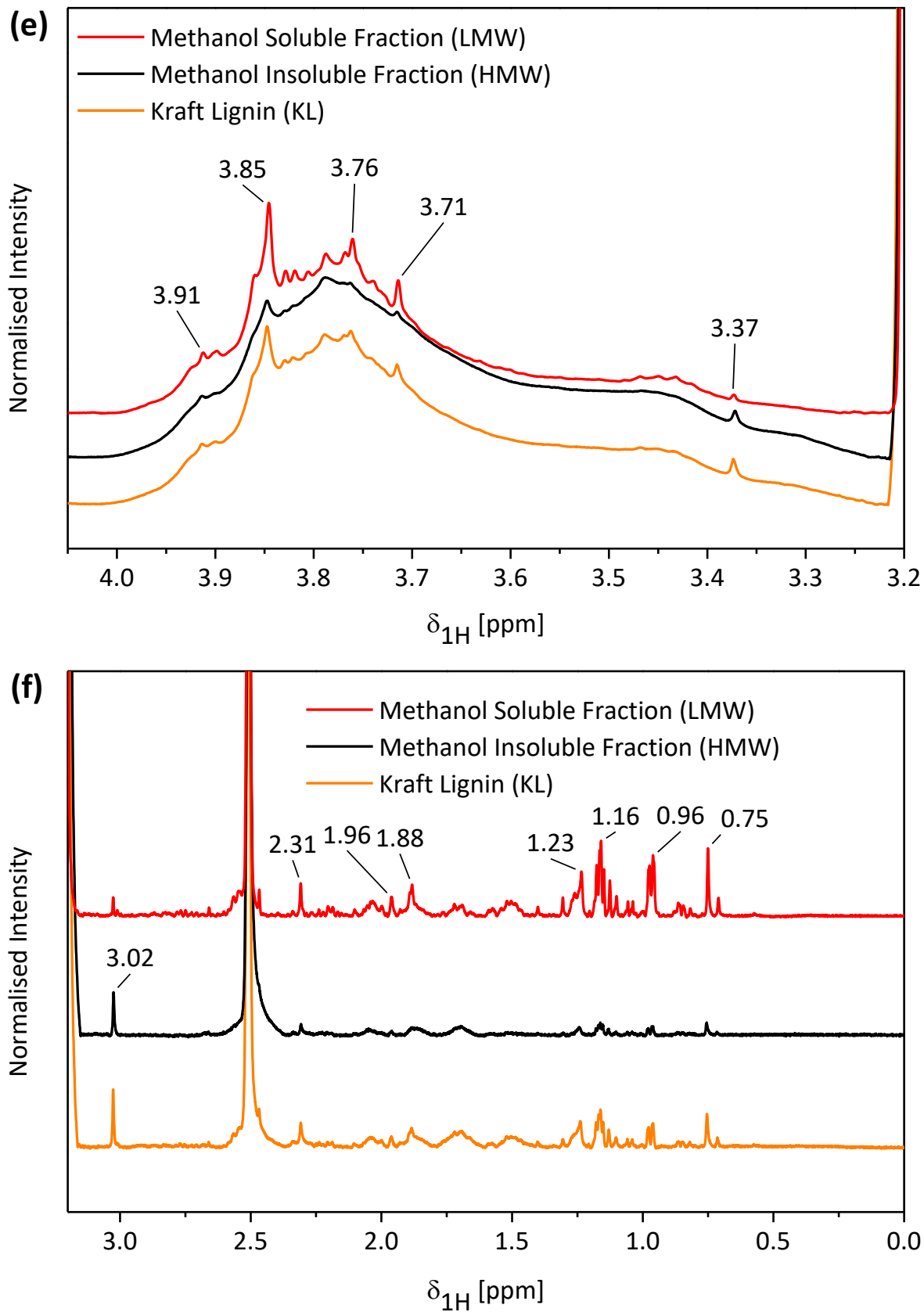


Figure A 6: ^1H NMR of KL, HMW, and LMW with zoomed areas. (a) area 1 from $\delta_{1H} = 10.10$ to 9.35 ppm, (b) area 2 from $\delta_{1H} = 9.35$ to 8.00 ppm, (c) area 3 from $\delta_{1H} = 8.00$ to 6.00 ppm, (d) area 4 from $\delta_{1H} = 6.00$ to 4.05 ppm, (e) area 5 from $\delta_{1H} = 4.05$ to 3.20 ppm, (f) area 6 from $\delta_{1H} = 3.20$ to 0 ppm

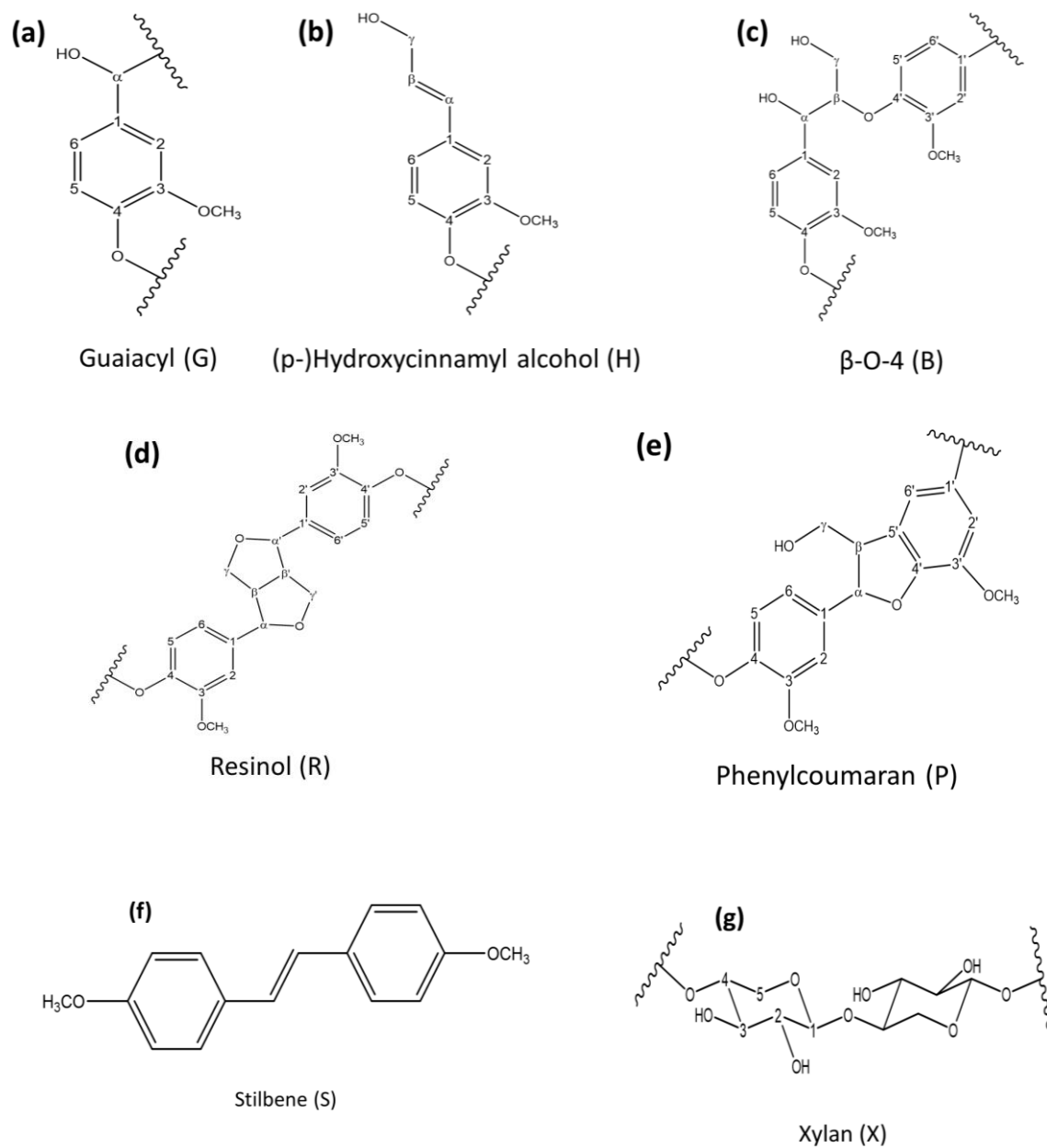


Figure A 7: Structures in lignin with numbered carbon atoms for identification via NMR.

Table A 3: ^1H - ^{13}C HSQC peak assignment. All sources used DMSO- d_6 as solvent

Label	Chemical shift [ppm]		Label	Chemical shift [ppm]	
	^{13}C	^1H		^{13}C	^1H
R_α	85.6	4.62 ¹²⁴	G_2	112.2	6.82 ¹²⁴
	85.7	4.60 ¹²⁵		109.6	7.12 ¹²⁵
	84.8	4.65 ¹²⁷		110.9	6.98 ¹²⁷
	85.7	4.6 ¹⁹⁸		111.4	7.0 ¹⁹⁸
	85.4	4.64 ¹⁹⁹		111.5	6.99 ¹⁹⁹
R_β	53.7	3.12 ¹⁹⁹	G_5	115.8	6.75 ¹²⁴
	54.1	3.06 ¹²⁴		115.6	6.8 – 6.6 ¹²⁵
	54.0	3.05 ¹²⁵		116.0	6.79 ¹²⁷
	53.5	3.06 ¹²⁷		115.0	6.8 ¹⁹⁸
R_γ	71.5	4.16, 3.78 ¹²⁴	G_6	115.2	6.94 and 6.71 ¹⁹⁹
	70.4	4.08, 3.73 ¹²⁵		120.0	6.94 ¹²⁴
	71.7	4.17, 3.81 ¹⁹⁹		121.0	7.23 ¹²⁴
B_α	71.5	4.75 ¹²⁴	$-OCH_3$	119.6	6.93 ¹²⁵
	72.0 – 71.0	4.85 – 4.75 ¹²⁵		119.0	6.80 ¹²⁷
	70.5	3.10 – 3.00 ¹²⁷		119.5	6.9 ¹⁹⁸
	72.0	4.8 ¹⁹⁸		119.5	6.83 ¹⁹⁹
	72.3	4.86 ¹⁹⁹		56.3	3.74 ¹²⁵
B_β	84.4	4.30 ¹²⁴	X_1	56.3	3.75 ¹²⁴
	81.5	4.75 ¹²⁵		56.0	3.88 – 3.62, 3.36 ¹²⁷
	83.9	4.29 ¹²⁷		55.7	3.8 ¹⁹⁸
	86.0	4.2 ¹⁹⁸		102.2	4.29 ¹²⁴
	84.1	4.28 ¹⁹⁹		73.0	3.06
B_γ	59.9 – 59.3	3.75, 3.30 ¹²⁴	X_2	74.4	3.26
	61.0 – 60.2	4.12, 3.57 ¹²⁵	X_3	75.8	3.52
	59.7 – 59.5	3.63, 3.40 ¹²⁷	X_4	63.6	3.90, 3.20
	60.0	3.71, 3.38 ¹⁹⁹	X_5	Aliphatics region (from Mattsson <i>et al.</i>) ¹³³	
H_γ	62.0	4.10 ¹²⁴	^1H chemical shift [ppm]		Description
	61.4	4.10 ¹²⁷	0 – 1.0	CH ₃ at γ or further to Ar	
	61.9	4.09 ¹⁹⁹	1.0 – 1.4	CH ₃ , CH ₂ β or CH at γ to Ar	
$H_{2,6}$	128.2	7.2	1.4 – 1.9	CH ₂ , CH β to Ar	
P_α	87.4	5.5 ¹⁹⁸	1.9 – 3.5	CH ₃ , CH ₂ , CH α to Ar	
	86.8	5.46 ¹²⁷	3.5 – 4.5	CH ₂ , CH α to two Ar e.g. Ar-CH ₂ -Ar, Ar-CH(R)-AR	
	87.7	5.45 ¹⁹⁹	^{13}C chemical shift [ppm]		
P_β	53.2	3.5 ¹⁹⁸	10 – 16	CH ₃	
	53.3	3.46 ¹²⁷	16 – 23	CH ₂ , CH ₃	
	53.7	3.44 ¹⁹⁹	23 – 30	CH, CH ₂ , CH ₃	
P_γ	62.5	3.73 ¹²⁷	30 – 38	CH ₂ , CH ₂ α and CH ₂ β in Ar-CH ₂ -CH ₂ -CH ₂ -OH	
	63.3	3.66 ¹⁹⁹	38 – 44	CH, CH ₂ , CH ₃ with electron with- drawing group	

	64.1	3.27^{125}			
$S_{\alpha,\beta}$	126.6	6.9^{128}			

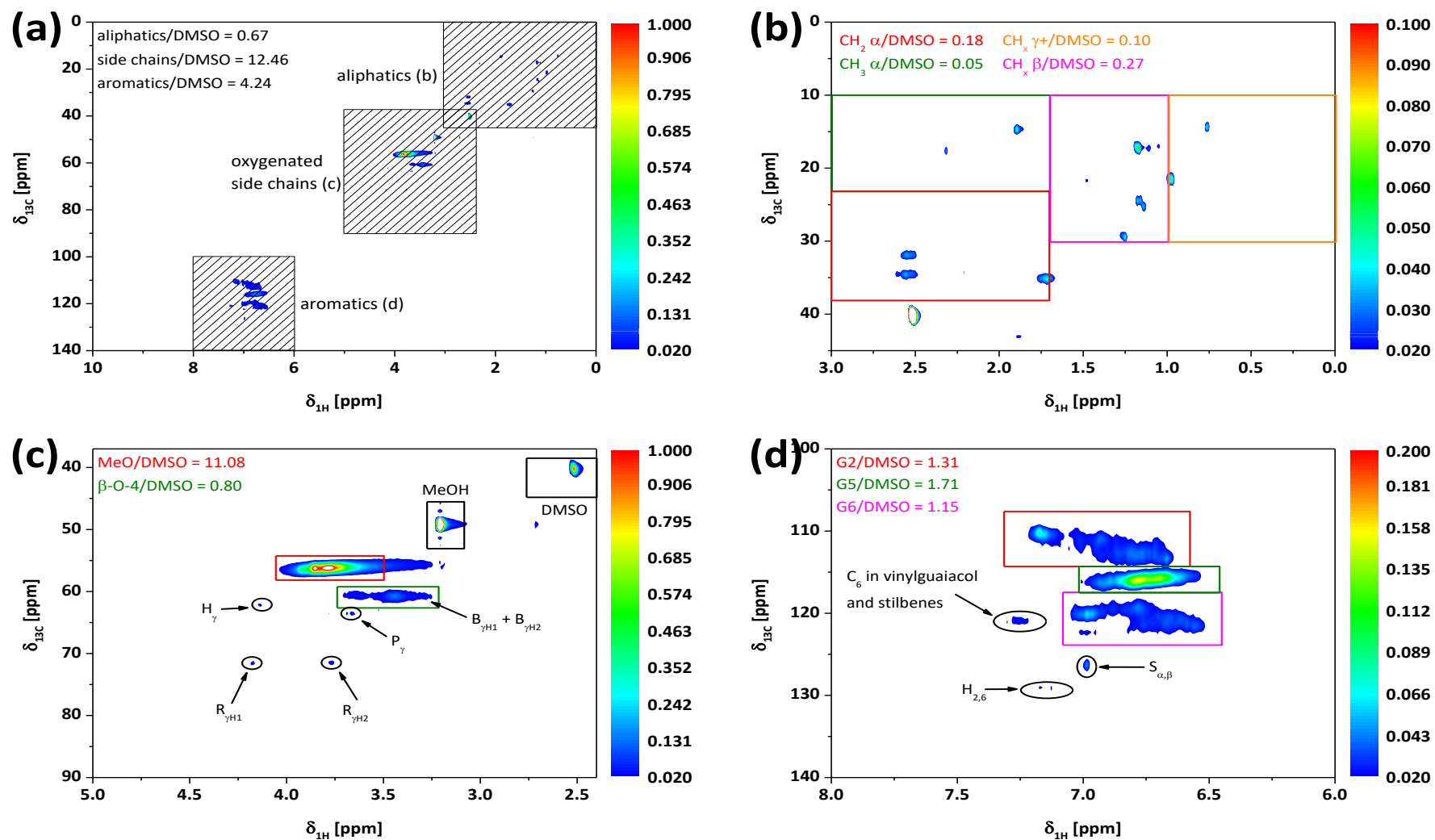


Figure A 8: 2D HSQC NMR spectra of KL. (a) overview with the three distinct areas and their respective integrated values in relation to the DMSO value, (b) aliphatics region, (c) oxygenated side chains, and (d) aromatics.

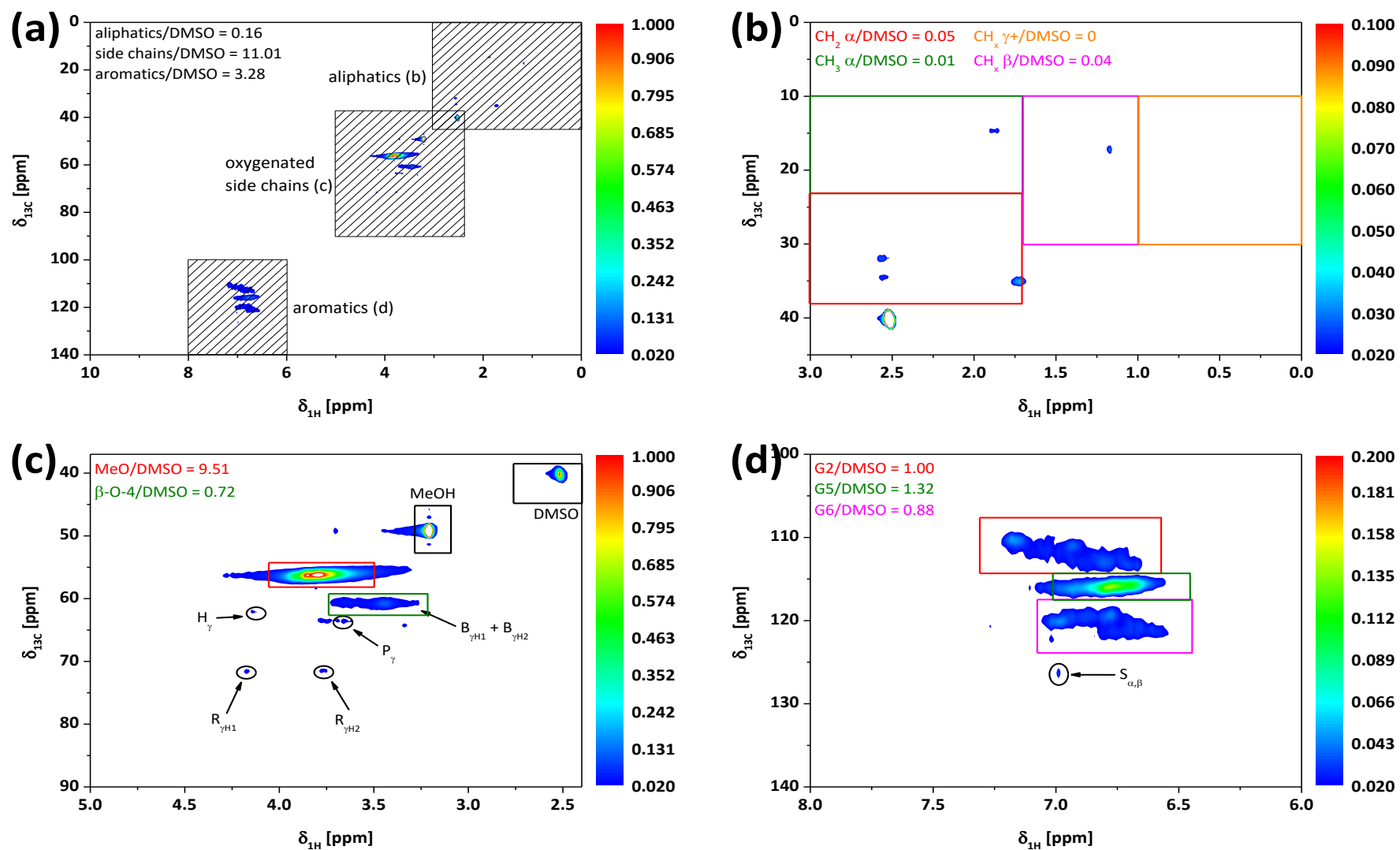


Figure A 9: 2D HSQC of HMW. (a) overview with the three distinct areas and their respective integrated values in relation to the DMSO value, (b) aliphatics region, (c) oxygenated side chains, and (d) aromatics.

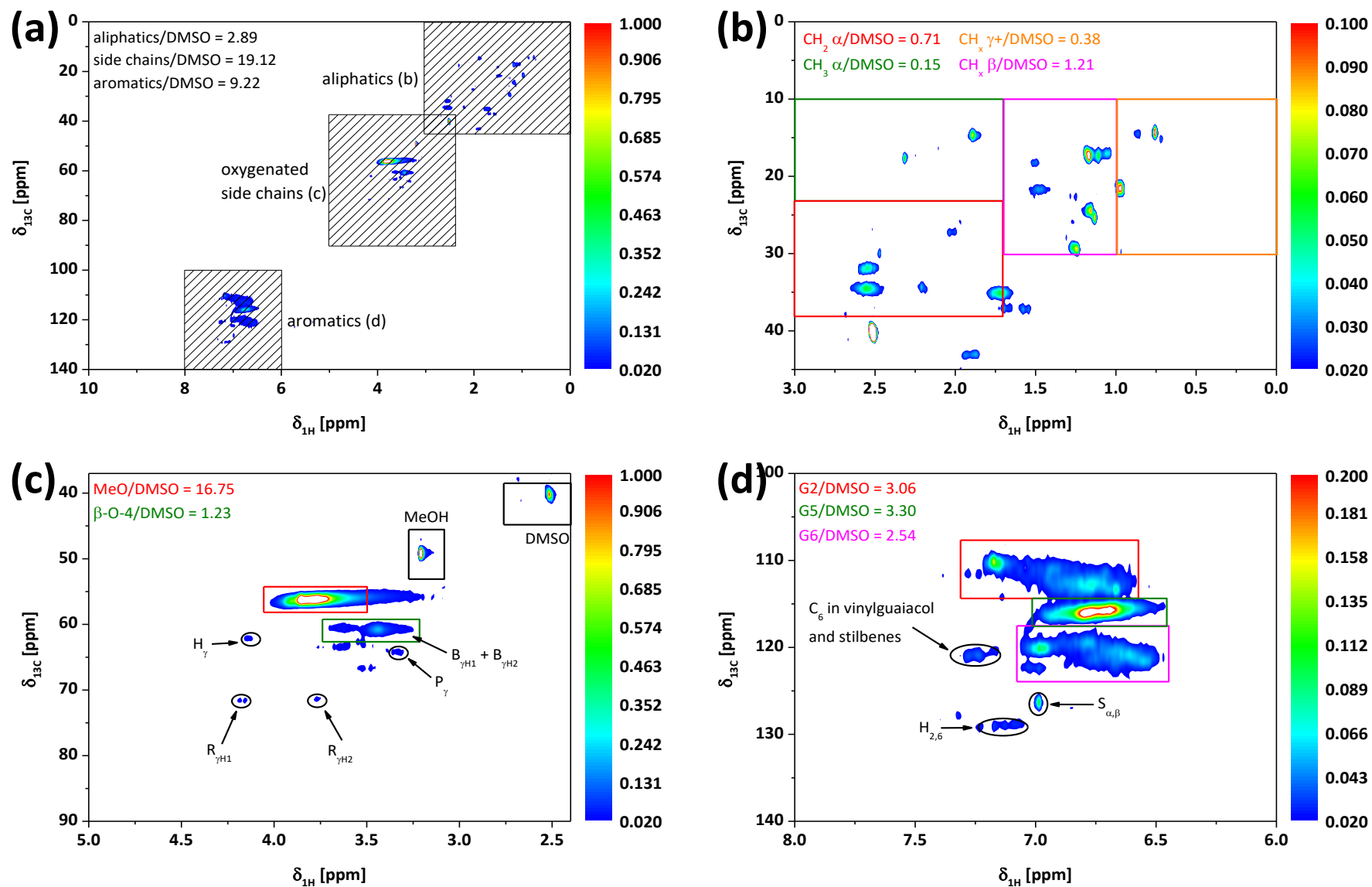


Figure A 10: 2D HSQC of LMW. (a) overview with the three distinct areas and their respective integrated values in relation to the DMSO value, (b) aliphatics region, (c) oxygenated side chains, and (d) aromatics

$$\frac{n_{\text{compound},i}}{m_{\text{lignin}}} = \frac{n_{\text{C-H of area}_i}}{m_{\text{lignin}} n_{\text{H of compound},i}} \quad (\text{A } 4)$$

$$\frac{m_{\text{compound},i}}{m_{\text{lignin}}} = \frac{n_{\text{compound},i} M_{\text{compound},i}}{m_{\text{lignin}}} \quad (\text{A } 5)$$

$$\frac{n_{\text{MeO}} M_{\text{MeO}}}{n_{\text{C}} M_{\text{C}} + n_{\text{H}} M_{\text{H}} + n_{\text{O}} M_{\text{O}} + n_{\text{S}} M_{\text{S}}} = \frac{m_{\text{OCH}_3}}{m_{\text{lignin}}} \quad (\text{A } 6)$$

RHS of equation (A 4) is the result of equation (multiplied by the number of protons of the compound i in the denominator taking into account that each C-H bond contributes to the area. Equation (A 5) is a straight forward calculation of the mass of the compound *via* its molar mass (e.g. $-\text{OCH}_3$ has $M_{\text{OCH}_3} = 31 \text{ g/mol}$). Finally, equation (A 6) is used for calculating the amount n_{MeO} when setting the n_{c} to 9. The RHS is provided *via* equation (A 5) and the LHS gives mass ratio of units of $-\text{OCH}_3$ to the total mass. C, H, O, and S in the denominator are masses of the elements present determined by EA. Afterwards the values are adjusted to a C_9 -formula by simple linear transformation.

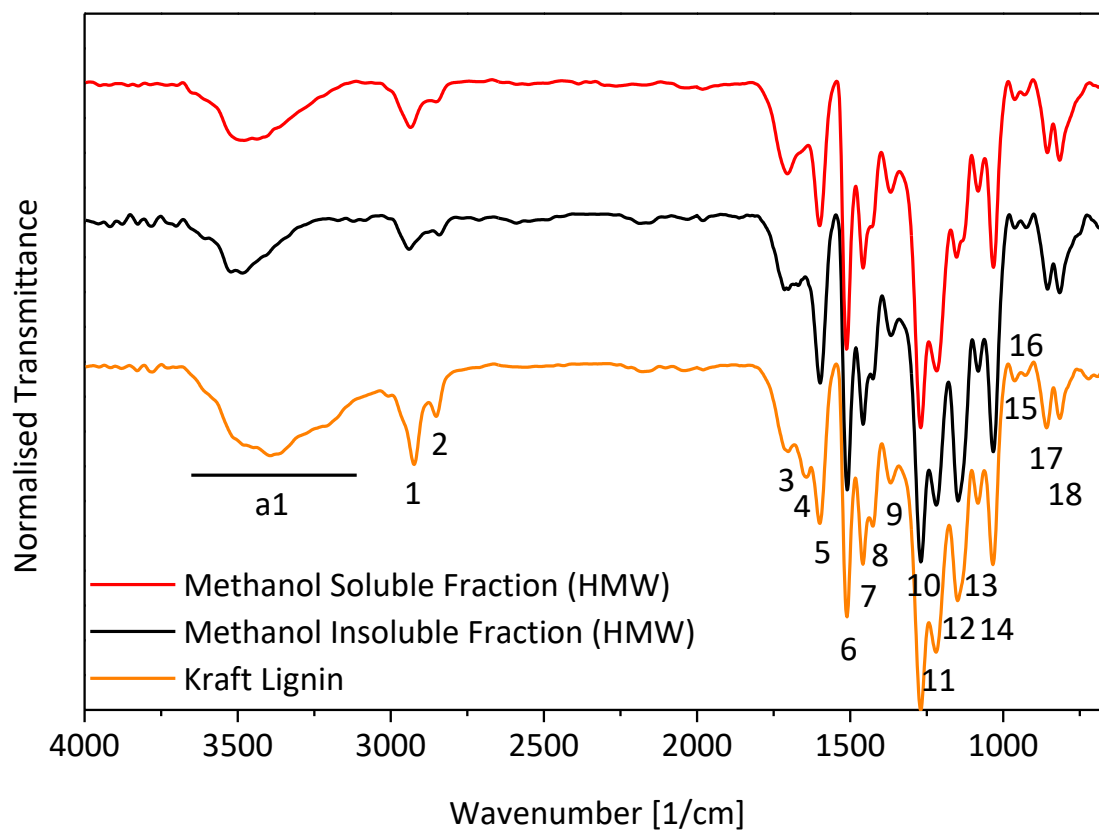


Figure A 11: Complete ATR FT-IR spectra of KL, MeOH Insoluble Fraction (HMW), and MeOH soluble fraction (LMW)

Table A 4: Absorption band assignments for the attenuated total reflection mid-infrared (ATR FT-IR) spectra. The assignments for the wavenumbers were taken from the book chapter of Faix¹³⁴ and the recent review paper of Lupoi et al.⁵⁸

Band number	Wavenumber [cm ⁻¹]			Assignment	
	KL	HMW	LMW	Wavenumber [cm ⁻¹]	Definition
a1	3678 - 3052	3656 – 3229	3675 - 3118	3430 to 3440 ⁵⁸ 3460 to 3412 ¹³⁴	OH stretch
1	2924	2941	2935	3000 to 2842 ¹³⁴ 2938 + 2840 ⁵⁸	CH stretch (methyl and methylene)
2	2852	2842	2849		
3	1702	n.a.	1704	1737, 1704, 1682 ⁵⁸ 1738 to 1709 and 1675 to 1655 ¹³⁴	C=O stretch
4	1644	n.a.	n.a.		probably also C=O stretch
5	1599	1598	1599	1600 to 1596 ⁵⁸ 1605 to 1593 ¹³⁴	aryl ring stretch, symmetric S > G, G condensed > G etherified
6	1510	1509	1511	1513 to 1506 ⁵⁸ 1515 to 1505 ¹³⁴	aryl ring stretch, asymmetric, G > S
7	1458	1458	1457	1465 ⁵⁸ 1470 to 1460 ¹³⁴	CH deformation, asymmetric
8	1426	1425	1428	1425 ⁵⁸	OCH ₃ CH deformation, asymmetric
				1428 ⁵⁸ 1430 to 1422 ¹³⁴	aromatic skeletal vibration, CH in-plane
9	1368	1367	1369	1379 ⁵⁸	aromatic skeletal vibration + CH in-plane deformation
				1370 to 1365 ¹³⁴	aliphatic CH stretch in CH ₃ (not in OCH ₃) + phenolic-OH
10	1270	1268	1270	1270 ⁵⁸ 1270 to 1266 ¹³⁴	aryl ring breathing mode; CO stretch; G-mode
11	1219	1219	1217	1230 to 1221 ¹³⁴	CC, CO, C=O, G condensed > G etherified
				1226 ⁵⁸	CC, CO, C=O stretch

				1215 ⁵⁸	CC, CO stretch
12	1149	1147	1152	1151 ⁵⁸	CH stretch in G-ring
				1140 ¹³⁴ 1142 ⁵⁸	aromatic CH in-plane typical for G-units; G condensed > G etherified
				1127 ⁵⁸	aromatic CH in-plane
13	1083	1082	1082	1086 ¹³⁴	CO in secondary alcohols and aliphatic esters
14	1034	1033	1032	1035 ⁵⁸ 1035 to 1030 ¹³⁴	aromatic CH in-plane, G > S
15	964	963	963	990 to 966 ¹³⁴	-HC=CH- out-of-plane
16	926	925	927	925 to 915 ¹³⁴	aromatic CH out-of-plane
17	859	855	856	858 to 853 ¹³⁴	CH out-of-plane of C ₂ , C ₅ , and C ₆ of G-units
18	815	816	815	832 to 817 ¹³⁴	CH out-of-plane of C ₂ , C ₅ , and C ₆ of G-units

Table A 5: Product separation and analytical techniques of the reactions with lignin in basic environment shown in Table 25

Source	Precipitation and acid used	Analytics ^a		Comments
		<i>Liquid phase</i>	<i>Solid phase</i>	
#1	pH <2 with 1 N HCl filtration	liquid-liquid extraction aqueous phase: HPLC organic phase: GC, mass	Elemental Analysis, 31P-NMR, mass	gas phase mass balance by difference -> leads to high gas masses (25 wt.%), probably coke included
#2	pH 1 with 37 wt.% HCl filtration	extraction with ethyl acetate organic phase: GC-MS dried -> MALDI-TOF	extracted with THF for 3 h undissolved: coke dissolved: unconverted lignin SEC Py-GC-MS	total mass balances: 50 to 55 %
#3	pH 7 with HCl (conc.?) centrifugation	freeze dried low molecular weight solids extraction with acetone GC-MS extraction with THF GPC	freeze dried high molecular weight solids ¹³ C-NMR extraction with THF GPC extraction with acetone GC-MS	
#4	pH 1.7 with 1 N HCl H ₂ O bath 70 °C, 15 min filtration	extraction with diethyl ether organic phase GC-MS aqueous phase none	extraction with THF soluble: oligomers insoluble: char	
#5	pH 2 with 1M H ₂ SO ₄ filtration	TOC-analyser	acetone extracted acetone soluble polyols (DL) acetone insoluble solid residue (SR) ATR FT-IR 1H NMR Elemental Analysis	

#6	pH 2 with conc. HCl (+32 wt.%) centrifugation	extraction with dichlormethane in centrifuge vial organic phase GC-FID aqueous phase none	GPC 13C NMR (in DMSO-d6 and NaOH) Elemental Analysis	reactions also performed with other bases (NH ₄ OH and KOH)
#7	pH 1 with HCl filtration	repeatedly extrated with ethyl ac- etate -> dried oil: MALDI-ToF dissolved in 50 mL ethyl acetate: GC-MS GC-FID	dried solids: weighed extraction with THF THF soluble (lignin, high moleuclar weight products): elemental analysis 1H and 13C NMR, 11B NMR THF insoluble: Coke elemental analysis	boric acid (H ₃ BO ₃) was used as cap- ping agent in batch runs ¹¹ B NMR only on samples with boric acid spectra of ¹ H and ¹³ C NMR are not provided in the paper and results of ¹³ C is also not mentioned in text, re- sults on elemental analysis also not provided.
#8	pH 3-4 with HCl filtration	extraction with methyl isobutyl ketone (MIBK) organic phase (MIBK): GC-MS-FID SEC elemental analysis aqueous phase: HPLC	washed with H ₂ O and dried on air and vac- uum elemental analysis SEC	
#9	pH 2 with HCl refrigerated over night filtration	extraction with ethyl acetate (this separation is only performed in one experiment)	dried extracted with diethyl ether -> ether soluble	

#10	pH 1 with HCl filtration	extraction with ethyl acetate -> oil MALDI-ToF GC-MS	extraction with THF THF soluble: residual lignin HP-SEC THF insoluble: char	reactions also performed with H ₃ BO ₃ and phenol as capping agent, the yields for the GC analysis of the phenol reactions give more than 100 %, although they are referred to to- tal oil mass
-----	-----------------------------	---	--	--

^a this is what is indicated in the works' materials and methods section, there are not necessarily results given

Table A 6: Mass balance and major monomeric compounds of the reactions in basic environment as described in Table 25.

Source	Conditions	Mass balance			Major oil components	Comments	
		Solid	Liquid	Gas			
#1	290 °C, 5 wt.% NaOH, 10 wt.% KL, 23 min	65	20	15	<u>yield of monomers</u>	gas phase by difference yield probably refers to total lignin	
					catechol		1.6
					4-methylcatechol		0.3
					3-methylcatechol		0.3
#2	300 °C, 4 wt.% NaOH, 5 wt.% acetosolv lignin, 80 min	35	18	1	<u>percentage of total oil</u>	incomplete mass balance	
					catechol		6.25
					4-methylcatechol		5.72
					3-methylcatechol		3.30
#3	300 °C, 4 wt.% NaOH, 10 wt.% KL, 40 min	61	23	4.7	<u>percentage of GC peaks</u>	4-methyl-4-penten-2-one 4-methyl-3-penten-2-one 4-hydroxy-4-methyl-2-pentanone found in aqueous phase, probably derivatised from acetone	
					catechol		26.2
					4-ethylcatechol		16.0
					4-methylcatechol		11.2
#4	300 °C, 5 wt.% NaOH, 10 wt.% softwood lignin, 45 min	70.3	5.5	n.d. ^a	<u>percentage of GC peaks</u>		
					guaiacol		52
					1,2-Dimethoxybenz.		15
					Acetovanillone		9
#5	300 °C, 5.5 wt.% NaOH, 20 wt.% softwood KL, 60 min	93	7	n.d.	n.d.	the acetone dissolvable lignin is included in the solids fraction	
#6	290 °C, 10 wt.% NaOH, OL, 15 min	no mass balance			<u>percentage of GC peaks</u>		
					catechol		~65
					4-methylcatechol		~15
					guaiacol		~15
#7	300 °C, 4 wt.% NaOH, 10 wt.% OL (probably hardwood), 8 min	80.2	19.2	n.d.	<u>percentage of total oil</u>		
					syringol		12
					guaiacol		5
					4-methylsyringol		2

#8	300 °C, 3 wt.% NaOH, hardwood OL, 10 min	+80	10	n.d.	<u>percentage of oil</u>		the oil composition is given as derivatives (der.) of the indicated types the yield of tar is not specifically indicated in the work and estimated from a diagram
					syringol der.	25.0	
					guaiacol der.	16.4	
#9	330 °C, 1 wt.% NaOH, 10 wt.% hardwood OL, 60 min with addition of 3.8 wt.% of CaO only a 60 min reaction was performed with quantification of the low pH aqueous phase	60	23	n.d.	n.d.		only 83% mass balance closed -> volatiles and gaseous products assumed the reactions concentrate on the ether soluble fraction and were also, in a previous study, performed in CH ₃ CH ₂ OH and CH ₃ OH as solvent (see ¹⁴²)
#10	300 °C, 4 wt.% NaOH, 5 wt.% hardwood OL (olive tree pruning), 40 min	50	20	n/d	<u>percentage of total oil</u>		70% mass balance, no further indication towards the losses
					catechol	10.2	
					4-methylcatechol	5.2	
					guaiacol	1.2	

^a not determined

Table A 7: Elemental analysis and molecular weight distribution of the solids fractions from reactions in basic aqueous environment presented in Table 25.

Source	Elemental analysis								M _w [g/mol]		PDI [-]	
	C [%]		H [%]		O [%]		S [%]		Before	After	Before	After
	Before	After	Before	After	Before	After	Before	After				
#1	63.1	70.5	5.5	5.6	29.9	21.1	0.6	--				
#2	n.d. ^a								16,416	13,214	10.75	16.41
#3	n.d.								strong reduction ^b		n.d.	
#5	63.8	71.0	5.4	5.0	25.6	23.1	5.2	0.9	n.d.			
#6	65.7	n.d.	6.0	n.d.	28.2	n.d.	--	n.d.	strong reduction ^c		n.d.	
#10	n.d.								7,232	19,957	3.40	4.19

^a not determined; ^b see figure 4d in ¹³⁶; ^c see figure 2.17 in ¹³⁹

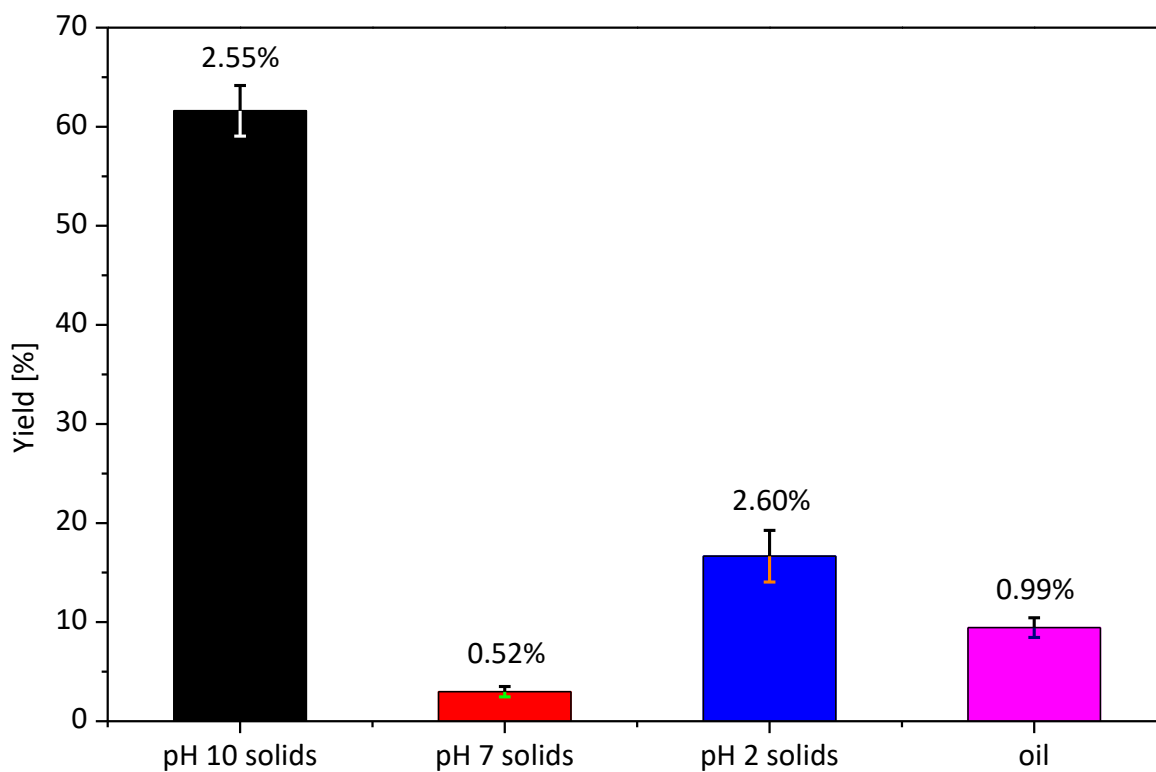


Figure A 12: Average yield (and standard deviation) of the runs #B1, #B2, and #B3.

Table A 8: Yield of the different fractions of the runs #B1-5

Run	pH		ρ [g/mL]		Mass fraction [%]				
	<i>Before</i>	<i>After</i>	<i>Before</i>	<i>After</i>	<i>pH 10</i>	<i>pH 7</i>	<i>pH 2</i>	<i>Oil</i>	<i>Total</i>
#B1	13.57	12.34	1.047	1.045	58.70	2.94	18.87	10.51	91.02
#B2	13.43	12.89	1.054	1.056	63.47	3.52	17.32	9.29	93.60
#B3	13.68	12.58	1.049	1.049	62.66	2.48	13.79	8.54	87.47
#B4	13.99	13.68	1.049	1.048	61.69	2.48	13.52	12.80	90.49
#B5	14.09	14.02	1.046	1.046	68.45	1.28	7.45	9.97	87.16

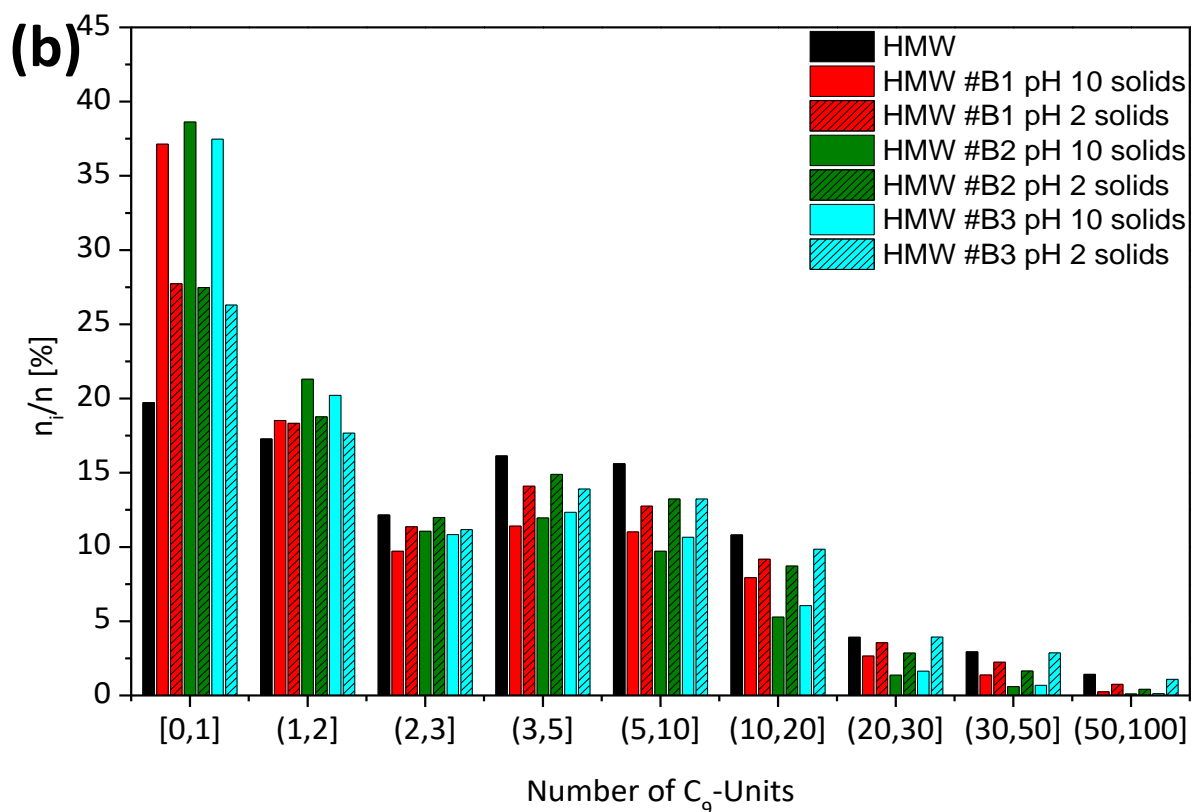
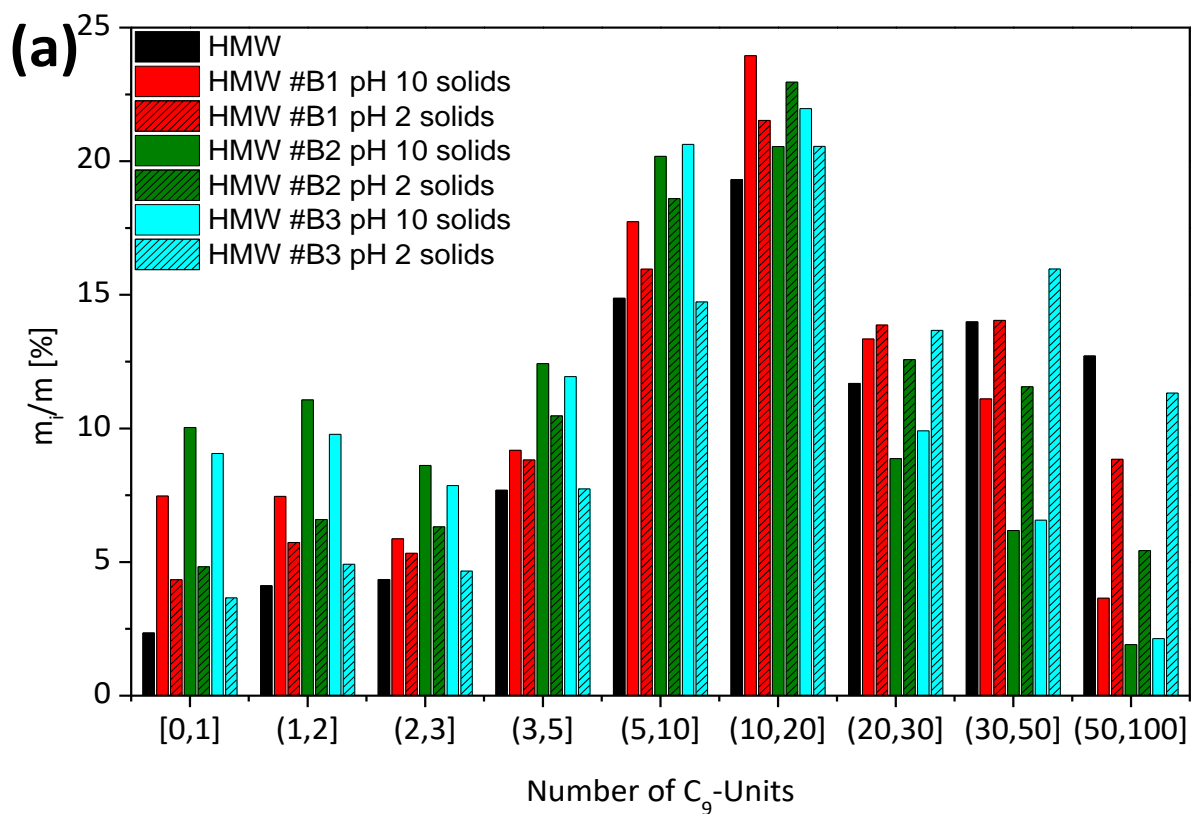


Figure A 13: (a) m_i/m and (b) n_i/n for specific chain length of runs #B1, #B2, and #B3 with HMW as feed. All three runs were conducted under the same conditions. The values are generated from the GPC data and chain length for M_i calculation is the mean value of the respective number range.

Table A 9: m_i/m and n_i/n for the fractions after #B runs for C9-Units > 100

Fraction		C ₉ -Units			
		<i>(100,200]</i>	<i>(200,500]</i>	<i>(500,1000]</i>	
#B1	m_i/m	[%]	0.2	0.0	0.0
pH 10	n_i/n		0.0	0.0	0.0
#B1	m_i/m		1.4	0.1	0.0
pH 2	n_i/n		0.1	0.0	0.0
#B2	m_i/m		0.1	0.0	0.0
pH 10	n_i/n		0.0	0.0	0.0
#B2	m_i/m		0.6	0.0	0.0
pH 2	n_i/n		0.0	0.0	0.0
#B3	m_i/m		0.1	0.0	0.0
pH 10	n_i/n		0.0	0.0	0.0
#B3	m_i/m		2.5	0.2	0.0
pH 2	n_i/n		0.1	0.0	0.0
#B4	m_i/m		0.1	0.0	0.0
pH 10	n_i/n		0.0	0.0	0.0
#B4	m_i/m		0.2	0.0	0.0
pH 2	n_i/n		0.0	0.0	0.0
#B5	m_i/m		0.1	0.0	0.0
pH 10	n_i/n		0.0	0.0	0.0
#B5	m_i/m		0.3	0.0	0.0
pH 2	n_i/n		0.0	0.0	0.0

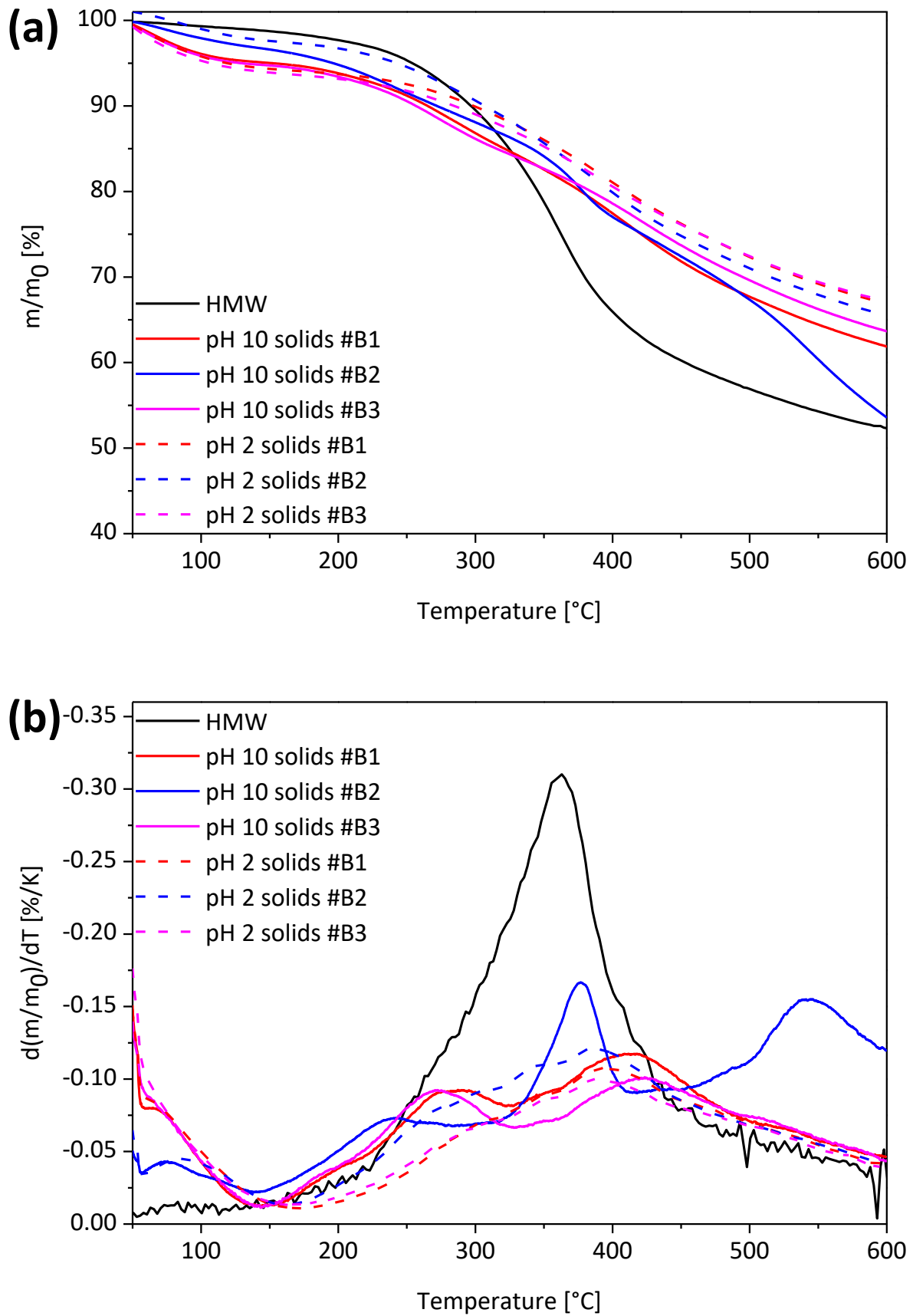


Figure A 14: TGA (a) and DTG (b) analysis of the pH 10 and pH 2 solids of runs #B.

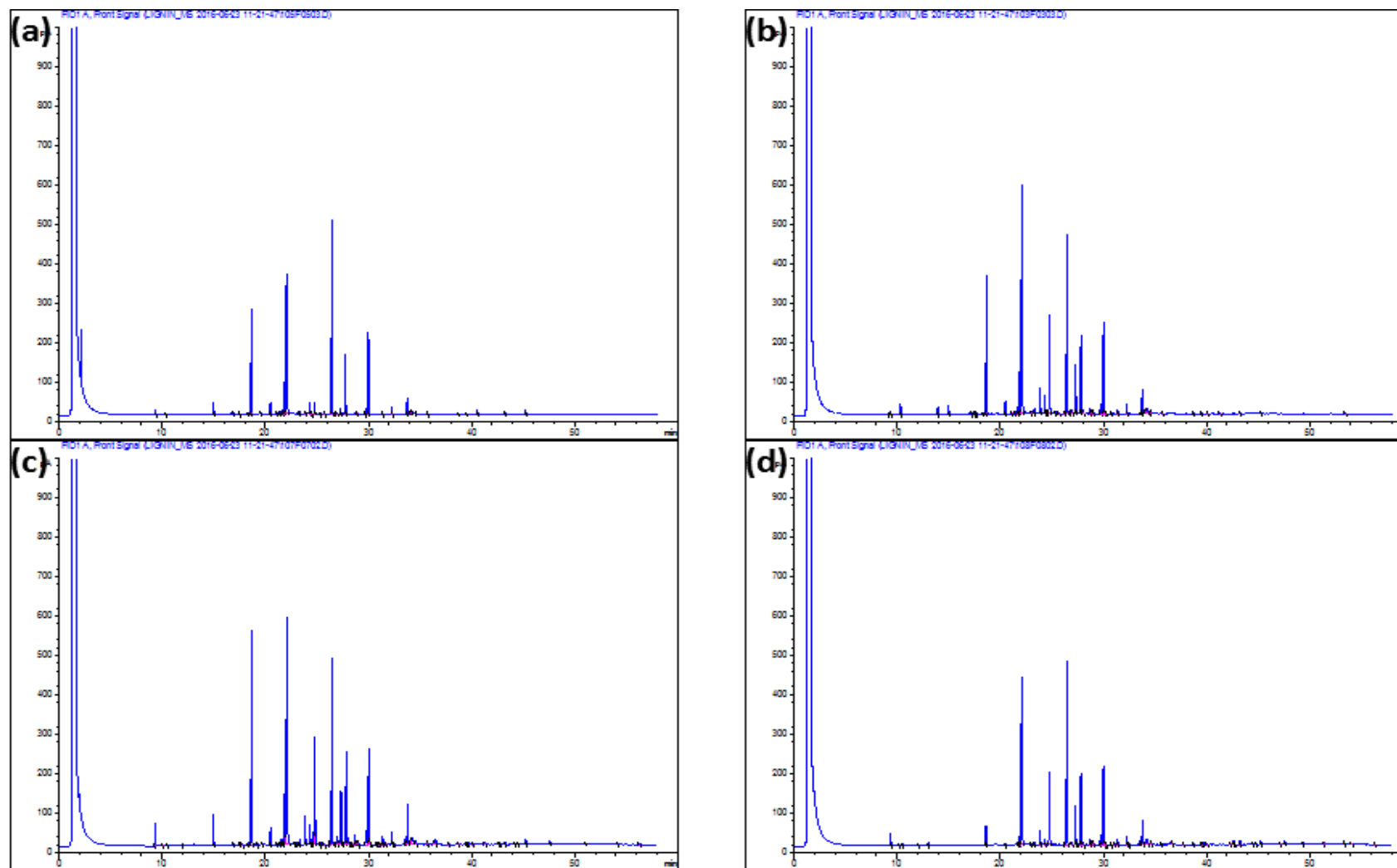
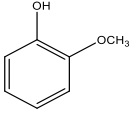
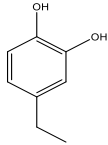
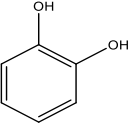
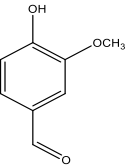
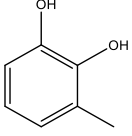
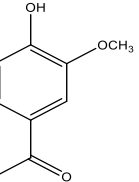
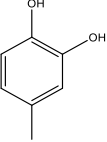
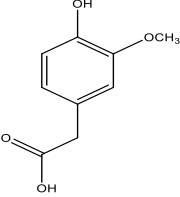
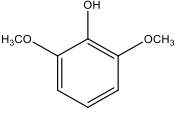
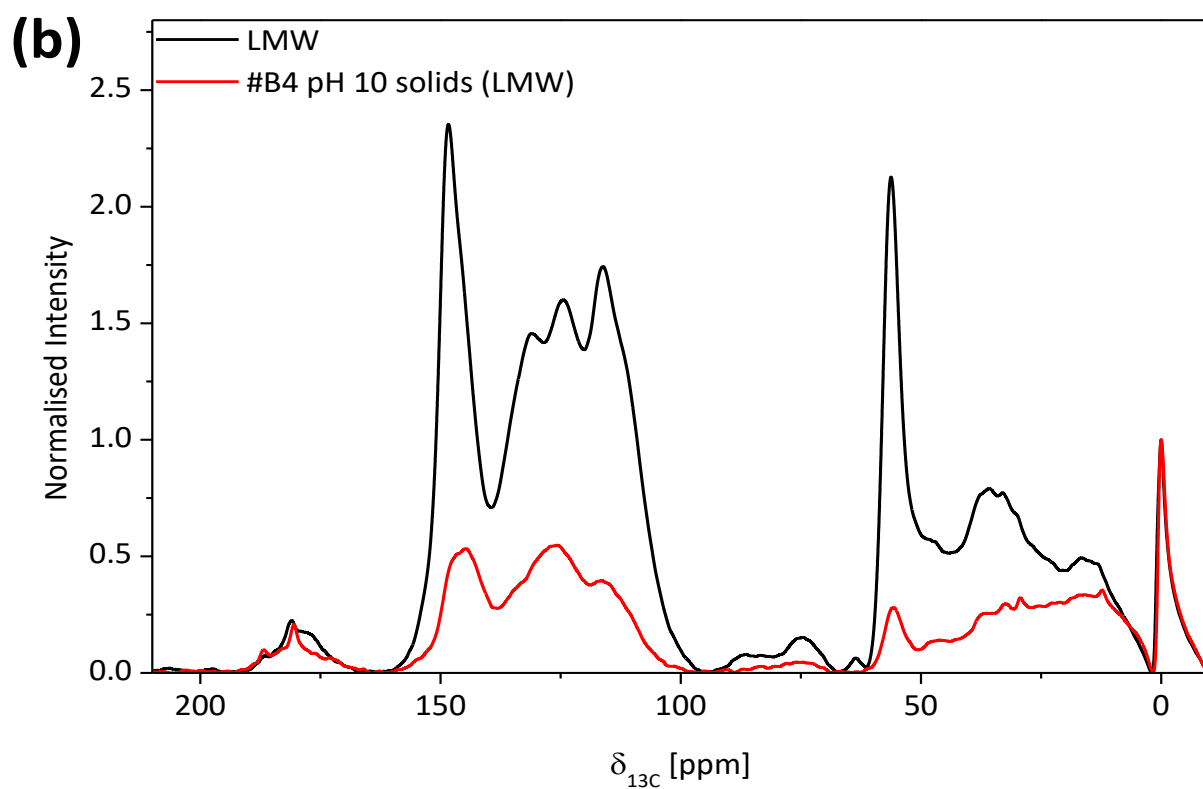
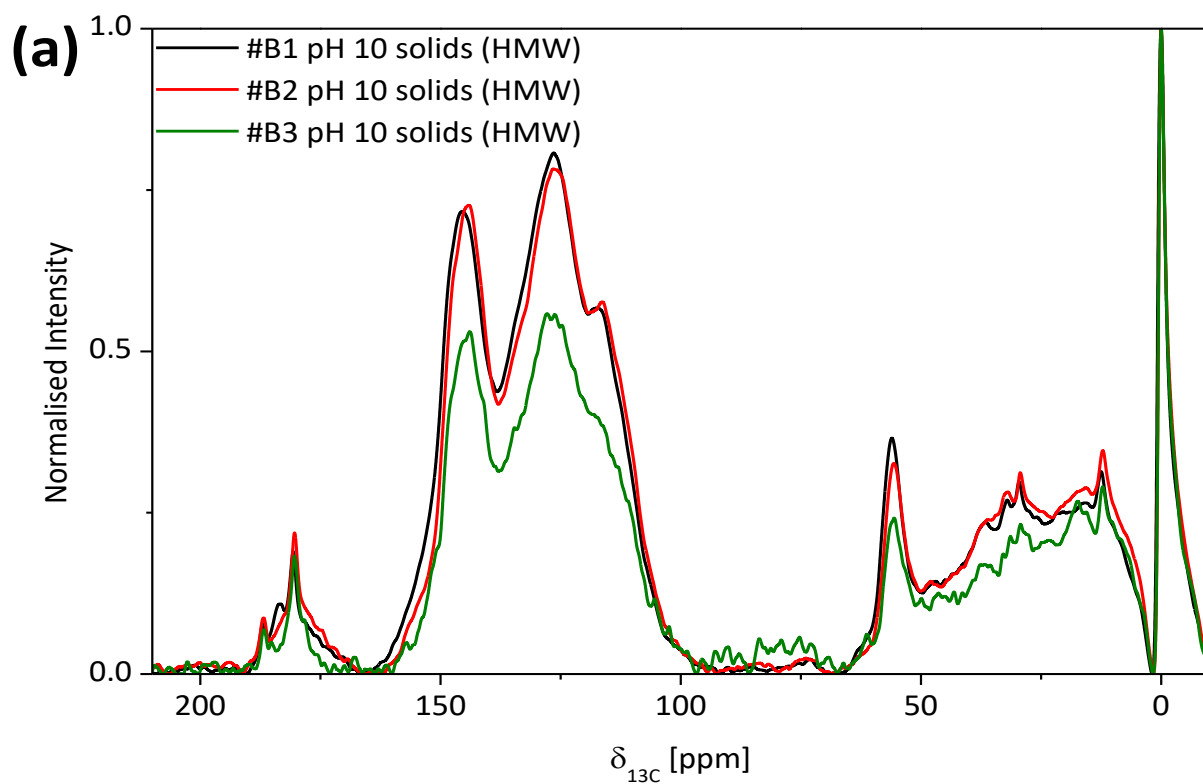


Figure A 15: GC-FID spectra of reactions #B1 (a) and #B2 (b) both performed with HMW as feed. Spectra (c) and (d) are of the runs #B4 and #B5. These used LMW and KL as feed, respectively.

Table A 10: Major monomeric products of reactions #B.

$t_{\text{retention}}$ [min]	Compound	Structural Formula	$t_{\text{retention}}$ [min]	Compound	Structural Formula
18.642	Guaiacol		27.309	4-ethylcatechol	
22.157	Catechol		27.831	Vanillin	
23.842	3-methylcatechol		30.034	Acetovanillone	
24.816	4-methylcatechol		33.770	Homovanillic acid	
26.489	Syringol (internal standard, 1 mg/mL)				



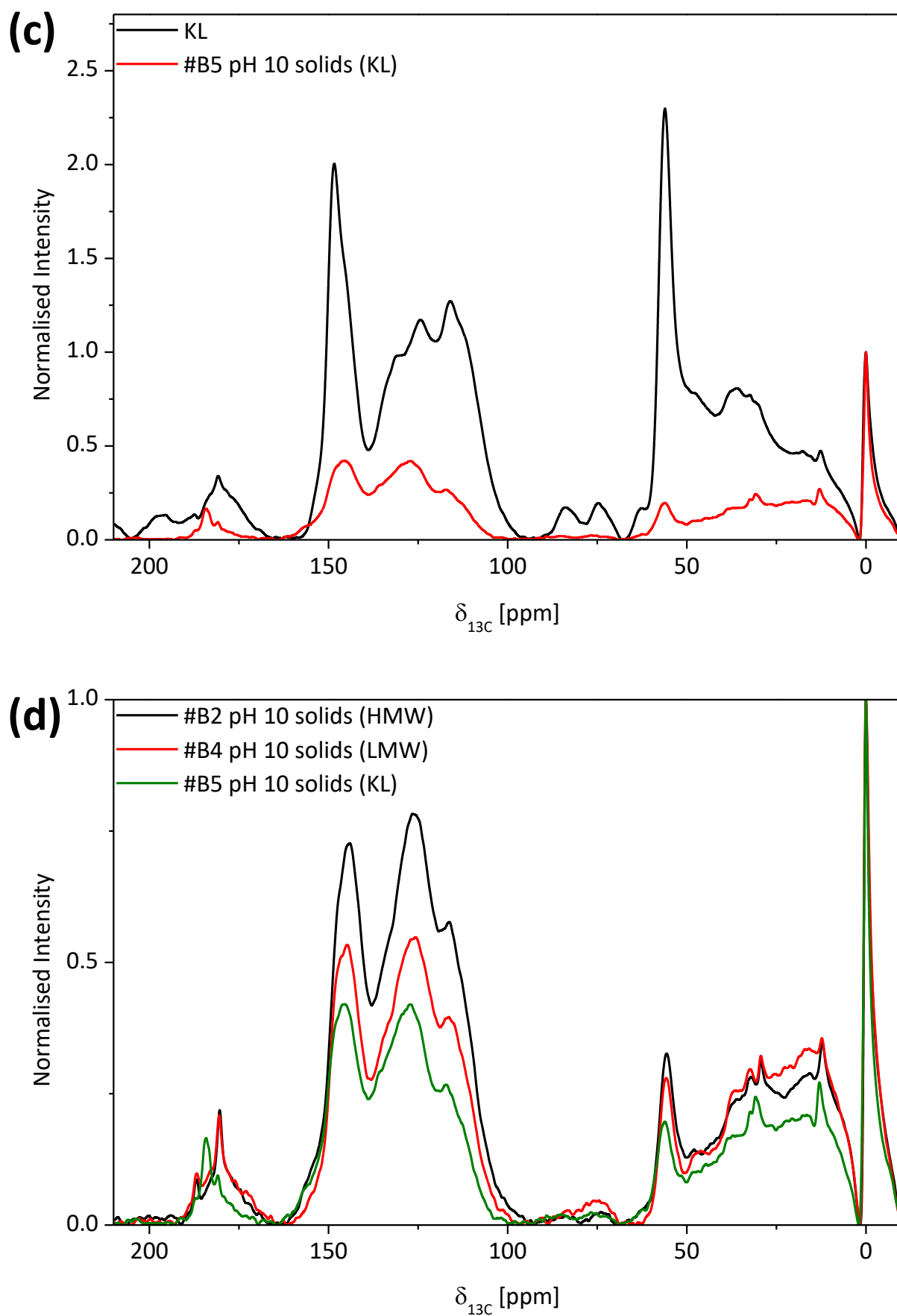
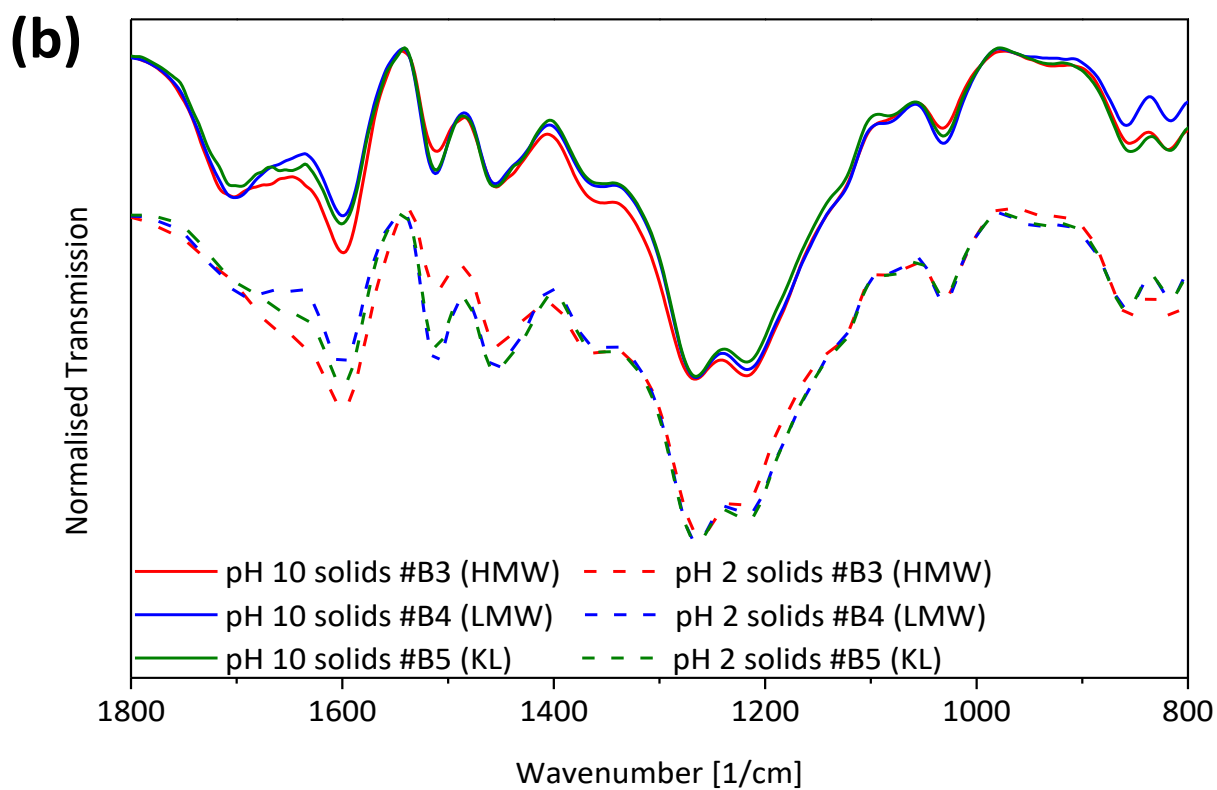
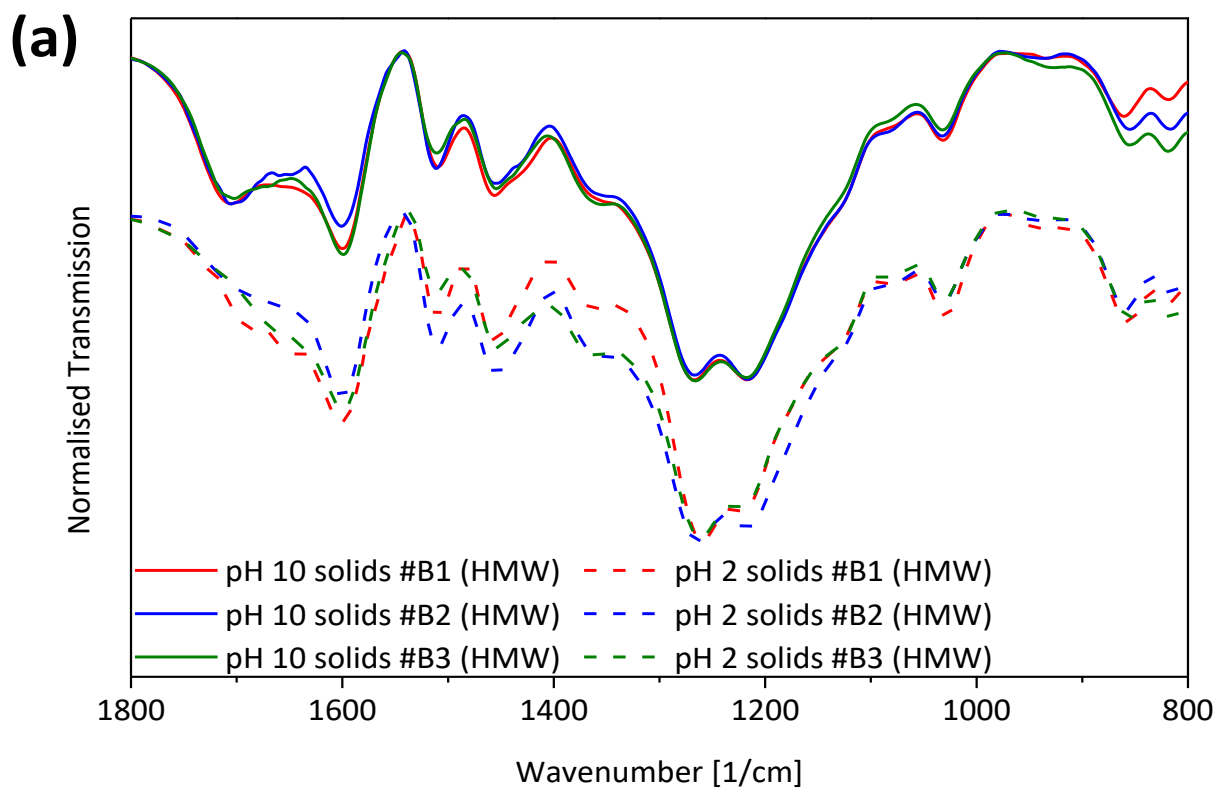
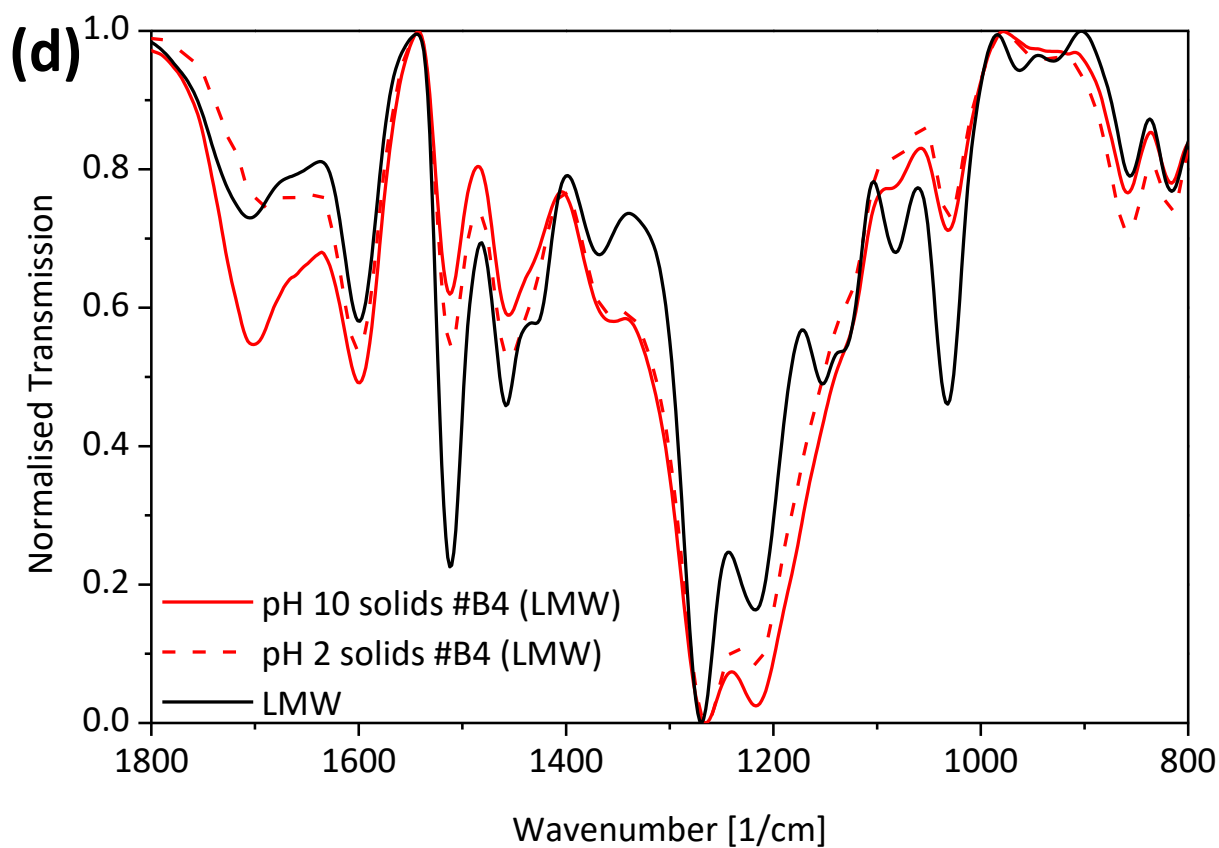
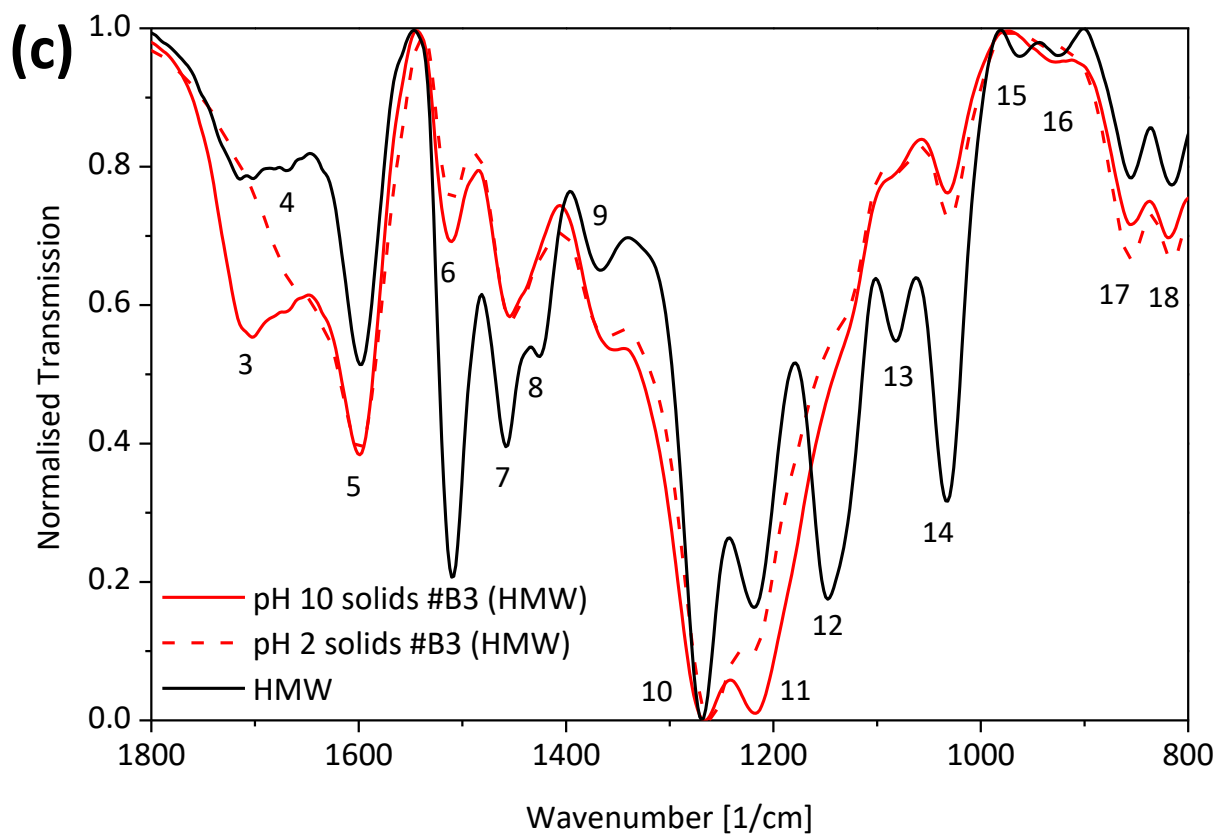


Figure A 16: ^{13}C CP MAS NMR spectra of the pH 10 solids of reaction #B: (a) #B5 with KL as feed; (b) #B4 with LMW fraction as feed; (c) comparison between #B1, #B2, and #B3 with HMW fraction as feed; (d) #B1, #B4, and #B5 with all three different feeds.





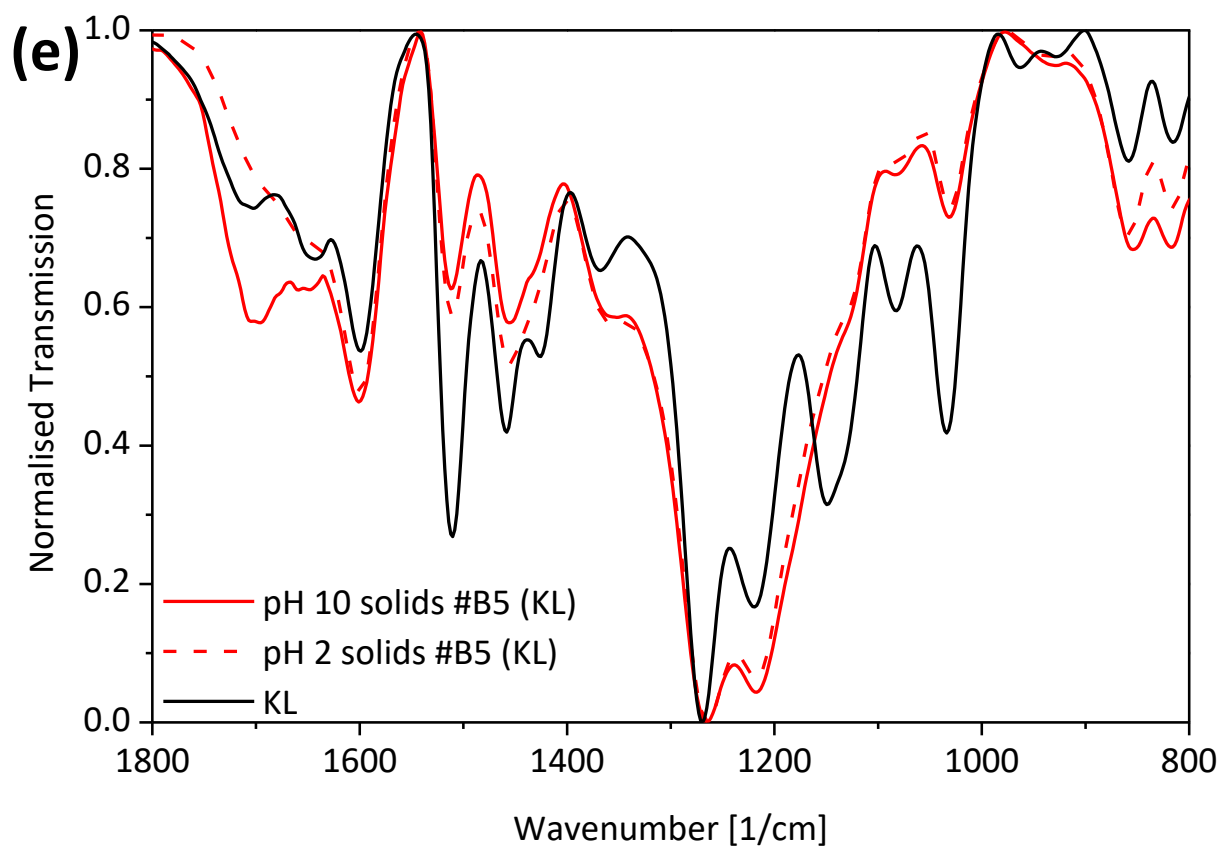


Figure A 17: ATR FT-IR spectra of: pH 10 and pH 2 solids of reactions #B3, #B4, and #B5 (a); pH 10 and pH 2 solids of reactions #B1, #B2, and #B3 (b), LMW fraction, pH 10 and pH 2 solids of reaction #B3 (c); LMW, pH 10 and pH 2 solids of reaction #B4 (d); KL fraction, pH 10 and pH 2 solids of reaction #B5 (e).

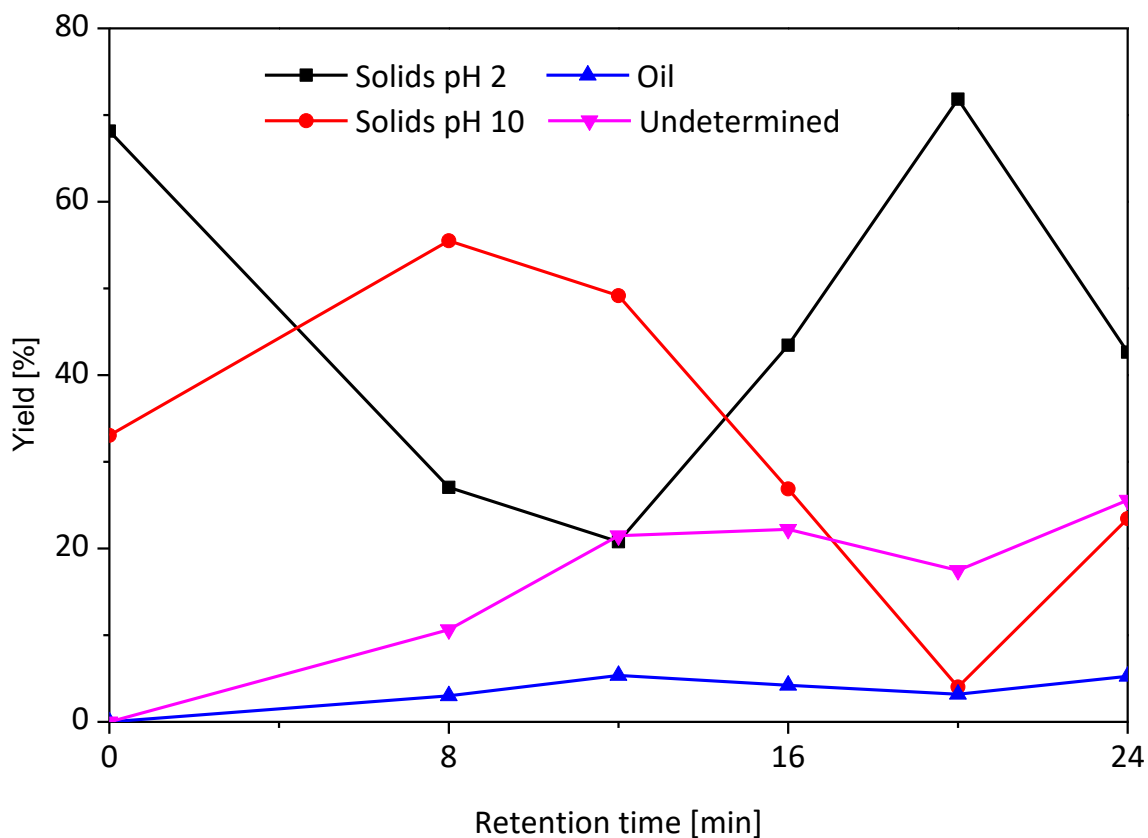


Figure A 18: Yields of the reactions #K1-5 with resolving between pH 10 and pH 2 solids.

Table A 11: pH, density, and mass fractions of the kinetic runs reactions #K1-5

Run/ $t_{\text{retention}}$ [min]	pH [-]		ρ [g/mL]		Mass fraction [%]			
	<i>Before</i>	<i>After</i>	<i>Before</i>	<i>After</i>	<i>pH 10</i>	<i>pH 2</i>	<i>Oil</i>	<i>Total</i>
Feed	n.d.	--	1.047	--	33.05	68.14	--	101.19
#K1 / 8	13.17	12.49	1.047	1.044	55.49	27.05	3.01	85.55
#K4 / 12	13.16	12.40	1.046	1.043	49.16	20.77	5.35	75.28
#K3 / 16	12.95	12.56	1.048	1.042	26.87	43.44	4.23	74.54
#K5 / 20	12.79	12.36	1.047	1.041	4.02	71.83	3.19	79.04
#K2 / 24	12.95	12.24	1.048	1.039	23.45	42.66	5.26	71.37

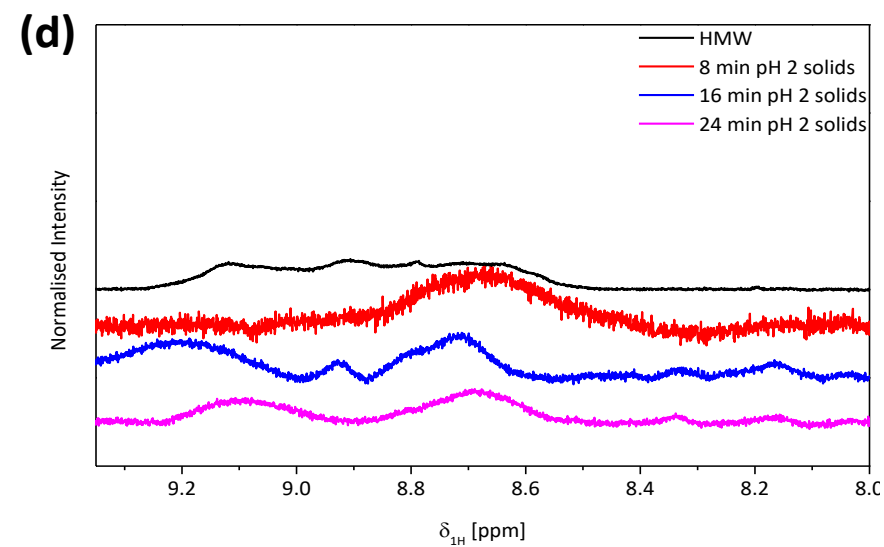
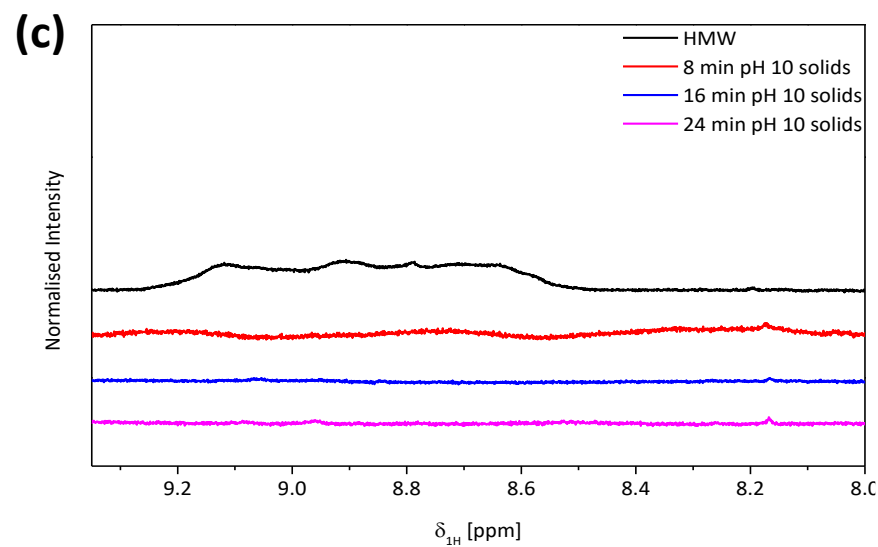
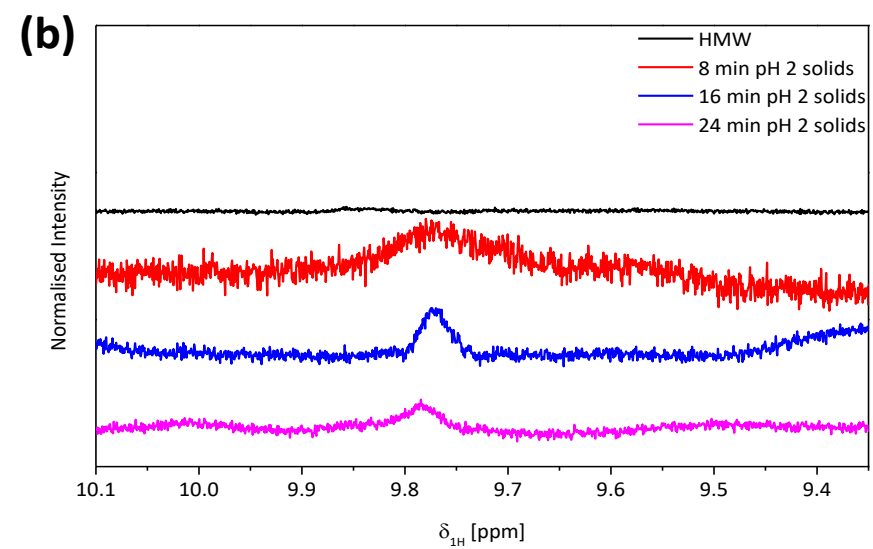
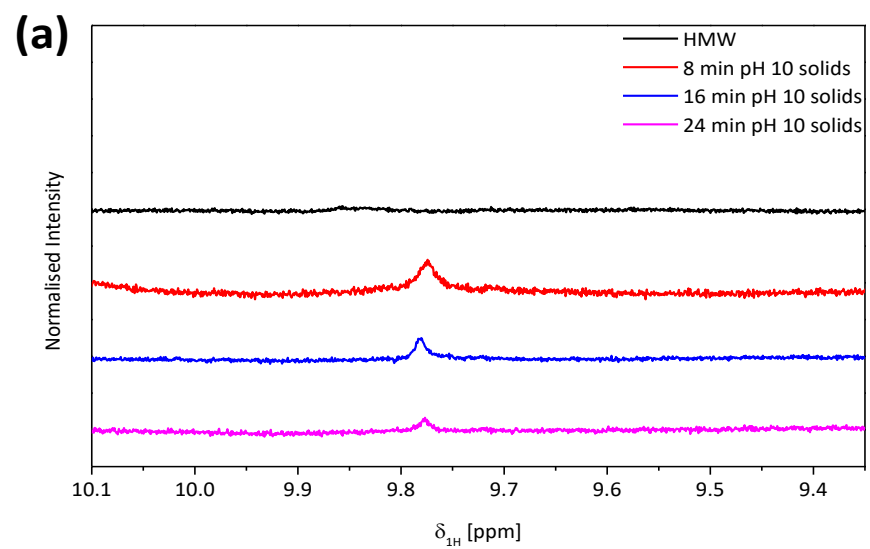
Table A 12: m_i/m and n_i/n for the fractions after #K runs for C9-Units > 100

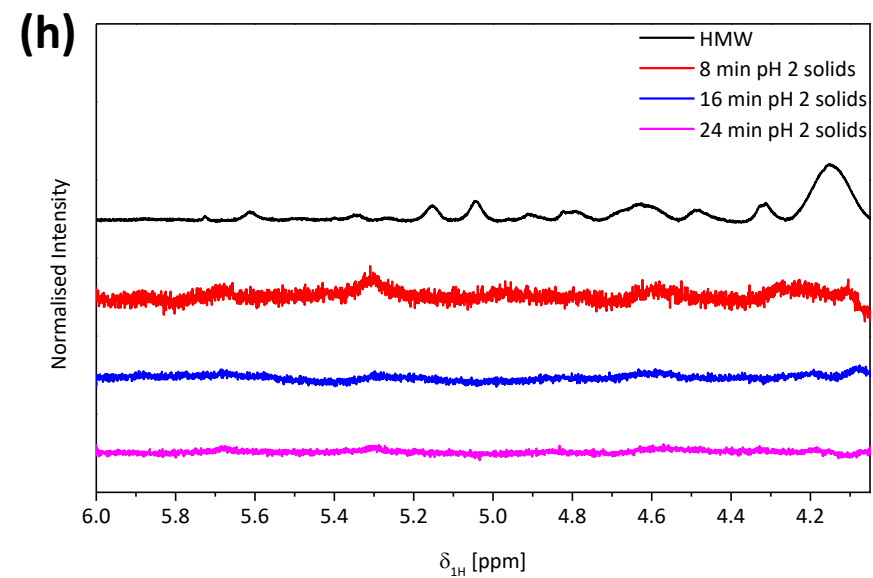
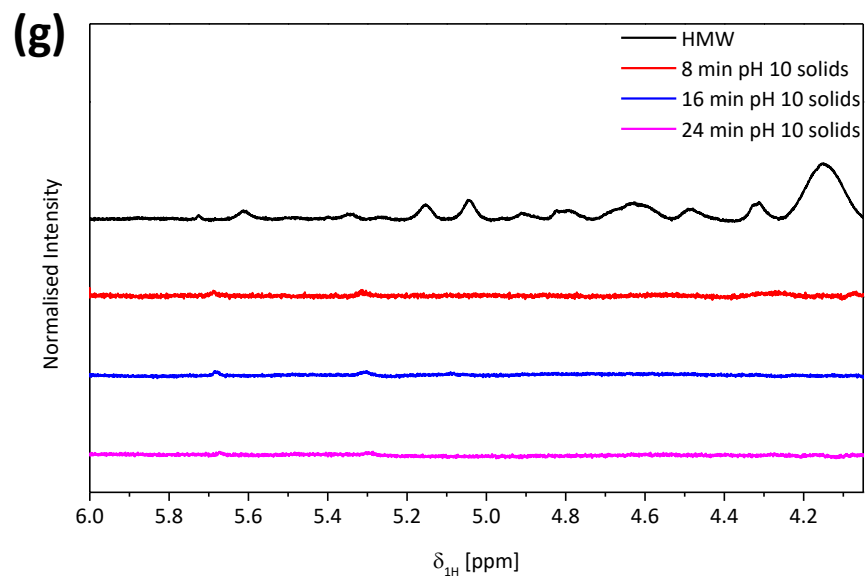
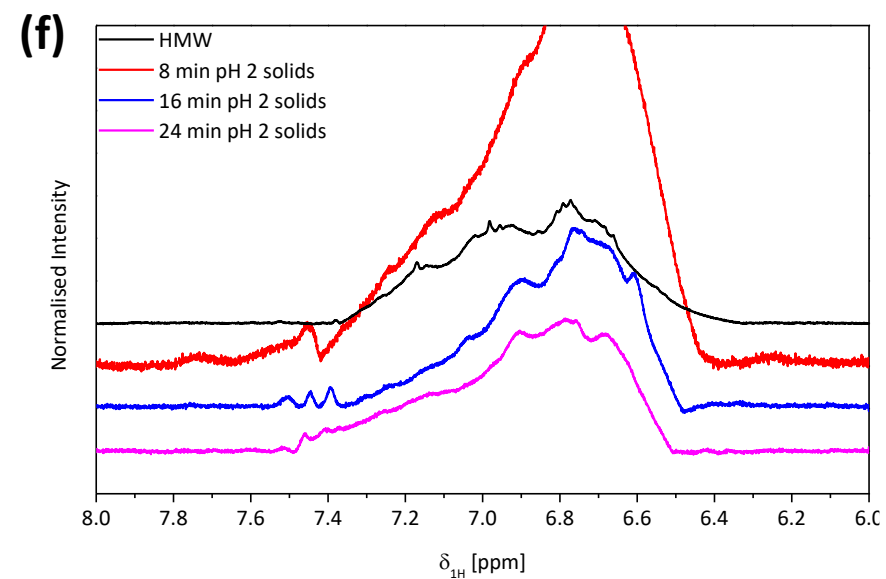
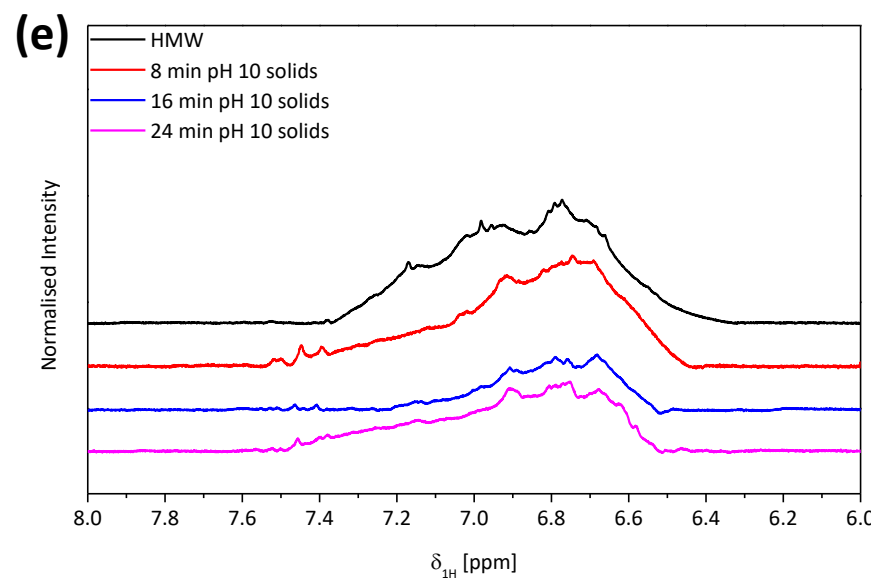
Fraction		C ₉ -Units			
		(100,200]	(200,500]	(500,1000]	
8 min pH 10	m_i/m	[%]	0.3	0.0	0.0
	n_i/n		0.0	0.0	0.0
8 min pH 2	m_i/m		0.2	0.0	0.0
	n_i/n		0.0	0.0	0.0
16 min pH 10	m_i/m		0.3	0.0	0.0
	n_i/n		0.0	0.0	0.0
16 min pH 2	m_i/m		0.1	0.0	0.0
	n_i/n		0.0	0.0	0.0
24 min pH 10	m_i/m		0.5	0.0	0.0
	n_i/n		0.0	0.0	0.0
24 min pH 2	m_i/m		0.4	0.0	0.0
	n_i/n		0.0	0.0	0.0

Table A 13: Generated amount of MeOH by transformation of the methoxy groups (MeO) of the #K runs. Relative amount of the MeOH C, H, and O of the lost mass.

$t_{\text{retention}}$ [min]	MeO [wt.%] ^{a,b}	MeOH [g]				MeOH amount of lost compounds [%]		
		Total	C	H	O	C	H	O
8	2.24 ^b	0.33	0.12	0.04	0.16	6.43	13.36	31.78 ^d
16	2.06	0.37	0.14	0.05	0.18	5.61	11.16	8.34
24	1.58	0.48	0.18	0.06	0.24	7.37	13.94	8.30

^a starting amount of methoxy groups (MeO) in HMW = 3.70 wt.%, ^b average of pH 10 and pH 2 solids, ^c only pH 10 solids, ^d higher number caused by the relative small amount of oxygen in the lost mass for this run





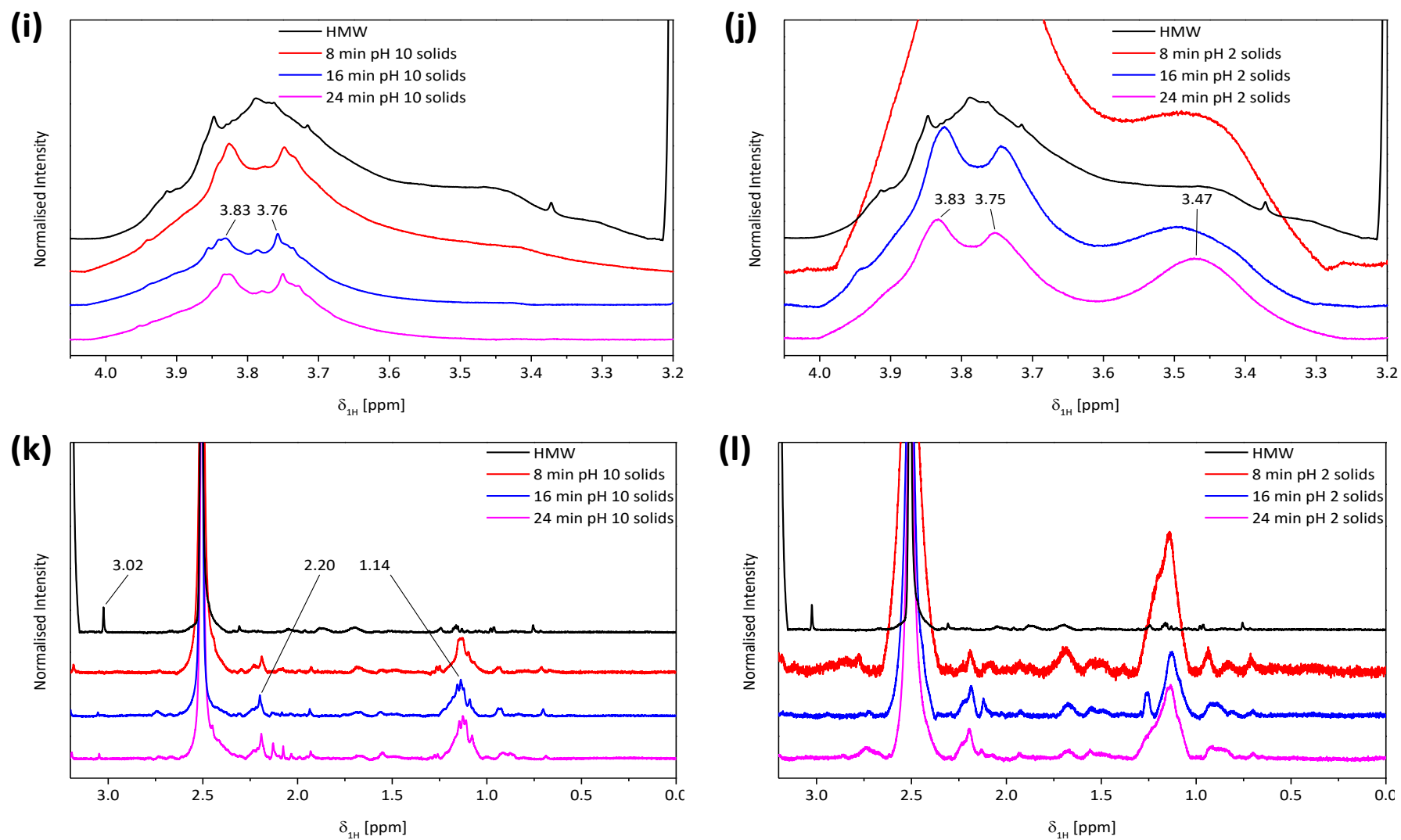


Figure A 19: Liquid phase ^1H NMR spectra in DMSO-d_6 of the runs #K1, #K2, and #K3 separated into six areas. The left column with (a), (c), (e), (g), (i), and (k) shows the pH 10 solids, the right column with (b), (d), (f), (h), (j), and (l) the pH 2 solids. It has to be noted that the signal of the 8 min pH 2 solids are in total a lot stronger compared to all other spectra.

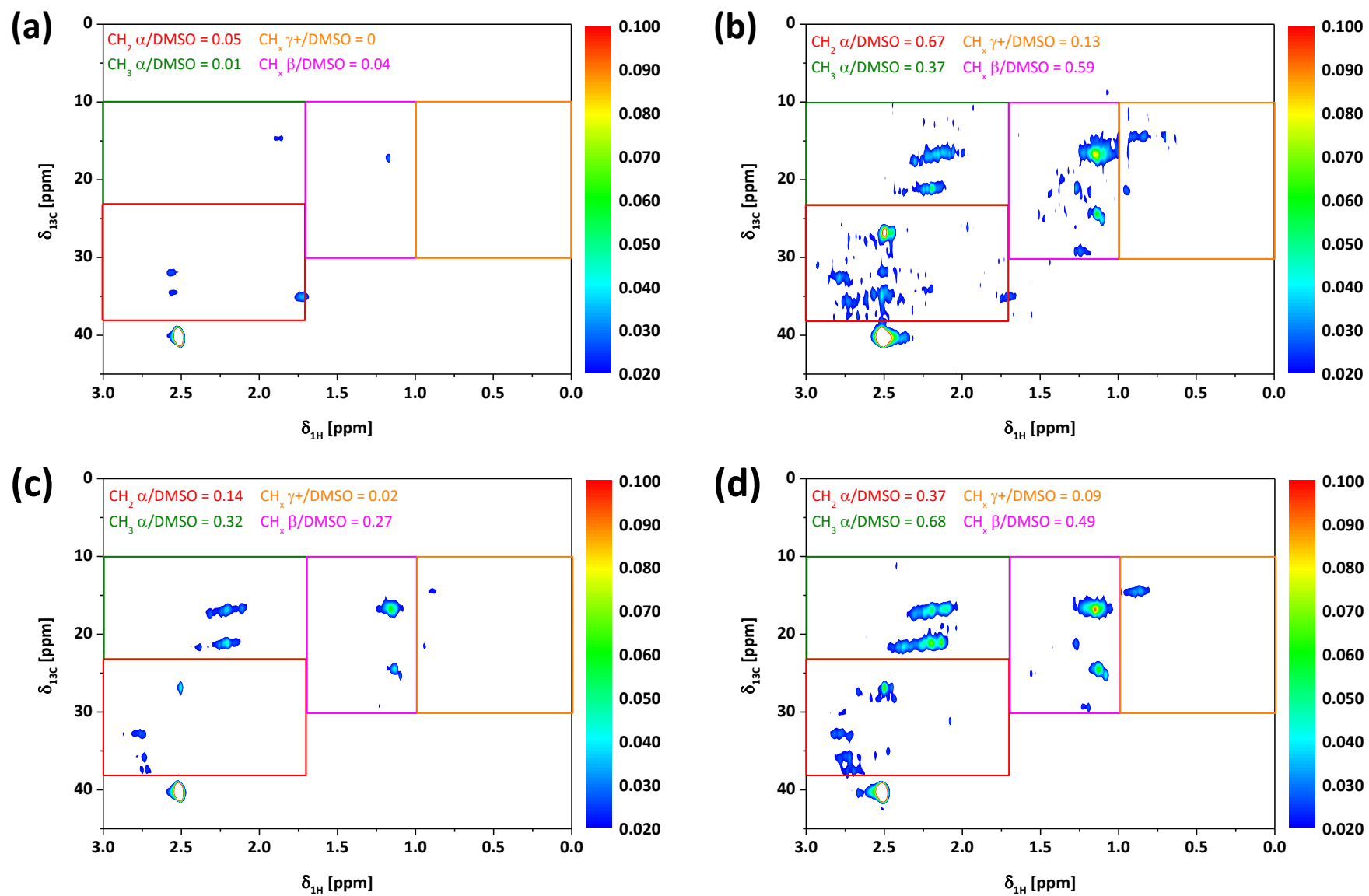


Figure A 20: 2D HSQC NMR spectra of the aliphatics region: HMW fraction (a); pH 10 solids after (b) 8 min; (c) 16 min; (d) 24 min

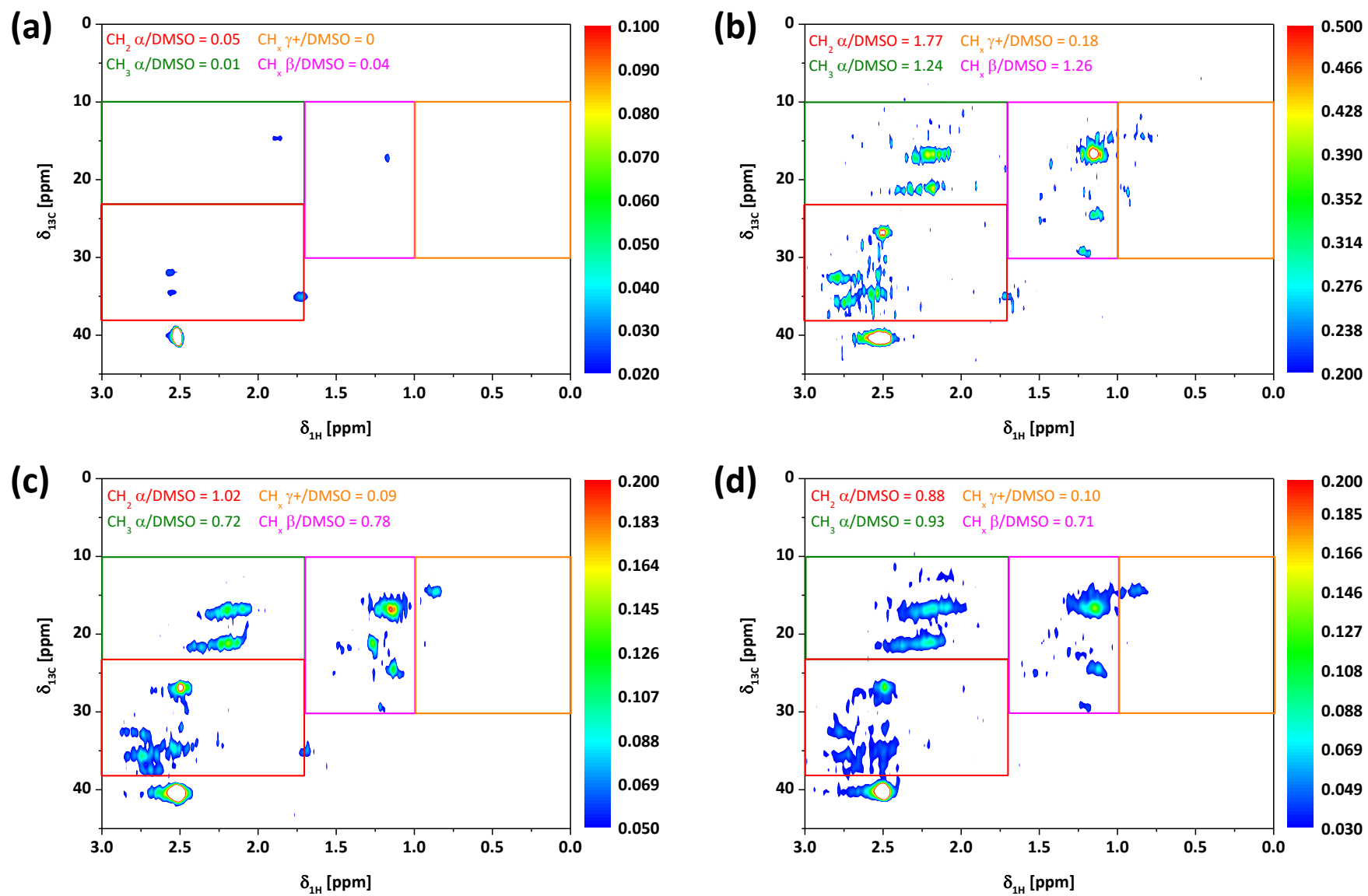


Figure A 21: 2D HSQC NMR spectra of the aliphatics region: HMW fraction (a); pH 2 solids at tretention = (b) 8 min; (c) 16 min; (d) 24 min.

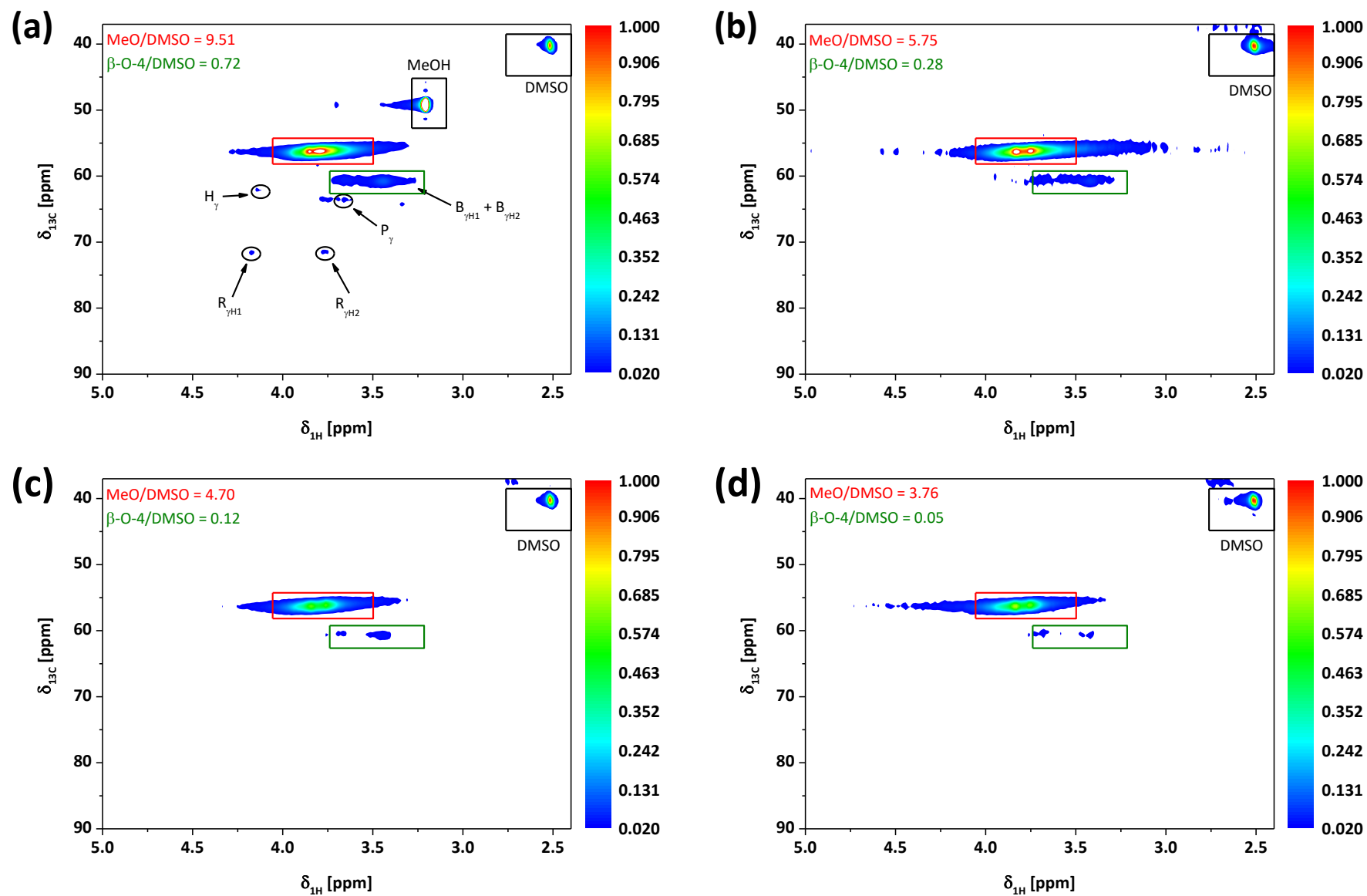


Figure A 22: 2D HSQC NMR spectra of the side chain region: HMW fraction (a); pH 10 solids at tretention = (b) 8 min; (c) 16 min; (d) 24 min

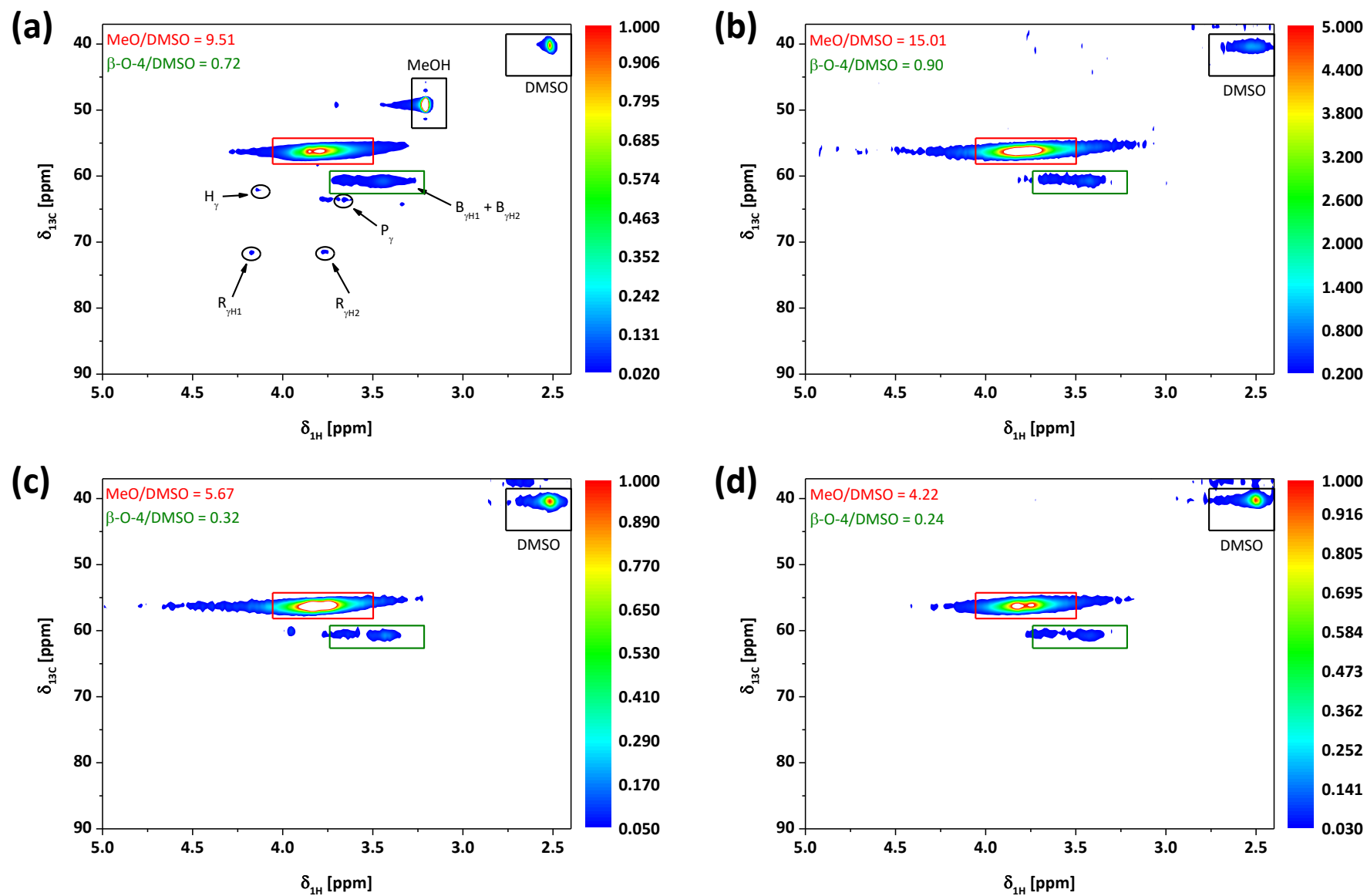


Figure A 23: 2D HSQC NMR spectra of the side chain region: HMW fraction (a); pH 2 solids at tretention = (b) 8 min; (c) 16 min; (d) 24 min.

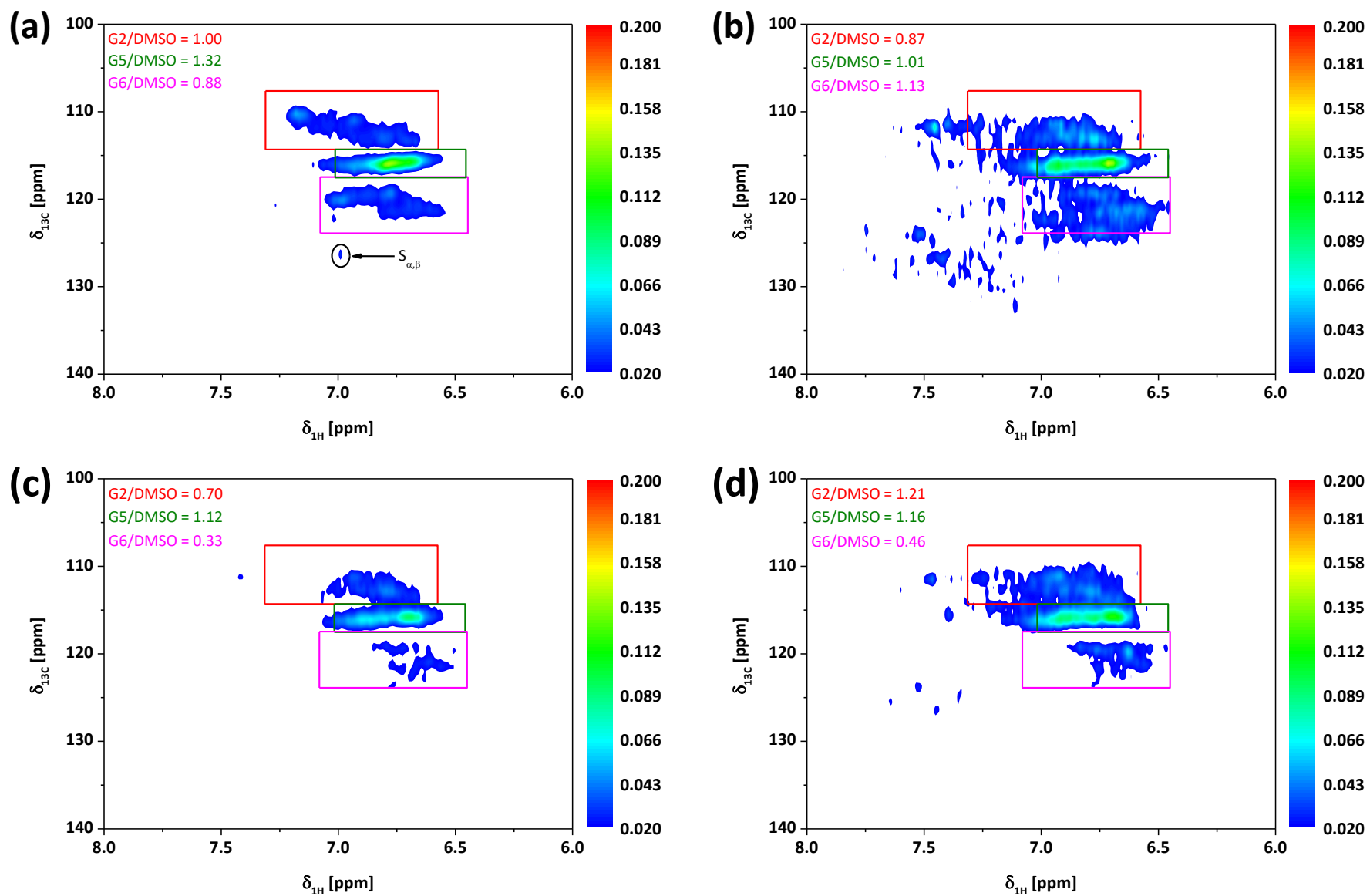


Figure A 24: 2D HSQC NMR spectra of the aromatics region: HMW fraction (a); pH 10 solids at tretention = (b) 8 min; (c) 16 min; (d) 24 min

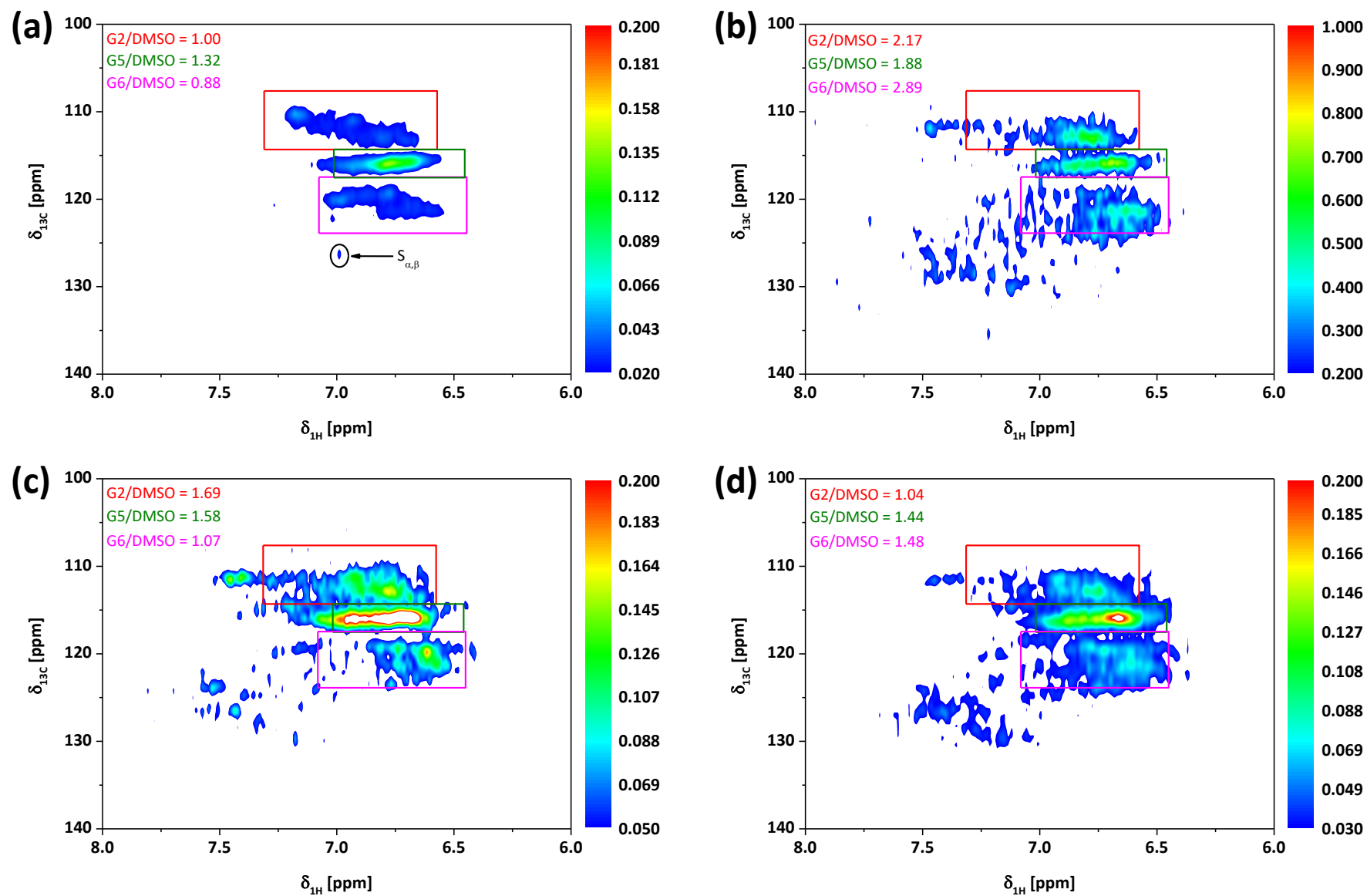


Figure A 25: 2D HSQC NMR spectra of the aromatics region: HMW fraction (a); pH 2 solids at tretention = (b) 8 min; (c) 16 min; (d) 24 min.

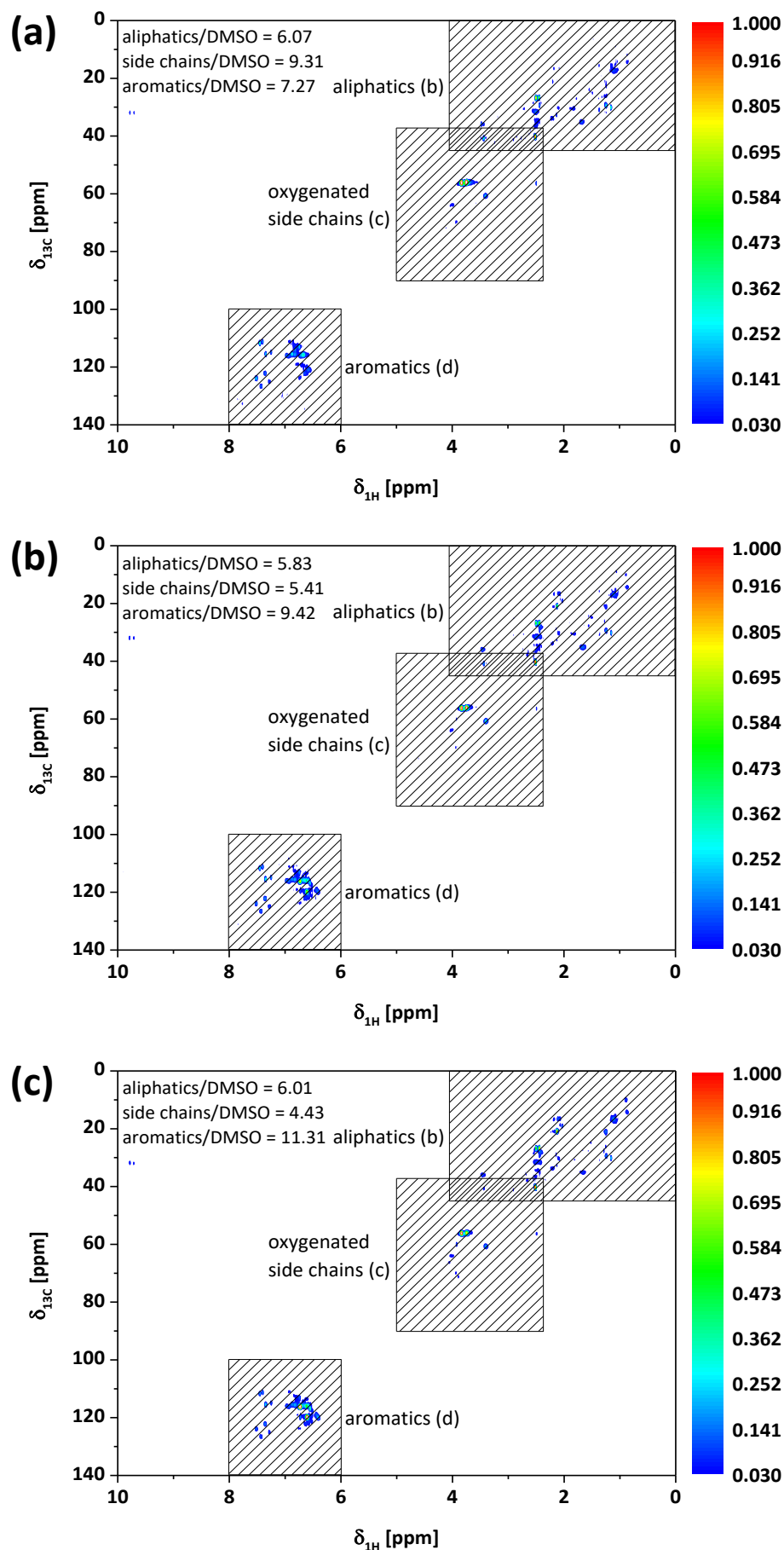


Figure A 26: 2D HSQC NMR spectra of the oil fractions as overview, at tretention = (a) 8 min, (b) 16 min, and (c) 24 min.

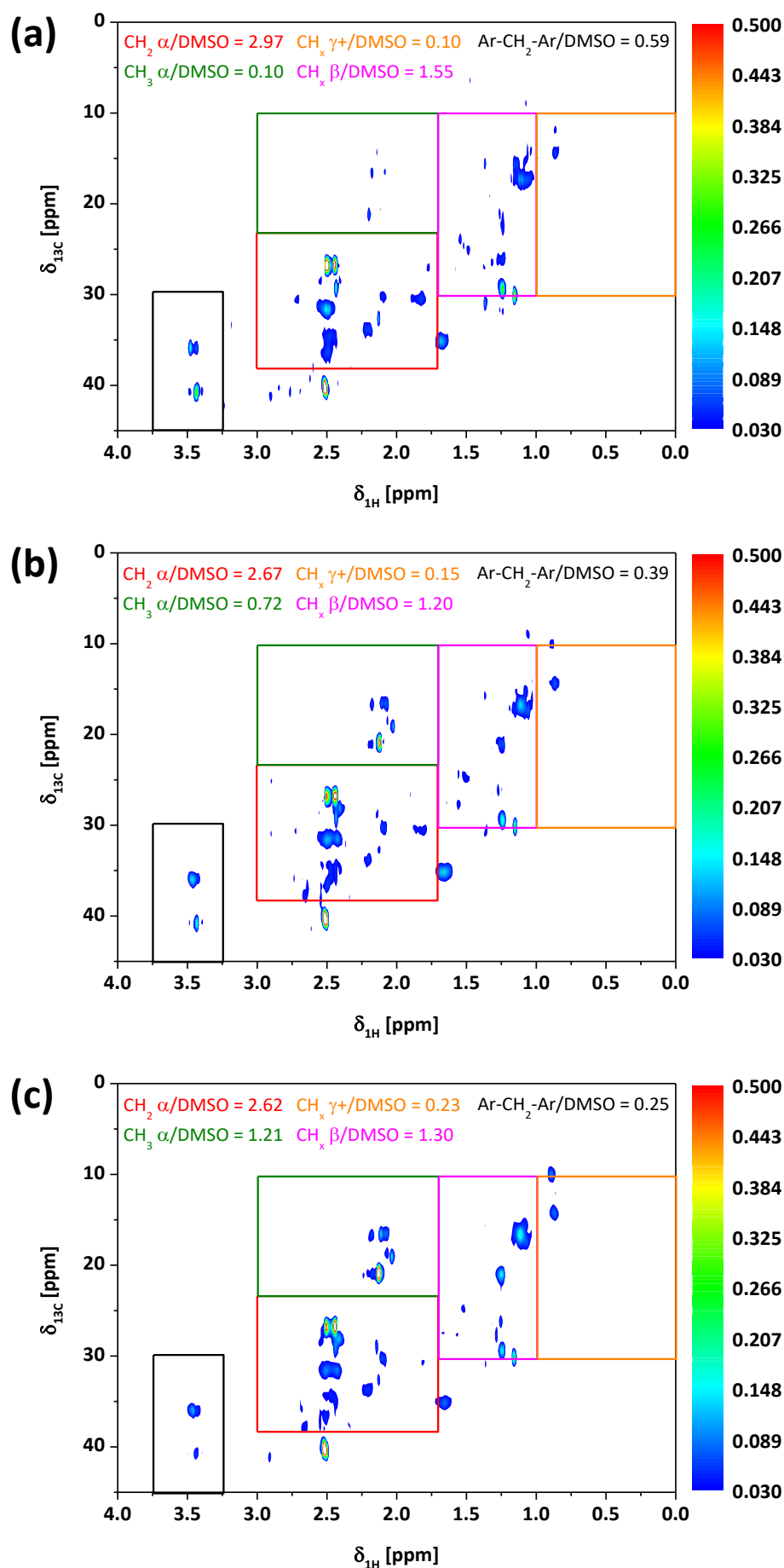


Figure A 27: 2D HSQC NMR spectra of the oil fractions' aliphatics region at tretention = (a) 8 min, (b) 16 min, and (c) 24 min.

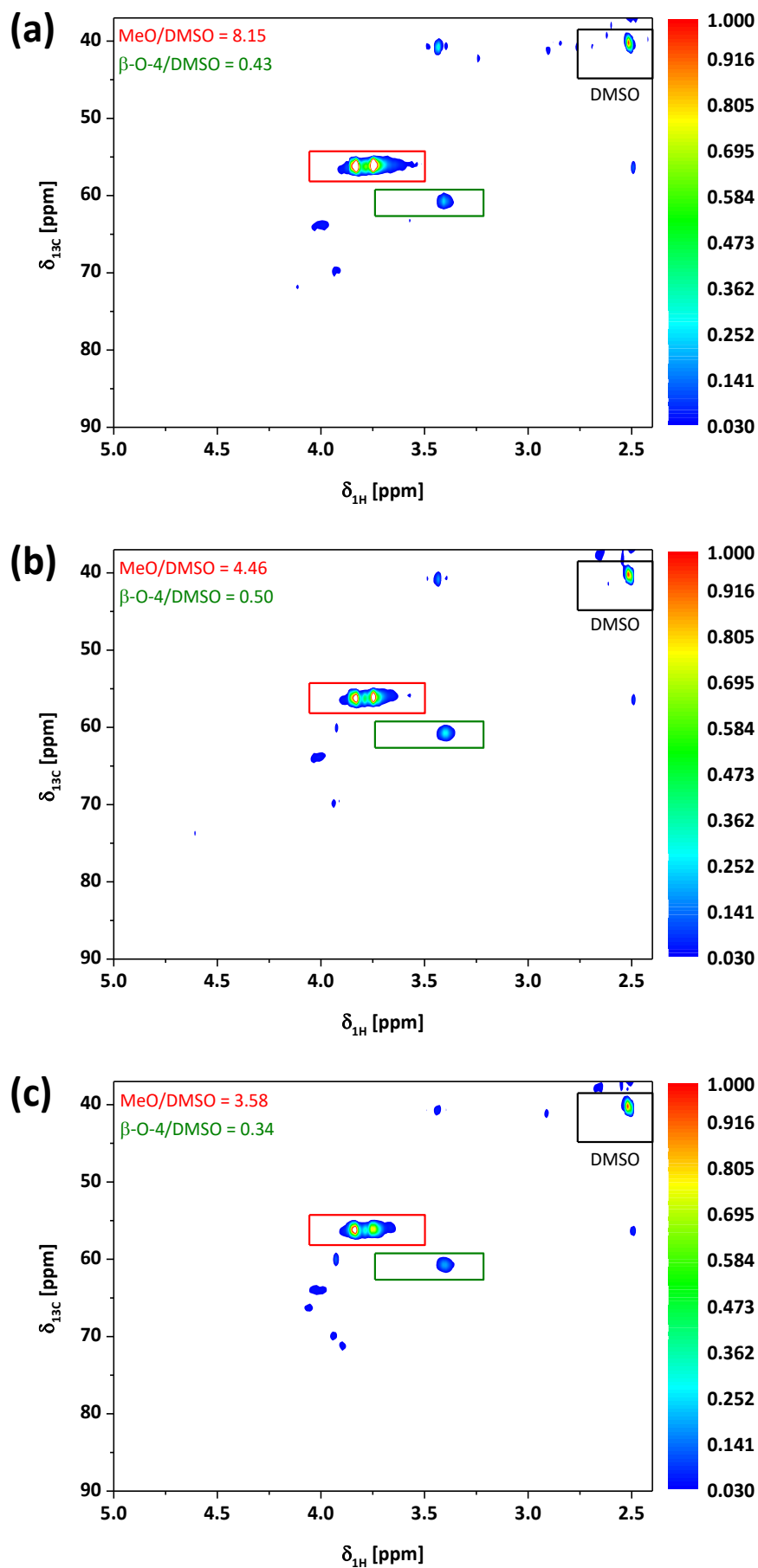


Figure A 28: 2D HSQC NMR spectra of the oil fractions' oxygenated side chain region, at tretention = (a) 8 min, (b) 16 min, and (c) 24 min.

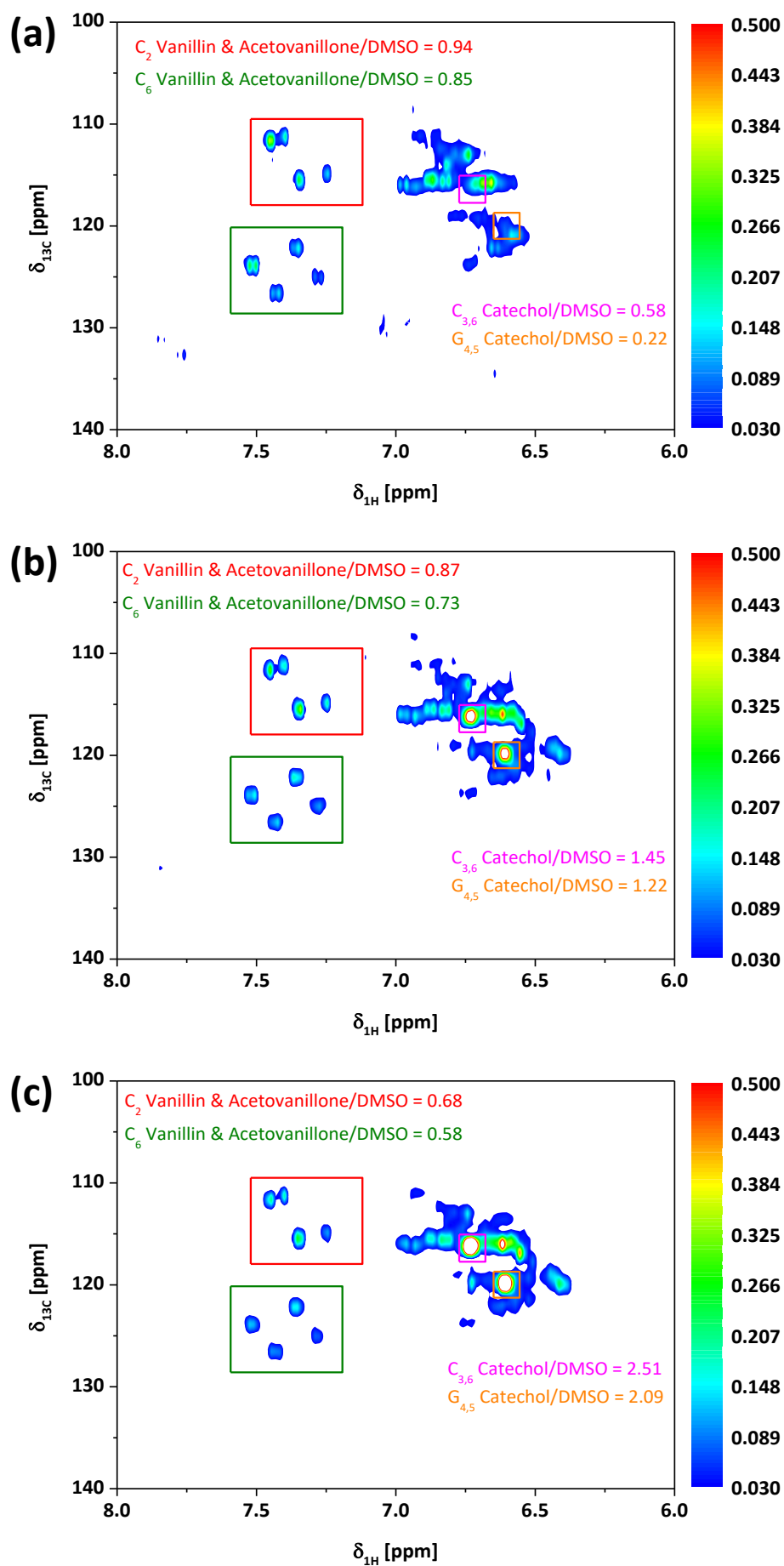


Figure A 29: 2D HSQC NMR spectra of the oil fractions' aromatics region, at tretention = (a) 8 min, (b) 16 min, and (c) 24 min.

Table A 14: Integration limits for the 2D HSQC NMR spectral regions.

2D HSQC Area	$\delta_{1H,min}$ [ppm]	$\delta_{1H,max}$ [ppm]	$\delta_{13C,min}$ [ppm]	$\delta_{13C,max}$ [ppm]
Total				
Aliphatics solids	0	3.0	0	45
Aliphatics oil	0	4.0	0	45
Side chains	2.4	5.0	37	90
Aromatics	6.0	8.0	100	140
Aliphatics				
CH ₂ α	1.90	3.00	23	38
CH ₃ α	1.90	3.00	10	23
CH _x β	1.00	1.90	10	30
CH _x $\gamma+$	0	1.00	10	30
Ar-CH ₂ -Ar	3.25	3.75	30	45
Side chains				
DMSO- <i>d</i> 6	2.40	2.70	38.5	45.0
MeOH	3.05	3.25	45.0	53.0
-OCH ₃	3.50	4.05	54.3	58.0
β -O-4	3.21	3.74	59.1	62.7
Aromatics				
G ₂	6.57	7.31	107.6	114.5
G ₅	6.45	7.01	114.5	117.5
G ₆	6.44	7.08	117.5	123.9
C ₂ Vanillin & Acetovanillone	7.12	7.52	109.4	117.9
C ₆ Vanillin & Acetovanillone	7.19	7.59	120.1	128.6
Single peaks				
δ_{1H} 9.71	9.680	9.740	31.0	33.0
δ_{1H} 9.79	9.740	9.830	31.0	33.0
C ₂ Acetovanillone	7.428	7.480	110.0	113.0
C ₂ Vanillin	7.315	7.388	114.0	117.0
C ₆ Acetovanillone	7.480	7.560	122.5	125.0
C ₆ Vanillin	7.320	7.400	121.0	123.5
C _{3,6} Catechol	6.700	6.762	115.1	117.1
C _{4,5} Catechol	6.580	6.636	118.9	120.8
CH ₃ 4-Methylcatechol	2.090	2.163	19.6	22.2
Ar-CH ₂ -Ar o- <i>p'</i>	3.398	3.511	34.8	37.4
Ar-CH ₂ -Ar p- <i>p'</i>	3.408	3.468	39.4	42.2

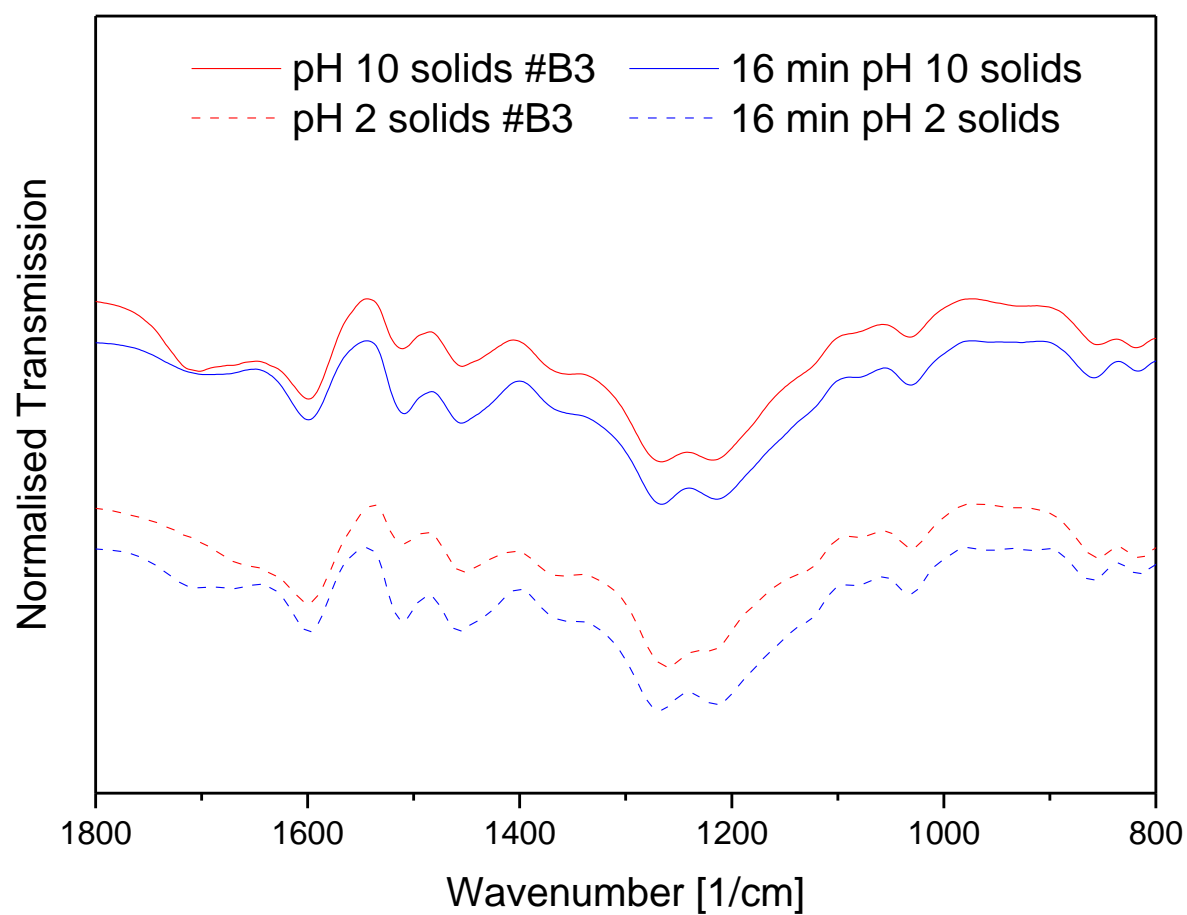


Figure A 30: ATR FT-IR spectra of the solids of run #B3 and #K3 both at $t_{\text{retention}} = 16$ min.

Table A 15: Composition and mass flows of streams defined in Figure 58.

Stream	Components mass flows [kg/h]								
	<i>H₂O</i>	<i>MeOH</i>	<i>HMW</i>	<i>LMW</i>	<i>NaOH</i>	<i>Product</i>	<i>H₂O Solu- bles</i>	<i>CO₂</i>	<i>H₂SO₄</i>
1	810.19	0.00	1620.37	694.44	0.00	0.00	0.00	0.00	0.00
2	651.80	0.00	0.00	0.00	0.00	0.00	0.00	0.00	0.00
3	158.38	0.00	1620.37	694.44	0.00	0.00	0.00	0.00	0.00
101	0.00	6451.57	0.00	0.00	0.00	0.00	0.00	0.00	0.00
102	102.96	0.00	0.00	0.00	0.00	0.00	0.00	0.00	0.00
103	0.00	872.51	0.00	0.00	0.00	0.00	0.00	0.00	0.00
104	0.00	7324.07	0.00	0.00	0.00	0.00	0.00	0.00	0.00
4	158.38	7324.07	1620.37	694.44	0.00	0.00	0.00	0.00	0.00
5	139.51	6451.57	0.00	694.44	0.00	0.00	0.00	0.00	0.00
6	36.55	0.00	0.00	694.44	0.00	0.00	0.00	0.00	0.00
7	18.87	872.51	1620.37	0.00	0.00	0.00	0.00	0.00	0.00
8	18.87	0.00	1620.37	0.00	0.00	0.00	0.00	0.00	0.00
9	14564.47	0.00	0.00	0.00	590.16	0.00	0.00	0.00	0.00
10	14583.33	0.00	1620.37	0.00	590.16	0.00	0.00	0.00	0.00
11	14583.33	0.00	0.00	0.00	590.16	1296.30	324.07	0.00	0.00
12	0.00	0.00	0.00	0.00	0.00	0.00	0.00	324.07	0.00
13	14583.33	0.00	0.00	0.00	590.16	1296.30	324.07	324.07	0.00
14	698.01	0.00	0.00	0.00	28.25	1296.30	0.00	15.51	0.00
201	13885.33	0.00	0.00	0.00	561.91	0.00	324.07	308.56	0.00
202	10968.66	0.00	0.00	0.00	26.56	0.00	0.00	14.58	1.70
203	24853.99	0.00	0.00	0.00	588.47	0.00	324.07	323.15	1.70
15	10968.66	0.00	0.00	0.00	0.00	0.00	0.00	0.00	1.81
16	11666.67	0.00	0.00	0.00	28.25	1296.30	0.00	15.51	1.81
17	698.01	0.00	0.00	0.00	1.69	1296.30	0.00	0.93	0.11
18	629.78	0.00	0.00	0.00	0.00	0.00	0.00	0.00	0.00
19	68.23	0.00	0.00	0.00	1.69	1296.30	0.00	0.93	0.11

Table A 16: Energy streams of the process shown in Figure 58.

Energies			
Heat		Electrical	
Flow #	[kW]	Flow #	[kW]
q1	943.16	e1	10
q2	1623.21	e2	6
q3	839.70	e3	7
q4	568.90	e4	95
q5	634.19	e5	7
q6	17309.58	e6	6
q7	1350.31	e7	5
		e8	6
Sum	20568.42	Sum	142

Table A 17: Need and costs for personnel

Personnel			
Type	<i>Amount</i> [-]	<i>Single cost</i> [€/a]	<i>Cumulative costs</i> [€/a]
Operating Staff	3	60000	180000
Technician	1	60000	60000
Administration (Production and Sales)	3	75000	225000
Engineer	1	90000	90000
Sum			555000

Eigenständigkeitserklärung:

Hiermit versichere ich, die Arbeit selbständig angefertigt und keine anderen als die angegebenen Quellen und Hilfsmittel benutzt zu haben. Es wurden alle wörtlich und inhaltlich übernommenen Stellen als solche kenntlich gemacht und die Satzung des KIT zur Sicherung guter wissenschaftlicher Praxis in ihrer Ausführung vom 27. November 2014 beachtet.

Malte Otromke

Mannheim, d. 15.10.2017